ELECTROCHEMICAL MECHANISMS IN NANO-STRUCTURED GRAPHITIC AND REDOX-ACTIVE POLYMERIC ARCHITECTURES

BY

JINGSHU HUI

DISSERTATION

Submitted in partial fulfillment of the requirements
for the degree of Doctor of Philosophy in Materials Science and Engineering
in the Graduate College of the
University of Illinois at Urbana-Champaign, 2017

Urbana, Illinois

Doctoral Committee:

Associate Professor Shen J. Dillon, Chair
Assistant Professor Joaqu ín Rodr íguez-L ópez, Director of Research
Professor Paul V. Braun
Professor Jianjun Cheng

ABSTRACT

One of the greatest challenges for our modern society is developing efficient and low-cost electrochemical energy storage and conversion systems for stationary and transportation applications. Understanding the detailed electrochemical mechanisms in energy-related materials with new designs and modification methods will help us break the ceiling of current existing systems. The goal of my Ph.D. is to combine the power of versatile electrochemistry techniques and materials with diversified architecture, and explore various mechanisms of different nano-structured energy storage and conversion materials.

The first part of this dissertation explores the application of ultra-thin graphene as an electronically transparent and physically impermeable interface. Outer-sphere reactions on metal substrate-modulated graphene prove the electronic transparency of the graphene interface. Inner-sphere oxygen reduction reaction activity changes demonstrate the electronic coupling between metal substrates and molecular adlayers above graphene. This work provides new strategies for systematically tuning the electrocatalytic reactivity using hybridized electrocatalyst structures. The second part of this dissertation utilizes few layer graphene as an ultra-thin bulk material that can reversibly intercalate alkali ions. The finite thickness of graphene leads to layer number-controlled Li-ion intercalation behavior. Passivating the few layer graphene surface can selectively facilitate stable K-ion intercalation while suppressing the K plating reaction. The last part of this dissertation introduces redox-active polymers and advanced redox-active colloids as electrochemical energy storage carriers, which have shown facile charge transfer kinetics and good charge storage ability. Combining these macromolecular electrolytes with size-exclusion porous membranes provides a potential solution to current ionic conductivity restriction in non-aqueous redox flow batteries.

To my father, mother,

and my husband

ACKNOWLEDGMENTS

All of the work I have accomplished in this dissertation was performed with the scientific and intellectual input from all researchers and advisors, as well as the support from colleagues, families and funding agencies.

I want to first express my sincere gratitude to my advisor, Prof. Joaquín Rodríguez-López, for his instruction, advice, support, and guidance in my five years graduate study. He taught me electrochemistry from zero, helped me build up my knowledge and experience in this field. He led me to establish my own strength in research and opened many doors for me in my career. Thanks to his help and trust, that helped me become who I am right now.

I want to thank my graduate research committee members, Prof. Shen J. Dillon, Prof. Paul V. Braun, and Prof. Jianjun Cheng for their valuable comments and suggestion on my thesis and projects.

I am grateful to all colleagues and lab members in Rodríguez-López group. A big hug to Zachary J. Barton, Burton Simpson, Teresa C. Cristarella for their help when I first came to US and joined this group. Thank for all of the teamwork and collaborations from Zachary J. Barton, Mark Burgess, Elena Montoto Blanco, Dr. Kenneth Hernandez-Burgos, Noah B. Schorr, and Dr. Xuan Zhou. I also appreciate scientific discussions and support from all other group members: Burton Simpson, Marie A. Claudio-Cintron, Mike Counihan, Zachary Gossage, and Mathew L. Kromer. All of the undergraduate student I mentored gave me lots of help on my research project, including Adam Chinderle, Richa Bhargava, Jiarui Zhang, and Annie Jiang, I hereby thank for all of their hard works and supports.

Multidisciplinary research projects cannot be perfect without the valuable effort of collaborators from different field. I would like to express my gratitude to all of my collaborators: Prof. Jeffery S. Moore, Dr. Nagarjuna Gavvalapalli, and Kevin Cheng from University of Illinois at Urbana-Champaign; Prof. Jose L. Mendoza-Cortes, Dr. Srimanta Pakhira, and Oluwagbenga O. Iyiola from Florida State University; and Dr. Joseph A. Dura at NIST Center for Neutron Research.

Thanks for the support from all funding resources: University of Illinois start-up funds; Joint Center for Energy Storage Research, an Energy Innovation Hub funded by the U.S. Department of Energy, Office of Science, Basic Energy Sciences; National Science Foundation under Grant No. DMR-1611268. Thanks for the instruments and facilities in Frederick Seitz Materials Research Laboratory Central Facilities and the Micro and Nanotechnology Laboratory at University of Illinois.

Finally, I want to take this chance to give my special thanks to my mom and dad, who gave me their entire love and support. My family always cheered me up during my study abroad. My deepest gratitude to my husband, Ziyuan Song, for his love, support, and company. I have enjoyed every day I spent with my husband and I am happy to share every success with him.

TABLE OF CONTENTS

CHAPTER 1 INTRODUCTION **1**

1.1 Electrochemical Energy Storage and Conversion Systems and Materials 1

1.2 Graphene and Graphitic Materials for Energy Storage and Conversion 4

1.3 Scope and Organization 7

1.4 References 8

CHAPTER 2 OUTER-SPHERE ELECTRON TRANSFER REACTIONS ON GRAPHENE — KINETIC MODULATION WITH METAL SUBSTRATE **22**

2.1 Introduction 22

2.2 Characterization of Graphene on Au Substrate 25

2.3 Enhanced $Fe(CN)_6^{4-}$ Oxidation Mechanism on Graphene/p-Au 27

2.4 Origins of Localized Modification of Outer-Sphere Electron Transfer Kinetics 30

2.5 Materials and Methods 34

2.6 Conclusion 38

2.7 References 39

CHAPTER 3 INNER-SPHERE ELECTRON TRANSFER REACTIONS ON GRAPHENE — SUB-SURFACE MODULATION OF ELECTROCATALYTIC ACTIVITY **48**

3.1 Introduction 48

3.2 Characterization of Graphene and Metal Substrates 51

3.3 Metal Substrate Effects 54

3.4 Metal Substrate Effects on Molecular Adsorption Layer above Graphene 57

3.5 Materials and Methods 65

3.6 Conclusion 69

3.7 References 71

CHAPTER 4 LI ION INTERCALATION ON FEW-LAYER GRAPHENE — LAYER NUMBER CONTROLLED STAGING MECHANISM AND SOLID ELECTROLYTE EVOLUTION **80**

4.1 Introduction 80

4.2 Few Layer Graphene Characterization 83

4.3 Patterning Few Layer Graphene 85

4.4 Layer Number Dependent Intercalation Behavior 87

4.5 *In-Situ* Monitoring SEI Growth *via* SECM 93

4.6 Li^+ Flux Changing During Intercalation 96

4.7 Materials and Methods 98

4.8 Conclusion 102

4.9 References 103

CHAPTER 5 ALKALI INTERCALATION ON MULTILAYER GRAPHENE — K ION (CO-)INTERCALATION **111**

5.1 Introduction 111

5.2 K ion (co-)intercalation on MLG 113

5.3 Detecting Potassium Ion Gradients at a Model Graphitic Interface 119

5.4 Materials and Methods 128

5.5 References 132

CHAPTER 6 REDOX ACTIVE POLYMERIC MATERIALS AS ENERGY STORAGE CARRIERS **138**

6.1 Introduction 138

6.2 Characterization of RAPs 1-5 142

6.3 Electrochemical Characterization of RAPs 1-5.....143
6.4 Charge storage in RAPs.....147
6.5 Size-Based Selectivity of COTS Porous Separators.....150
6.6 Charge-Discharge Property of Proxy Non-Aqueous Flow Cell.....153
6.7 RAC Monolayer Fabrication.....155
6.8 RAC Monolayer Reactivity.....158
6.9 Materials and Methods.....159
6.10 Conclusion.....162
6.11 References.....164

APPENDIX A SUPPLEMENTARY INFORMATION OF CHAPTER 3.....**172**

APPENDIX B SUPPLEMENTARY INFORMATION OF CHAPTER 4.....**176**

B.1 Calculation of De-intercalation Charge and Theoretical Charge for FLG.....177

APPENDIX C SUPPLEMENTARY INFORMATION OF CHAPTER 5.....**180**

C.1 Stripping-Based Approach to HOPG.....183
C.2 References.....187

APPENDIX D SUPPLEMENTARY INFORMATION OF CHAPTER 6.....**188**

D.1 General Information.....188
D.2 Synthesis of Monomer and Polymers.....190
D.3 Redox Active Polymer Characterization.....192
D.4 Redox Active Polymer Physical Properties.....194
D.5 Electrochemical Characterization of RAPs 1-5.....197
D.6 Charge Storage in RAPs.....200
D.7 Hindered RAP Transport Across COTS Separators.....204

D.8 Charge/Discharge Behavior in a Proxy Non-Aqueous Redox Flow Cell 209

D.9 References 212

CHAPTER 1

INTRODUCTION

1.1 Electrochemical Energy Storage and Conversion Systems and Materials

One of the greatest challenges for our modern society is developing efficient and low-cost electrochemical energy storage and conversion systems for stationary and transportation applications.[1] In these cases, energy storage and conversion devices, including fuel cells, batteries, and supercapacitors, play an important role in clean and efficient applications of electrochemical energy.[2] Among them, fuel cells, Li-ion batteries, and redox flow batteries are good examples for application in different scales in transportation, portable, and stationary storage devices, and are the focus of this dissertation.

A fuel cell is a galvanostatic electrochemical device, in which the free chemical energy of fuels is converted into electrical energy. Among them, the most well studied system is the proton exchange membrane fuel cell (PEMFC), in which hydrogen and air are used as fuels with heat and water/steam as byproducts.[3] During operation, the anodic hydrogen oxidation and cathodic oxygen reduction reactions happen on the surface of an electrocatalyst. The major challenge that limits the performance of PEMFC is the activity of the cathode, where the oxygen reduction reaction (ORR) on the cathode is more than six order of magnitude slower than hydrogen oxidation on the anode.[4] Recent progress in ORR electrocatalysis has focused on Pt-based catalysts with outstanding performance, such as different Pt-transition metal alloys (*e.g.* Pt_3Ni and Pt_3Co),[5] and ordered Pt structures with controlled shapes (*e.g.* nanocrystals).[6-8] Other efforts have led to the development of less expensive catalysts, including carbon-based non-noble metal

composites (*e.g.* Fe/C/N type materials)[9-11] and metal-free doped carbon materials (*e.g.* doped graphene).[12-15]

The traditional Li ion battery (LIB) is an electrochemical energy storage device which consists of metal-oxide cathode, graphite anode, electrolyte, and membrane separator. It operates by reversibly (de-)intercalating Li ions into layer-structured cathode and anode during charge/discharge cycles.[16-18] Due to the exceptional characteristics of Li, including the lowest reduction potential, third lightest element weight, and smallest ionic radius of a singly charged ion, LIBs have high gravimetric and volumetric capacity and power density.[19] Traditional cathode materials are transition metal oxides, *e.g.* $LiCoO_2$, which have high volumetric capacity, high discharge voltage, and good cycling performance.[20, 21] Replacing the Co with other transition metals can grant reduced cost (*e.g.* $LiNiO_2$, $LiMnO_2$)[22, 23] or enhanced structural stability (*e.g.* $LiNi_xCo_yMn_zO_2$).[24] Another group of cathode material is polyanion electrodes (e.g. $LiFePO_4$), which have high thermal stability and high power capacity but low average potential.[19] As for anode materials, instead of directly using Li metal (which forms dendrites during cycling), graphitic materials were commonly used in LIBs to avoid the short circuiting effect.[25] Li storage in graphite follows a staging-type mechanism with a fully intercalated stage-1 compound of LiC_6.[26, 27] During early stage cycling, a layer of solid-electrolyte interphase forms on the electrode surface, which can prevent further solvent and electrolyte degradation while allowing Li ion transport.[28, 29] This material has the advantage of low cost, high electrical conductivity, low delithiation potential, and low volume change during cycling.[19] Compared to the highly ordered graphitic structure, hard carbon materials are a new generation of carbon anodes. The decreased grain size and disordered orientation allow hard carbon to maintain high gravimetric capacity and stability.[30, 31] Another important anode material is Si, which forms

alloys with Li during lithiation.[32] Compared to carbon materials, Si anodes have the advantage of about 10 times higher specific capacity than graphite, but undergo large volume changes during lithiation.[33]

Redox flow batteries (RFBs) are grid-scale energy storage systems, which separate the energy density and capacity need of traditional batteries by using solid electrodes and flowable electrolyte for both anode and cathode chambers.[34] Traditional RFBs operate in aqueous systems, in which an ion selective membrane is used to separate positive and negative redox species. Examples of aqueous RFBs (ARFBs) are all-vanadium (1.26 V) and Zn/Br (1.85 V) systems.[35, 36] Restricted by the thermodynamic limits of the aqueous solution potential window, together with the high molecular weight and high cost of electrolytes, ARFBs technologies have not seen broad market penetration.[37] Replacing aqueous soluble electrolytes with nonaqueous-based redox molecules offers the benefits of a wide working potential range, high energy density, and chemical flexibility.[38] Nonaqueous RFBs (NRFBs) can operate at a potential window as high as 4.52 V using biphenyl radical anion and octafluoronaphthalene radical cation prototype cell.[38] These small redox molecule NRFBs system still suffer from high internal resistance and low ionic conductivity.[39] Recently our group has proved that by using macromolecular redox-active polymers (RAPs) as electrolytes and a size-selective membrane, the ionic conductivity of NRFBs can be largely enhanced, while still maintaining 90 % rejection of active species crossing during operation.[40] RAPs and the integrated redox-active colloids (RACs) have shown facile charge transfer kinetics, good charge storage abilities, and tunable sizes, which make them great candidates for next generation NRFBs.[40-47]

Among all of the materials introduced above for different energy storage and conversion systems, this dissertation focuses on application and nanoscale engineering of graphene/graphitic type materials, as well as synthesized redox-active polymeric materials.

1.2 Graphene and Graphitic Materials for Energy Storage and Conversion[†]

1.2.1 Graphene Materials – Properties and Applications

Graphene, a one atom thick, two-dimensional sheet of sp^2-hybridized carbon, has attracted great attention recently.[48, 49] The extremely thin graphene layer exhibits high electrical conductivity (~2,000 S cm^{-1}),[50] exceptional electron mobility (200,000 cm^2 V^{-1} s^{-1}),[51, 52] strong mechanical strength (1.0 TPa),[53] high thermal conductivity (above 3000 W m^{-1} K^{-1}),[54] chemical inertness, high specific surface area (~1,500 m^2 g^{-1}),[55] and high transparency (~2.3 % decrease in transmittance for each layer).[56] These properties make graphene an attractive platform for energy storage and conversion applications,[57, 58] including electrocatalysis,[59] Li ion batteries,[60-63] supercapacitors,[64] and dye-sensitized solar cells.[65]

1.2.2 Fabrication of Graphene

Multiple methods have been applied to obtain graphene analogue materials, including single layer graphene (SLG), multilayer graphene (MLG), and reduced graphene oxide (r-GO). Exfoliation and chemical vapor deposition (CVD) based techniques are widely used for fabrication of graphene samples for electrochemical energy-related applications.

[†] Part of this section is adapted from the publication: Hui, J. S.; Zhou, X.; Bhargava, R.; Chinderle, A.; Zhang, J. R.; Rodriguez-Lopez, J. Kinetic Modulation of Outer-Sphere Electron Transfer Reactions on Graphene Electrode with a Sub-surface Metal Substrate. *Electrochim. Acta* 2016, *211*, 1016-1023.

The first method discovered to yield a reproducible preparation of graphene was mechanical exfoliation, which used Scotch tape to peel off thin graphite flakes multiple times and transfer them to a certain substrate for further examination.[66, 67] Since the graphene sheet directly originates from graphite materials, this method provides graphene sheets with the best quality, but is hard to scale for mass production.

Another exfoliation method is liquid phase exfoliation. The modified Hummers method is one of the most commonly used methods,[68] which utilizes the hydrophobicity of graphite oxide and ultrasonication to exfoliation graphene oxide (GO) flakes, and reduce them to r-GO form.[69] Due to the surface energy similarities, sonicating graphite in N-methyl-pyrrolidone solvent also leads to the production of single to few-layer graphene sheets.[70] Liquid phase exfoliation methods have the advantage of large quantity production of graphene type materials, but have poor control of chemical defects and layer thicknesses.

Compared to previous exfoliation based methods, chemical vapor deposition (CVD) methods provide alternative solutions to fabricate large-area uniform polycrystalline graphene films.[71] Ni thin films were first applied as metal catalysts for graphene synthesis, which catalyze carbon precursor (e.g. CH_4) decomposition at high temperatures (1000 ℃) under low pressure.[72, 73] The graphene formation is attributed to good carbon solubility in Ni, which segregate out during the controlled cooling steps.[73, 74] This method provides a fabrication method for few layer graphene samples, which can be easily transferred onto various substrates via wet-transfer procedures.[74] Cu foil soon became a popular alternative deposition catalyst for single and double layer graphene fabrication[75] due to its zero carbon solubility and self-limiting growth mechanism.[76, 77] Performing CVD growth in ambient pressure also leads to multilayer graphene samples of variable thickness.[78, 79] Cu-catalyzed CVD growth methods are capable of

synthesizing graphene with extremely large area single layer graphene sheets (*e.g.* 30-inch)[80] and large millimeter sized single-crystal graphene (*e.g.* 5 mm grains).[81-83] Compared to exfoliation techniques, CVD grown graphene samples have the advantage of controllable size, thickness, and morphology. Therefore, this method was chosen to fabricate the single and multilayer graphene samples used in this dissertation.

1.2.3 Nanoscale Engineering Methods of Graphene/Graphitic materials

Other than directly controlling the size and morphology of graphene from various synthesis procedures, multiple modification methods have been used to functionalize graphene. Hence graphene has found several niches and applications including large area flexible electronics, catalysts, energy-related materials, sensors, and supercapacitors.[84] Surface modification, substitutional doping, and substrate modulation are three commonly used strategies for graphene functionalization.

Surface modification: Both covalent and non-covalent methods are applied to tune the surface property of graphene samples by introducing additional function groups.[85] Covalent modification of graphene is usually based on the unsaturated π bonds of carbon and selected functional groups with either a free radical or dienophiles as the anchor,[86] transforming sp^2 hybridized carbon to sp^3. Non-covalent functionalization of graphene is usually done through π-π interactions, van der Waals force, electrostatic interactions, etc.[84] For example, attaching porphyrins and phthalocyanine complexes largely improve the ORR-catalytic property of the graphene substrate.[87, 88] TiO_2 nanoparticles and r-GO hybridized LIB anodes exhibit high electrical conductivity, good cycling stability, and high capacity.[89]

Substitutional doping: Doping is a promising technique to tailor the electronic property of graphene samples *via* charge injection and extraction from the substituted sites.[85] Introducing

nitrogen and boron heteroatoms create n- and p-type doping of graphene, which alter graphene's work function,[90] magnetic moment,[91] and photoluminescence properties.[92] These doped materials also show promising activity as low cost electrocatalysts for oxygen reduction and hydrogen and oxygen evolution reactions.[93]

Substrate modulation: Due to the atomically-thin thickness, the perturbation of graphene is known in different contexts. The Raman spectrum[94] and bandgap opening[95] of epitaxial graphene are affected by the graphene-substrate interaction, which can be sufficiently strong to change the graphene lattice symmetry. Chemical functionalities such as underlayer dielectrics can also change the electronic structure of graphene, thus modifying its carrier mobility.[96, 97] The electron-transfer chemistries for both outer-sphere and inner-sphere catalytic reactions on graphene have shown kinetic dependence on underlying metal substrates.[98, 99]

1.3 Scope and Organization

The goal of my Ph.D. is to combine the power of versatile electrochemical techniques and diversified materials architecture, and explore various electrochemical mechanisms of different nano-structured energy storage and conversion materials. Different ultra-thin graphene architectures and synthetic redox-active polymers are studied in this dissertation. Chapters 2-5 focus on graphene-based materials for ORR catalysis and alkali ion battery applications. Chapters 2-3 utilize ultra-thin graphene as an interface and explore the impact of substrate on outer-sphere (Chapter 2) and inner-sphere catalytic reaction (Chapter 3) kinetics on graphene. Chapters 4-5 treat few layer graphene as an ultra-thin bulk material and cover Li ion intercalation (Chapter 4) and K ion intercalation (Chapter 5) mechanisms in this material. Chapter 6 studies the electrochemical properties of viologen-based redox-active polymers as well as cross-linked

3D redox-active colloids and discusses the application of them as energy storage materials for NRFBs.

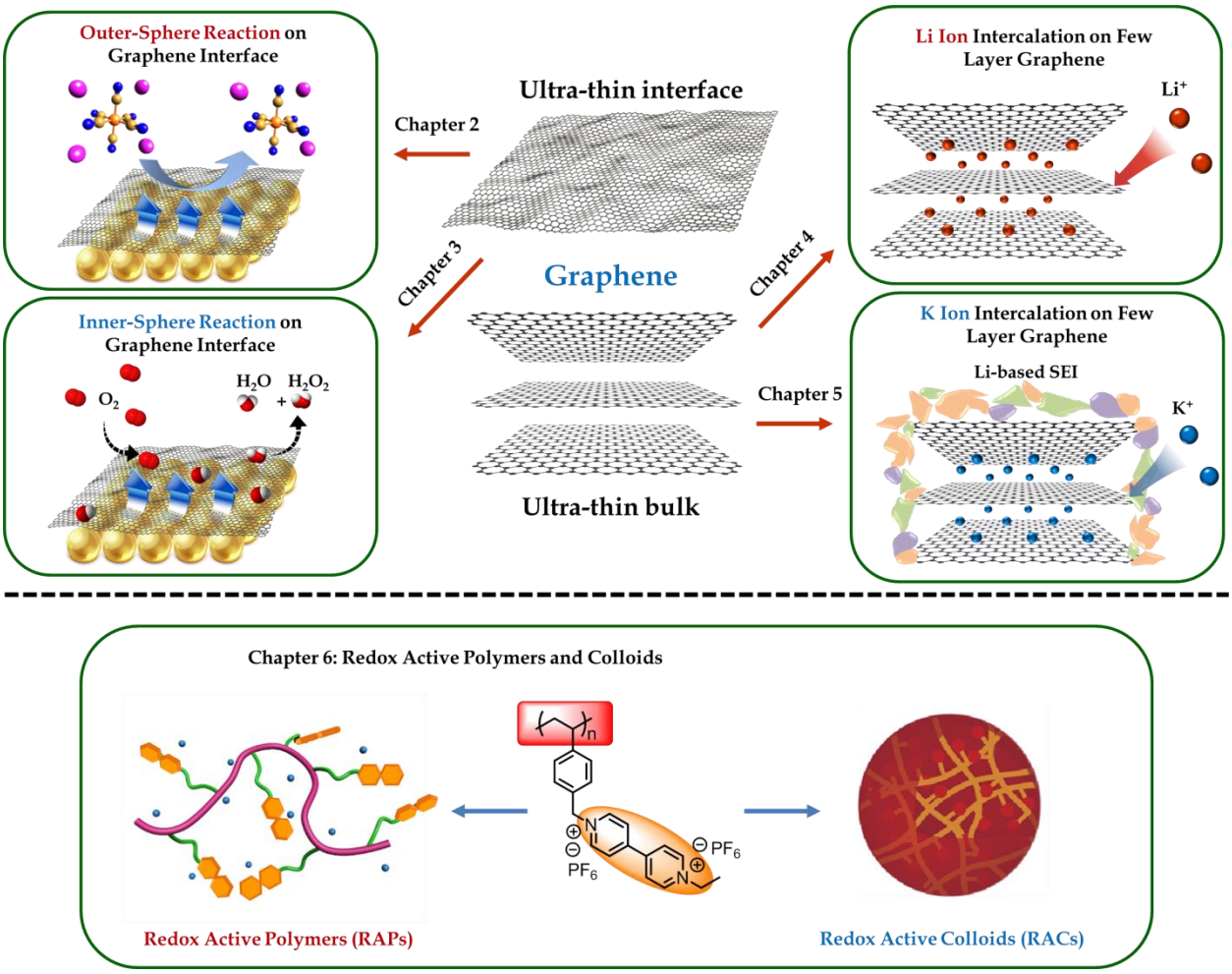

Figure 1.1 Organization of the dissertation.

1.4 References

1. Whittingham, M. S. Materials Challenges Facing Electrical Energy Storage. *MRS Bulletin* **2011**, *33*, 411-419.

2. Goodenough, J. B.; Abruna, H. D.; Buchanan, M. V. *Basic Research Needs for Electrical Energy Storage. Report of the Basic Energy Sciences Workshop on Electrical Energy Storage*,

April 2-4, 2007; TRN: US200816%%791 United States 10.2172/935429; DOESC (USDOE Office of Science (SC)): 2007; p Medium: ED.

3. Whittingham, M. S.; Savinell, R. F.; Zawodzinski, T. Introduction: Batteries and fuel cells. *Chemical Reviews* **2004**, *104*, 4243-4244.

4. Debe, M. K. Electrocatalyst approaches and challenges for automotive fuel cells. *Nature* **2012**, *486*, 43-51.

5. Stamenkovic, V. R.; Mun, B. S.; Arenz, M.; Mayrhofer, K. J. J.; Lucas, C. A.; Wang, G. F.; Ross, P. N.; Markovic, N. M. Trends in electrocatalysis on extended and nanoscale Pt-bimetallic alloy surfaces. *Nat Mater* **2007**, *6*, 241-247.

6. Chen, Q. S.; Vidal-Iglesias, F. J.; Solla-Gullon, J.; Sun, S. G.; Feliu, J. M. Role of surface defect sites: from Pt model surfaces to shape-controlled nanoparticles. *Chem Sci* **2012**, *3*, 136-147.

7. Macia, M. D.; Campina, J. M.; Herrero, E.; Feliu, J. M. On the kinetics of oxygen reduction on platinum stepped surfaces in acidic media. *Journal of Electroanalytical Chemistry* **2004**, *564*, 141-150.

8. Stamenkovic, V.; Mun, B. S.; Mayrhofer, K. J. J.; Ross, P. N.; Markovic, N. M.; Rossmeisl, J.; Greeley, J.; Norskov, J. K. Changing the activity of electrocatalysts for oxygen reduction by tuning the surface electronic structure. *Angew Chem Int Edit* **2006**, *45*, 2897-2901.

9. Jaouen, F.; Proietti, E.; Lefevre, M.; Chenitz, R.; Dodelet, J. P.; Wu, G.; Chung, H. T.; Johnston, C. M.; Zelenay, P. Recent advances in non-precious metal catalysis for oxygen-reduction reaction in polymer electrolyte fuel cells. *Energy & Environmental Science* **2011**, *4*, 114-130.

10. Bezerra, C. W. B.; Zhang, L.; Lee, K. C.; Liu, H. S.; Marques, A. L. B.; Marques, E. P.; Wang, H. J.; Zhang, J. J. A review of Fe-N/C and Co-N/C catalysts for the oxygen reduction reaction. *Electrochim Acta* **2008**, *53*, 4937-4951.

11. Chen, Z. W.; Higgins, D.; Yu, A. P.; Zhang, L.; Zhang, J. J. A review on non-precious metal electrocatalysts for PEM fuel cells. *Energy & Environmental Science* **2011**, *4*, 3167-3192.

12. Daems, N.; Sheng, X.; Vankelecom, I. F. J.; Pescarmona, P. P. Metal-free doped carbon materials as electrocatalysts for the oxygen reduction reaction. *J Mater Chem A* **2014**, *2*, 4085-4110.

13. Mamtani, K.; Ozkan, U. S. Heteroatom-Doped Carbon Nanostructures as Oxygen Reduction Reaction Catalysts in Acidic Media: An Overview. *Catal Lett* **2015**, *145*, 436-450.

14. Jiang, R. Z.; Tran, D. T.; McClure, J.; Chu, D. Heat-treated hemin supported on graphene nanoplatelets for the oxygen reduction reaction. *Electrochem Commun* **2012**, *19*, 73-76.

15. Ding, W.; Wei, Z. D.; Chen, S. G.; Qi, X. Q.; Yang, T.; Hu, J. S.; Wang, D.; Wan, L. J.; Alvi, S. F.; Li, L. Space-Confinement-Induced Synthesis of Pyridinic- and Pyrrolic-Nitrogen-Doped Graphene for the Catalysis of Oxygen Reduction. *Angew Chem Int Edit* **2013**, *52*, 11755-11759.

16. Liu, C.; Li, F.; Ma, L. P.; Cheng, H. M. Advanced Materials for Energy Storage. *Adv Mater* **2010**, *22*, E28-+.

17. Arico, A. S.; Bruce, P.; Scrosati, B.; Tarascon, J. M.; Van Schalkwijk, W. Nanostructured materials for advanced energy conversion and storage devices. *Nat Mater* **2005**, *4*, 366-377.

18. Scrosati, B.; Garche, J. Lithium batteries: Status, prospects and future. *Journal of Power Sources* **2010**, *195*, 2419-2430.

19. Nitta, N.; Wu, F. X.; Lee, J. T.; Yushin, G. Li-ion battery materials: present and future. *Mater Today* **2015**, *18*, 252-264.

20. Mizushima, K.; Jones, P. C.; Wiseman, P. J.; Goodenough, J. B. Lixcoo2 "(Oless-Thanxless-Than-or-Equal-To1) - a New Cathode Material for Batteries of High-Energy Density. *Mater Res Bull* **1980**, *15*, 783-789.

21. Du Pasquier, A.; Plitz, I.; Menocal, S.; Amatucci, G. A comparative study of Li-ion battery, supercapacitor and nonaqueous asymmetric hybrid devices for automotive applications. *Journal of Power Sources* **2003**, *115*, 171-178.

22. Rougier, A.; Gravereau, P.; Delmas, C. Optimization of the composition of the Li1-zNi1+zO2 electrode materials: Structural, magnetic, and electrochemical studies. *J Electrochem Soc* **1996**, *143*, 1168-1175.

23. Armstrong, A. R.; Bruce, P. G. Synthesis of layered LiMnO2 as an electrode for rechargeable lithium batteries. *Nature* **1996**, *381*, 499-500.

24. Yabuuchi, N.; Ohzuku, T. Novel lithium insertion material of LiCo1/3Ni1/3Mn1/3O2 for advanced lithium-ion batteries. *Journal of Power Sources* **2003**, *119*, 171-174.

25. Li, Z.; Huang, J.; Liaw, B. Y.; Metzler, V.; Zhang, J. B. A review of lithium deposition in lithium-ion and lithium metal secondary batteries. *Journal of Power Sources* **2014**, *254*, 168-182.

26. Aurbach, D.; Markovsky, B.; Weissman, I.; Levi, E.; Ein-Eli, Y. On the correlation between surface chemistry and performance of graphite negative electrodes for Li ion batteries. *Electrochim Acta* **1999**, *45*, 67-86.

27. Levi, M. D.; Aurbach, D. Simultaneous measurements and modeling of the electrochemical impedance and the cyclic voltammetric characteristics of graphite electrodes doped with lithium. *J Phys Chem B* **1997**, *101*, 4630-4640.

28. Agubra, V. A.; Fergus, J. W. The formation and stability of the solid electrolyte interface on the graphite anode. *Journal of Power Sources* **2014**, *268*, 153-162.

29. Zhang, S. S.; Ding, M. S.; Xu, K.; Allen, J.; Jow, T. R. Understanding solid electrolyte interface film formation on graphite electrodes. *Electrochem Solid St* **2001**, *4*, A206-A208.

30. Ni, J. F.; Huang, Y. Y.; Gao, L. J. A high-performance hard carbon for Li-ion batteries and supercapacitors application. *Journal of Power Sources* **2013**, *223*, 306-311.

31. Kaskhedikar, N. A.; Maier, J. Lithium Storage in Carbon Nanostructures. *Adv Mater* **2009**, *21*, 2664-2680.

32. Hatchard, T. D.; Dahn, J. R. In situ XRD and electrochemical study of the reaction of lithium with amorphous silicon. *J Electrochem Soc* **2004**, *151*, A838-A842.

33. Chan, M. K. Y.; Wolverton, C.; Greeley, J. P. First Principles Simulations of the Electrochemical Lithiation and Delithiation of Faceted Crystalline Silicon. *Journal of the American Chemical Society* **2012**, *134*, 14362-14374.

34. Dunn, B.; Kamath, H.; Tarascon, J. M. Electrical Energy Storage for the Grid: A Battery of Choices. *Science* **2011**, *334*, 928-935.

35. Bartolozzi, M. Development of Redox Flow Batteries - a Historical Bibliography. *Journal of Power Sources* **1989**, *27*, 219-234.

36. Skyllas-Kazacos, M.; Rychcik, M.; Robins, R. G.; Fane, A. G.; Green, M. A. New All-Vanadium Redox Flow Cell. *J Electrochem Soc* **1986**, *133*, 1057-1058.

37. Yang, Z. G.; Zhang, J. L.; Kintner-Meyer, M. C. W.; Lu, X. C.; Choi, D. W.; Lemmon, J. P.; Liu, J. Electrochemical Energy Storage for Green Grid. *Chemical Reviews* **2011**, *111*, 3577-3613.

38. Gong, K.; Fang, Q. R.; Gu, S.; Li, S. F. Y.; Yan, Y. S. Nonaqueous redox-flow batteries: organic solvents, supporting electrolytes, and redox pairs. *Energy & Environmental Science* **2015**, *8*, 3515-3530.

39. Shin, S. H.; Yun, S. H.; Moon, S. H. A review of current developments in non-aqueous redox flow batteries: characterization of their membranes for design perspective. *Rsc Advances* **2013**, *3*, 9095-9116.

40. Nagarjuna, G.; Hui, J. S.; Cheng, K. J.; Lichtenstein, T.; Shen, M.; Moore, J. S.; Rodriguez-Lopez, J. Impact of Redox-Active Polymer Molecular Weight on the Electrochemical Properties and Transport Across Porous Separators in Nonaqueous Solvents. *Journal of the American Chemical Society* **2014**, *136*, 16309-16316.

41. Burgess, M.; Chenard, E.; Hernandez-Burgos, K.; Nagarjuna, G.; Assary, R. S.; Hui, J. S.; Moore, J. S.; Rodriguez-Lopez, J. Impact of Backbone Tether Length and Structure on the Electrochemical Performance of Viologen Redox Active Polymers. *Chem Mater* **2016**, *28*, 7362-7374.

42. Burgess, M.; Hernandez-Burgos, K.; Cheng, K. J.; Moore, J. S.; Rodriguez-Lopez, J. Impact of electrolyte composition on the reactivity of a redox active polymer studied through surface interrogation and ion-sensitive scanning electrochemical microscopy. *Analyst* **2016**, *141*, 3842-3850.

43. Burgess, M.; Hernandez-Burgos, K.; Simpson, B. H.; Lichtenstein, T.; Avetian, S.; Nagarjuna, G.; Cheng, K. J.; Moore, J. S.; Rodriguez-Lopez, J. Scanning Electrochemical Microscopy and Hydrodynamic Voltammetry Investigation of Charge Transfer Mechanisms on Redox Active Polymers. *J Electrochem Soc* **2016**, *163*, H3006-H3013.

44. Burgess, M.; Moore, J. S.; Rodriguez-Lopez, J. Redox Active Polymers as Soluble Nanomaterials for Energy Storage. *Accounts Chem Res* **2016**, *49*, 2649-2657.

45. Gossage, Z. T.; Schorr, N. B.; Hernandez-Burgos, K.; Hui, J.; Simpson, B. H.; Montoto, E. C.; Rodriguez-Lopez, J. Interrogating Charge Storage on Redox Active Colloids via Combined Raman Spectroscopy and Scanning Electrochemical Microscopy. *Langmuir* **2017**.

46. Montoto, E. C.; Nagarjuna, G.; Hui, J. S.; Burgess, M.; Sekerak, N. M.; Hernandez-Burgos, K.; Wei, T. S.; Kneer, M.; Grolman, J.; Cheng, K. J.; Lewis, J. A.; Moore, J. S.; Rodriguez-Lopez, J. Redox Active Colloids as Discrete Energy Storage Carriers. *Journal of the American Chemical Society* **2016**, *138*, 13230-13237.

47. Montoto, E. C.; Nagarjuna, G.; Moore, J. S.; Rodríguez-López, J. Redox Active Polymers for Non-Aqueous Redox Flow Batteries: Validation of the Size-Exclusion Approach. *J Electrochem Soc* **2017**, *164*, A1688-A1694.

48. Geim, A. K.; Novoselov, K. S. The rise of graphene. *Nat Mater* **2007**, *6*, 183-191.

49. Geim, A. K. Graphene: Status and Prospects. *Science* **2009**, *324*, 1530-1534.

50. Novoselov, K. S.; Falko, V. I.; Colombo, L.; Gellert, P. R.; Schwab, M. G.; Kim, K. A roadmap for graphene. *Nature* **2012**, *490*, 192-200.

51. Bolotin, K. I.; Sikes, K. J.; Jiang, Z.; Klima, M.; Fudenberg, G.; Hone, J.; Kim, P.; Stormer, H. L. Ultrahigh electron mobility in suspended graphene. *Solid State Communications* **2008**, *146*, 351-355.

52. Du, X.; Skachko, I.; Barker, A.; Andrei, E. Y. Approaching ballistic transport in suspended graphene. *Nat Nanotechnol* **2008**, *3*, 491-495.

53. Lee, C.; Wei, X. D.; Kysar, J. W.; Hone, J. Measurement of the elastic properties and intrinsic strength of monolayer graphene. *Science* **2008**, *321*, 385-388.

54. Balandin, A. A.; Ghosh, S.; Bao, W. Z.; Calizo, I.; Teweldebrhan, D.; Miao, F.; Lau, C. N. Superior thermal conductivity of single-layer graphene. *Nano Lett* **2008**, *8*, 902-907.

55. Raccichini, R.; Varzi, A.; Passerini, S.; Scrosati, B. The role of graphene for electrochemical energy storage. *Nat Mater* **2015**, *14*, 271-279.

56. Nair, R. R.; Blake, P.; Grigorenko, A. N.; Novoselov, K. S.; Booth, T. J.; Stauber, T.; Peres, N. M. R.; Geim, A. K. Fine structure constant defines visual transparency of graphene. *Science* **2008**, *320*, 1308-1308.

57. Zhu, J. X.; Yang, D.; Yin, Z. Y.; Yan, Q. Y.; Zhang, H. Graphene and Graphene-Based Materials for Energy Storage Applications. *Small* **2014**, *10*, 3480-3498.

58. Jing, Y.; Zhou, Z.; Cabrera, C. R.; Chen, Z. F. Graphene, inorganic graphene analogs and their composites for lithium ion batteries. *J Mater Chem A* **2014**, *2*, 12104-12122.

59. Qu, L.; Liu, Y.; Baek, J.-B.; Dai, L. Nitrogen-Doped Graphene as Efficient Metal-Free Electrocatalyst for Oxygen Reduction in Fuel Cells. *Acs Nano* **2010**, *4*, 1321-1326.

60. Petnikota, S.; Rotte, N. K.; Srikanth, V. V. S. S.; Kota, B. S. R.; Reddy, M. V.; Loh, K. P.; Chowdari, B. V. R. Electrochemical studies of few-layered graphene as an anode material for Li ion batteries. *J Solid State Electr* **2014**, *18*, 941-949.

61. Hui, J.; Burgess, M.; Zhang, J.; Rodríguez-López, J. Layer number dependence of Li^+ intercalation on few-layer graphene and electrochemical imaging of its solid–electrolyte interphase evolution. *Acs Nano* **2016**, *10*, 4248-4257.

62. Guo, P.; Song, H. H.; Chen, X. H. Electrochemical performance of graphene nanosheets as anode material for lithium-ion batteries. *Electrochem Commun* **2009**, *11*, 1320-1324.

63. Yoo, E.; Kim, J.; Hosono, E.; Zhou, H.; Kudo, T.; Honma, I. Large reversible Li storage of graphene nanosheet families for use in rechargeable lithium ion batteries. *Nano Lett* **2008**, *8*, 2277-2282.

64. Zhu, Y.; Murali, S.; Stoller, M. D.; Ganesh, K. J.; Cai, W.; Ferreira, P. J.; Pirkle, A.; Wallace, R. M.; Cychosz, K. A.; Thommes, M.; Su, D.; Stach, E. A.; Ruoff, R. S. Carbon-Based Supercapacitors Produced by Activation of Graphene. *Science* **2011**, *332*, 1537-1541.

65. Wang, X.; Zhi, L.; Müllen, K. Transparent, Conductive Graphene Electrodes for Dye-Sensitized Solar Cells. *Nano Lett* **2008**, *8*, 323-327.

66. Novoselov, K. S.; Geim, A. K.; Morozov, S. V.; Jiang, D.; Zhang, Y.; Dubonos, S. V.; Grigorieva, I. V.; Firsov, A. A. Electric field effect in atomically thin carbon films. *Science* **2004**, *306*, 666-669.

67. Novoselov, K. S.; Jiang, D.; Schedin, F.; Booth, T. J.; Khotkevich, V. V.; Morozov, S. V.; Geim, A. K. Two-dimensional atomic crystals. *P Natl Acad Sci USA* **2005**, *102*, 10451-10453.

68. Hummers, W. S.; Offeman, R. E. Preparation of Graphitic Oxide. *Journal of the American Chemical Society* **1958**, *80*, 1339-1339.

69. Stankovich, S.; Dikin, D. A.; Piner, R. D.; Kohlhaas, K. A.; Kleinhammes, A.; Jia, Y.; Wu, Y.; Nguyen, S. T.; Ruoff, R. S. Synthesis of graphene-based nanosheets via chemical reduction of exfoliated graphite oxide. *Carbon* **2007**, *45*, 1558-1565.

70. Hernandez, Y.; Nicolosi, V.; Lotya, M.; Blighe, F. M.; Sun, Z. Y.; De, S.; McGovern, I. T.; Holland, B.; Byrne, M.; Gun'ko, Y. K.; Boland, J. J.; Niraj, P.; Duesberg, G.; Krishnamurthy, S.; Goodhue, R.; Hutchison, J.; Scardaci, V.; Ferrari, A. C.; Coleman, J. N. High-yield production of graphene by liquid-phase exfoliation of graphite. *Nat Nanotechnol* **2008**, *3*, 563-568.

71. Obraztsov, A. N. Chemical Vapour Deposition Making Graphene on a Large Scale. *Nat Nanotechnol* **2009**, *4*, 212-213.

72. Obraztsov, A. N.; Obraztsova, E. A.; Tyurnina, A. V.; Zolotukhin, A. A. Chemical vapor deposition of thin graphite films of nanometer thickness. *Carbon* **2007**, *45*, 2017-2021.

73. Reina, A.; Thiele, S.; Jia, X. T.; Bhaviripudi, S.; Dresselhaus, M. S.; Schaefer, J. A.; Kong, J. Growth of Large-Area Single- and Bi-Layer Graphene by Controlled Carbon Precipitation on Polycrystalline Ni Surfaces. *Nano Res* **2009**, *2*, 509-516.

74. Huang, L.; Chang, Q. H.; Guo, G. L.; Liu, Y.; Xie, Y. Q.; Wang, T.; Ling, B.; Yang, H. F. Synthesis of high-quality graphene films on nickel foils by rapid thermal chemical vapor deposition. *Carbon* **2012**, *50*, 551-556.

75. Li, X. S.; Cai, W. W.; An, J. H.; Kim, S.; Nah, J.; Yang, D. X.; Piner, R.; Velamakanni, A.; Jung, I.; Tutuc, E.; Banerjee, S. K.; Colombo, L.; Ruoff, R. S. Large-Area Synthesis of High-Quality and Uniform Graphene Films on Copper Foils. *Science* **2009**, *324*, 1312-1314.

76. Lin, H. C.; Chen, Y. Z.; Wang, Y. C.; Chueh, Y. L. The Essential Role of Cu Vapor for the Self-Limit Graphene via the Cu Catalytic CVD Method. *J Phys Chem C* **2015**, *119*, 6835-6842.

77. Zhao, P.; Kumamoto, A.; Kim, S.; Chen, X.; Hou, B.; Chiashi, S.; Einarsson, E.; Ikuhara, Y.; Maruyama, S. Self-Limiting Chemical Vapor Deposition Growth of Monolayer Graphene from Ethanol. *J Phys Chem C* **2013**, *117*, 10755-10763.

78. Robertson, A. W.; Warner, J. H. Hexagonal Single Crystal Domains of Few-Layer Graphene on Copper Foils. *Nano Lett* **2011**, *11*, 1182-1189.

79. Bhaviripudi, S.; Jia, X. T.; Dresselhaus, M. S.; Kong, J. Role of Kinetic Factors in Chemical Vapor Deposition Synthesis of Uniform Large Area Graphene Using Copper Catalyst. *Nano Lett* **2010**, *10*, 4128-4133.

80. Bae, S.; Kim, H.; Lee, Y.; Xu, X. F.; Park, J. S.; Zheng, Y.; Balakrishnan, J.; Lei, T.; Kim, H. R.; Song, Y. I.; Kim, Y. J.; Kim, K. S.; Ozyilmaz, B.; Ahn, J. H.; Hong, B. H.; Iijima, S. Roll-to-roll production of 30-inch graphene films for transparent electrodes. *Nat Nanotechnol* **2010**, *5*, 574-578.

81. Hao, Y. F.; Bharathi, M. S.; Wang, L.; Liu, Y. Y.; Chen, H.; Nie, S.; Wang, X. H.; Chou, H.; Tan, C.; Fallahazad, B.; Ramanarayan, H.; Magnuson, C. W.; Tutuc, E.; Yakobson, B. I.; McCarty, K. F.; Zhang, Y. W.; Kim, P.; Hone, J.; Colombo, L.; Ruoff, R. S. The Role of Surface Oxygen in the Growth of Large Single-Crystal Graphene on Copper. *Science* **2013**, *342*, 720-723.

82. Gao, L. B.; Ren, W. C.; Xu, H. L.; Jin, L.; Wang, Z. X.; Ma, T.; Ma, L. P.; Zhang, Z. Y.; Fu, Q.; Peng, L. M.; Bao, X. H.; Cheng, H. M. Repeated growth and bubbling transfer of graphene with millimetre-size single-crystal grains using platinum. *Nat Commun* **2012**, *3*.

83. Chen, X.; Zhao, P.; Xiang, R.; Kim, S.; Cha, J.; Chiashi, S.; Maruyama, S. Chemical vapor deposition growth of 5 mm hexagonal single-crystal graphene from ethanol. *Carbon* **2015**, *94*, 810-815.

84. Georgakilas, V.; Tiwari, J. N.; Kemp, K. C.; Perman, J. A.; Bourlinos, A. B.; Kim, K. S.; Zboril, R. Noncovalent Functionalization of Graphene and Graphene Oxide for Energy Materials, Biosensing, Catalytic, and Biomedical Applications. *Chemical Reviews* **2016**, *116*, 5464-5519.

85. Wang, X. L.; Shi, G. Q. An introduction to the chemistry of graphene. *Phys Chem Chem Phys* **2015**, *17*, 28484-28504.

86. Mao, H. Y.; Lu, Y. H.; Lin, J. D.; Zhong, S.; Wee, A. T. S.; Chen, W. Manipulating the electronic and chemical properties of graphene via molecular functionalization. *Prog Surf Sci* **2013**, *88*, 132-159.

87. Tang, H. J.; Yin, H. J.; Wang, J. Y.; Yang, N. L.; Wang, D.; Tang, Z. Y. Molecular Architecture of Cobalt Porphyrin Multilayers on Reduced Graphene Oxide Sheets for High-Performance Oxygen Reduction Reaction. *Angew Chem Int Edit* **2013**, *52*, 5585-5589.

88. Byon, H. R.; Suntivich, J.; Shao-Horn, Y. Graphene-Based Non-Noble-Metal Catalysts for Oxygen Reduction Reaction in Acid. *Chem Mater* **2011**, *23*, 3421-3428.

89. Yang, S. L.; Cao, C. Y.; Huang, P. P.; Peng, L.; Sun, Y. B.; Wei, F.; Song, W. G. Sandwich-like porous TiO2/reduced graphene oxide (rGO) for high-performance lithium-ion batteries. *J Mater Chem A* **2015**, *3*, 8701-8705.

90. Schiros, T.; Nordlund, D.; Palova, L.; Prezzi, D.; Zhao, L. Y.; Kim, K. S.; Wurstbauer, U.; Gutierrez, C.; Delongchamp, D.; Jaye, C.; Fischer, D.; Ogasawara, H.; Pettersson, L. G. M.; Reichman, D. R.; Kim, P.; Hybertsen, M. S.; Pasupathy, A. N. Connecting Dopant Bond Type with Electronic Structure in N-Doped Graphene. *Nano Lett* **2012**, *12*, 4025-4031.

91. Liu, Y.; Feng, Q.; Tang, N. J.; Wan, X. G.; Liu, F. C.; Lv, L. Y.; Du, Y. W. Increased magnetization of reduced graphene oxide by nitrogen-doping. *Carbon* **2013**, *60*, 549-551.

92. Chiou, J. W.; Ray, S. C.; Peng, S. I.; Chuang, C. H.; Wang, B. Y.; Tsai, H. M.; Pao, C. W.; Lin, H. J.; Shao, Y. C.; Wang, Y. F.; Chen, S. C.; Pong, W. F.; Yeh, Y. C.; Chen, C. W.; Chen, L. C.; Chen, K. H.; Tsai, M. H.; Kumar, A.; Ganguly, A.; Papakonstantinou, P.; Yamane, H.; Kosugi, N.; Regier, T.; Liu, L.; Sham, T. K. Nitrogen-Functionalized Graphene Nanoflakes (GNFs:N): Tunable Photoluminescence and Electronic Structures. *J Phys Chem C* **2012**, *116*, 16251-16258.

93. Duan, J. J.; Chen, S.; Jaroniec, M.; Qiao, S. Z. Heteroatom-Doped Graphene-Based Materials for Energy-Relevant Electrocatalytic Processes. *Acs Catal* **2015**, *5*, 5207-5234.

94. Wang, Y. Y.; Ni, Z. H.; Yu, T.; Shen, Z. X.; Wang, H. M.; Wu, Y. H.; Chen, W.; Wee, A. T. S. Raman studies of monolayer graphene: The substrate effect. *J Phys Chem C* **2008**, *112*, 10637-10640.

95. Zhou, S. Y.; Gweon, G. H.; Fedorov, A. V.; First, P. N.; De Heer, W. A.; Lee, D. H.; Guinea, F.; Castro Neto, A. H.; Lanzara, A. Substrate-induced bandgap opening in epitaxial graphene. *Nat Mater* **2007**, *6*, 916-916.

96. Hu, Z. Y.; Sinha, D. P.; Lee, J. U.; Liehr, M. Substrate dielectric effects on graphene field effect transistors. *Journal of Applied Physics* **2014**, *115*.

97. Fratini, S.; Guinea, F. Substrate-limited electron dynamics in graphene. *Phys Rev B* **2008**, *77*.

98. Hui, J.; Zhou, X.; Bhargava, R.; Chinderle, A.; Zhang, J.; Rodríguez-López, J. Kinetic modulation of outer-sphere electron transfer reactions on graphene electrode with a sub-surface metal substrate. *Electrochim Acta* **2016**, *211*, 1016-1023.

99. Hui, J.; Pakhira, S.; Bhargava, R.; Barton, Z. J.; Zhou, X.; Chinderle, A. J.; Iyiola, O. O.; Mendoza-Cortes, J. L.; Rodríguez-López, J. Sub-Surface Modulation of Electrocatalytic Activity via Graphene-Mediated Electronic Coupling. *Submitted* **2017**.

CHAPTER 2

OUTER-SPHERE ELECTRON TRANSFER REACTIONS ON GRAPHENE — KINETIC MODULATION WITH METAL SUBSTRATE[†]

2.1 Introduction

Although graphene-like materials produced by exfoliation have experienced an explosion in their type and uses, it is only recently that the electrochemical techniques to explore truly monolayer and bilayer extended electrodes have been developed.[1-6] The extremely thin two dimensional graphene exhibits high electrical conductivity with exceptional electron mobility (200,000 $cm^2 V^{-1} S^{-1}$),[7, 8] strong mechanical strength (1.0 TPa),[9] and high transparency (~2.3 % decrease in transmittance for each layer).[10] These properties make graphene an attractive platform for electrochemical applications, including electrocatalysis,[11] supercapacitors,[12] electrochemical luminescence,[13] electrochemical sensors,[14] and dye-sensitized solar cells.[15] But in spite of these applications, the electrochemical evaluation of pristine graphene electrodes has shown that the basal plane of chemical vapor deposition grown monolayer graphene can experience severe electron transfer kinetic limitations,[16-20] while the presence of structural and chemical defects can increase dramatically its electrochemical activity.[21] However, it is well known from scanning tunneling microscopy experiments on graphite surfaces that the electronic density of states of layers beneath the topmost carbon sheet can have a strong impact on the

[†] Part of this chapter is adapted from the publication: Hui, J. S.; Zhou, X.; Bhargava, R.; Chinderle, A.; Zhang, J. R.; Rodriguez-Lopez, J. Kinetic Modulation of Outer-Sphere Electron Transfer Reactions on Graphene Electrode with a Sub-surface Metal Substrate. *Electrochim. Acta* 2016, *211*, 1016-1023.

measured surface electronic structure.[22-25] Because graphene is atomically thin,[7, 8, 26, 27] we hypothesized that such electronic effects created by an "underlayer" could permeate through ultrathin graphene electrode to affect the rate and mechanisms of "overlayer" solution exposed electrochemical reactions at the metal/graphene/solution interface. Here, we report on the impact of Au on the electrochemical activity of pristine bilayer graphene electrodes towards the electron transfer to solution mediators.

The perturbation of graphene as an atomically-thin material is known in other contexts. The Raman spectrum[28] and bandgap opening[29] of epitaxial graphene are affected by the graphene-substrate interaction, which can be sufficiently strong to change the graphene lattice symmetry. Chemical functionalities such as underlayer dielectrics can also change the electronic structure of graphene, thus modifying its carrier mobility.[30, 31] The electron-transfer chemistry of graphene can be affected via interaction with the underlying substrate as molecular grafting with aryl diazonium salts demonstrates substrate-dependent reaction rates.[32] One possible explanation of this substrate effect would be that charge-donating impurities below graphene cause charge puddles that lead to electron-density inhomogeneities.[33, 34] Recently, similar 2-D materials boron nanosheet has been proved to be a good electrocatalyst when supported on Au, its catalytic activity varies with different substrate support.[35-37] It is reasonable to assume the different substrates may have some influence on graphene's electronic properties, and thus its electrochemical reaction kinetics.

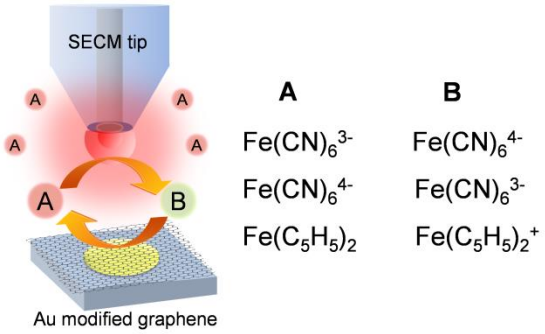

Figure 2.1 Schematic diagram of SECM feedback mode and selected outer-sphere reaction mediators. $Fe(CN)_6^{3-/4-}$ = ferricyanide/ferrocyanide redox pair, $Fe(C_6H_5)_2^{0/+}$ = ferrocene/ferrocenium redox pair.

In order to prove our hypothesis, we used scanning electrochemical microscopy (SECM) to study the substrate effect on graphene for electrochemical reactions. SECM is a powerful tool to image highly localized substrate electrochemical processes, and provides a convenient platform to test comparisons between materials and substrate conditions in the same experiment, in the absence of adventitious changes in conditions from sample to sample.[38-40] In this study, we chose to pattern micro-sized spots of Au (p-Au) in order to decorate the underlayer of graphene (graphene/p-Au). As shown in Figure 2.1, SECM was then used to image and quantify the differences in electrode electrochemical activity, thus elucidating the influence of metal substrate on graphene's electron transfer kinetics. Three different outer-sphere electron transfer species were selected in our experiments, including ferrocyanide, ferricyanide, and ferrocene. As reported in literature, ferrocyanide and ferricyanide have slower to sluggish reaction kinetics with standard rate constant k^0 of 3×10^{-4} m/s on Au,[41] 9.5×10^{-6} m/s (ferrocyanide) and 1.9×10^{-5} m/s (ferricyanide) on graphene,[19] while ferrocene represents fast reaction kinetics with k^0 of 1×10^{-2} m/s on Pt.[42] Outer-sphere electrode reactions proceed through direct tunneling of electrons between redox species and the electrode and do not typically involve an intimate interaction

between reactant and electrode, nor the formation of adsorbed or catalytic intermediates.[43] These reactions thus proceed with relative independence of the electrode material used. However, in the context of microscopic theories of electron transfer, the overlap between the electrode and reactant wave functions, as well as the density of states of the electrode, can influence the electrochemical rate constant and display differences between electrode materials for the same reaction.[43, 44] In specific, pristine CVD-graphene electrodes have been recently found to exhibit clear kinetic limitations in comparison to their metal counterparts,[13, 18, 45] as well as a dependence of the electron transfer kinetics on the number of layers[20] and the presence of defects[21], which can influence the electronic properties of the surface beyond the individually-affected carbon-carbon bonds. While the exact reason for the lower reactivity observed for graphene electrodes is not yet completely established, here we present experiments that demonstrate that the electronic influence of metal underlayers can dramatically enhance the rate for electron transfer.

2.2 Characterization of Graphene on Au Substrate

The property of CVD grown graphene was examined via Raman spectrometry. Figure 2.2a shows the Raman 2D/G intensity ratio mapping of graphene sample used in our experiments. The graphene is a large continuous sheet with tens of microns grain size. The averaged Raman spectrum of whole area is shown in Figure 2.2b. It has a small D band around 1370 cm^{-1}, which indicates high quality sheets with few structural defects.[46] From Raman image and spectrum, the majority of graphene has a ratio of the G band (around 1590 cm^{-1}) to 2D band (2690 cm^{-1}) intensity close to 1, which represents bilayer graphene structure.[47, 48] The sheet resistance of same graphene sample on glass slide was reported on a previous work: 575 $\pm$ 77 $\Omega/\square$.[13]

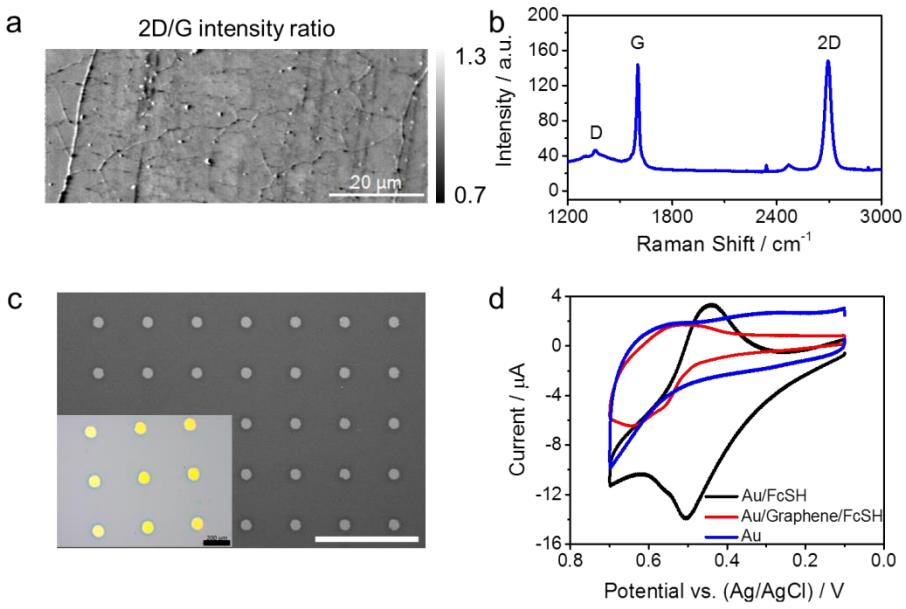

Figure 2.2 Sample Characterization. a, Raman 2D/G intensity ratio mapping of pristine graphene on Si/SiO_2 wafer. b, Average Raman spectrum of pristine graphene on Si/SiO_2 wafer. D, G and 2D peaks area labelled in Figure. c, Scanning electron microscopy image of graphene/p-Au sample with a white scale bar of 1 mm. Inset is optical microscope image of same sample with a black scale bar of 400 μm. d, Cyclic voltammograms of Au, Au with one monolayer of FcSH, and graphene/Au with one monolayer of FcSH. Solution: blank 0.1 M KNO_3 aqueous solution. Scan rate: 0.1 V/s.

The graphene samples were transferred onto metal films and patterned metal substrates via wet etching procedure for electrochemical tests. Figure 2.2c is the SEM and microscope image of graphene/p-Au substrate. The size and shape of metal enhanced areas match with the SEM image and inset optical microscope in Figure 2.2c. After whole graphene transfer process, the graphene had a high coverage throughout the whole sample surface without any observable damage.

In order to discard the possibility of trivial effects in following SECM results, such as the exposure of the metal underlayer to solution through holes in the graphene structure or by means of a "leaky" contact between graphene and the metal, we verified the exposure of Au to the electrolyte by means of a surface probe. A monolayer of FcSH was adsorbed on our graphene/Au sample, as well as on blank Au substrates, and tested the CV based on the adsorbed ferrocene redox couple, as shown in Figure 2.2d. The absorbed FcSH layer on Au substrate exhibited a clear peak around 0.5 V vs. Ag/AgCl for ferrocene end group oxidation. When Au substrate was covered with graphene, this signal was largely suppressed due to the lack of available exposed Au for FcSH modification. Compared to a blank sample of Au without any overlayer graphene, we observed that less than 3% of the surface consisted of Au exposed to the solution environment, as determined by integration of the area below the FcSH oxidation peak around 0.57 V vs. Ag/AgCl on FcSH/Graphene/Au CV in Figure 2.2d. This is a small percentage of exposed sites that were not detected in our samples as major holes, however small pinholes and grain boundaries could contribute significantly to the SECM response. The experiments shown below, in the absence and presence of a molecular blocking agent, show that metal exposure was not determining.

2.3 Enhanced $Fe(CN)_6^{4-}$ Oxidation Mechanism on Graphene/p-Au

The $[Fe(CN)_6]^{3-}/[Fe(CN)_6]^{4-}$ redox pair has been demonstrated to exhibit sluggish electron transfer kinetics on pristine graphene electrodes,[21, 49] although it exhibits much faster kinetics on Au electrodes. This unique property makes the $[Fe(CN)_6]^{3-}/[Fe(CN)_6]^{4-}$ pair a suitable redox mediator for detecting the local activity change on graphene under the effect of metal substrates. SECM image was first collected with ferricyanide ($[Fe(CN)_6]^{3-}$) solution to examine the heterogeneous rate constant change of the $[Fe(CN)_6]^{4-}$ oxidation on substrate electrode. The

selected test area consisted of an exposed Au spot and a graphene/p-Au spot with large graphene sheet background connection.

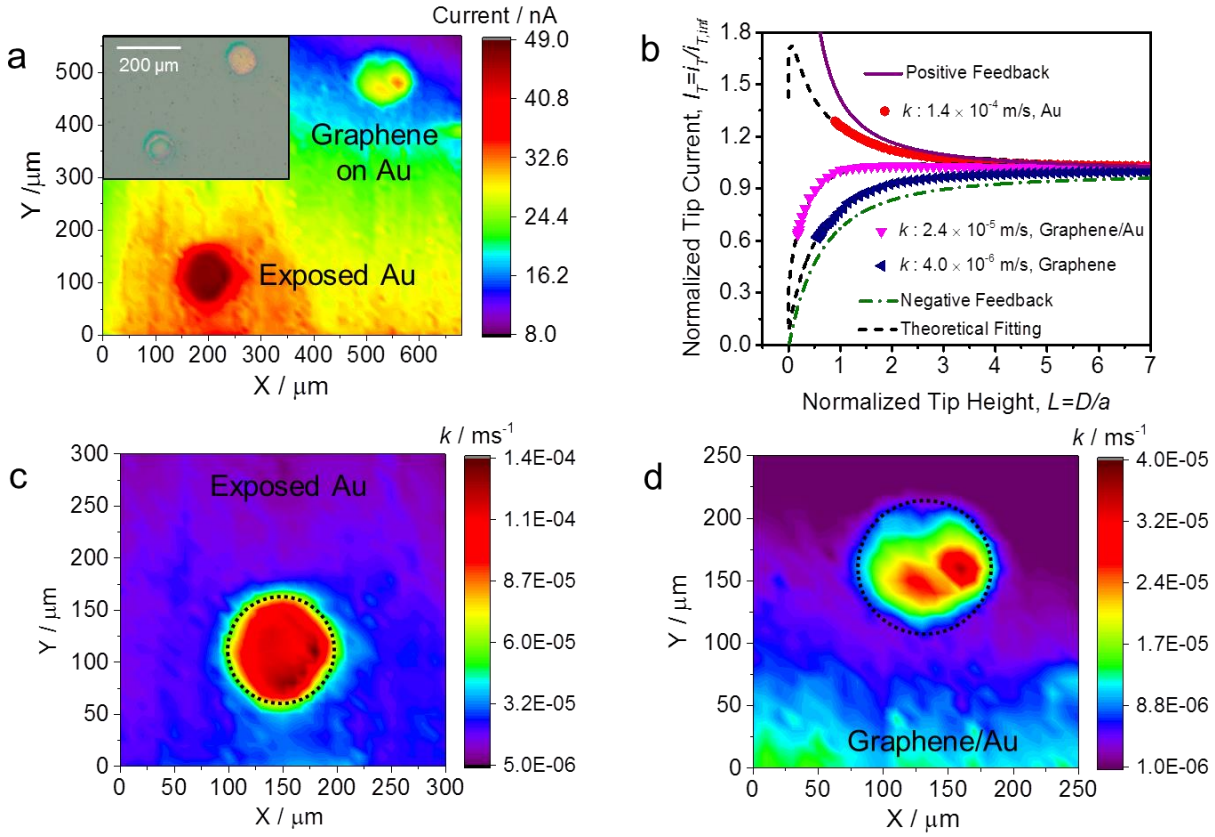

Figure 2.3 SECM study of graphene activity towards an outer-sphere reaction over a graphene/p-Au spot with ferricyanide used as redox mediator. a, SECM feedback image of graphene/p-Au spot and exposed Au spot, the scanning area is indicated as insert microscope image. In this experiment $Fe(CN)_6^{3-}$ was reduced to $Fe(CN)_6^{4-}$ at Pt UME, and then became oxidized at the graphene substrate. The round pattern centered as x = 200 μm, y = 100 μm is exposed Au spot, the other round pattern at x = 550 μm, y = 500 μm is the graphene/p-Au area. b, Approach curves to Au, graphene/Au, and graphene area. Theoretical fittings of each curve with calculated *k* values were exhibited in this Figure. Pure positive feedback and negative feedback approach curves were listed for comparison. c and d, Calculated *k* mapping of ferrocyanide

(*Figure 2.3 Continued*) oxidation kinetics at exposed Au area and graphene/p-Au area, respectively. The 100 μm diameter dashed circles in panel c and panel d indicates the possible position of Au or graphene/p-Au spot.

As shown in Figure 2.3a, SECM scans on the graphene/p-Au spot (x = 550 μm, y = 500 μm) resulted in a higher feedback current that was detected at this area. We also included an exposed Au area (x = 200 μm, y = 100 μm), whose edge was connected with the graphene sheet in same Figure for comparison. This same spot is shown in the insert optical microscope image in Figure 2.3a. Overall, there was an increase of feedback current at the graphene/p-Au area, and this enhancement was smaller than pure exposed Au area. Overall, the order in reactivity was: Au > graphene/Au > bare graphene. Figure 2.3b summarizes the approach curves under the same electrode polarization conditions to Au, graphene/Au and graphene surface with theoretical fitting, which yielded heterogeneous rate constant k of 1.4×10^{-4} m/s, 2.4×10^{-5} m/s, and 4.0×10^{-6} m/s, respectively. The calculated k mapping of exposed Au area (Figure 2.3c) and graphene/Au area (Figure 2.3d) matched well with fitted data from approach curves. The kinetics enhancement at graphene/Au area was estimated by comparing the averaged heterogeneous rate constant at 30×30 μm^2 area of graphene/Au and pristine graphene. Ferrocyanide oxidation reaction at graphene/Au area was 5.5 ± 1.0 times faster than graphene. The inhomogeneity in Figure 2.3d can be attributed to a differently-formed contact between graphene and p-Au. Since the amorphous Au pattern was deposited via E-beam evaporation method, there is inevitably one to several atomic size height differences between different domains. At sites with pristine graphene, the tip-generated $[Fe(CN)_6]^{4-}$ was not successfully oxidized due to the sluggish reaction kinetics of this mediator over graphene, while at the graphene above Au substrate, the reaction was facilitated under the influence the metal substrate. This suggests that although

graphene exhibits sluggish reaction for $[Fe(CN)_6]^{4-}$oxidation, adding an underlayer that displays faster kinetics will help enhance its interfacial reactivity.

2.4 Origins of Localized Modification of Outer-Sphere Electron Transfer Kinetics

After analyzing the kinetics change at graphene/p-Au surface, we primarily hypothesized that the metal underlayer affects the electronic properties of graphene by increasing its electron density at the interface, i.e. displaying a permeation through the thin graphene layer that affects the outer-sphere reaction above it. This effect can be explained as change of electron density of state near Fermi level, where its position will dominate the electron transfer kinetics in electrochemical reactions.[43] The second possible explanation would be the change of graphene's Fermi level by charge doping from Au substrate due to the difference in their work functions. It has been studied by first-principles calculations that the binding between graphene surface and metals can adopt different characters, ranging from "physisorption", where the band structure of graphene is largely intact, to the formation of a new surface phase, in which "chemisorption" takes place.[50] For Au, the interaction corresponds to the "physisorption" model, which leads to no significant disruption to the band structure of graphene except a small shift of the Fermi level. If doping is the main effect, then the polarized shift of Fermi Level might primarily enhance the oxidation reaction kinetics on graphene/Au surface, but show no improvement or negative effect for reduction reactions.

In order to test these effects, we tested the electrochemical activity of the interface using ferrocyanide instead of ferricyanide as original species. The calculated *k* at graphene/p-Au area is plotted in Figure 2.4a. In general, similar kinetics enhancements for ferricyanide reduction were observed at graphene/p-Au. Moreover, comparing to Figure 2.3d, ferrocyanide and ferricyanide exhibited same magnitude *k* at graphene/p-Au spot at similar overpotential of 0.25 V, with

slightly larger rate constant of ferricyanide reduction. This result matched with previously reported data of $[Fe(CN)_6]^{3-}$ and $[Fe(CN)_6]^{4-}$ electron transfer kinetics on single layer graphene.[19] Overall, the metal underlayer exhibited non-polarized enhancement to both oxidation and reduction reactions on graphene surface, which can preclude the second hypothesis of polarized enhancement due to charge doping from Au substrate.

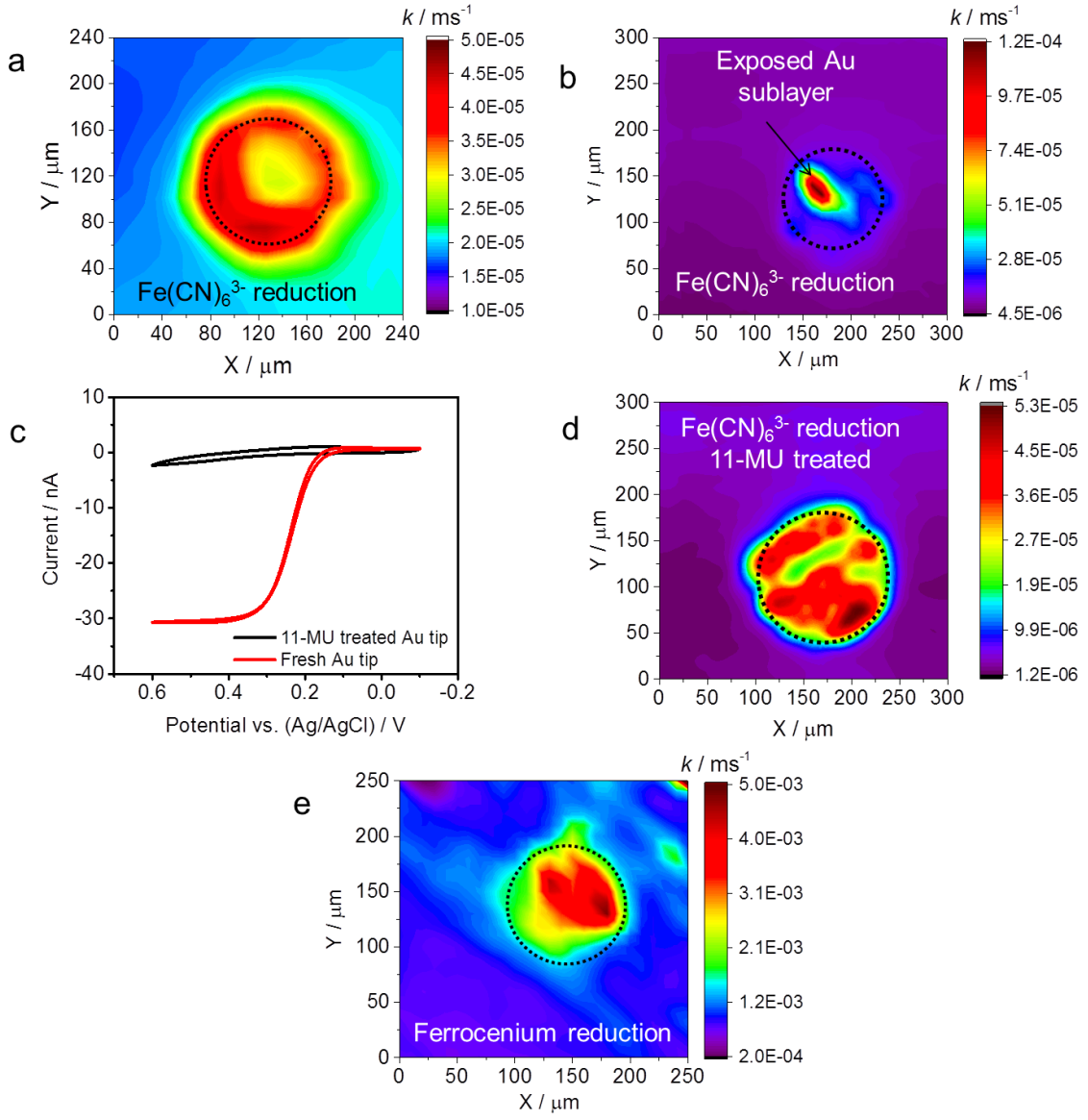

Figure 2.4 Heterogeneous electron transfer rate constant *k* images of graphene activity towards outer-sphere reactions over underlayer Au modified graphene area. a, Calculated ferricyanide

(*Figure 2.4 Continued*) reduction kinetics *k* mapping on graphene/Au electrode. b, Calculated ferricyanide reduction kinetics *k* mapping on a graphene/Au electrode with small exposed Au area at x = 160 μm, y = 140 μm. c, Comparison of ferrocyanide oxidation CVs on fresh Au tip and 11-mercapto-1-undercanol (11-MU) self-assembled monolayer modified Au tip. d, Calculated ferricyanide reduction kinetics *k* mapping on 11-MU treated graphene/Au electrode, 11-MU was used to fully block any exposed pinholes of Au substrate. e, Calculated ferrocenium reduction kinetics *k* mapping on a graphene/Au electrode. The dashed circles indicate the possible position of graphene/Au spot in each graph.

A more trivial mechanism would apply if exposed Au was artificially enhancing the measured *k* at the graphene-metal spots. While the control experiments using the ferrocene surface probe indicated to us that this was not a large component of the surface, we found it instructive to evaluate the influence of a small portion of exposed Au on the graphene/p-Au performance. First we selected a graphene/p-Au sample with a tiny exposed Au area at ca. x = 160 μm, y = 140 μm. The kinetics mapping of ferricyanide reduction on this sample is shown in Figure 2.4b, where a large rate of electron transfer was observed on a highly-localized spot within the area of graphene modified by Au. Because these defects on graphene are easily recognized through the SECM imaging, it is easy to discard results from such spots after ex-situ microscopic inspection. However, even if we are aware of the presence of large holes, we still cannot preclude the possibility that small pinholes from graphene defects and grain boundaries impact the SECM response. Since these nanometer-sized exposed Au areas cannot be imaged using the current SECM setup, we chose to selectively block the Au surface towards electron transfer using the molecular blocking probe 11-MU. 11-MU forms a self-assembled monolayer on top of Au surface via Au-S bond, where the densely-packed long carbon chain hinders

electron tunneling.[51] The property of this 11-MU SAM was verified by examining ferrocyanide oxidation on a 12.5 μm Au tip. As shown in Figure 2.4c, an 11-MU modified Au tip exhibited a dramatic decrease in its electron transfer kinetics, with a modified standard rate constant on the order of 10^{-7} m/s, well-below the k^0 of the ferro/ferricynanide redox pair on unmodified graphene. Comparison of Figure 2.4a and 2.4d reveals similar kinetics enhancement on the graphene/p-Au surface with and without 11-MU treatment. Therefore, all of the localized enhancement we observed for ferricyanide and ferrocyanide reactions come from the electronic coupling between graphene and Au substrate and the contribution from pinholes is largely discarded.

Recently, there has been debate about the potential limitation and reliability of ferricyanide and ferrocyanide redox mediator as kinetic probes for graphene type materials.[52] Thus, we confirmed our measurements using a traditionally-fast redox mediator such as ferrocene in organic media (Figure 2.4e). Observable enhancement was found on the graphene/p-Au area, with an overall increase of 5.1 ± 0.5 times of the heterogeneous rate constant. It is also important to point out that even if some electrode fouling was occurring due to decomposition of the redox mediator at the graphene surface,[52] or due to the presence of residues from graphene processing,[53, 54] these effects should affect similarly metal modified and unmodified areas. What we observe is that regardless of the surface condition, the areas modified with metals exhibit larger rates of electron transfer. These enhancements can be reasonably attributed to donation of electron density state from metal substrate. It has been reported that metal substrates can tune the Fermi-level shift[55], potential-energy surface[56], and scanning tunneling spectra[57] of graphene sheets above metal layers. Au has higher electron density near Fermi level and can donate some electron to graphene and increase its electron density of states. Regardless of the mechanism, the

end result is a dramatically-enhanced rate of electron transfer at the modified graphene sites, despite the lack of access of the metal to the solution.

2.5 Materials and Methods

Chemicals. All chemicals were commercially purchased and used as received. Potassium nitrate (KNO_3, 99.0 %), ferrocene (98 %), lithium tetrafluoroborate ($LiBF_4$, 98 %), 11-mercapto-1-undecanol (11-MU, 95 %), ethylenediaminetetraacetic acid disodium salt dihydrate (EDTA, 99.0 %), acetone (99.5 %), isopropyl alcohol (99.5 %), anisole (99 %), dichloromethane (99.5 %) were all purchased from Sigma-Aldrich. Potassium ferrocyanide ($K_4[Fe(CN)_6]\ 3H_2O$, 98.5 %) was purchased from Strem Chemicals Inc. Potassium ferricyanide ($K_3[Fe(CN)_6]$, 99 %) was purchased from J. T. Baker. 25 μm copper foil was purchased from Alfa Aesar. Two poly(methyl methacrylate) (PMMA) solutions, NanoTM 950K A4 (Mw 950,000 PMMA, 4 w% solution in anisole) and 495K A2 (Mw 495,000 PMMA, 2 w% solution in anisole), were purchased from MicroChem. CE-100 copper etchant was purchased from Transene Company. Si wafer were purchased from Monsanto. Si wafer with 300 nm SiO_2 (Si/SiO_2 wafer) was purchased from University Wafer. The deionized water (DI water) was filtered using a Millipore system.

Substrate Fabrication and Characterization. E-Beam evaporation was applied to deposit 100 nm thick Au on substrates with 5 nm Ti as adhesion layer. Shadow mask with 100 μm diameter holes, 500 μm center-to-center distance was used to cover Si/SiO_2 wafer surface during deposition to create Au patterns (p-Au). Continuous Au film was also deposited on Si wafer for the thiolation test mentioned below. Graphene was fabricated using previously reported chemical vapor deposition (CVD) method[13] under 1000 ℃, 40 mTorr, 100 sccm CH_4 and 50 sccm H_2 for 25 min. Graphene was transferred to different substrates, including Si/SiO_2 wafer, Au film on Si wafer, and p-Au on Si/SiO_2 wafer, via wet-etching method developed in our

group[13]. In general, the graphene was protected by PMMA film, while the bottom Cu was etched away in Cu etchant. After that, several cleaning procedures were processed to remove trace amount of ions (4 times rinse with DI water, 1h EDTA treatment, and 4 times rinse with DI water) and the clean graphene was transfer onto target substrate. The PMMA protection layer was removed by soaking in organic solvents with 2h in anisole, 4 h in acetone dichloromethane 1:1 ratio and 2 h in isopropanol, thus clean graphene surface was exposed.

The optical and spectroscopic properties of the various substrates were characterized via optical microscopy (Zeiss Axio Lab.A1), scanning electron microscopy (SEM, Philips XL30 ESEM-FEG), and Raman spectroscopy (Nanophoton Raman-11) before and after experiments.

Thiolation of Graphene on Au substrate. In order to discard the presence of holes on graphene/metal electrodes that could impact its interfacial activity, we selected 6-hexaneferrocylthiol (FcSH) as a probe to detect possible exposed Au area. FcSH can selectively adsorb on Au surface but not graphene, to form stable Au-S bonded self-assembled monolayer.[58] The ferrocene end group is electroactive which can be detected via cyclic voltammetry (CV). The adsorption procedure is a modified version from literature.[59] In general, the substrate (Au, graphene or graphene/Au) was soaked in 2 mg/mL FcSH ethanol solution for 16 hours to form a stable monolayer on Au and then rinsed with ethanol four times to remove physisorption species and blow dried with Ar. CVs of each electrode after FcSH adsorption were tested to verify the existence of ferrocene group, and hence the exposed Au surface.

Experiments were performed in order to verify and discard the role that pinhole exposure of Au could have on the observed electrochemical response. 11-mercapto-1-undecanol (11-MU) was chosen to purposely block Au surface. The substrates (graphene/p-Au or 12.5 μm radius Au tip) were immersed in 2 mM 11-MU ethanol solution for 12 h to form a stable 11-MU self-

assembled monolayer (SAM) and then rinsed with copiously with ethanol and blow dried with Ar. The electron blocking property of 11-MU SAM was verified by comparing the CVs of fresh and 11-MU modified Au tip in 10 mM $K_4[Fe(CN)_6]$, 0.1 M KNO_3 aqueous solution. The 11-MU treated graphene/p-Au substrate was used for SECM testing.

Scanning Electrochemical Microscopy. SECM was conducted on a CHI920D workstation (CH Instruments) with a four electrode configuration: 12.5 μm radius Pt ultramicroelectrode (UME) as working electrode, Pt wire as counter electrode, Ag/AgCl saturated KCl reference electrode for ferricyanide/ferrocyanide experiments (isolated from the working electrolyte solution through an agar/0.1 M potassium nitrate bridge), Ag quasi-reference electrode (QRE) for ferrocene experiment in acetonitrile, and Au patterned graphene as substrate electrodes. The substrates were sealed inside a homemade Teflon cell, with 0.07 cm^2 exposed area.

General SECM methods. In SECM technique, usually a UME is used as a probe to detect local changes in electrochemical activity. The steady-state current at the UME changes with tip-substrate distance (d) and heterogeneous electron transfer rate constant (k) of the mediator at substrate electrode. This relationship of normalized tip height (L) and normalized tip current (I_T) is known as approach curve, where $L = d/a$ is the ratio of the absolute distance (d) to the tip radius (a), and $I_T = i_T/i_{T,inf}$ is the ratio of tip current to steady-state current (i_T) at a large distance from the substrate ($i_{T,inf}$). Electron transfer kinetics, k, were be obtained by fitting approach curve with equations developed by Lefrou and Cornut,[60] with known tip geometry and mediator diffusion coefficient.

After approaching UME tip close to the substrate within feedback range, SECM feedback images were obtained by biasing UME and substrate at different potential and sensing the current

change at different location. As shown schematically in Figure 2.1, species A is reduced/(oxidized) to form species B at UME surface, which is then oxidized/(reduced) to regenerate A at substrate electrode. This feedback loop enables the recycled flux of mediator, generating an increased current on the tip electrode as a function of substrate activity. SECM images were obtained by scanning the tip at constant height above substrate surface and collecting feedback current at each location. *k* was calculated with normalized tip height-current relationship for every pixel.

SECM of $[Fe(CN)_6]^{3-}$/$[Fe(CN)_6]^{4-}$ redox pair. The ferricyanide/ferrocyanide redox pair showed a half wave potential, $E_{1/2}$=0.25 vs. Ag/AgCl in 0.1 M KNO_3. In a first experiment, 10 mM $K_3[Fe(CN)_6]$ in aqueous solution with 0.1 M KNO_3 supporting electrolyte was used as reaction media. After approaching the tip to the substrate using SECM negative feedback with the substrate at open circuit [5], ca. to L = 0.34 (4.25 μm), SECM images were obtained in the feedback mode. The tip was held at 0 V to generate $[Fe(CN)_6]^{4-}$ and the substrate was held at 0.5 V to locally regenerate the $[Fe(CN)_6]^{3-}$ ion. This regeneration caused the tip current to be modulated by the local substrate kinetics, permitting a mapping of the local electron transfer rate of $[Fe(CN)_6]^{4-}$ oxidation reaction.[38, 40, 49, 61, 62] The testing area consisted of one exposed Au spot with graphene connected to its edge and one Au spot fully covered with graphene sheet (graphene/p-Au), thus approach curves to three respective area: exposed Au, graphene, and graphene covered Au spot (graphene/Au) were tested and fitted with theoretical curve to obtain heterogeneous electron transfer rate constant (k) of $[Fe(CN)_6]^{4-}$ oxidation reaction at different area. Based on the SECM feedback image and fitted L, the current mapping was transferred to k mappings at exposed Au area and graphene/Au area.

In a second experiment, 10 mM $K_4[Fe(CN)_6]$ in aqueous solution with 0.1 M KNO_3 supporting electrolyte was used as reaction media. Similar SECM feedback current images were obtained at various substrates: graphene/p-Au, graphene/Au with small piece exposure of Au substrate and graphene/p-Au substrate with 11-MU self-assembled monolayer to block exposed Au pinholes. The tip was held at 0.5 V to generate $[Fe(CN)_6]^{3-}$ and the substrate was held at 0 V to locally regenerate the $[Fe(CN)_6]^{4-}$ ion. The current images were transferred to *k* mappings with similar procedure as $K_3[Fe(CN)_6]$ mediator.

SECM of ferrocene/ferrocenium redox pair. Ferrocene/ferrocenium redox pair showed a half wave potential, ca. $E_{1/2}$=0.44 vs. Ag QRE, in 0.5 mM ferrocene in acetonitrile solution with 0.1 M $LiBF_4$ as supporting electrolyte was used as reaction media. SECM feedback current images were obtained at exposed Au spot and graphene/p-Au area at ca. L = 0.89 (11.1 μm) and transferred to *k* mappings. The tip was held at 0.6 V vs. to generate ferrocenium and the substrate was held at 0.25V to locally regenerate the ferrocene.

2.6 Conclusion

We have shown here a study of the impact of sub-surface buried Au on the electrochemical activity of CVD-grown graphene sheets through the simplest form of interfacial electron transfer using outer sphere redox mediators. SECM in the feedback mode was used to compare in-situ the redox kinetics of areas modified by metals to those of the pristine graphene and the pristine metal. In the case of the ferrocyanide/ferricyanide system, which shows sluggish reaction kinetics at pristine graphene, we observed a 5.5 ± 1.0 times increase in heterogeneous rate constant on Au-modified areas. Moreover, similar kinetic improvement was observed on ferrocene/ferrocenium reaction, the graphene/p-Au area has 5.1 ± 0.5 times increase of electron transfer rates. The use of redox-active surface probes to estimate the metal exposed to solution,

SEM and optical imaging, and calculations based on known-models of substrates with pinholes, give us arguments to discard the possibility that the observed effects are due to exposed metal surface. We ascribe instead the observed enhancements on an electron-donating effect from the metal sub-surface, which enhances the electron density of states and Fermi level of graphene.

The results presented here suggest new methods for tuning electrochemical reaction rates with ultra-thin materials and various sub-surface modification methods. Such modified interfaces might lead to new strategies for electrode fabrication and patterning. Furthermore, the ultra-thin graphene interface might serve as a protection layer for sub-surface materials, protecting them from the electrolyte environment while selectively depolarizing electrochemical reactions at the otherwise sluggish graphene/electrolyte interface.

2.7 References

1. Li, X.; Zhu, Y.; Cai, W.; Borysiak, M.; Han, B.; Chen, D.; Piner, R. D.; Colombo, L.; Ruoff, R. S. Transfer of Large-Area Graphene Films for High-Performance Transparent Conductive Electrodes. *Nano Letters* **2009**, *9*, 4359-4363.

2. Kim, K. S.; Zhao, Y.; Jang, H.; Lee, S. Y.; Kim, J. M.; Kim, K. S.; Ahn, J.-H.; Kim, P.; Choi, J.-Y.; Hong, B. H. Large-scale pattern growth of graphene films for stretchable transparent electrodes. *Nature* **2009**, *457*, 706-710.

3. Valota, A. T.; Kinloch, I. A.; Novoselov, K. S.; Casiraghi, C.; Eckmann, A.; Hill, E. W.; Dryfe, R. A. W. Electrochemical Behavior of Monolayer and Bilayer Graphene. *Acs Nano* **2011**, *5*, 8809-8815.

4. Velicky, M.; Bradley, D. F.; Cooper, A. J.; Hill, E. W.; Kinloch, I. A.; Mishchenko, A.; Novoselov, K. S.; Patten, H. V.; Toth, P. S.; Valota, A. T.; Worrall, S. D.; Dryfe, R. A. W. Electron Transfer Kinetics on Mono- and Multilayer Graphene. *Acs Nano* **2014**, *8*, 10089-10100.

5. Rodriguez-Lopez, J.; Ritzert, N. L.; Mann, J. A.; Tan, C.; Dichtel, W. R.; Abruna, H. D. Quantification of the surface diffusion of tripodal binding motifs on graphene using scanning electrochemical microscopy. *JACS* **2012**, *134*, 6224-6236.

6. Wang, J. Z.; Manga, K. K.; Bao, Q. L.; Loh, K. P. High-Yield Synthesis of Few-Layer Graphene Flakes through Electrochemical Expansion of Graphite in Propylene Carbonate Electrolyte. *Journal of the American Chemical Society* **2011**, *133*, 8888-8891.

7. Bolotin, K. I.; Sikes, K. J.; Jiang, Z.; Klima, M.; Fudenberg, G.; Hone, J.; Kim, P.; Stormer, H. L. Ultrahigh electron mobility in suspended graphene. *Solid State Communications* **2008**, *146*, 351-355.

8. Du, X.; Skachko, I.; Barker, A.; Andrei, E. Y. Approaching ballistic transport in suspended graphene. *Nature Nanotechnology* **2008**, *3*, 491-495.

9. Lee, C.; Wei, X. D.; Kysar, J. W.; Hone, J. Measurement of the elastic properties and intrinsic strength of monolayer graphene. *Science* **2008**, *321*, 385-388.

10. Nair, R. R.; Blake, P.; Grigorenko, A. N.; Novoselov, K. S.; Booth, T. J.; Stauber, T.; Peres, N. M. R.; Geim, A. K. Fine structure constant defines visual transparency of graphene. *Science* **2008**, *320*, 1308-1308.

11. Qu, L.; Liu, Y.; Baek, J.-B.; Dai, L. Nitrogen-Doped Graphene as Efficient Metal-Free Electrocatalyst for Oxygen Reduction in Fuel Cells. *ACS Nano* **2010**, *4*, 1321-1326.

12. Zhu, Y.; Murali, S.; Stoller, M. D.; Ganesh, K. J.; Cai, W.; Ferreira, P. J.; Pirkle, A.; Wallace, R. M.; Cychosz, K. A.; Thommes, M.; Su, D.; Stach, E. A.; Ruoff, R. S. Carbon-Based Supercapacitors Produced by Activation of Graphene. *Science* **2011**, *332*, 1537-1541.

13. Cristarella, T. C.; Chinderle, A. J.; Hui, J.; Rodríguez-López, J. Single-layer graphene as a stable and transparent electrode for nonaqueous radical annihilation electrogenerated chemiluminescence. *Langmuir* **2015**, *31*, 3999-4007.

14. Shao, Y.; Wang, J.; Wu, H.; Liu, J.; Aksay, I. A.; Lin, Y. Graphene Based Electrochemical Sensors and Biosensors: A Review. *Electroanalysis* **2010**, *22*, 1027-1036.

15. Wang, X.; Zhi, L.; Müllen, K. Transparent, Conductive Graphene Electrodes for Dye-Sensitized Solar Cells. *Nano Letters* **2008**, *8*, 323-327.

16. Brownson, D. A. C.; Varey, S. A.; Hussain, F.; Haigh, S. J.; Banks, C. E. Electrochemical properties of CVD grown pristine graphene: monolayer- vs. quasi-graphene. *Nanoscale* **2014**, *6*, 1607-1621.

17. Yuan, W. J.; Zhou, Y.; Li, Y. R.; Li, C.; Peng, H. L.; Zhang, J.; Liu, Z. F.; Dai, L. M.; Shi, G. Q. The edge- and basal-plane-specific electrochemistry of a single-layer graphene sheet. *Scientific Reports* **2013**, *3*.

18. Tan, C.; Rodriguez-Lopez, J.; Parks, J. J.; Ritzert, N. L.; Ralph, D. C.; Abruna, H. D. Reactivity of Monolayer Chemical Vapor Deposited Graphene Imperfections Studied Using Scanning Electrochemical Microscopy. *Acs Nano* **2012**, *6*, 3070-3079.

19. Ritzert, N. L.; Rodríguez-López, J.; Tan, C.; Abruña, H. D. Kinetics of Interfacial Electron Transfer at Single-Layer Graphene Electrodes in Aqueous and Nonaqueous Solutions. *Langmuir* **2013**, *29*, 1683-1694.

20. Guell, A. G.; Ebejer, N.; Snowden, M. E.; Macpherson, J. V.; Unwin, P. R. Structural Correlations in Heterogeneous Electron Transfer at Monolayer and Multilayer Graphene Electrodes. *Journal of the American Chemical Society* **2012**, *134*, 7258-7261.

21. Zhong, J. H.; Zhang, J.; Jin, X.; Liu, J. Y.; Li, Q.; Li, M. H.; Cai, W.; Wu, D. Y.; Zhan, D.; Ren, B. Quantitative correlation between defect density and heterogeneous electron transfer rate of single layer graphene. *J Am Chem Soc* **2014**, *136*, 16609-17.

22. Rutter, G. M.; Crain, J. N.; Guisinger, N. P.; Li, T.; First, P. N.; Stroscio, J. A. Scattering and interference in epitaxial graphene. *Science* **2007**, *317*, 219-222.

23. Ishigami, M.; Chen, J. H.; Cullen, W. G.; Fuhrer, M. S.; Williams, E. D. Atomic structure of graphene on SiO_2. *Nano Letters* **2007**, *7*, 1643-1648.

24. Decker, R.; Wang, Y.; Brar, V. W.; Regan, W.; Tsai, H.-Z.; Wu, Q.; Gannett, W.; Zettl, A.; Crommie, M. F. Local electronic properties of graphene on a BN substrate via scanning tunneling microscopy. *Nano Letters* **2011**, *11*, 2291-2295.

25. Varykhalov, A.; Sanchez-Barriga, J.; Shikin, A. M.; Biswas, C.; Vescovo, E.; Rybkin, A.; Marchenko, D.; Rader, O. Electronic and Magnetic Properties of Quasifreestanding Graphene on Ni. *Physical Review Letters* **2008**, *101*.

26. Geim, A. K.; Novoselov, K. S. The rise of graphene. *Nature Materials* **2007**, *6*, 183-191.

27. Geim, A. K. Graphene: Status and Prospects. *Science* **2009**, *324*, 1530-1534.

28. Wang, Y. Y.; Ni, Z. H.; Yu, T.; Shen, Z. X.; Wang, H. M.; Wu, Y. H.; Chen, W.; Wee, A. T. S. Raman studies of monolayer graphene: The substrate effect. *Journal of Physical Chemistry C* **2008**, *112*, 10637-10640.

29. Zhou, S. Y.; Gweon, G. H.; Fedorov, A. V.; First, P. N.; De Heer, W. A.; Lee, D. H.; Guinea, F.; Castro Neto, A. H.; Lanzara, A. Substrate-induced bandgap opening in epitaxial graphene. *Nature Materials* **2007**, *6*, 916-916.

30. Hu, Z. Y.; Sinha, D. P.; Lee, J. U.; Liehr, M. Substrate dielectric effects on graphene field effect transistors. *Journal of Applied Physics* **2014**, *115*.

31. Fratini, S.; Guinea, F. Substrate-limited electron dynamics in graphene. *Physical Review B* **2008**, *77*.

32. Wang, Q. H.; Jin, Z.; Kim, K. K.; Hilmer, A. J.; Paulus, G. L. C.; Shih, C. J.; Ham, M. H.; Sanchez-Yamagishi, J. D.; Watanabe, K.; Taniguchi, T.; Kong, J.; Jarillo-Herrero, P.; Strano, M. S. Understanding and controlling the substrate effect on graphene electron-transfer chemistry via reactivity imprint lithography. *Nature Chemistry* **2012**, *4*, 724-732.

33. Chen, J. H.; Jang, C.; Adam, S.; Fuhrer, M. S.; Williams, E. D.; Ishigami, M. Charged-impurity scattering in graphene. *Nature Physics* **2008**, *4*, 377-381.

34. Zhang, Y. B.; Brar, V. W.; Girit, C.; Zettl, A.; Crommie, M. F. Origin of spatial charge inhomogeneity in graphene. *Nature Physics* **2009**, *5*, 722-726.

35. Uosaki, K.; Elumalai, G.; Noguchi, H.; Masuda, T.; Lyalin, A.; Nakayama, A.; Taketsugu, T. Boron Nitride Nanosheet on Gold as an Electrocatalyst for Oxygen Reduction Reaction: Theoretical Suggestion and Experimental Proof. *Journal of the American Chemical Society* **2014**, *136*, 6542-6545.

36. Koitz, R.; Norskov, J. K.; Studt, F. A systematic study of metal-supported boron nitride materials for the oxygen reduction reaction. *Physical Chemistry Chemical Physics* **2015**, *17*, 12722-12727.

37. Elumalai, G.; Noguchi, H.; Uosaki, K. Electrocatalytic activity of various types of h-BN for the oxygen reduction reaction. *Physical Chemistry Chemical Physics* **2014**, *16*, 13755-13761.

38. Bard, A. J.; Denuault, G.; Lee, C.; Mandler, D.; Wipf, D. O. Scanning Electrochemical Microscopy - a New Technique for the Characterization and Modification of Surfaces. *Accounts of Chemical Research* **1990**, *23*, 357-363.

39. Bard, A. J.; Mirkin, M. V.; Unwin, P. R.; Wipf, D. O. Scanning Electrochemical Microscopy .12. Theory and Experiment of the Feedback Mode with Finite Heterogeneous Electron-Transfer Kinetics and Arbitrary Substrate Size. *Journal of Physical Chemistry* **1992**, *96*, 1861-1868.

40. Bard, A. J.; Mirkin, M. V. *Scanning Electrochemical Microscopy, Second Edition*. 2012.

41. Cannes, C.; Kanoufi, F.; Bard, A. J. Cyclic voltammetry and scanning electrochemical microscopy of ferrocenemethanol at monolayer and bilayer-modified gold electrodes. *Journal of Electroanalytical Chemistry* **2003**, *547*, 83-91.

42. Clegg, A. D.; Rees, N. V.; Klymenko, O. V.; Coles, B. A.; Compton, R. G. Marcus theory of outer-sphere heterogeneous electron transfer reactions: High precision steady-state measurements of the standard electrochemical rate constant for ferrocene derivatives in alkyl cyanide solvents. *Journal of Electroanalytical Chemistry* **2005**, *580*, 78-86.

43. Bard, A. J.; Faulkner, L. R. *Electrochemical methods: fundamentals and applications, 2nd Edition*. 2001.

44. Marcus, R. A. Chemical and Electrochemical Electron-Transfer Theory. *Annual Review of Physical Chemistry* **1964**, *15*, 155-196.

45. Kneten, K. R.; Mccreery, R. L. Effects of Redox System Structure on Electron-Transfer Kinetics at Ordered Graphite and Glassy-Carbon Electrodes. *Analytical Chemistry* **1992**, *64*, 2518-2524.

46. Ferrari, A. C.; Basko, D. M. Raman spectroscopy as a versatile tool for studying the properties of graphene. *Nature Nanotechnology* **2013**, *8*, 235-246.

47. Graf, D.; Molitor, F.; Ensslin, K.; Stampfer, C.; Jungen, A.; Hierold, C.; Wirtz, L. Spatially resolved raman spectroscopy of single- and few-layer graphene. *Nano Letters* **2007**, *7*, 238-242.

48. Li, X. S.; Cai, W. W.; An, J. H.; Kim, S.; Nah, J.; Yang, D. X.; Piner, R.; Velamakanni, A.; Jung, I.; Tutuc, E.; Banerjee, S. K.; Colombo, L.; Ruoff, R. S. Large-area synthesis of high-quality and uniform graphene films on copper foils. *Science* **2009**, *324*, 1312-1314.

49. Ritzert, N. L.; Rodriguez-Lopez, J.; Tan, C.; Abruna, H. D. Kinetics of Interfacial Electron Transfer at Single-Layer Graphene Electrodes in Aqueous and Nonaqueous Solutions. *Langmuir* **2013**, *29*, 1683-1694.

50. Khomyakov, P. A.; Giovannetti, G.; Rusu, P. C.; Brocks, G.; van den Brink, J.; Kelly, P. J. First-principles study of the interaction and charge transfer between graphene and metals. *Physical Review B* **2009**, *79*, 195425.

51. Yang, Y. C.; Chang, T. Y.; Lee, Y. L. Adsorption behavior of 11-mercapto-1-undecanol on Au(111) electrode in an electrochemical system. *J. Phys. Chem. C* **2007**, *111*, 4014-4020.

52. Patel, A. N.; Collignon, M. G.; O'Connell, M. A.; Hung, W. O. Y.; McKelvey, K.; Macpherson, J. V.; Unwin, P. R. A New View of Electrochemistry at Highly Oriented Pyrolytic Graphite. *JACS* **2012**, *134*, 20117-20130.

53. Chen, R.; Nioradze, N.; Santhosh, P.; Li, Z. T.; Surwade, S. P.; Shenoy, G. I.; Parobek, D. G.; Kim, M. A.; Liu, H. T.; Amemiya, S. Ultrafast Electron Transfer Kinetics of Graphene Grown by Chemical Vapor Deposition. *Angewandte Chemie-International Edition* **2015**, *54*, 15134-15137.

54. Zhang, G. H.; Guell, A. G.; Kirkman, P. M.; Lazenby, R. A.; Miller, T. S.; Unwin, P. R. Versatile Polymer-Free Graphene Transfer Method and Applications. *Acs Applied Materials & Interfaces* **2016**, *8*, 8008-8016.

55. Sławińska, J.; Dabrowski, P.; Zasada, I. Doping of graphene by a Au(111) substrate: Calculation strategy within the local density approximation and a semiempirical van der Waals approach. *Physical Review B* **2011**, *83*, 245429.

56. Toyoda, K.; Nozawa, K.; Matsukawa, N.; Yoshii, S. Density Functional Theoretical Study of Graphene on Transition-Metal Surfaces: The Role of Metal d-Band in the Potential-Energy Surface. *The Journal of Physical Chemistry C* **2013**, *117*, 8156-8160.

57. Sławińska, J.; Zasada, I. Fingerprints of Dirac points in first-principles calculations of scanning tunneling spectra of graphene on a metal substrate. *Physical Review B* **2011**, *84*, 235445.

58. Love, J. C.; Estroff, L. A.; Kriebel, J. K.; Nuzzo, R. G.; Whitesides, G. M. Self-assembled monolayers of thiolates on metals as a form of nanotechnology. *Chemical Reviews* **2005**, *105*, 1103-1169.

59. Yildirim, N.; Demirkol, D. O.; Timur, S. Modified Gold Surfaces with Gold Nanoparticles and 6-(Ferrocenyl)hexanethiol: Design of a Mediated Microbial Sensor. *Electroanalysis* **2015**, *27*, 52-57.

60. Lefrou, C.; Cornut, R. Analytical Expressions for Quantitative Scanning Electrochemical Microscopy (SECM). *ChemPhysChem* **2010**, *11*, 547-556.

61. Rodriguez-Lopez, J.; Bard, A. J. Scanning Electrochemical Microscopy: Surface Interrogation of Adsorbed Hydrogen and the Open Circuit Catalytic Decomposition of Formic Acid at Platinum. *Journal of the American Chemical Society* **2010**, *132*, 5121-5129.

62. Rodriguez-Lopez, J.; Alpuche-Aviles, M. A.; Bard, A. J. Interrogation of Surfaces for the Quantification of Adsorbed Species on Electrodes: Oxygen on Gold and Platinum in Neutral Media. *Journal of the American Chemical Society* **2008**, *130*, 16985-16995.

CHAPTER 3

INNER-SPHERE ELECTRON TRANSFER REACTIONS ON GRAPHENE — SUB-SURFACE MODULATION OF ELECTROCATALYTIC ACTIVITY[†]

3.1 Introduction

Coupling materials with the intention of synergistically modifying their electronic structure has garnered much interest recently as a strategy for creating superior electrocatalysts.[1-6] Unfortunately, these combinations often exhibit surface degradation processes during electrochemical testing that obscure experimental interpretation.[7-9] We reasoned that a platform that enabled electronic interactions between two materials at atomic scales would be desirable to test such electrocatalyst synergies. With its demonstrated electrical conductivity,[10] low interfacial reactivity,[11, 12] and prospects as electrocatalyst support and adsorbing surface,[13, 14] graphene stands out as an excellent candidate for such platform. Here, we demonstrate that a layer of graphene placed between two redox-active materials enables electronic interactions commensurate with its atomic thickness, having a profound impact on the electrocatalytic reactivity of the interface towards the oxygen reduction reaction (ORR).

[†] Part of this chapter is adapted from the publication: Hui, J.; Pakhira, S.; Bhargava, R.; Barton, Z. J.; Zhou, X.; Chinderle, A. J.; Iyiola, O. O.; Mendoza-Cortes, J. L.; Rodriguez-Lopez, J., Sub-Surface Modulation of Electrocatalytic Activity *via* Graphene-Mediated Electronic Coupling. Submitted.

[†] Collaboration and contribution statement: This work was collaborated with Prof. Jose L. Mendoza-Cortes group at Florida State University. The theoretical simulated results were collected by Srimanta Pakhira, Oluwagbenga O. Iyiola, and Prof. Jose L. Mendoza-Cortes.

Inspired by the well-known effects induced by underlying electronic states on the surface electronic structure of pyrolytic graphite,[15-17] we hypothesized that the atomic thickness of graphene would enable "underlayer" electronic effects to permeate towards "overlayer" species in contact with a graphene interface as shown in Figure 3.1. Charge doping and Fermi level shifts between graphene and metal substrates have been studied previously by scanning tunneling microscopy(STM),[18, 19] density functional theory (DFT),[20, 21] and x-ray photoemission spectroscopy (XPS).[22] We recently demonstrated that the kinetics of electron transfer to a series of mediators in solution were increased six-fold when graphene was deposited on Au instead of SiO_2, firmly establishing the potential to study more complex reactions (Figure 3.1a).[23] Because the rates and mechanisms for electrocatalytic reactions are responsive to surface electronic structure and density of states (DOS), these effects are known to have a dramatic impact on kinetically-limited outer-sphere reactions.[23] Furthermore, similar charge coupling effects between adsorbed metal-phthalocyanine molecules and metal substrates mediated by a graphene interface have been identified by STM, DFT, and XPS.[24-26] Therefore, we reasoned that this charge coupling effect of three layer electrode structure (Figure 3.1b) – surface adsorbed molecular catalyst adlayer, graphene interface, and metal substrate from top to bottom – would offer unique benefits for electrochemical reactions. Here, we take a critical step forward on these concepts and demonstrate through scanning electrochemical microscopy (SECM) and first-principle dispersion-corrected density-functional theory (DFT-D) calculations that metal underlayers modulate not only the reactivity of graphene towards inner-sphere electrocatalysis but also that of adsorbed molecular catalyst above graphene.

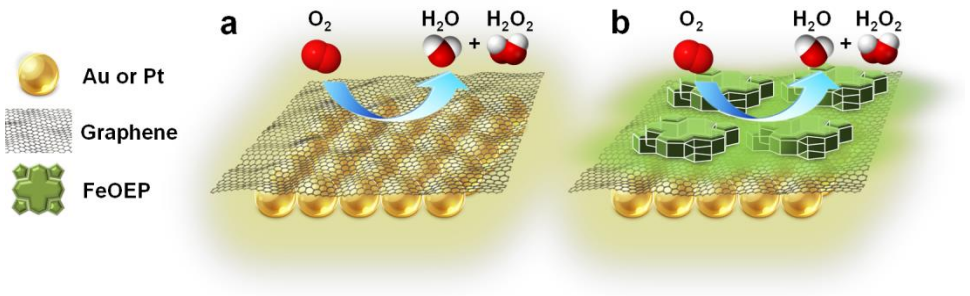

Figure 3.1 Depiction of multi-layer electrocatalysts hybridized with electronically "semi-transparent" graphene. a, Two-layer hybrid structure of graphene supported on metal. The metal underlayer affects ORR above graphene. b, Three-layer hybrid structure of a molecular catalyst layer adsorbed to graphene supported on a metal substrate. The metal underlayer's electronic effect permeates across the graphene interface and couples with the FeOEP adlayer to influence the electrochemical reactions above.

The ORR is a promising and well-studied cathodic reaction in fuel cells and metal-air batteries.[27-29] The ORR follows an inner-sphere mechanism, where the electrode material determines the rate of reaction through the formation of specific bond-breaking steps.[30] We chose the ORR as an electrocatalytic probe as it conveniently demonstrates the potential of metal/graphene interfaces for characterizing synergetic processes: while the underlayer metal strongly modulates the reaction potential, the overlayer exhibits reaction mechanisms highly reminiscent of the unperturbed surface. Oxygen can be reduced directly to water through a four-electron reaction or reduced to hydrogen peroxide through two-electron reaction:[31]

Four-electron route: $O_2 + 4H^+ + 4e^- \rightarrow 2H_2O$ $\quad E° = 1.23$ V *vs*. NHE

Two-electron route: $O_2 + 4H^+ + 2e^- \rightarrow 2H_2O_2$ $\quad E° = 0.695$ V *vs*. NHE

The number of electrons transferred during ORR depends on the catalyst identity and the extent of electrode activation. Pt-based catalysts typically proceed primarily through the more efficient

4-electron route,[6] while other metals such as Au predominately operate through the 2-electron route.[32, 33] In addition to metals, transition metal N_4-macrocycles such as porphyrins and phthalocyanines are promising cost-effective molecular candidate catalysts for the ORR.[34-36] Both the substrate and molecular adlayer can be electrocatalytically active towards ORR, so we chose Pt or Au substrates as "underlayer" materials and 2,3,7,8,12,13,17,18-octaethyl-21*H*,23*H*-porphine iron(III) chloride (FeOEP) as a molecular adlayer catalyst, making use of the observation that FeOEP adsorbs easily on graphitic surfaces due to strong π-π stacking interactions.[37, 38] Experiments with FeOEP adsorbed on graphene demonstrate the ORR mechanism is guided by the surface chemistry of the overlayer component while the reaction activation potential benefits from the underlying metal support. We further demonstrate that the ultra-thin graphene layer may be leveraged as a platform to mitigate fouling or poisoning in electrocatalytic systems without sacrificing catalytic performance, as uniquely enabled by the electronic interactions across graphene's thin yet impermeable structure.

3.2 Characterization of Graphene and Metal Substrates

Large, continuous graphene sheets grown by chemical vapor deposition (CVD) were used in all experiments and characterized *via* Raman spectroscopy and scanning electron microscopy (SEM). The Raman 2D/G intensity ratio map (Figure 3.2a) shows large gray areas of bilayer graphene, indicated by a 2D/G ratio close to unity, interrupted by brighter and darker areas of monolayer and triple layer graphene, respectively.[39, 40] Areal spectra of each selected region (Figure 3.2b) show a small D band around 1370 cm^{-1}, which suggests few structural defects are present.[41] In spite of the small interlayer inhomogeneities, the graphene sheet consisted primarily of a continuous bilayer structure.[23] The graphene samples were transferred onto metal films and patterned metal substrates by a wet etching procedure for electrochemical tests.

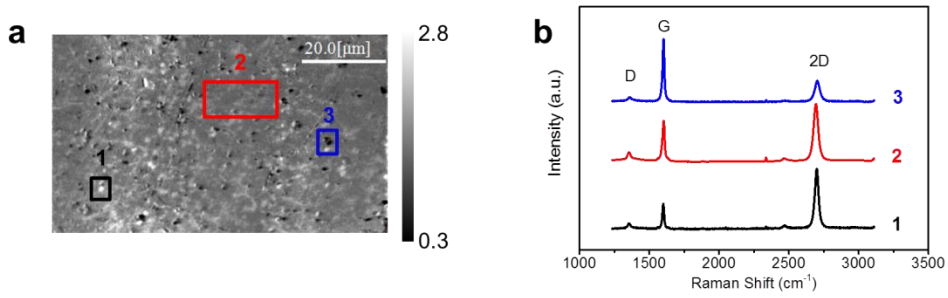

Figure 3.2 Characterization of pristine graphene on SiO_2 wafer and patterned metal substrates. a, Raman map of the 2D/G ratio of graphene supported on SiO_2. The color bar shows the 2D/G ratio scale. The boxed regions enclose examples of single- (black line, area 1), double- (red line, area 2) and triple- (blue line, area 3) layer graphene. b, Areal Raman spectra of the boxed regions indicated in a.

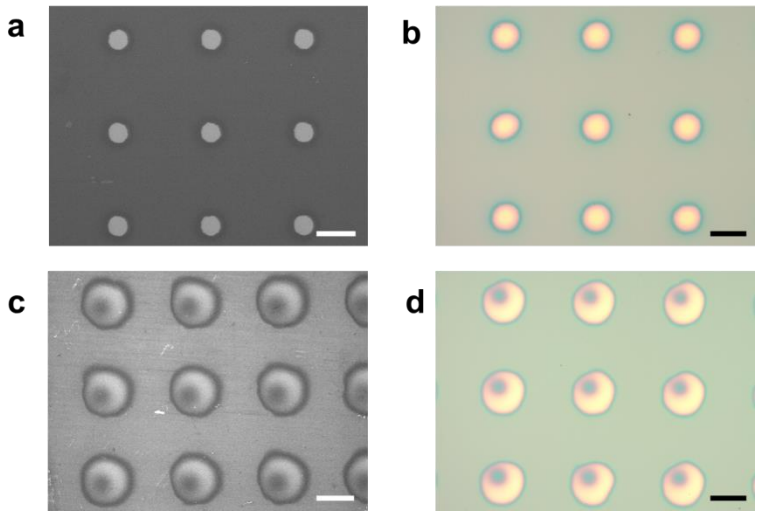

Figure 3.3 SEM and photomicrograph images of graphene/p-Au (a and b) and graphene/p-Pt (c and d). The scale bars indicate 200 μm.

SEM and optical microscope images (Figure 3.3) of graphene on Au pattern (graphene/p-Au) and graphene on Pt pattern (graphene/p-Pt) show continuous coverage of the Au and Pt patterns by graphene. Maps of the Raman 2D peak intensity at freshly-deposited graphene/p-Au and graphene/p-Pt (Figure 3.4a, 3.4c) also indicate full coverage of the surface by graphene. The

two maps use different intensity scales due to differences in the substrate background fluorescence. Associated areal Raman spectra are shown in Figure 3.4b and Figure 3.4d for graphene/p-Au and graphene/p-Pt, respectively.

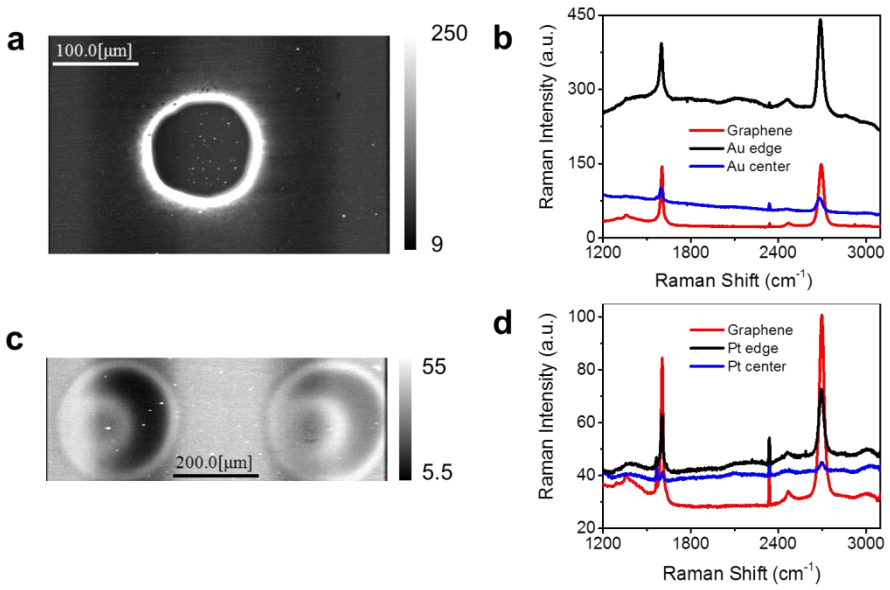

Figure 3.4 Raman characterizations of graphene/p-Au and graphene/p-Pt. a, Raman map of the 2D band intensity of graphene supported on p-Au. b, Raman evidence of full graphene coverage of p-Au substrate, with the comparison between Raman spectra taken from the center of the Au-backed area, the edge of Au-backed area, and the pure graphene area in panel a. c, Raman map of the 2D band intensity of graphene supported on p-Pt. d, Raman evidence of full graphene coverage of p-Pt substrate, with the comparison between Raman spectra taken from the center of the Pt-backed area, the edge of Pt-backed area, and the pure graphene area in panel c. The color bars in a, c show the 2D band intensity scale. Graphene supported on a Au or Pt underlayer exhibits a larger fluorescence background but does not yield substantially different Raman peak shapes or the 2D/G ratios from those observed for graphene on SiO_2.

3.3 Metal Substrate Effects

The ORR electrocatalytic activities of freshly obtained graphene/metal substrates were investigated *via* SECM for any localized enhancement of graphene by a metal underlayer. Because ORR on carbon materials proceeds primarily through the two-electron route, we focused on the collection by the SECM tip of substrate-generated H_2O_2 (Figure 3.5a). Line-scans over a graphene/p-Au spot (Figure 3.5b) show increasing H_2O_2 generation at the graphene/p-Au spot in response to increasingly negative substrate bias up to -0.4 V. The full SECM images to which the line-scans belong (Figure 3.5d–g) demonstrate that the contrast between H_2O_2 collection currents over graphene/p-Au and pristine graphene decreased as the substrate potential was made less negative. The absence of significant ORR activity at -0.1 V (Figure 3.5g) shows that the currents are not attributable to exposed Au regions. Therefore, the observed local H_2O_2 production over graphene/p-Au spots implies an activating contribution toward two-electron ORR from the Au underlayer.

We repeated the same experiment on graphene/p-Pt substrates at various potentials. SECM line-scans (Figures 3.5c) and corresponding images (Figure 3.5h–k) over a graphene/p-Pt were tested. Comparing the results over graphene/p-Au (Figure 3.5d–g) and graphene/p-Pt (Figure 3.5h–k) suggests that the underlying metals have a profound impact on the catalytic activity observed over graphene. In fact, graphene/p-Pt requires 300 mV less overpotential to achieve an equivalent enhancement on graphene/p-Au. Pristine Pt is known to be a much better ORR catalyst than Au,[27, 28] and it is interesting that this behavior is preserved even through a layer of graphene.

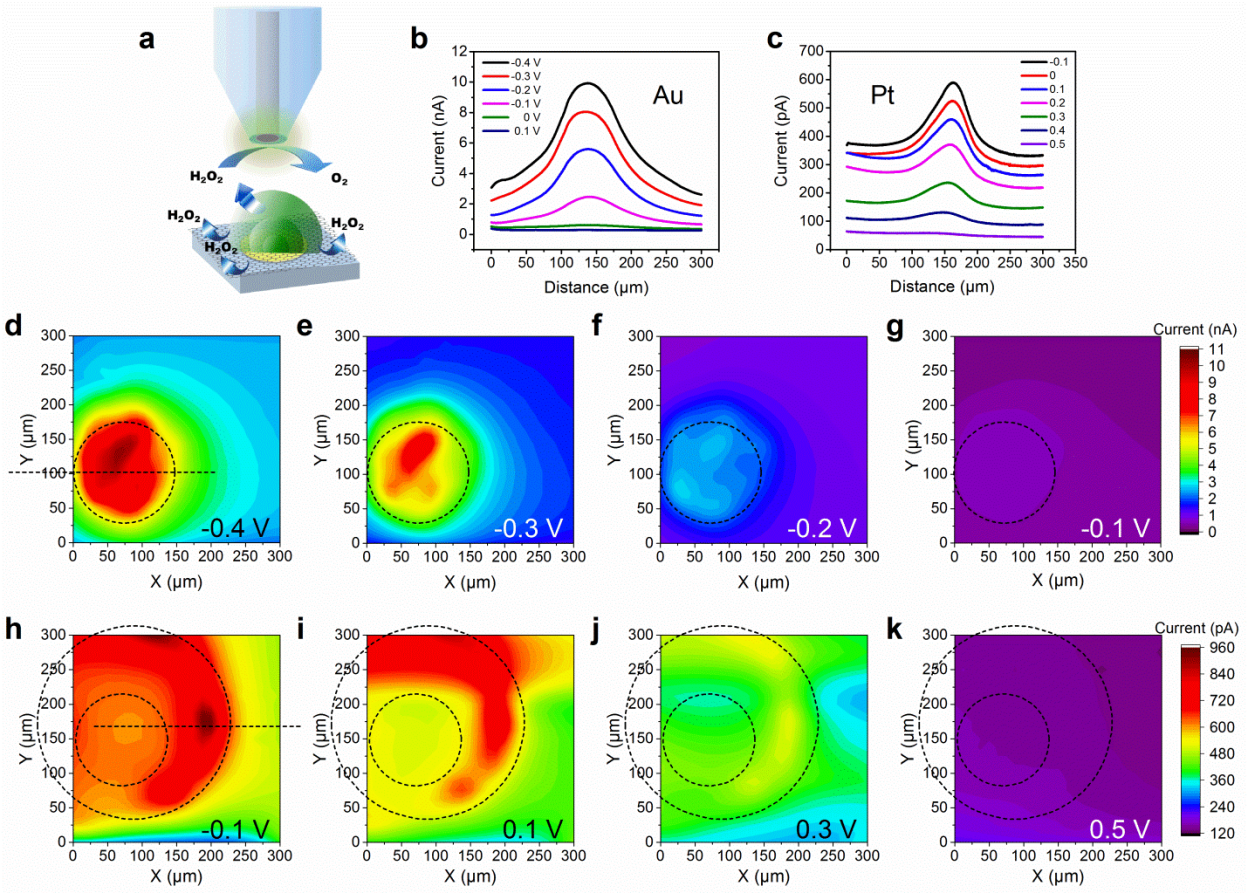

Figure 3.5 SECM maps of ORR products collected at graphene supported on p-Au or p-Pt. a, Schematic of SECM substrate-generation/tip-collection mode (SG/TC). The substrate generates H_2O_2 by a two-electron reduction of O_2. A Pt UME is raster-scanned parallel to the surface while collecting the substrate-generated H_2O_2 and oxidizing it back to O_2. b, Lateral scans across the graphene/Au region indicated in d with incremental deactivation of ORR at the substrate. Graphene supported on Au remains catalytically active at potentials too small to stimulate ORR at graphene on SiO_2 wafer. c, Lateral scans across the graphene/Pt region indicated in h with incremental deactivation of ORR at the substrate. Graphene supported on Pt remains catalytically active at potentials too small to stimulate ORR at graphene on SiO_2 wafer. Graphene/Pt exhibits electrocatalytic enhancement with substantially less input potential than required for graphene/Au. d–g, SECM SG/TC maps of substrate H_2O_2 production taken at a tip–substrate gap

(*Figure 3.5 Continued*) of 7.5 μm over graphene/p-Au with sequentially decreasing substrate activation towards ORR. The dashed circle indicates the approximate location of a circular Au underlayer. h–k, SECM SG/TC maps of substrate H_2O_2 production taken at a tip–substrate gap of 8.8 μm over graphene/p-Pt with sequentially decreasing substrate activation towards ORR. The area between the two dashed circles indicates the approximate location of an asymmetric toroidal Pt underlayer. All data were obtained with a Pt UME (r_{Pt} = 12.5 μm, R_G = 4) poised at 1.0 V *vs*. Ag/AgCl in a solution of 10 mM H_2SO_4 and 0.1 M Na_2SO_4 in O_2-saturated water.

To evaluate the possible *d*-band contributions, we conducted DFT-D calculations of the electronic properties of the 2D layered graphene/Au(111) and graphene/Pt(111) nanostructure materials. Pristine graphene showed semi-metallic behavior with a unique linear band structure around the Fermi level (E_F), forming a Dirac cone at the K-point of its Brillouin zone as shown in Figure 3.6a. In contrast, graphene/Au(111) and graphene/Pt(111) exhibited metallic behavior and downshifting of the Dirac cone at the K point (Figure 3.6b, 3.6c). Total DOSs calculations show the charge carrier density was redistributed in the form of an apparent electron transfer from Au(111) or Pt(111) layers to the graphene layer leading to an electron rich region around the E_F (Figure 3.6b, 3.6c). The majority of DOSs reflect the *d*-subshell of Au(111) (Figure 3.6b) or Pt(111) (Figure 3.6c). The catalysts' surface electronic structure, especially the *d*-band center, is a determining factor for oxygen chemisorption energy, which is crucial to ORR kinetics.[2, 4] Because Au and Pt contribute significant and similar *d*-subshell structures to the total DOS, graphene/p-Au and graphene/p-Pt exhibit ORR activation potentials similar to those observed for Au and Pt. This explains the agreement in H_2O_2 onset potentials observed over metal-supported graphene spots in Figure 3.5d-k. Experimental SECM imaging and theoretical DFT-D modeling

both demonstrate the substantial catalytic advantages achieved by the addition of underlayer metal supports for graphene.

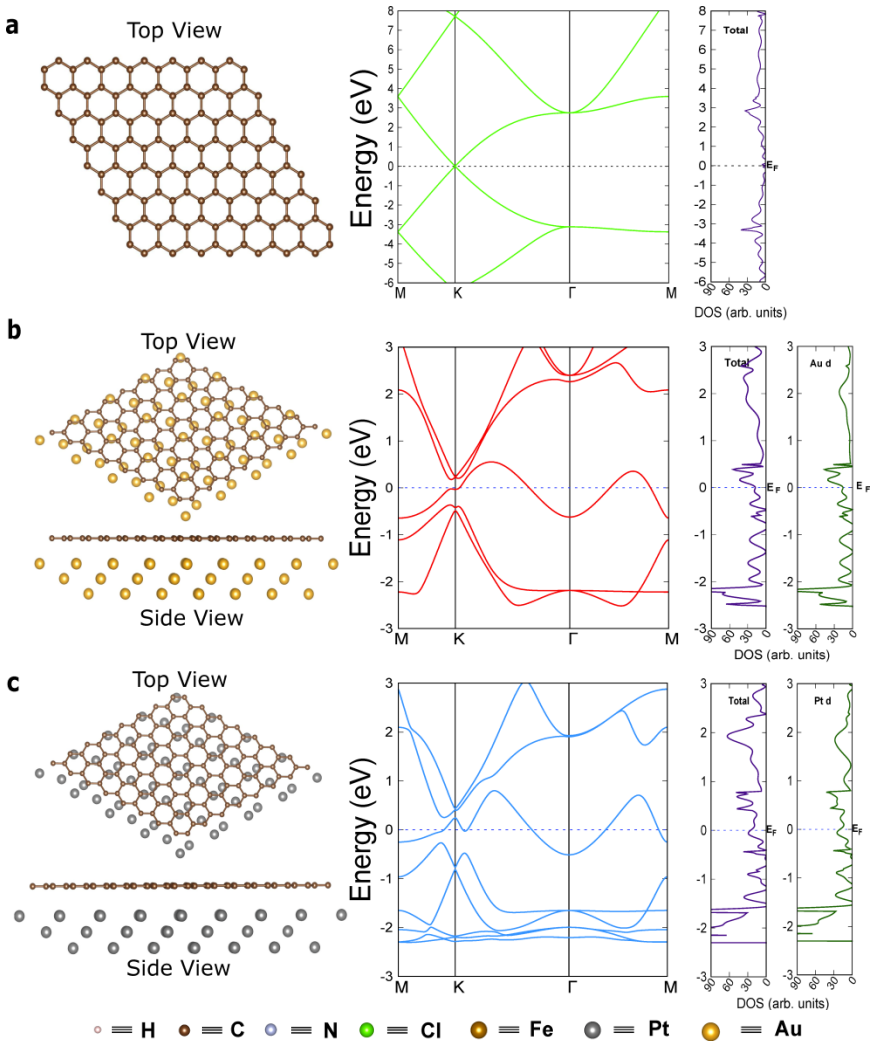

Figure 3.6 Electronic structure of (a) graphene, (b) graphene/Au(111), (c) graphene/Pt(111). Each panel contains the top view and side view of equilibrium structure, band structure, total DOSs, and projected DOSs for metal *d*-subshell electrons (exclude pure graphene system), from left to right.

3.4 Metal Substrate Effects on Molecular Adsorption Layer above Graphene

Although the results in Figure 3.5 show the clear influence of the underlayer metal, pristine graphene is not an attractive electrocatalyst for ORR. Aiming to increase ORR activity

above metal-supported graphene, we designed a three-layer electrode consisting of FeOEP catalyst adsorbed on graphene and supported on a metal substrate. Interactions across graphene between the molecular adsorption layer with the metal substrate were then evaluated by comparing the ORR peak position and current intensity.

FeOEP was shown to strongly adsorb onto graphene. Cyclic voltammetry (CV) of a tetrahydrofuran solution containing FeOEP on a graphene electrode shows a quasi-reversible charge transfer at ~ -0.3 V *vs*. Ag quasi-reference electrode (Ag QRE) for the Fe(III)/Fe(II) redox couple, and a reversible charge transfer process at ~ -1.4 V *vs*. Ag QRE for the Fe(II)/Fe(I) redox couple (Figure 3.7).

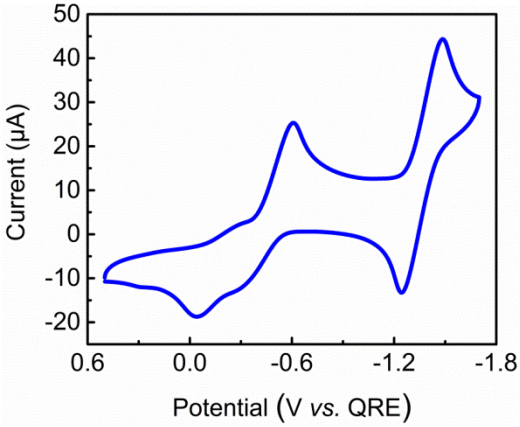

Figure 3.7 CV at graphene taken at 0.1 V s^{-1} in a solution consisting of 0.2 mM FeOEP and 0.1 M $TBAPF_6$ in THF.

Molecular electrocatalysis for ORR proceeds first through the Fe(III)/Fe(II) redox couple, so we now focus on this redox process. With a low solution concentration of FeOEP, adsorption of this molecule onto graphene dominates the voltammetric signatures. Figure 3.8a shows the gradual change of CVs at different scan rates for 0.5 μM FeOEP in tetrahydrofuran solution at graphene electrode. The peak current depends linearly on the potential sweep rate (Figure 3.8b), which indicates the surface-confined adsorption of FeOEP on the graphene electrode.[30] CVs of

FeOEP on a wide variety of substrates exhibit a similar adsorption peak (Figure A.1). Integration of the peak current area yields the total charge transferred (*Q*), which in turn allows calculation of the surface coverage (Γ) (Figure 3.8c).[14] This is described well by a Langmuir isotherm:

$$Q = nFA\Gamma$$

$$\Gamma = \Gamma_s KC\,(KC+1)^{-1}$$

From these calculations, the monolayer adsorption coverage (Γ_s) is 157 pmol cm^{-2} and the Gibbs free energy of adsorption (ΔG_{ads}) is -35.2 kJ mol^{-1}. FeOEP thus formed an energetically-favorable and stable layer on graphene.

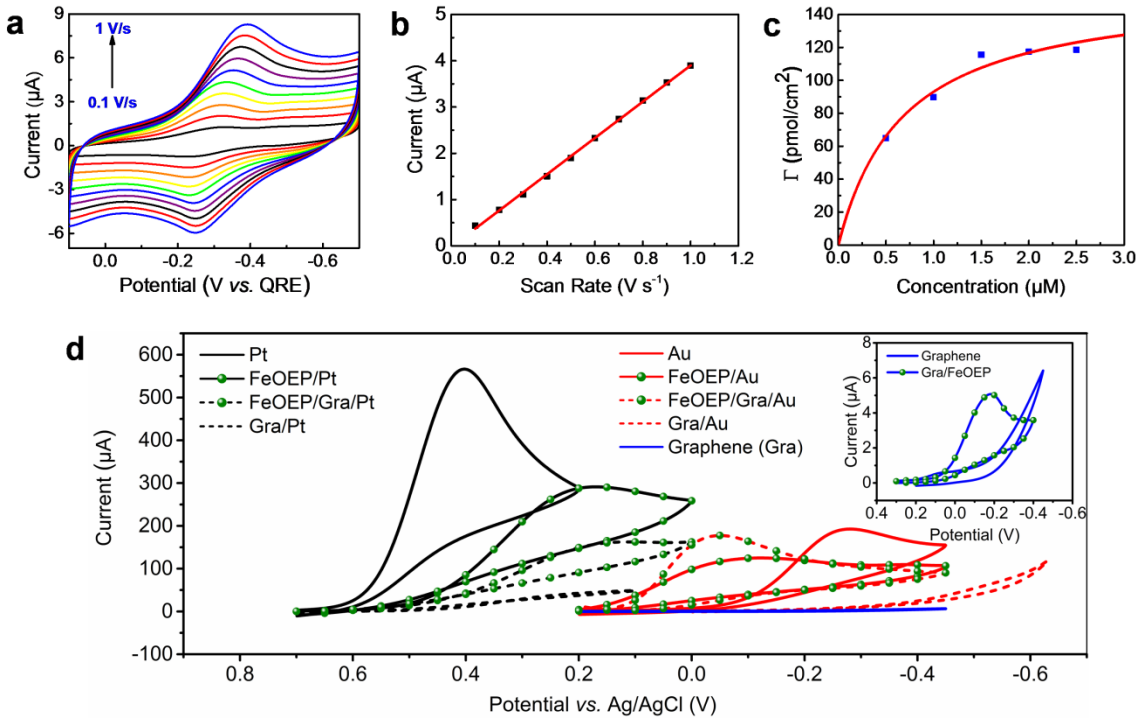

Figure 3.8 FeOEP adsorption behavior on graphene and CVs of ORR at various substrates. a, CVs of FeOEP adsorption on graphene at various scan rates. The solution consisted of 0.5 μM FeOEP and 0.1 M $TBAPF_6$ in THF. b, Surface confined FeOEP adsorption behavior demonstrated by the linear fit of peak currents extracted from panel a as a function of the potential scan rate. c, Langmuir adsorption isotherm of FeOEP on graphene derived from

(*Figure 3.8 Continued*) integrated CV data taken in various concentrations of FeOEP. d, CVs of ORR at 0.1 V s^{-1} at various electrode combinations. The solution consisted of 10 mM H_2SO_4 and 0.1 M Na_2SO_4 in O_2-saturated water. The electrode structures are listed in Figure.

Following FeOEP adsorption, the differential ORR activity of ten modified graphene substrates *via* CVs in O_2-saturated 10 mM H_2SO_4 solution (Figure 3.8d) were tested. Each CV trace is the average of at least six individual tests, with their standard deviation zones available as Figure A.2. Adsorption of FeOEP on Au (FeOEP/Au trace) decreased the overpotential for ORR by 160 mV but also caused a decrease in the peak current compared to bare Au. This may reflect a shift to a predominantly two-electron route for FeOEP on Au. In contrast, since Pt is a much better electrocatalyst for ORR than either Au or FeOEP, adding a FeOEP layer to Pt (FeOEP/Pt trace) led to a negative potential shift of 230 mV and a substantial decrease in the peak current compared to bare Pt. Detailed peak information is available as Table 3.1. This decrease in current reflects a mechanistic change from a predominantly four-electron route on bare Pt to a two-electron route for FeOEP on Pt, as observed for FeOEP on Au. Importantly, compared to FeOEP/Au and FeOEP/Pt, the presence of a graphene layer between the metal substrate and the molecular catalyst does not greatly affect the voltammetric response. The persistence of these differential ORR activation behaviors on modified substrates is evidence of electronic communication between the metal underlayer and the molecular adlayer through the graphene interface. Despite differences in the activation overpotential, the FeOEP/graphene/Pt and FeOEP/graphene/Au displayed similar current intensities, suggesting that the FeOEP/graphene overlayer plays a greater role in determining the overall surface mechanism while the metal underlayer contributes more substantially to the observed overpotential.

Table 3.1 Extrapolated CV peak ORR currents and positions for the substrates in Figure 3.8d.

Substrate	Potential/V	Current/ μA
Pt	0.40	566
FeOEP/Pt	0.17	291
FeOEP/Graphene/Pt	0.12	163
Graphene/Pt	0.10	49
Au	-0.28	193
FeOEP/Au	-0.12	125
Au/Graphene/FeOEP	-0.05	178
Graphene/Au	-0.52	60
Graphene	--	--
FeOEP/Graphene	-0.18	5

To further verify the catalytic enhancement of FeOEP/graphene by a metal underlayer, SECM redox competition mode images (Figure 3.9a) were obtained over a FeOEP, graphene, and patterned Pt three-layer stacked substrate. In this mode, an Hg-capped SECM tip, chosen for its current stability, and the layered substrate were simultaneously biased to perform ORR, leading to decreased tip current over active substrate regions. Spatially heterogeneous consumption of O_2 by the substrate at various activation potentials results from differences in surface reactivity and is reflected in the current registered at the probe. As the substrate potential decreased from +0.5 V to +0.1 V (Figure 3.9b–d), the FeOEP/graphene/p-Pt area became activated for ORR and thus decreased the local O_2 concentration. When the substrate potential was pushed to -0.2 V (Figure 3.9e), the remaining FeOEP/graphene area was also activated for ORR, consuming O_2 and decreasing the spatial contrast between currents registered at the SECM tip. The greatest contrast in ORR activity as measured by competitive depletion of O_2 from solution is observed at the intermediate +0.1 V activation potential. This agrees with the behavior

expected from substrate CVs (Figure 3.8d). The agreement between the current distribution (Figure 3.9f) and the known metal underlayer geometry (Figure 3.3c, 3.3d) supports the conclusion that the enhanced O_2 consumption at substrate is attributable specifically to electronic donation from the Pt underlayer to the molecular adlayer through the electronically "semi-transparent" graphene interface.

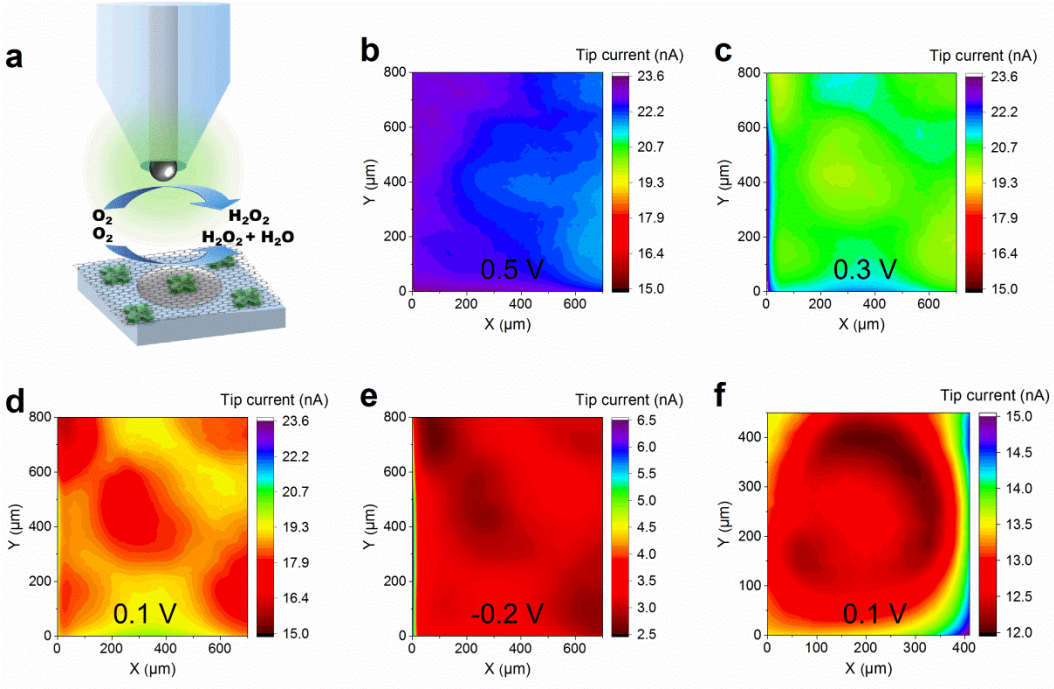

Figure 3.9 SECM maps of ORR activity at FeOEP/graphene supported on p-Pt. a, Schematic of SECM redox competition mode. The substrate and Hg-capped Pt UME are simultaneously biased to reduce O_2. As the Hg probe is rastered parallel to the surface, it registers less current over electrocatalytically active regions due to localized O_2 depletion. b–e, SECM maps of O_2 redox competition taken at a tip–substrate gap of 41 μm over FeOEP/graphene/p-Pt with sequentially increasing substrate activation towards ORR. f, SECM map of the active region centered at [X, Y] = [0 μm, 800 μm] in panel d. Electronic coupling with an asymmetric toroidal Pt underlayer increases the local competitive consumption of O_2 by FeOEP adsorbed on

(*Figure 3.9 Continued*) graphene, resulting in the observed red annulus of low probe current. All data in panel b–f were collected with a Hg-capped Pt tip held at -0.6 V *vs*. Ag/AgCl in a solution of 10 mM H_2SO_4 and 0.1 M Na_2SO_4 in O_2-saturated water.

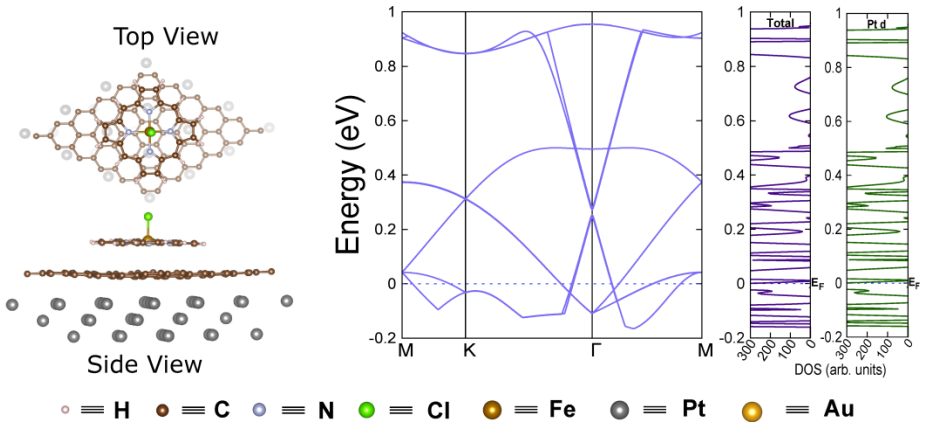

Figure 3.10 Electronic structure and electronic properties (band structures and density of states (DOSs), and projected DOSs for Pt *d*-subshell electrons from left to right) of the FeOEP/graphene/Pt materials.

In order to further understand our results, we investigated the adlayer effects on the FeOEP catalyst considering atomistic models for the FeOEP/graphene/Pt and FeOEP/graphene/Au systems shown in Figure 3.10 and Figure A.3, respectively. The atomistic simulations reveal that these structures have metallic behavior as depicted in the band structure and DOS calculations. The total DOS calculation shows a large electron density around the E_F, and an increased charge density that is redistributed in the form of an apparent electron transfer from Pt or Au to the graphene layer. This might explain the enhancement of the ORR catalytic activity. Furthermore, the DFT-D calculations predict the previously mentioned d-subshell donation effect of underlying metal can permeate through the graphene interface and couple with the adsorbed FeOEP layer above graphene (Figure 3.10). This change in the electron

accumulation around the E_F indicates high electron mobility, which is a significant factor for the electrocatalytic ORR.

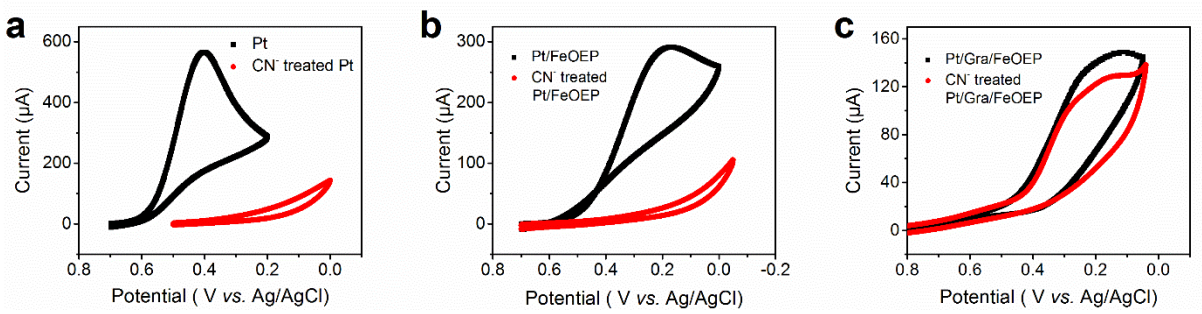

Figure 3.11 CVs of ORR at various Pt-based electrodes before and after CN^- poisoning. Pt (**a**) and FeOEP/Pt (**b**) electrodes both exhibited significantly decreased ORR activity following CN^- poisoning, but FeOEP/graphene/Pt maintained similar behavior. This demonstrates the protection that graphene can provide against small molecular poisoners.

With the recent refinement of several ultra-thin electrochemical interfaces such as BN,[42] MoS_2[43, 44] and MXenes[45, 46], we foresee that understanding charge-transfer interactions between electrocatalytic components across thin structures will continue to gain momentum. Furthermore, ultra-thin interfaces may gain attention as a means of mitigating the deleterious effects of reactive environments on precious substrate metals, as shown by the cyanide exposure experiments in Figure 3.11. Here, the graphene layer provided a stable interface on which cyanide was not capable of poisoning the underlying Pt substrate, thus preventing the loss of activity of the metal and the desorption of FeOEP by site displacement. The ability to promote catalyst stability while retaining electrocatalytic performance as demonstrated here can inform the rational design of future electrocatalytic platforms, expand present technologies to otherwise inaccessible environments, and enable applications in previously unexplored chemical scenarios.[1-3]

3.5 Materials and Methods

Materials. All chemicals were purchased from commercial sources and used as received. Sodium sulfate (99.0%), sulfuric acid (99.999%), tetrahydrofuran (anhydrous, 99.9%), 2,3,7,8,12,13,17,18-octaethyl-21*H*,23*H*-porphine iron(III) chloride (FeOEP), tetrabutylammonium hexafluorophosphate ($TBAPF_6$, 99.0%), potassium cyanide (KCN, 96.0 %) , sodium hydroxide (NaOH, 98.0 %), ethylenediaminetetraacetic acid disodium salt dihydrate ($Na_2EDTA\ 2H_2O$, 99.0%), acetone (99.5%), dichloromethane (DCM, 99.9%), isopropanol (99.5%) and glacial acetic acid (99.5%) were all purchased from Sigma-Aldrich. Si wafers were purchased from Monsanto. Si wafer with a 300 nm SiO_2 layer (Si/SiO_2 wafer) was purchased from University Wafer. 25 μm copper foil was purchased from Alfa Aesar. Two poly(methyl methacrylate) (PMMA) solutions, NanoTM 950K A4 (MW 950,000 PMMA, 4 w. % solution in anisole) and 495K A2 (MW 495,000 PMMA, 2 w% solution in anisole), were purchased from MicroChem. Copper etchant (CE-100) was purchased from Transene Company. Deionized water (DI water) was filtered using a Millipore system. Ultra-high purity (UHP) argon was obtained from Airgas.

Graphene growth and transfer. Graphene was fabricated by chemical vapor deposition (CVD) on 25 μm thick copper foil. Copper foil was pre-treated by sequential exposure to acetone for 10 s, DI water for 10 s, acetic acid for 10 min, DI water for 10 s, acetone for 10 s, and lastly isopropanol for 10 s.[47] Following this cleaning procedure, the copper foil were placed in a tube furnace at 1000 ℃ and 40 mTorr with 100 sccm CH_4 and 50 sccm H_2 flowing for 25 min.[48]

A wet-etching procedure was applied to transfer graphene onto various substrates as described below. After CVD growth, the exposed surface of graphene supported on Cu foil was protected with 3 layers of spin-coated PMMA at 4000 rpm spin rate. The additions of the initial

495K A2 layer and the two subsequent 950K A4 layers were each followed by a 2 min curing process at 200 ℃. The combined PMMA/graphene/Cu substrates were placed in copper etchant solution and allowed to float there at 40 °C for 4 h to dissolve the Cu foil. To eliminate any residual Cu metal, the floating PMMA/graphene sheets were subsequently rinsed with DI water 4 times, exposed to 0.1 M Na_2EDTA for 1 h, and then rinsed again with DI water 4 times. Cleaned graphene/PMMA sheets were transferred onto the desired substrates and then blow-dried with UHP argon. The protective PMMA layers were then dissolved by sequential exposure to anisole for 2 h, a DCM:acetone mixture (1:1 vol.) for 4 h, and lastly isopropanol for 2 h.

Substrate Fabrication and Characterization. Physical deposition methods were applied to fabricate metal substrates, including a 100 nm thick Au film on Si wafer, a 100 nm thick Au pattern (p-Au) on Si/SiO_2 wafer, a 100 nm thick Pt film on Si wafer, and a 100 nm thick Pt pattern (p-Pt) on Si/SiO_2 wafer. Electron beam evaporation was used to deposit Au films/patterns, and sputtering deposition was used to make Pt films/patterns. Shadow masks of a square array of 100 μm holes with a 500 μm center-to-center distance were used to produce Au and Pt patterns. Due to a broadening effect in the sputtering method, each individual spot in the Pt pattern was a 200 μm asymmetric toroid. Graphene was fabricated using a previously published CVD method[49] and transferred to different substrates by a wet-etching process. Detailed procedures can be found the Supporting Information. Graphene on Si/SiO_2 wafer, graphene on metal films, or graphene on patterned metal substrates were characterized by optical microscopy (Zeiss AxioLab.A1), scanning electron microscopy (SEM, Philips XL30 ESEM-FEG), and Raman spectroscopy (Nanophoton Laser Raman Microscope RAMAN-11).

Porphyrin Adsorption Properties on Graphene. To declare the stability of the FeOEP adlayer, a series of FeOEP adsorption characterizations on pristine graphene were performed

inside an MBRAUN UniLab glovebox filled with UHP argon and with less than 0.1 ppm each of oxygen and moisture. Electrochemical measurements were carried out with CH Instrument 920D workstation in a three electrode configuration with Pt wire as the counter electrode, Ag wire as a QRE, and graphene on Si/SiO_2 wafer as the working electrode. CVs of FeOEP in bulk solution and adsorbed on graphene were tested in 0.5, 1.0, 1.5, 2.0, 2.5, and 200 μM FeOEP THF solution with 0.1 M $TBAPF_6$ as supporting electrolyte at various scan rates.

ORR Activity Measurements. CV and SECM experiments were performed to obtain bulk and localized information of ORR activity of various electrode structures, using CH Instrument 760E bipotentiostat and CH Instrument 920D workstation, respectively. A Au wire counter electrode and a Ag/AgCl reference electrode were used in all cases. All experiments were performed in O_2-saturated 10 mM H_2SO_4 aqueous solution with 0.1 M Na_2SO_4 as the supporting electrolyte. Oxygen saturation was maintained by bubbling oxygen into solution through a humidifier for 10 min before testing and keeping an oxygen blanket over the solution during testing.

The bulk ORR behavior on various substrate electrodes and modification conditions – Au, Pt, graphene, graphene/Au, graphene/Pt, FeOEP/graphene, FeOEP/Au, FeOEP/Pt, FeOEP/graphene/Au, and FeOEP/graphene/Pt, CN^- treated Pt, CN^- treated FeOEP/Pt, CN^- treated FeOEP/Graphene/Pt – was collected through CV. The exposed working electrode area was 7 mm^2 (3 mm diameter). All CVs were performed with a 0.1 V s^{-1} potential scan rate. FeOEP-modified substrates were fabricated by coating substrates with a solution of 0.1 mM FeOEP in THF for 10 min. These were then rinsed 2 times with THF and 3 times with DI water to remove excess FeOEP solution. The cyanide poisoning conditions were achieved by exposing

substrates with a 10 mM KCN in 0.1 M NaOH aqueous solution for 30 min inside a fume hood. Followed by thorough rinsing of 3 times with 0.1 M NaOH solution and 3 times with DI water.

The effect of metal substrates on ORR kinetics above graphene was investigated by SECM using a Pt tip (r_{Pt} = 12.5 μm) as the primary working electrode and a graphene-covered patterned metal substrate (graphene/p-M, M = Pt, Au. Total working area = 7 mm^2) as the secondary working electrode. The Pt tip was approached with open circuit negative feedback while poised to reduce O_2 to a final distance of 7.5 μm from the graphene/p-Au and 8.8 μm from the graphene/p-Pt. SECM images were collected using the substrate-generation/tip-collection mode, in which substrates were biased at various potentials to reduce O_2, while the Pt tip was held at 1 V *vs*. Ag/AgCl to locally oxidize the H_2O_2 generated from the substrate.[31, 50, 51]

The effect of a metal substrate on an adsorbed molecular layer across graphene was investigated by SECM using a Hg-capped Pt tip (r_{Pt} = 12.5 μm) as the primary working electrode and a FeOEP/graphene/p-Pt substrate (total working area = 7 mm^2) as the secondary working electrode. The traditional Pt UME was exchanged for a Hg-capped Pt UME so as to mitigate electrode fouling by residual impurities from FeOEP adsorption procedure. The fabrication of Hg-capped Pt UME is delineated elsewhere.[52] The probe was approached to a final tip–substrate gap of 41 μm while monitoring negative feedback of O_2 reduction. SECM images were collected using the redox competition mode, in which the probe and the substrate were simultaneously poised to reduce O_2.

Computational Details. First-principle calculations were performed with the CRYSTAL14[53] suite program. All the structures were optimized with the dispersion-corrected hybrid B3LYP, B3LYP-D2[54-60] method (i.e. DFT-D) which has been shown to give correct electronic properties of the 2D layered materials.[45] Each metal substrate was modeled as a slab of

three stacked metal atom layers in a 2x2 supercell. Simulations of graphene adsorbed on Au(111) and Pt(111) consisted of a graphene monolayer placed on the top of the appropriate metal atom layers and about ~500 Å vacuum region. The equilibrium geometry of the graphene/Au(111) and graphene/Pt(111) materials are shown in Figure 3.6b, 3.6c. We choose the in-plane lattice constant of graphene equal to its optimized DFT value (a=b=2.445 Å) adapting the lattice constants of the metals accordingly as initial guess to construct the multilayer models, adopting the lattice constants of the metal accordingly. The graphene honeycomb lattice is matched with the triangular lattice of the metal-(111) surfaces of both Pt and Au in the lateral unit cells shown in Figure 3.6b, 3.6c, 3.10. These atomistic simulation models were fully relaxed to a threshold value of 10^{-7} dyne/Å for the force and 10^{-7} hartree per particle for the energy. In the present computation, triple-zeta valence with polarization quality (TZVP) basis sets were used for the H, N, C, Cl[61] and Weihrich basis sets with effective core potential (ECP)[62-64] for both Pt and Au. Integrations inside of the first Brillouin zone were sampled on 15x15x1 Monkhorst-Pack[65] k-mesh grids for graphene/Pt(111) and graphene/Au(111), while 5x5x1 k-mesh grids for FeOEP/graphene/Pt, FeOEP/graphene/Au systems. Visualization and analysis were performed using VESTA.[66]

3.6 Conclusion

Our multi-faceted study of graphene as an electrochemical interface reveals the ability of underlayer metals to impact inner-sphere reactions through electronic interactions across its ultra-thin bulk. DFT-D computations suggest that the substrate-enhanced behavior may be explained by electronic contributions from metal substrates, which change the effective DOSs and E_F of the system. Detection of H_2O_2, the main product of ORR at graphene, is consistent with the notion that the mechanism for the reaction is dominated by catalysis at the overlayer

structure. Of interest however, an earlier onset of activity was observed for H_2O_2 generation when either Au or Pt was used as underlayer metals, in comparison to bare graphene.

CVs at a wide variety of electrodes demonstrate that this electronic donation further extends across a mediating graphene interface to couple with an adsorbed electrocatalyst (FeOEP) and enhance its ORR performance. We measured the stability of an adsorbed FeOEP layer on graphene *via* construction of its isotherm, and confirmed that the presence of the underlayer metal leads to electrocatalytic enhancement. These enhancements were unambiguously probed via SECM maps of O_2 consumption on metal underlayer patterned electrodes, showing agreement with CV measurements and removing any uncertainties related to sample preparation. Mirroring the observations on bare graphene, the FeOEP/graphene surface played the major role in guiding the ORR mechanism, while the metal substrate contributed more substantially to the observed activation potential.

Graphene's capacity to adsorb molecules and its similarity to commonly used graphitic supports highlight the potential of our platform to design new schemes for the ORR. The ability to influence electrocatalysis from behind an electronically "semi-transparent" yet physically impermeable interface allows remote tuning of existing catalysts while also enabling the development of unprecedented electrocatalytic hybrid architectures. Ultra-thin interfaces such as graphene also offer cost-effective protection against leaching and fouling of metallic catalysts, expanding their operation to otherwise inhospitable environments.

3.7 References

1. Greeley, J.; Stephens, I. E. L.; Bondarenko, A. S.; Johansson, T. P.; Hansen, H. A.; Jaramillo, T. F.; Rossmeisl, J.; Chorkendorff, I.; Norskov, J. K. Alloys of platinum and early transition metals as oxygen reduction electrocatalysts. *Nature Chemistry* **2009**, *1*, 552-556.

2. Stamenkovic, V.; Mun, B. S.; Mayrhofer, K. J. J.; Ross, P. N.; Markovic, N. M.; Rossmeisl, J.; Greeley, J.; Norskov, J. K. Changing the activity of electrocatalysts for oxygen reduction by tuning the surface electronic structure. *Angewandte Chemie-International Edition* **2006**, *45*, 2897-2901.

3. Bligaard, T.; Norskov, J. K. Ligand effects in heterogeneous catalysis and electrochemistry. *Electrochimica Acta* **2007**, *52*, 5512-5516.

4. Lima, F. H. B.; Zhang, J.; Shao, M. H.; Sasaki, K.; Vukmirovic, M. B.; Ticianelli, E. A.; Adzic, R. R. Catalytic activity–d-band center correlation for the O_2 reduction reaction on platinum in alkaline solutions. *Journal of Physical Chemistry C* **2007**, *111*, 404-410.

5. Koper, M. T. M. Thermodynamic theory of multi-electron transfer reactions: Implications for electrocatalysis. *Journal of Electroanalytical Chemistry* **2011**, *660*, 254-260.

6. Markovic, N. M.; Schmidt, T. J.; Stamenkovic, V.; Ross, P. N. Oxygen reduction reaction on Pt and Pt bimetallic surfaces: A selective review. *Fuel Cells* **2001**, *1*, 105-116.

7. Stamenkovic, V.; Schmidt, T. J.; Ross, P. N.; Markovic, N. M. Surface composition effects in electrocatalysis: Kinetics of oxygen reduction on well-defined Pt3Ni and Pt3Co alloy surfaces. *Journal of Physical Chemistry B* **2002**, *106*, 11970-11979.

8. Chen, S.; Sheng, W. C.; Yabuuchi, N.; Ferreira, P. J.; Allard, L. F.; Shao-Horn, Y. Origin of oxygen reduction reaction activity on "Pt3Co" nanoparticles: atomically resolved chemical compositions and ctructures. *Journal of Physical Chemistry C* **2009**, *113*, 1109-1125.

9. Cui, C. H.; Gan, L.; Heggen, M.; Rudi, S.; Strasser, P. Compositional segregation in shaped Pt alloy nanoparticles and their structural behaviour during electrocatalysis. *Nature Materials* **2013**, *12*, 765-771.

10. Bolotin, K. I.; Sikes, K. J.; Jiang, Z.; Klima, M.; Fudenberg, G.; Hone, J.; Kim, P.; Stormer, H. L. Ultrahigh electron mobility in suspended graphene. *Solid State Communications* **2008**, *146*, 351-355.

11. Tan, C.; Rodriguez-Lopez, J.; Parks, J. J.; Ritzert, N. L.; Ralph, D. C.; Abruna, H. D. Reactivity of Monolayer Chemical Vapor Deposited Graphene Imperfections Studied Using Scanning Electrochemical Microscopy. *Acs Nano* **2012**, *6*, 3070-3079.

12. Guell, A. G.; Ebejer, N.; Snowden, M. E.; Macpherson, J. V.; Unwin, P. R. Structural Correlations in Heterogeneous Electron Transfer at Monolayer and Multilayer Graphene Electrodes. *Journal of the American Chemical Society* **2012**, *134*, 7258-7261.

13. Rodriguez-Lopez, J.; Ritzert, N. L.; Mann, J. A.; Tan, C.; Dichtel, W. R.; Abruna, H. D. Quantification of the Surface Diffusion of Tripodal Binding Motifs on Graphene Using Scanning Electrochemical Microscopy. *Journal of the American Chemical Society* **2012**, *134*, 6224-6236.

14. Mann, J. A.; Rodriguez-Lopez, J.; Abruna, H. D.; Dichtel, W. R. Multivalent binding motifs for the noncovalent functionalization of graphene. *Journal of the American Chemical Society* **2011**, *133*, 17614-17617.

15. Rutter, G. M.; Crain, J. N.; Guisinger, N. P.; Li, T.; First, P. N.; Stroscio, J. A. Scattering and interference in epitaxial graphene. *Science* **2007**, *317*, 219-222.

16. Ishigami, M.; Chen, J. H.; Cullen, W. G.; Fuhrer, M. S.; Williams, E. D. Atomic structure of graphene on SiO_2. *Nano Letters* **2007**, *7*, 1643-1648.

17. Decker, R.; Wang, Y.; Brar, V. W.; Regan, W.; Tsai, H.-Z.; Wu, Q.; Gannett, W.; Zettl, A.; Crommie, M. F. Local electronic properties of graphene on a BN substrate via scanning tunneling microscopy. *Nano Letters* **2011**, *11*, 2291-2295.

18. Wintterlin, J.; Bocquet, M. L. Graphene on metal surfaces. *Surface Science* **2009**, *603*, 1841-1852.

19. Batzill, M. The surface science of graphene: Metal interfaces, CVD synthesis, nanoribbons, chemical modifications, and defects. *Surface Science Reports* **2012**, *67*, 83-115.

20. Giovannetti, G.; Khomyakov, P. A.; Brocks, G.; Karpan, V. M.; van den Brink, J.; Kelly, P. J. Doping graphene with metal contacts. *Physical Review Letters* **2008**, *101*.

21. Khomyakov, P. A.; Giovannetti, G.; Rusu, P. C.; Brocks, G.; van den Brink, J.; Kelly, P. J. First-principles study of the interaction and charge transfer between graphene and metals. *Physical Review B* **2009**, *79*.

22. Dahal, A.; Addou, R.; Coy-Diaz, H.; Lallo, J.; Batzill, M. Charge doping of graphene in metal/graphene/dielectric sandwich structures evaluated by C-1s core level photoemission spectroscopy. *Apl Materials* **2013**, *1*.

23. Hui, J.; Zhou, X.; Bhargava, R.; Chinderle, A.; Zhang, J.; Rodríguez-López, J. Kinetic modulation of outer-sphere electron transfer reactions on graphene electrode with a sub-surface metal substrate. *Electrochimica Acta* **2016**, *211*, 1016-1023.

24. Scardamaglia, M.; Struzzi, C.; Lizzit, S.; Dalmiglio, M.; Lacovig, P.; Baraldi, A.; Mariani, C.; Betti, M. G. Energetics and hierarchical interactions of metal phthalocyanines adsorbed on graphene/Ir(111). *Langmuir* **2013**, *29*, 10440-10447.

25. Avvisati, G.; Lisi, S.; Gargiani, P.; Della Pia, A.; De Luca, O.; Pacilé, D.; Cardoso, C.; Varsano, D.; Prezzi, D.; Ferretti, A.; Betti, M. G. FePc adsorption on the Moiré superstructure of graphene intercalated with a cobalt layer. *The Journal of Physical Chemistry C* **2017**, *121*, 1639-1647.

26. Altenburg, S. J.; Lattelais, M.; Wang, B.; Bocquet, M.-L.; Berndt, R. Reaction of phthalocyanines with graphene on Ir(111). *Journal of the American Chemical Society* **2015**.

27. Nie, Y.; Li, L.; Wei, Z. Recent advancements in Pt and Pt-free catalysts for oxygen reduction reaction. *Chemical Society Reviews* **2015**, *44*, 2168-2201.

28. Ben Liew, K.; Daud, W. R. W.; Ghasemi, M.; Leong, J. X.; Su Lim, S.; Ismail, M. Non-Pt catalyst as oxygen reduction reaction in microbial fuel cells: A review. *International Journal of Hydrogen Energy* **2014**, *39*, 4870-4883.

29. Bezerra, C. W. B.; Zhang, L.; Lee, K.; Liu, H.; Marques, A. L. B.; Marques, E. P.; Wang, H.; Zhang, J. A review of Fe–N/C and Co–N/C catalysts for the oxygen reduction reaction. *Electrochimica Acta* **2008**, *53*, 4937-4951.

30. Bard, A. J.; Faulkner, L. R. *Electrochemical methods: fundamentals and applications, 2nd Edition*. 2001.

31. Sanchez-Sanchez, C. M.; Rodiriguez-Lopez, J.; Bard, A. J. Scanning electrochemical microscopy. 60. Quantitative calibration of the SECM substrate generation/tip collection mode

and its use for the study of the oxygen reduction mechanism. *Analytical Chemistry* **2008**, *80*, 3254-3260.

32. Blizanac, B. B.; Lucas, C. A.; Gallagher, M. E.; Arenz, M.; Ross, P. N.; Marković, N. M. Anion adsorption, CO oxidation, and oxygen reduction reaction on a Au(100) surface: The pH effect. *Journal of Physical Chemistry B* **2004**, *108*, 625-634.

33. Zurilla, R. W.; Sen, R. K.; Yeager, E. The kinetics of the oxygen reduction reaction on gold in alkaline solution. *Journal of The Electrochemical Society* **1978**, *125*, 1103-1109.

34. Yoshimoto, S.; Inukai, J.; Tada, A.; Abe, T.; Morimoto, T.; Osuka, A.; Furuta, H.; Itaya, K. Adlayer structure of and electrochemical O_2 reduction on cobalt porphine-modiried and cobalt octaethylporphyrin-modifled Au(111) in HClO4. *Journal of Physical Chemistry B* **2004**, *108*, 1948-1954.

35. Zagal, J.; Paez, M.; Tanaka, A. A.; Dossantos, J. R.; Linkous, C. A. Electrocatalytic activity of metal phthalocyanines for oxygen reduction. *Journal of Electroanalytical Chemistry* **1992**, *339*, 13-30.

36. Khorasani-Motlagh, M.; Noroozifar, M.; Ghaemi, A.; Safari, N. Iron(III) octaethylporphyrin chloride supported on glassy carbon as an electrocatalyst for oxygen reduction. *Journal of Electroanalytical Chemistry* **2004**, *565*, 115-120.

37. Tang, H. J.; Yin, H. J.; Wang, J. Y.; Yang, N. L.; Wang, D.; Tang, Z. Y. Molecular architecture of cobalt porphyrin multilayers on reduced graphene oxide sheets for high-performance oxygen reduction reaction. *Angewandte Chemie-International Edition* **2013**, *52*, 5585-5589.

38. Geng, J. X.; Jung, H. Porphyrin functionalized graphene sheets in aqueous suspensions: From the preparation of graphene sheets to highly conductive graphene films. *Journal of Physical Chemistry C* **2010**, *114*, 8227-8234.

39. Graf, D.; Molitor, F.; Ensslin, K.; Stampfer, C.; Jungen, A.; Hierold, C.; Wirtz, L. Spatially resolved raman spectroscopy of single- and few-layer graphene. *Nano Letters* **2007**, *7*, 238-242.

40. Li, X. S.; Cai, W. W.; An, J. H.; Kim, S.; Nah, J.; Yang, D. X.; Piner, R.; Velamakanni, A.; Jung, I.; Tutuc, E.; Banerjee, S. K.; Colombo, L.; Ruoff, R. S. Large-area synthesis of high-quality and uniform graphene films on copper foils. *Science* **2009**, *324*, 1312-1314.

41. Ferrari, A. C.; Basko, D. M. Raman spectroscopy as a versatile tool for studying the properties of graphene. *Nature Nanotechnology* **2013**, *8*, 235-246.

42. Koitz, R.; Norskov, J. K.; Studt, F. A systematic study of metal-supported boron nitride materials for the oxygen reduction reaction. *Physical Chemistry Chemical Physics* **2015**, *17*, 12722-12727.

43. Kibsgaard, J.; Chen, Z. B.; Reinecke, B. N.; Jaramillo, T. F. Engineering the surface structure of MoS_2 to preferentially expose active edge sites for electrocatalysis. *Nature Materials* **2012**, *11*, 963-969.

44. Jaramillo, T. F.; Jorgensen, K. P.; Bonde, J.; Nielsen, J. H.; Horch, S.; Chorkendorff, I. Identification of active edge sites for electrochemical H_2 evolution from MoS_2 nanocatalysts. *Science* **2007**, *317*, 100-102.

45. Xie, Y.; Dall'Agnese, Y.; Naguib, M.; Gogotsi, Y.; Barsoum, M. W.; Zhuang, H. L. L.; Kent, P. R. C. Prediction and characterization of MXene nanosheet anodes for non-lithium-ion batteries. *ACS Nano* **2014**, *8*, 9606-9615.

46. Naguib, M.; Mochalin, V. N.; Barsoum, M. W.; Gogotsi, Y. 25th anniversary article: MXenes: a new family of two-dimensional materials. *Advanced Materials* **2014**, *26*, 992-1005.

47. Cristarella, T. C.; Chinderle, A. J.; Hui, J.; Rodríguez-López, J. Single-layer graphene as a stable and transparent electrode for nonaqueous radical annihilation electrogenerated chemiluminescence. *Langmuir* **2015**, *31*, 3999-4007.

48. Wood, J. D.; Schmucker, S. W.; Lyons, A. S.; Pop, E.; Lyding, J. W. Effects of polycrystalline Cu substrate on graphene growth by chemical vapor deposition. *Nano Letters* **2011**, *11*, 4547-4554.

49. Hui, J.; Burgess, M.; Zhang, J.; Rodríguez-López, J. Layer number dependence of Li^+ intercalation on few-layer graphene and electrochemical imaging of its solid–electrolyte interphase evolution. *ACS Nano* **2016**, *10*, 4248-4257.

50. Sanchez-Sanchez, C. M.; Bard, A. J. Hydrogen peroxide production in the oxygen reduction reaction at different electrocatalysts as quantified by scanning electrochemical microscopy. *Analytical Chemistry* **2009**, *81*, 8094-8100.

51. Mezour, M. A.; Cornut, R.; Hussien, E. M.; Morin, M.; Mauzeroll, J. Detection of hydrogen peroxide produced during the oxygen reduction reaction at self-assembled thiol-porphyrin monolayers on gold using SECM and nanoelectrodes. *Langmuir* **2010**, *26*, 13000-13006.

52. Barton, Z. J.; Rodríguez-López, J. Lithium ion quantification using mercury amalgams as in situ electrochemical probes in nonaqueous media. *Analytical Chemistry* **2014**, *86*, 10660-10667.

53. Dovesi, R.; Orlando, R.; Erba, A.; Zicovich-Wilson, C. M.; Civalleri, B.; Casassa, S.; Maschio, L.; Ferrabone, M.; De La Pierre, M.; D'Arco, P.; Noel, Y.; Causa, M.; Rerat, M.; Kirtman, B. CRYSTAL14: A program for the ab initio investigation of crystalline solids. *International Journal of Quantum Chemistry* **2014**, *114*, 1287-1317.

54. Becke, A. D. Density-functional thermochemistry. III. The role of exact exchange. *The Journal of Chemical Physics* **1993**, *98*, 5648-5652.

55. Lee, C. T.; Yang, W. T.; Parr, R. G. Development of the Colle-Salvetti correlation-energy formula into a functional of the electron density. *Physical Review B* **1988**, *37*, 785-789.

56. Pakhira, S.; Lengeling, B. S.; Olatunji-Ojo, O.; Caffarel, M.; Frenklach, M.; Lester, W. A. A quantum Monte Carlo study of the reactions of CH with acrolein. *Journal of Physical Chemistry A* **2015**, *119*, 4214-4223.

57. Grimme, S. Semiempirical GGA-type density functional constructed with a long-range dispersion correction. *Journal of Computational Chemistry* **2006**, *27*, 1787-1799.

58. Pakhira, S.; Sahu, C.; Sen, K.; Das, A. K. Can two T-shaped isomers of OCS-C_2H_2 van der Waals complex exist? *Chemical Physics Letters* **2012**, *549*, 6-11.

59. Pakhira, S.; Sen, K.; Sahu, C.; Das, A. K. Performance of dispersion-corrected double hybrid density functional theory: A computational study of OCS-hydrocarbon van der Waals complexes. *Journal of Chemical Physics* **2013**, *138*.

60. Pakhira, S. L., K. P.; Mendoza-Cortes, J. L. An alternative strategy to control the electronic properties of bilayer graphene: semi-metal to metal transition and a 2D material with Dirac Cone. **2016**.

61. Peintinger, M. F.; Oliveira, D. V.; Bredow, T. Consistent Gaussian basis sets of triple-zeta valence with polarization quality for solid-state calculations. *Journal of Computational Chemistry* **2013**, *34*, 451-459.

62. Hay, P. J.; Wadt, W. R. Ab initio effective core potentials for molecular calculations. Potentials for K to Au including the outermost core orbitals. *The Journal of Chemical Physics* **1985**, *82*, 299-310.

63. Weihrich, R.; Anusca, I. Halbantiperowskite II: zur Kristallstruktur des $Pd_3Bi_2S_2$. *Zeitschrift für anorganische und allgemeine Chemie* **2006**, *632*, 335-342.

64. Doll, K. CO adsorption on the Pt(111) surface: a comparison of a gradient corrected functional and a hybrid functional. *Surface Science* **2004**, *573*, 464-473.

65. Monkhorst, H. J.; Pack, J. D. Special points for brillouin-zone integrations. *Physical Review B* **1976**, *13*, 5188-5192.

66. Momma, K.; Izumi, F. VESTA 3 for three-dimensional visualization of crystal, volumetric and morphology data. *Journal of Applied Crystallography* **2011**, *44*, 1272-1276.

CHAPTER 4

LI ION INTERCALATION ON FEW-LAYER GRAPHENE — LAYER NUMBER CONTROLLED STAGING MECHANISM AND SOLID ELECTROLYTE EVOLUTION[†]

4.1 Introduction

Li-ion batteries are a mature rechargeable energy storage platform that utilizes the reversible intercalation of Li^+ into carbonaceous materials and transition metal oxides used as anodes and cathodes respectively. Graphite's intrinsic layered structure has made this material a workhorse in the battery community for Li-ion battery anodes. In the past few decades, research on the layered properties of graphitic anode materials has focused on exploring its intercalation mechanisms,[1-3] solid-electrolyte interface (SEI) formation, composition and structure,[4-6] and ways to improve its structural stability and cyclability.[7-9]

The emergence of carbon-based two-dimensional materials, such as electrodes composed of few layers of graphene (FLG),[10-12] have prompted the search for materials with a distinct or superior performance towards intercalation than that of bulk graphite. Arguments for improvements over graphite tend to gravitate towards the enhanced electrical properties of

[†] Part of this chapter is adapted from the publication: Hui, J.; Burgess, M.; Zhang, J. R.; Rodriguez-Lopez, J., Layer Number Dependence of Li^+ Intercalation on Few-Layer Graphene and Electrochemical Imaging of Its Solid-Electrolyte Interphase Evolution. ACS Nano **2016**, *10*, 4248-4257.

[†] Collaboration and contribution statement: This work was collaborated with group colleague Mark Burgess. The *in-situ* SECM experiments were performed together with him.

graphene, their large surface area, or their processability.[13-16] However, other fundamental differences in the intercalation mechanism of Li^+ on FLG can be proposed. Here, we address the question of whether graphite's bulk properties for Li^+ intercalation and SEI formation are maintained in a carbon material with a finite number of layers, or if they take on electrochemical properties unique to themselves.

The Li^+ intercalation process into graphite follows a staging mechanism, in which Li ions do not randomly insert into any available empty interlayer galleries simultaneously, but instead intercalate into specific interlayers at a time.[17-20] It has been reported that Li ions first randomly occupy available sites (dilute stage-1, LiC_{72}), then diffuse to fill every four layers of the graphene planes (stage-4, LiC_{36}), and finally concentrate to fill every three (stage-3, LiC_{27}), two (stage-2, LiC_{12}), and one (stage-1, LiC_6) layer(s) respectively.[8, 21] Thus, in graphite the intercalation process is strongly dependent on the number of neighboring delithiated interlayers at any given time. FLG naturally displays limited numbers of available intercalation sites; therefore, we hypothesize that the staging of lithiation will be necessarily limited as certain charge stages are not accessible. For example, stage-4 may not be possible in FLG with less than 5 layer graphene. With limited interlayers for Li^+ intercalation in FLG, this process might reveal different phase transitions between stages and a deviation from intercalation potentials when compared to bulk graphite.

Apart from Li^+ intercalation, a solid-electrolyte interphase (SEI) is also generated at the early stages of cycling on graphite anodes. The SEI forms because the negatively polarized anode causes the degradation of electrolyte and solvent, causing deposition of inorganic and organic decomposition products, onto the surface of the graphite. However, after formation and stabilization, the SEI layer prevents further degradation of electrolyte and solvent as this layer is

largely electronically insulating, thus blocking electron transport across it.[4-6] Yet, even with the SEI completely formed, the anode maintains high Li^+ conductivity which ensures long term cyclability. Compared to graphite, FLG has similar surface properties and electrochemical characteristics,[22] thus may exhibit similar SEI formation processes. However, the stability of the SEI on FLG, together with its electronic and ionic conductivity properties, have not been fully addressed.

In this paper, we explored Li^+ intercalation and SEI formation on FLG *via* stationary voltammetry and electrochemical imaging methods. Two synthetic routes were used to fabricate FLG. One consisted of the direct growth of multilayer graphene (MLG), which had on average 10 graphene layers. The other methodology consisted of the layer-by-layer transfer of bilayer graphene (BLG), to controllably produce layered number graphene samples (2-6 layers). FLG samples revealed a layer number dependence for the number and location of intercalation peaks, which is representative of the existence of a staging-type mechanism.

Previous studies of the SEI on graphite were focused on the structural, compositional and stability changes with different carbon materials, solvents, electrolytes, and temperatures using spectroscopic and microscopic methods such XPS,[23, 24] FT-IR,[25] mass spectrometry,[24] XRD,[26] and electron microscopy.[24] Electrochemical impedance spectroscopy (EIS) is the most common method to explore SEI's conductivity after formation, but the information from these experiments is spatially-averaged.[27] Here, we introduce scanning electrochemical microscopy (SECM) to visualize *in situ* the local electronic transfer and ionic transport properties of FLG electrodes after SEI formation. SECM is a powerful tool to image highly localized substrate electrochemical processes, and provides a convenient platform to test comparisons between materials and substrate conditions within the same experiment. In our experiment, a Pt nano-

electrode was used to sense and image local electrochemical kinetic changes before and after SEI formation through SECM feedback experiments. Additionally, a Hg-capped Pt ultra-micro electrode was used as a spatially resolved selective Li-ion sensor *via* stripping voltammetry[28] to explore Li^+ uptake into FLG with a formed SEI layer. Spatially-resolved information about electron transfer kinetics and ionic transport of SEI coated MLG samples provided details of SEI layer behavior changes *in situ,* and guided us to better understand the SEI properties on ultra-thin FLG samples.

4.2 Few Layer Graphene Characterization

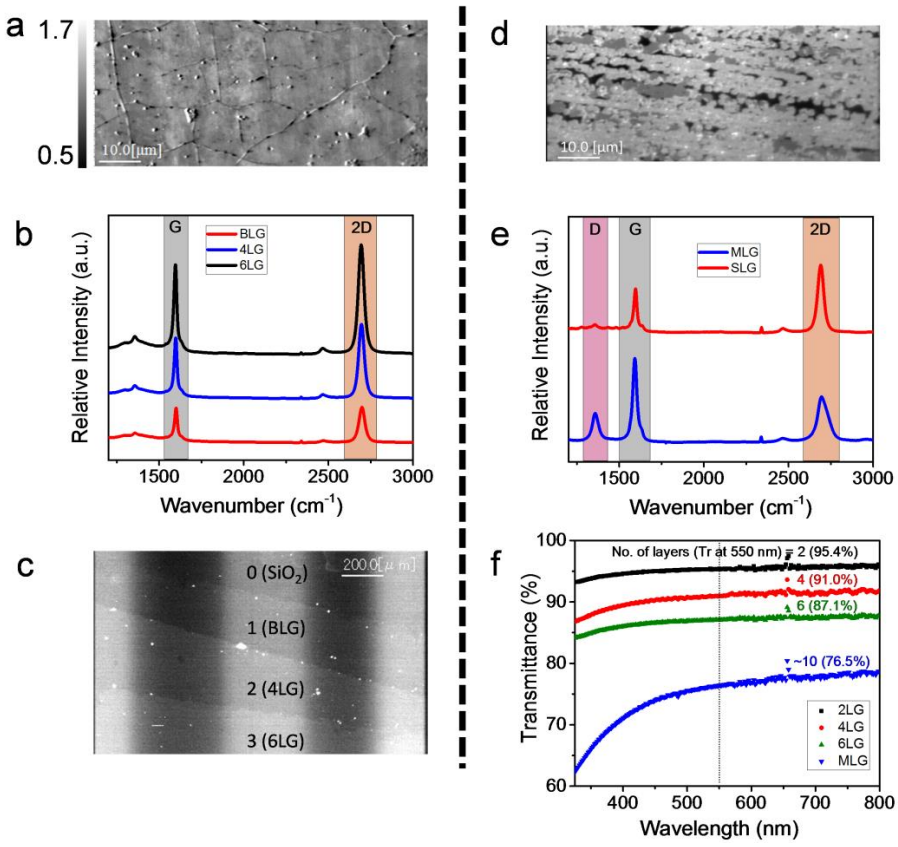

Figure 4.1 Spectroscopic characterization of FLG samples. a, Raman 2D/G intensity ratio mapping of CVD-grown BLG sample on Si/SiO_2 wafer. The graphene is primarily composed of double layers with tens of micron grain size. b, Raman spectra of layer-by-layer transferred

(*Figure 4.1 Continued*) samples: BLG, 4LG, and 6LG. Each transfer maintained the 2D/G intensity ratio double layer characteristics of BLG but contribute to accumulated spectrum intensity. c, Raman 2D intensity mapping multiple graphene transfers. From top to bottom: SiO_2, 1 times transferred BLG, 2 times transferred 4LG, 3 times transferred 6LG, respectively. Each layer can be easily identified through its intensity change and the observed sharp edges between layers. d, Raman 2D intensity mapping of directly grown MLG sample. The sample consisted mostly of micron sized MLG domains (bright region), decorated with few SLG (grey region) and holes (black region). The Raman spectra of MLG and SLG region is shown in e. f, UV-Vis transmittance of layer-by-layer transferred BLG, 4LG, and 6LG samples, together with directly grown MLG samples (~ 10 layers).

In order to explore Li^+ intercalation into FLG with different number of layers, two different types of graphene substrates were grown using chemical vapor deposition (CVD). One CVD method reliably produced double layer graphene, which after layer-by-layer transfer, yielded graphene with 2, 4 or 6 layers as needed. The other CVD method directly grew multilayer graphene. Figure 4.1 summarizes the properties of different graphene samples. The Raman 2D/G ratio mapping in Figure 4.1a reflects the double layer structure of graphene, which displays a 2D/G intensity ratio around 1.[29, 30]

Graphene samples showed a uniform and continuous sheet with tens of microns domain size. After layer-by-layer transfer of bilayer graphene sheets, 2-layer, 4-layer and 6-layer graphene substrates were obtained. Figure 4.1c is the Raman 2D intensity mapping of a three times transferred graphene sample where each layer can be recognized with sharp edges, indicating the integrity of these samples was maintained after a layer-by-layer wet transfer. A zoomed-in view of each layer, the Raman spectra of 1, 2 and 3 times transfer graphene samples

are shown in Figure 4.1b. From these spectra, it is clear that each layer preserved a 2D/G intensity ratio of about 1, and double and triple transferred samples exhibited 2 or 3 times higher intensities.[31] With this method, we can successfully manufacture bilayer graphene (BLG), 4 layer graphene (4LG), and 6 layer graphene (6LG) samples verified by Raman analysis. Figure 4.1d shows the Raman 2D intensity mapping of directly grown multilayer graphene (MLG), where Raman spectra of representative areas in MLG are shown in Figure 4.1e. In this Figure, the white areas are multilayer graphene domains, grey areas are single layer domains, and black areas are holes. Additional methods were used to characterize graphene samples for verification. The gradual decrease of UV-Vis transmittance (Figure 4.1f) for the progression from single, double and triple layer-by-layer transferred bilayer graphene on glass agrees well with Raman images. According to previous reports, single layers of graphene contribute to a 2.3 % transmittance decrease at 550 nm,[32] as quantitatively observed for our 2, 4, and 6 layer graphene sheets. From the transmittance data of MLG (~ 76 %), this material was roughly equivalent to 10 layers of graphene.

4.3 Patterning Few Layer Graphene

After successfully making the graphene samples (2, 4, 6 layer graphene and directly grown multilayer graphene), photolithography and reactive ion etching methods were applied to create ionic openings for Li^+ to intercalate in-between graphene sheets. The fabrication procedure is summarized in Figure 4.2a, the graphene on Si/SiO_2 wafer sample - ① went through one step photolithography to create 3 m round windows on S1813 photoresist - ②, RIE etching of exposed graphene under S1813 windows - ③, and stripping off the rest of photoresist to yield patterned graphene samples - ④.

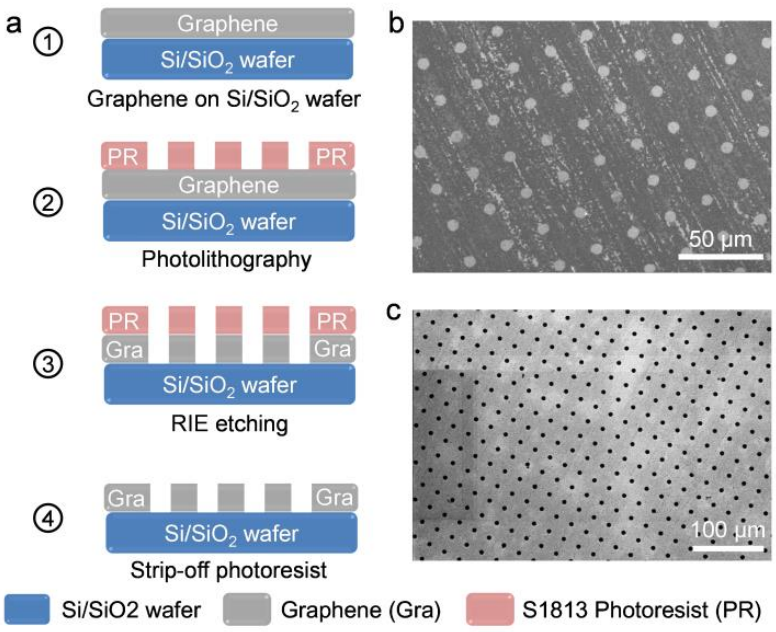

Figure 4.2 FLG patterning procedure and results. a, schematic procedure to create point of entry holes for ionic intercalation on FLG. Graphene samples - ① were patterned *via* photolithography with S1813 as photoresist, leaving patterned 3 μm window openings - ②. Oxygen plasma was applied to etch exposed graphene area - ③. After carefully removing photoresist, patterned openings were generated on FLG sample - ④. b, SEM image of patterned MLG sample. c, SEM image of patterned SLG sample (exfoliated BLG sample). This last image was taken after days of electrochemical experimentation with SLG.

As shown in Figure 4.2b and 4.2c, the patterned openings were imbedded into the graphene basal planes and generated additional edge planes for Li^+ to intercalate. Figure 4.2b is the SEM of patterned MLG before intercalation test which matches well with the Raman image in Figure 4.1d. Figure 4.2c is the SEM image of patterned "bilayer graphene" after days of experimentation in electrolyte. The graphene sheets maintained their integrity without any obvious mechanical damage. However, as discussed later in more detail, after the entire

patterning process, the top layer of bilayer graphene peeled off and left only the bottom layer on Si/SiO_2 wafer intact, which is referred as a patterned SLG later. The stripping of the top graphene layer might originate from the strain generated from the Si/SiO_2 substrate,[33] which decreases the attraction between bottom and top basal planes. The stripped top graphene layer came off during the acetone rinsing step that removes the photoresist, thus BLG was not obtained for electrochemical experiments. Instead we used the resulting SLG surface.

4.4 Layer Number Dependent Intercalation Behavior

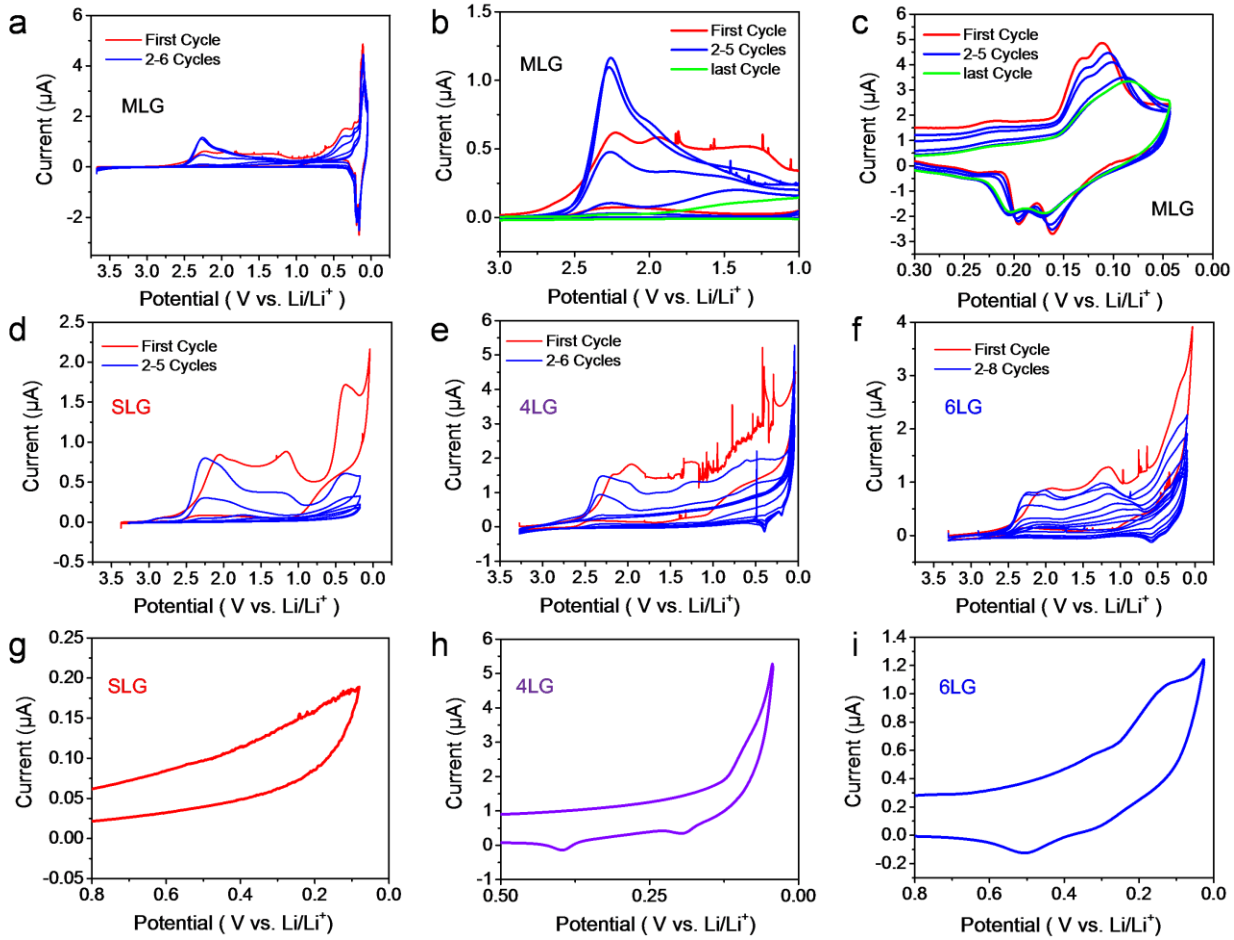

Figure 4.3 Cyclic voltammograms of FLG. a, Cycling behavior of MLG; the first cycle is labelled with red color to distinguish it from following cycles in blue. The zoomed in Figures of

(*Figure 4.3 Continued*) SEI region and Li^+ intercalation region are shown in b and c, respectively. In b and c, the sixth (last) cycle is labeled in green. d, cycling behavior of patterned SLG sample with first cycle labeled in red. After stabilization, the last cycle in the intercalation region is shown in g. Similarly, e and h, f and i are the full cycling CVs and stabilized intercalation behaviors for 4LG and 6LG respectively. Test condition: 0.1 M $LiBF_4$ in 50:50 ratio PC/EC, electrode area was 4.9 mm^2.

We first examined Li^+ intercalation into MLG. The first several full CV cycles of MLG are shown in Figure 4.3a, and can be divided into two regions: SEI formation and Li intercalation, in which the zoomed-in results are shown in Figure 4.3b and 4.3c. The SEI formation region is mainly located between 3.0 V – 0.4 V vs. Li/Li^+ and has multiple peaks and evolution with cycling that match well with previously reported results of graphite.[4, 34] Only a small portion of SEI processes which rapidly fade upon cycling contribute to the background in the Li^+ intercalation regime.[6]

In the first cycle (red curve in Figure 4.3b), the SEI formation was activated on the MLG surface. Due to the self-passivating nature of the SEI, less of it was generated with each subsequent cycle until no new growth is evident after the sixth cycle (highlighted as green curve in Figure 4.3b). In comparison, the Li^+ intercalation region in Figure 4.3c had much less change from cycle-to-cycle, nearly maintaining the same current levels and intercalation potentials. Comparing the first cycle (red curve in Figure 4.3c) to previous studies on graphite with a sub-μm thickness,[21] we can assign the three intercalation peaks at 0.22 V, 0.14 V, and 0.11 V to changes between dilute stage 1 to stage 4, stage 3 to stage 2, and stage 2 to stage 1, respectively. For all of the scan rates in CV tests of FLG samples, we chose a scan rate of 1 mV/s. Previous studies on ultrathin graphite materials have been performed up to hundreds of times slower,

however the fast diffusion of Li in FLG makes the relatively high scan rate possible while still maintaining distinguishable CV signals.[35] On FLG with more than 10 layers, *i.e.* MLG, the full spectrum of Li insertion staging steps is observed, consistent with bulk graphite. This result substantiates our hypothesis that fewer layer graphene electrodes are required to explore the early state staging mechanisms.

Preliminary studies of Li^+ intercalation on unpatterned BLG, 4LG and HOPG (highly oriented pyrolytic graphite) showed no clear evidence of this process due to the low mechanical defect density of the samples used. Figure B.1 shows voltammograms of these samples where unstable electrochemical signals were obtained, and often exfoliation was observed. It is known that the intercalation of Li ion occurs through the edge plane of graphite, such that high-quality pristine unpatterned FLG electrodes do not contain enough points of access for Li ion insertion.[36] When patterned, SLG, 4LG and 6LG displayed contrasting intercalation signatures. Full CVs of the first several cycles of these three samples are shown in Figure 4.3d–f. They all display a similar SEI evolution region between 3.0 V and 0.4 V, but have diverse intercalation properties between 0.4 V and 0V. In all three curves, the SEI formation follows the same trend as MLG where there is an initial conditioning and growth which eventually stabilizes after several cycles. Similar conditioning steps also appeared in the Li^+ intercalation regions of patterned SLG, 4LG and 6LG. The steady intercalation behaviors for these samples are summarized in Figure 4.3g–i, which displays the last voltammetric cycle in each. As expected, due to the lack of galleries found between adjacent graphene sheets, in SLG (Figure 4.3g) no intercalation occurs. While we cannot discard a contribution from adsorbing ions or Li plating to the electrode, intercalation peaks were not observed. The peak observed for SLG around 0.4 V in the first cycle can be still

attributed to SEI formation, since the position matches well with the SEI peak observed at 0.4 V in MLG. Additionally, this signal fades and is not observable in subsequent cycles (Figure 4.3d).

Table 4.1 Intercalation and de-intercalation peak distributions of 4LG, 6LG and MLG.[a]

	4LG	6LG	MLG
Intercalation -- 3	--	0.38-0.27	0.259-0.21
Intercalation -- 2	0.12-0.06	0.25-0.07	0.16-0.13
Intercalation -- 1			0.13-0.06
De-intercalation -- 1	0.17-0.23	0.08-0.19	0.10-0.18
De-intercalation -- 2	0.36-0.44	0.23-0.37	0.18-0.21
De-intercalation -- 3	--	0.39-0.63	0.22-0.26

[a] Data were derived from Figure 4.3c (first cycle), 4.3h, and 4.3i.

In contrast to SLG, patterned 4LG and 6LG (Figure 4.3h and 4.3i) have clearly observable intercalation/de-intercalation peaks. The intercalation and de-intercalation peak ranges are summarized in Table 4.1 and Figure B.2. Since there are only four graphene sheets in 4LG, two de-intercalation peaks reflect the changes between stages 3/2, and 2/1, observed at 0.4 V and 0.2 V, respectively. However, in the intercalation region only one broad peak exists. We note a similar phenomenon for MLG, shown in Figure 4.3c, in which the two intercalation peaks at 0.14 V and 0.11 V (red curve) gradually merge into one broad peak (green curve). Consequently, the two intercalation peaks in 4LG could presumably also combine into one signal. However, the reason for this merging of peaks might be of different origin. In MLG at least, the evolution of intercalation peaks suggests that it might come from a conditioning of the material, where structural changes induced by multiple Li ion insertions and extractions lead to a distribution of intercalation sites. When the direction of the potential sweep is reversed, the back diffusion and de-intercalation of Li-ion is largely controlled by the intrinsic properties of the already lithiated graphene electrode, thus yielding discrete de-intercalation peaks. As the layer

number of graphene is increased to 6 layers, there are sufficient graphene sheets for all four staging states to be observed.

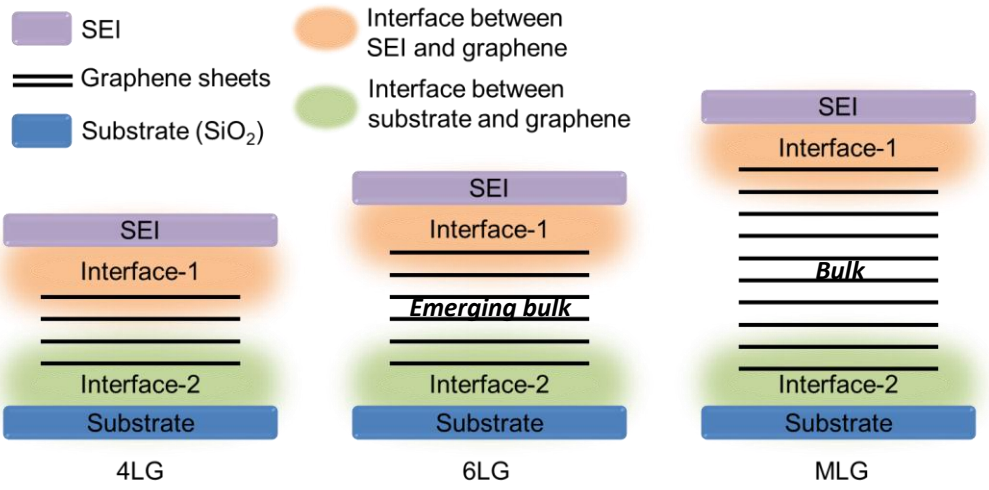

Figure 4.4 Schematic diagram of 4LG, 6LG and MLG sample structures. Solid-electrolyte interphase (SEI), graphene sheets, SiO_2 wafer substrate, together with the SEI/graphene and graphene/substrate interfaces are indicated in Figure.

From Table 4.1 and Figure 4.3c, 4.3h and 4.3i, we noticed a continuous shift of first and second de-intercalation peaks among 4LG, 6LG and MLG. Assuming MLG represents mostly bulk graphite's properties, the positive potential shifts at 4LG and 6LG might come from the effect of SEI/graphene and graphene/substrate interface. The chemical environment induced by these two interfaces might shift the energetics of the de-intercalation process. As shown schematically in Figure 4.4, the impact of these interfaces decreases as FLG transitions into MLG by forming a better-defined bulk. We also note that differences in the background currents in Figure 4.3c, 4.3g, 4.3h, and 4.3i, likely result from different contributions of each sample to their capacitive current and from residual SEI growth. SLG showed the lowest background current, reflecting its lowest activity towards reaction with Li and its lowest density of states which contribute to its capacitance. 4LG, 6LG and MLG displayed a similar background current

of 0.8 μA, 0.3 μA, and c.a. 1.0 μA respectively, which was observed to decrease with an increasing cycling number.

We note that the observed peaks in 6LG are broader than those in 4LG. We believe this is a consequence of the broader range of configurations and interactions available with a growing number of layers. Observing a progressive change is important in the context of the effects that turbostratic disorder, *i.e.* random rotations and translations on pairs of graphene layers, potentially brings to the response of the lithium intercalation signal.[20] In the layer-by-layer transfer procedure used here, it is difficult to control turbostratic disorder, however, we believe that the existence of such disorder does not preclude the validity of the number of layer dependent observations done here. In the first place, 4LG and 6LG samples displayed marked voltammetric differences as a function of the number of layers, despite being produced using a common building material, *i.e.* bilayer graphene. Even if the galleries formed by the layer-by-layer transfer stacking of two BLG sheets were less active than the ones formed by the native BLG, ionic interactions between Li^+ ions would still be expected to occur and to affect the electrostatic interactions perpendicular to the surface. Secondly, lithiation is capable of inducing the re-stacking of layers, provided the material is capable of accommodating the necessary structural changes.[20, 37] As observed during our transfer procedure, "peeling off" of monolayer graphene is possible, thus our layers are probably less bound than on natural graphite. This might facilitate structural changes after a few lithiation cycles and relieve some of the original turbostratic disorder. Finally, turbostratic disorder has been shown to strongly impact the amount of Li^+ that can be intercalated on carbons. The integrated charge of the de-intercalation peaks in Figures 4.3h and 4.3i, shown in detail in Figure B.2 and Table 4.1, yields the equivalents of Li^+ diffused into FLG planes. 4LG yielded a de-intercalation charge of 12.2 μC (85 % of calculated

theoretical charge), and 6LG has 15.7 μC (65 % of calculated theoretical charge). Both Figures show evidence for a largely lithiated interface. Even with a relatively fast scan rate and turbostatic disordered structures, FLG can still maintain enough ability for Li insertion.[19, 20, 38] The observations provided in this article set a precedent in which new mechanistic insights derived from the transition of bulk graphite to an atomically thin interface can be explored.

4.5 *In-Situ* Monitoring SEI Growth *via* SECM

In addition to its intercalation behavior, it is instructive to explore the similarities and differences in the electronic and ionic surface reactivity of graphene in the context of our current understanding of carbon materials. Specifically, we addressed the evolution of SEI conductivity and the role of the fabricated ionic-channels in facilitating Li ion intercalation. For this purpose we used scanning electrochemical microscopy, a versatile tool for detecting reactivity at operating electrodes. In order to further explore the properties of the SEI, SECM operated in the feedback mode (Figure 4.5a) was used to image the spatially resolved rate of electron transfer of a patterned MLG electrode at various stages of SEI formation. According to the CVs of FLG (Figure 4.3), all electrodes displayed qualitatively the same SEI evolution process. Because MLG gave larger intercalation signatures, this electrode was chosen as representative of FLG samples to study SEI properties. When a nano-dimensioned SECM tip was first approached to a pristine substrate of patterned multilayer graphene, positive feedback was observed indicating that the substrate was electronically conductive, even at open circuit when unbiased (Figure 4.5c, black curve). SECM imaging was performed at various substrate potentials to observe the feedback response as a function of electrode activation.

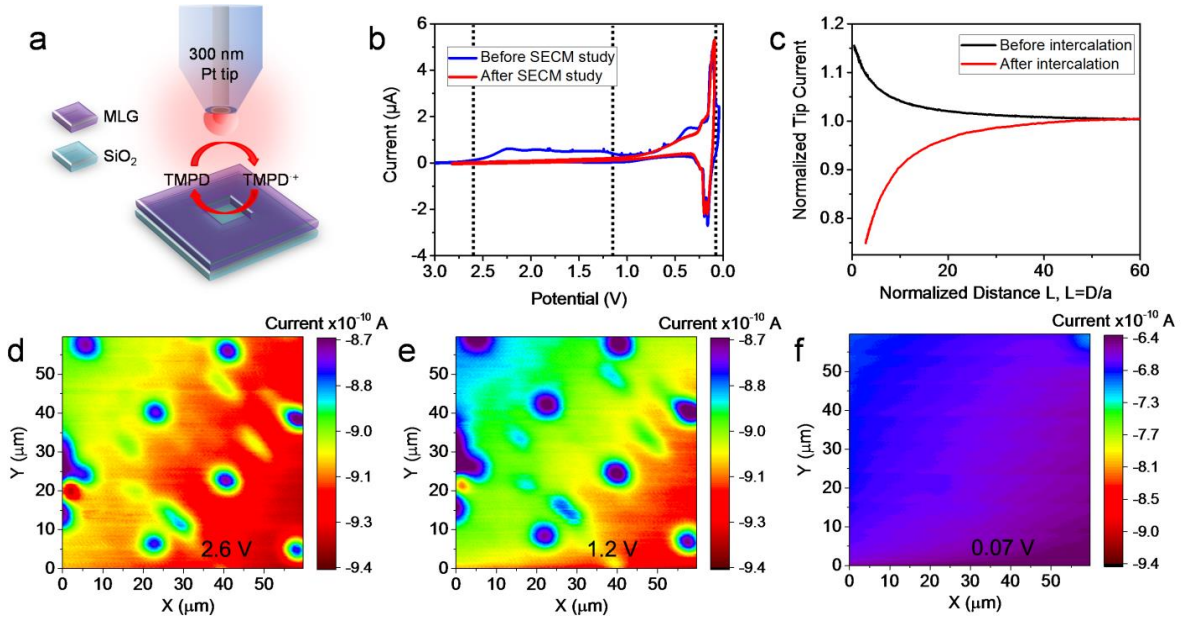

Figure 4.5 Feedback SECM imaging of SEI formation on fresh patterned MLG. a, Schematic diagram of SECM feedback mode for the imaging of patterned MLG. The SECM tip was scanned over the substrate at 133 nm of tip-substrate distance. N,N,N',N'-tetramethyl p-phenylenediamine (TMPD) was used as a redox mediator. This species was oxidized at Pt tip while MLG reduced it back, generating a feedback signal. b, CVs comparing a fresh patterned MLG substrate (blue) and after SECM experimentation (red) showed no change in the intercalation signatures, but a fully-developed SEI with no further electrochemical evidence of growth at the end of the experiment. The dashed lines represent the selected substrate potentials for imaging, chosen to be before and during SEI formation. c, Tip approaching curves to MLG surface before/after SEI formation, which indicate that the fresh MLG surface is electroactive while the formation of the SEI layer blocks electron transfer. The limiting tip current far from the substrate was 9.3×10^{-10} A. d-f, SECM feedback images of TMPD at various substrate potentials listed in each panel, the current changes reflect the changes in substrate kinetics following SEI formation.

Open circuit SECM images (E_{sub} ~ 3.3 V vs. Li/Li^+) revealed nano-resolved features on the surface with clearly identifiable circular patterns on the substrate that correspond perfectly to the fabricated graphene patterns observed under SEM with the same center to center distances for the holes. SECM images were collected at progressively more negative substrate potentials at a tip-substrate distance of 133 nm. As pointed out through the dashed lines in Figure 4.5b, we chose conditions before, during and after SEI formation, at 2.6 V, 1.2 V and 0.07 V vs. Li/Li^+ respectively. The SECM image at E_{sub} 2.6 V (Figure 4.5d) shows good contrast between patterned holes and the MLG surface, with some contrast at defective regions that respond more to substrate overpotential. These defect regions have faster electron transfer kinetics than pristine graphene and have been observed previously *via* SECM[39] and with droplet based SECM probes.[40]

In following images, the substrate potential was ramped more negatively, now forming an SEI, which progressively showed a decreasing tip feedback response due to decreased substrate kinetics (Figure 4.5e and 4.5f). An overall decrease in tip current observed starting at E_{sub} 1.2 V (Figure 4.5e), suggests the formation of a homogeneous SEI layer that partially hinders electron transfer at MLG surface. At E_{sub} 0.07 V (Figure 4.5f), the pattern was indistinguishable, yielding only negative feedback to the tip signal. Negative feedback suggests a slowed-down regeneration of the mediator, indicative of lowered substrate kinetics that are unable to keep up with the mass transport imposed by the tip. We note that the impact of the SEI on electron transfer is opposite to that expected by a large overpotential for the mediator regeneration reaction at the substrate. However, the growing SEI on the surface caused the surface to no longer be electronically conductive.[41-43] The contrasting behavior of the surface before and after SEI formation is also represented *via* feedback approach curves (Figure 4.5c). Imaging shows in larger detail that the

original surface heterogeneity is eliminated after complete coverage of the substrate with the SEI (Figure 4.5f). The substrate was verified to still be electrochemically active after SECM imaging by measuring a voltammogram in which the intercalation of Li^+ is still clearly visible (Figure 4.5b – red curve). However, the SEI remained as a passivating layer, blocking electron transfer to TMPD even an image performed in the conditions of Figure 4.5d was repeated (Figure B.3).

4.6 Li^+ Flux Changing During Intercalation

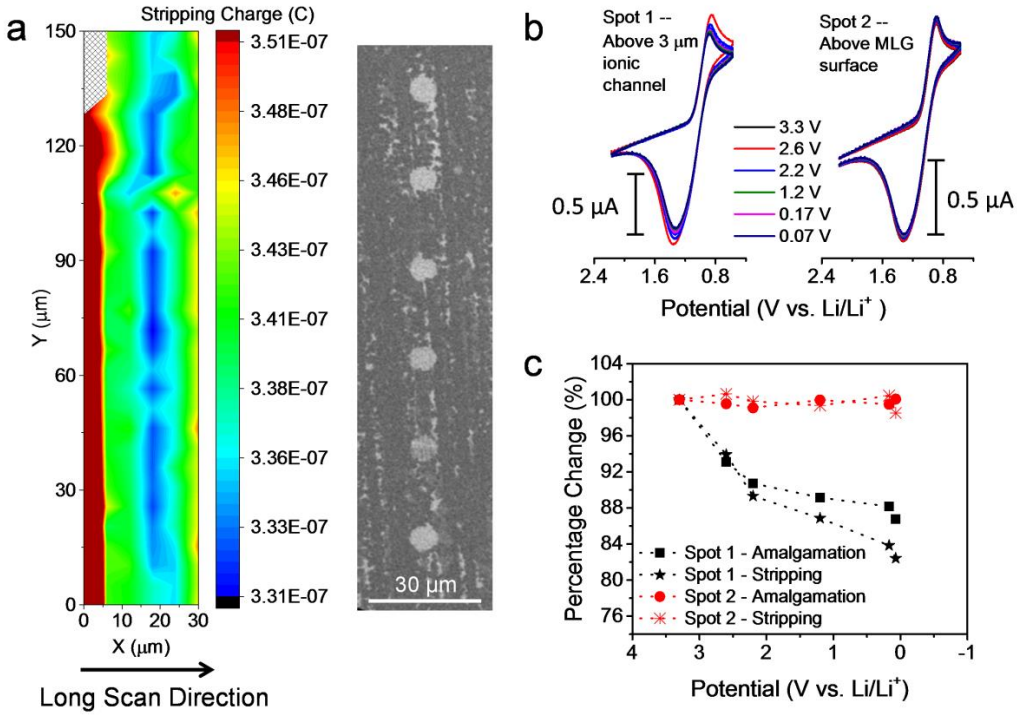

Figure 4.6 Li-ion flux study of MLG sample after SEI formation. a, CV-SECM image of patterned MLG sample after SEI formation-left. Substrate was biased at 0.07 V to intercalate Li^+ for all experiments shown here. A series of CVs were taken at each position at 25 V/s with 5 µm steps, each pixel is the integrated stripping charge of CV, which reflects amplified changes in the local Li^+ concentration. Blue-shifted signals represent areas of lower Li^+ concentration, therefore indicating a larger flux towards the substrate electrode. Their distribution matches with the patterned hole openings designed for Li^+ insertion. SEM image of a similar area is placed to the

(*Figure 4.6 Continued*) right for comparison. The X direction served as the long axis of the raster scan. The off-scale data (dark red color) and pixels where no data was taken (mesh pattern) in the first column of the image is likely an experimental or instrumental artifact. b, Local stripping tip voltammograms showing the tip current as function of tip potential over an active hole (left, on top of 3 μm ionic channel) and over the less active MLG surface (right), while the substrate activates Li^+ intercalation at various potentials imposed to the substrate. c. Percentage change of amalgamation and stripping peak currents derived from b, showing the clear potential dependence of Li^+ flux into the holes but not on the MLG surface.

Each pixel in the CV-SECM image (Figure 4.6a-left) collected with our mercury probes corresponds to the stripping charge calculated from the integrated current of stripping Li^+. While the mercury capped SECM tip was measuring stripping voltammetry at every pixel, the substrate was continuously poised at 0.07V in order to have intercalation of Li^+ occur. While a constant background is present in the entire image due to a flux of Li^+ from the electrolyte into the probe, the spots in the CV-SECM image that have the lowest stripping charge correspond to regions on the substrate that give the most competition for the local source of Li^+ and are seen in blue. This scheme of redox competition has previously been used in SECM to generate high resolution images that do not require the tip to be extremely close to the substrate.[48, 49] The blue spots in the CV-SECM image match well with the spatial distribution of the etched openings in the graphene pattern (Figure 4.6a-left), showing that the substrate design is indeed facilitating Li^+ intercalation and that the formation of the SEI is not consuming the underlying active material. To further demonstrate this effect at specific sites, the Hg probe was placed directly on top of both a hole opening area and flat MLG surface. SECM tip CVs at various substrate potential were collected at each described spot and are listed in Figure 4.6b with their amalgamation and stripping peak

current changes shown in Figure 4.6c. A decrease for both amalgamation and stripping currents was observed at the etched holes, which contain edge plane openings that induce strong competition for Li^+ at these sites. In contrast, stripping CVs right above MLG basal planes remained constant without any dependence on substrate potential. Collectively, these observations demonstrate that Li ions migrate into graphene interlayers more efficiently through the edge planes. This work would be the first time that SECM has been used to visualize ionic fluxes through an SEI on a battery material in real time, and help validate results suggesting that FLG electrodes are a viable platform for studying fundamental intercalation effects on graphitic materials.

4.7 Materials and Methods

Chemicals. All chemicals were purchased from commercial sources and used as received. Propylene carbonate (PC, anhydrous, 99.7%), ethylene carbonate (EC, anhydrous, 99%), lithium tetrafluoroborate ($LiBF_4$, 98%), silver nitrate ($AgNO_3$, 99%), mercury (II) chloride ($HgCl_2$, 99.5%), N,N,N',N'-Tetramethyl-p-phenylenediamine (TMPD, 99%), acetone (99.5%), isopropyl alcohol (99.5%), glacial acetic acid (99.5%) and ethylenediaminetetraacetic acid disodium salt dihydrate ($Na_2EDTA\ 2H_2O$, 99.0%) were all purchased from Sigma-Aldrich. 25 μm copper foil was purchased from Alfa Aesar. NanoTM 950K A4 PMMA, 495K A2 PMMA, and Microposit S1813 photoresist were purchased from MicroChem. AZ 917 MIF developer was purchased from AZ Electronic Materials. CE-100 Copper etchant was purchased from Transene Company. SiO_2/Si wafer (3 inch B-doped P-type Si wafer with 300 nm wet thermal oxide) was purchased from University Wafer. The deionized water (DI water) was filtered using a Millipore system.

Graphene growth procedure. Multilayer graphene and bilayer graphene were grown by chemical vapor deposition (CVD) using methane and 25 μm Cu foil as catalyst. Prior to growth,

the Cu foil was treated in acetone (10s), water (10s), glacial acetic acid (10 min), water (10s), acetone (10s), and IPA (10s) to remove any surface oxides. The Cu foil was then mounted in CVD chamber for graphene growth with different recipes. Bilayer graphene was grown with previously established recipe[50] at 0.04 torr with two steps: annealing under 1000 °C, 1000 sccm Ar and 50 sccm H_2 for 30 min; graphene growing at 1000 °C, 100 sccm CH_4 and 50 sccm H_2 for 25 min. Multilayer graphene was grown using a modified recipe from previously reported atmosphere pressure CVD method[51] with no annealing step and growth at 960 °C, 10 sccm CH_4 and 30 sccm H_2 for 5 min.

Graphene transfer. CVD grown graphene was transferred onto different substrates (SiO_2/Si wafer, and glass) through a wet transfer method. After graphene growth, one side of the Cu foil with graphene was protected with 1 layer of 495K A2 PMMA and 2 layers of 950K A4 PMMA *via* spin-coating at 3000 rpm for 30s. The protected graphene was floated on top of Cu etchant for 4 hours at 40 °C to remove Cu foil beneath the graphene. The floating graphene/PMMA sheet went through 4 rinse steps with DI water, 1 h treatment with 0.1 M Na_2EDTA aqueous solution, and 4 rinse steps with DI water again to fully remove any metal residue. The clean graphene/PMMA sheet was finally transferred onto the desired substrate and blow dried under Argon. Additional organic solvent treatments were then applied to remove PMMA protecting layer: 2 h in anisole, 4 h in dichloromethane: acetone mixture (1:1 ratio), and 2 h in isopropanol. Repetition of this process yields multilayered graphene samples.

Patterning graphene. Photolithography and reactive ion etching (RIE) methods were applied to define and create two dimensional micron patterns on graphene. For photolithography, positive photoresist S1813 were selected to create patterned openings, 3 μm square array with 24 μm center-to-center distance, on graphene. S1813 layer was spin coated onto graphene at 4000

rpm for 45 s and soft baked at 115 °C for 1.5 min. Karl Suss MJB3 contact mask aligner was used to transfer the pattern from the mask to the photoresist layer. After developing in AZ 917 MIF developer for 15 s, 3 μm square array openings were created on top of graphene. A Plasma Lab Freon/O_2 RIE system was applied to selectively etch the exposed graphene area under 20 sccm O_2, 37 mW RF energy and 40 mtorr pressure for 30 s. The etched graphene sample was carefully rinsed with acetone to remove photoresist layer which left a pristine patterned graphene on the substrate.

Wollaston tip fabrication. Wollaston wire (Goodfellow, Purity 99.9%, 600 nm radius) was sealed in a glass capillary (World Precision Instruments, Sarasota, FL). A 1 cm length of Wollaston Pt wire was placed halfway up a capillary and was chemically etched on the bottom half of the wire to remove the protective layer of silver using a solution of concentrated nitric acid utilizing capillary action to pull the acid solution up the tube. The nitric acid was removed from the capillary using a KimWipe leaving a half chemically etched Wollaston wire in the capillary. The Wollaston wire was then sealed in the glass capillary using a standard method previously described elsewhere.[52] The sealed Wollaston electrode was then sharpened using silicon carbide sandpaper with the aid of an optical microscope. The final RG, radius of glass sheath including the electrode divided by the radius of the electrode, was approximately 25. The large value of RG is uncharacteristic of a typical SECM tip, which will limit the proximity placement of the tip to the substrate, but high resolution SECM images were still able to be collected because extreme closeness to the substrate is not necessary to measure SECM feedback differences.[53]

Sample characterization. Graphene samples were characterized *via* optical microscopy (Zeiss Axio Lab.A1, Germany), scanning electron microscopy (SEM, Hitachi S-4800 high

resolution SEM, Japan), Raman spectroscopy (Nanophoton Laser Raman Microscope RAMAN-11, Japan) and UV-Vis spectroscopy (Shimadzu, Japan). Raman measurements were used in both spectroscopic and imaging modes.

Electrochemical test. All electrochemical experiments were conducted using a CHI 920D SECM from CH Instruments (Austin, TX) inside of a glovebox (MBraun, Stratham, NH) with mindful control of the oxygen and water levels in the atmosphere to be less than 0.1 ppm respectively. A Pt wire and an Ag/Ag^+ (0.1 M $AgNO_3$ in a 50:50 mixture of PC/EC) electrode were used as the counter and reference electrodes. 0.1 M $LiBF_4$ solution in 50:50 PC:EC mixture was used as stock solution.

Li intercalation with cyclic voltammetry (CV). We chose slow scan CV to obtain Li intercalation information into graphene samples. Different graphene samples (MLG, patterned SLG, 4LG, 6LG) were used as working electrode, with a SECM Teflon cell defined working area of 4.9 mm^2. After adding stock solution, CVs were taken at low scan rate 1 mV/s over multiple cycles to test SEI formation and Li intercalation processes.

Nano-SECM Feedback Imaging. Nanometer sized SECM tips with a 300 nm radius platinum electrode were fabricated using Wollaston wire with an RG of approximately 25, the detailed fabrication procedure is listed in supporting information. Fresh MLG with patterned 3 μm openings was used to explore SEI electronic conductivity characteristics. The Wollaston wire electrodes were approached to the patterned graphene substrate in the feedback mode of SECM using a solution of 10 mM TMPD in stock solution as an electrochemical mediator. SECM images were collected at various substrate bias steps from open circuit (3.3 V) to SEI fully formed (0.07 V) to monitor surface kinetics changes as the SEI is formed on fresh MLG samples.

CV-SECM imaging. 5μm radius platinum electrodes (RG ~ 2) were purchased from CH Instruments (Austin, TX). Mercury capped SECM tips were fabricated inside of the glovebox from a non-aqeuous solution by depositing mercury on the surface from a 0.1 M solution of $HgCl_2$ with 0.1 M $TBAPF_6$ in DMF through a chronoamperometric step at -0.8 V vs a tungsten wire for 144 seconds to deposit 34 μC (0.34 nanomole) of mercury on the surface. The presence of mercury on the SECM tip was verified by performing stripping voltammetry in the presence of the electrolyte used for lithium intercalation for the patterned graphene (0.1 M $LiBF_4$). Stripping voltammetry showed clean and clear amalgamation formation for lithium at 1 V vs. Li/Li^+ with reversible stripping.

The tip was approached to the surface with 10 mM TMPD using only the first oxidation as mercury itself will strip off the surface if the second oxidation is accessed. Cyclic voltammetry SECM (CV-SECM) imaging was performed by measuring 3 complete cyclic voltammograms at 25 V/s to show the amalgamation and stripping of Li^+ at every single pixel in the image where every pixel was 5 micrometers large. The last voltammogram measured at every pixel was integrated to find the stripping charge and plotted as a function of surface location to generate a CV-SECM image.

4.8 Conclusion

In this work, we used few layer graphene, both directly growth and layer-by-layer transferred, to explore Li^+ intercalation on an atomically-thin interface. Li^+ insertion in FLG follows a staging mechanism, reminiscent of graphite, but the limited number of graphene sheets cause significant deviations in the intercalation mechanism, as evaluated *via* cyclic voltammetry. Due to the physical restriction, no Li intercalation was found in single layer graphene sample. In FLG less than 5 layers, 4LG as example, only stage 1-3 can be resolved. In spite potential

difference of intercalation/de-intercalation, 6LG already exhibit similar staging mechanism as ~ 10 layer MLG and graphite. This work verifies the universality of staging mechanism in layered carbonaceous materials, and it provides insight into the early-state Li^+ intercalation process in graphene-type materials. Additionally, this work also opens interesting avenues in the control of ion insertion mechanisms and insertion energies *via* electrode nano-structuring.

As a spatially resolved electrochemical probing platform, SECM provided information on both the electronic and ionic reactivity of the graphene substrate. SECM feedback images monitored the impact of SEI formation under different substrate bias, until the stable and condensed SEI layer totally blocked electron transfer. In contrast, CV-SECM experiments using a Hg-capped Pt tip as Li^+ sensitive ionic probe were applied to demonstrate that electrode patterning leads to points of access for Li^+ intercalation preferentially on regions where the edge plane of graphene is exposed. Current efforts in our laboratory will focus on increasing the temporal and spatial resolution of CV-SECM methods for exploring ionic pathways within defects on the SEI. This work highlights the impact of nano-structure and micro-structure on macroscopic electrochemical behavior and opens the door to the mechanistic control of ion intercalation using graphene, an atomically thin interface where surface and bulk reactivity converge.

4.9 References

1. Yazami, R.; Touzain, P. A Reversible Graphite Lithium Negative Electrode for Electrochemical Generators. *J. Power Sources* **1983**, *9*, 365-371.

2. Levi, M. D.; Aurbach, D. The Mechanism of Lithium Intercalation in Graphite Film Electrodes in Aprotic Media. Part 1. High Resolution Slow Scan Rate Cyclic Voltammetric Studies and Modeling. *J. Electroanal. Chem.* **1997**, *421*, 79-88.

3. Levi, M. D.; Levi, E. A.; Aurbach, D. The Mechanism of Lithium Intercalation in Graphite Film Electrodes in Aprotic Media. Part 2. Potentiostatic Intermittent Titration and *in situ* XRD Studies of the Solid-State Ionic Diffusion. *J. Electroanal. Chem.* **1997**, *421*, 89-97.

4. Verma, P.; Maire, P.; Novák, P. A Review of the Features and Analyses of the Solid Electrolyte Interphase in Li-Ion Batteries. *Electrochim. Acta* **2010**, *55*, 6332-6341.

5. Agubra, V. A.; Fergus, J. W. The Formation and Stability of the Solid Electrolyte Interface on the Graphite Anode. *J. Power Sources* **2014**, *268*, 153-162.

6. Zhang, S.; Ding, M. S.; Xu, K.; Allen, J.; Jow, T. R. Understanding Solid Electrolyte Interface Film Formation on Graphite Electrodes. *Electrochem. Solid-State Lett.* **2001**, *4*, A206-A208.

7. Herstedt, M.; Stjerndahl, M.; Gustafsson, T.; Edström, K. Anion Receptor for Enhanced Thermal Stability of the Graphite Anode Interface in a Li-Ion Battery. *Electrochem. Commun.* **2003**, *5*, 467-472.

8. Aurbach, D.; Markovsky, B.; Weissman, I.; Levi, E.; Ein-Eli, Y. On the Correlation Between Surface Chemistry and Performance of Graphite Negative Electrodes for Li Ion Batteries. *Electrochim. Acta* **1999**, *45*, 67-86.

9. Etacheri, V.; Marom, R.; Elazari, R.; Salitra, G.; Aurbach, D. Challenges in the Development of Advanced Li-Ion Batteries: a Review. *Energy Environ. Sci.* **2011**, *4*, 3243-3262.

10. Petnikota, S.; Rotte, N.; Srikanth, V. S. S.; Kota, B. R.; Reddy, M. V.; Loh, K.; Chowdari, B. V. R. Electrochemical Studies of Few-Layered Graphene as an Anode Material for Li Ion Batteries. *J. Solid State Electrochem.* **2014**, *18*, 941-949.

11. Pollak, E.; Geng, B.; Jeon, K.-J.; Lucas, I. T.; Richardson, T. J.; Wang, F.; Kostecki, R. The Interaction of Li^+ with Single-Layer and Few-Layer Graphene. *Nano Lett.* **2010**, *10*, 3386-3388.

12. Lee, E.; Persson, K. A. Li Absorption and Intercalation in Single Layer Graphene and Few Layer Graphene by First Principles. *Nano Lett.* **2012**, *12*, 4624-4628.

13. Liang, Y. T.; Hersam, M. C. Towards Rationally Designed Graphene-Based Materials and Devices. *Macromol. Chem. Phys.* **2012**, *213*, 1091-1100.

14. Geim, A. K. Graphene: Status and Prospects. *Science* **2009**, *324*, 1530-1534.

15. Geim, A. K.; Novoselov, K. S. The Rise of Graphene. *Nat. Mater.* **2007**, *6*, 183-191.

16. Liao, L.; Peng, H.; Liu, Z. Chemistry Makes Graphene beyond Graphene. *J. Am. Chem. Soc.* **2014**, *136*, 12194-12200.

17. Dahn, J. R. Phase Diagram of Li_xC_6. *Phys. Rev. B* **1991**, *44*, 9170-9177.

18. Song, M. K.; Hong, S. D.; No, K. T. The Structure of Lithium Intercalated Graphite Using an Effective Atomic Charge of Lithium. *J. Electrochem. Soc.* **2001**, *148*, A1159-A1163.

19. Zheng, T.; Dahn, J. R. Effect of Turbostratic Disorder on the Staging Phase Diagram of Lithium-Intercalated Graphitic Carbon Hosts. *Phys. Rev. B* **1996**, *53*, 3061-3071.

20. Zheng, T.; Reimers, J. N.; Dahn, J. R. Effect of Turbostratic Disorder in Graphitic Carbon Hosts on the Intercalation of Lithium. *Phys. Rev. B* **1995**, *51*, 734-741.

21. Levi, M. D.; Aurbach, D. Simultaneous Measurements and Modeling of the Electrochemical Impedance and the Cyclic Voltammetric Characteristics of Graphite Electrodes Doped with Lithium. *J. Phys. Chem. B* **1997**, *101*, 4630-4640.

22. Ritzert, N. L.; Rodriguez-Lopez, J.; Tan, C.; Abruna, H. D. Kinetics of Interfacial Electron Transfer at Single-Layer Graphene Electrodes in Aqueous and Nonaqueous Solutions. *Langmuir* **2013**, *29*, 1683-1694.

23. Eshkenazi, V.; Peled, E.; Burstein, L.; Golodnitsky, D. XPS Analysis of the SEI Formed on Carbonaceous Materials. *Solid State Ionics* **2004**, *170*, 83-91.

24. Lee, J. T.; Nitta, N.; Benson, J.; Magasinski, A.; Fuller, T. F.; Yushin, G. Comparative Study of the Solid Electrolyte Interphase on Graphite in Full Li-Ion Battery Cells Using X-Ray Photoelectron Spectroscopy, Secondary Ion Mass Spectrometry, and Electron Microscopy. *Carbon* **2013**, *52*, 388-397.

25. Santner, H. J.; Korepp, C.; Winter, M.; Besenhard, J. O.; Möller, K. C. In-situ FTIR Investigations on the Reduction of Vinylene Electrolyte Additives Suitable for Use in Lithium-Ion Batteries. *Anal. Bioanal. Chem.* **2004**, *379*, 266-271.

26. Chattopadhyay, S.; Lipson, A. L.; Karmel, H. J.; Emery, J. D.; Fister, T. T.; Fenter, P. A.; Hersam, M. C.; Bedzyk, M. J. *In Situ* X-ray Study of the Solid Electrolyte Interphase (SEI) Formation on Graphene as a Model Li-ion Battery Anode. *Chem. Mater.* **2012**, *24*, 3038-3043.

27. Zhang, S. S.; Xu, K.; Jow, T. R. EIS Study on the Formation of Solid Electrolyte Interface in Li-Ion Battery. *Electrochim. Acta* **2006**, 51, 1636-1640.

28. Barton, Z. J.; Rodriguez-Lopez, J. Lithium Ion Quantification Using Mercury Amalgams as *in Situ* Electrochemical Probes in Nonaqueous Media. *Anal. Chem.* **2014**, *86*, 10660-10667.

29. Graf, D.; Molitor, F.; Ensslin, K.; Stampfer, C.; Jungen, A.; Hierold, C.; Wirtz, L. Spatially Resolved Raman Spectroscopy of Single- and Few-Layer Graphene. *Nano Lett.* **2007**, *7*, 238-242.

30. Li, X. S.; Cai, W. W.; An, J. H.; Kim, S.; Nah, J.; Yang, D. X.; Piner, R.; Velamakanni, A.; Jung, I.; Tutuc, E.; Banerjee, S. K.; Colombo, L.; Ruoff, R. S. Large-Area Synthesis of High-Quality and Uniform Graphene Films on Copper Foils. *Science* **2009**, *324*, 1312-1314.

31. Bae, S.; Kim, H.; Lee, Y.; Xu, X.; Park, J.-S.; Zheng, Y.; Balakrishnan, J.; Lei, T.; Ri Kim, H.; Song, Y. I.; Kim, Y.-J.; Kim, K. S.; Ozyilmaz, B.; Ahn, J.-H.; Hong, B. H.; Iijima, S. Roll-to-Roll Production of 30-inch Graphene Films for Transparent Electrodes. *Nat. Nanotechnol.* **2010**, *5*, 574-578.

32. Nair, R. R.; Blake, P.; Grigorenko, A. N.; Novoselov, K. S.; Booth, T. J.; Stauber, T.; Peres, N. M. R.; Geim, A. K. Fine Structure Constant Defines Visual Transparency of Graphene. *Science* **2008**, *320*, 1308.

33. Ishigami, M.; Chen, J. H.; Cullen, W. G.; Fuhrer, M. S.; Williams, E. D. Atomic Structure of Graphene on SiO_2. *Nano Lett.* **2007**, *7*, 1643-1648.

34. Nie, M.; Chalasani, D.; Abraham, D. P.; Chen, Y.; Bose, A.; Lucht, B. L. Lithium Ion Battery Graphite Solid Electrolyte Interphase Revealed by Microscopy and Spectroscopy. *J. Phys. Chem. C* **2013**, *117*, 1257-1267.

35. Sole, C.; Drewett, N. E.; Liu, F.; Abdelkader, A. M.; Kinloch, I. A.; Hardwick, L. J. The Role of Re-Aggregation on the Performance of Electrochemically Exfoliated Many-Layer Graphene for Li-Ion Batteries. *J. Electroanal. Chem.* **2015**, *753*, 35-41.

36. Yamada, Y.; Miyazaki, K.; Abe, T. Role of Edge Orientation in Kinetics of Electrochemical Intercalation of Lithium-Ion at Graphite. *Langmuir* **2010**, *26*, 14990-14994.

37. Boehm, R. C.; Banerjee, A. Theoretical Study of Lithium Intercalated Graphite. *J. Chem. Phys.* **1992**, *96*, 1150-1157.

38. Dahn, J. R.; Sleigh, A. K.; Shi, H.; Reimers, J. N.; Zhong, Q.; Way, B. M. Dependence of the Electrochemical Intercalation of Lithium in Carbons on the Crystal-Structure of the Carbon. *Electrochim. Acta* **1993**, *38*, 1179-1191.

39. Tan, C.; Rodríguez-López, J.; Parks, J. J.; Ritzert, N. L.; Ralph, D. C.; Abruña, H. D. Reactivity of Monolayer Chemical Vapor Deposited Graphene Imperfections Studied Using Scanning Electrochemical Microscopy. *ACS nano* **2012**, *6*, 3070-3079.

40. Guell, A. G.; Cuharuc, A. S.; Kim, Y. R.; Zhang, G. H.; Tan, S. Y.; Ebejer, N.; Unwin, P. R. Redox-Dependent Spatially Resolved Electrochemistry at Graphene and Graphite Step Edges. *ACS nano* **2015**, *9*, 3558-3571.

41. Zampardi, G.; La Mantia, F.; Schuhmann, W. Determination of the Formation and Range of Stability of the SEI on Glassy Carbon by Local Electrochemistry. *RSC Adv.* **2015**, *5*, 31166-31171.

42. Zampardi, G.; La Mantia, F.; Schuhmann, W. In-Operando Evaluation of the Effect of Vinylene Carbonate on the Insulating Character of the Solid Electrolyte Interphase. *Electrochem. Commun.* **2015**, *58*, 1-5.

43. Zampardi, G.; Ventosa, E.; La Mantia, F.; Schuhmann, W. *In Situ* Visualization of Li-Ion Intercalation and Formation of the Solid Electrolyte Interphase on TiO_2 Based Paste Electrodes Using Scanning Electrochemical Microscopy. *Chem. Commun.* **2013**, *49*, 9347-9349.

44. Alpuche-Aviles, M. A.; Baur, J. E.; Wipf, D. O. Imaging of Metal Ion Dissolution and Electrodeposition by Anodic Stripping Voltammetry-Scanning Electrochemical Microscopy. *Anal. Chem.* **2008**, *80*, 3612-3621.

45. Diaz-Ballote, L.; Alpuche-Aviles, M.; Wipf, D. O. Fast-Scan Cyclic Voltammetry-Scanning Electrochemical Microscopy. *J. Electroanal. Chem.* **2007**, *604*, 17-25.

46. Chen, C. H.; Jacobse, L.; McKelvey, K.; Lai, S. C. S.; Koper, M. T. M.; Unwin, P. R. Voltammetric Scanning Electrochemical Cell Microscopy: Dynamic Imaging of Hydrazine Electro-oxidation on Platinum Electrodes. *Anal. Chem.* **2015**, *87*, 5782-5789.

47. Takahashi, Y.; Kumatani, A.; Munakata, H.; Inomata, H.; Ito, K.; Ino, K.; Shiku, H.; Unwin, P. R.; Korchev, Y. E.; Kanamura, K.; Matsue, T. Nanoscale Visualization of Redox Activity at Lithium-Ion Battery Cathodes. *Nat. Commun.* **2014**, *5*:5450.

48. Eckhard, K.; Chen, X. X.; Turcu, F.; Schuhmann, W. Redox Competition Mode of Scanning Electrochemical Microscopy (RC-SECM) for Visualisation of Local Catalytic Activity. *Phys. Chem. Chem. Phys.* **2006**, *8*, 5359-5365.

49. Zoski, C. G.; Aguilar, J. C.; Bard, A. J. Scanning Electrochemical Microscopy. 46. Shielding Effects on Reversible and Quasireversible Reactions. *Anal. Chem.* **2003**, *75*, 2959-2966.

50. Cristarella, T. C.; Chinderle, A. J.; Hui, J.; Rodríguez-López, J. Single-Layer Graphene as a Stable and Transparent Electrode for Nonaqueous Radical Annihilation Electrogenerated Chemiluminescence. *Langmuir* **2015**, *31*, 3999-4007.

51. Tu, Z.; Liu, Z.; Li, Y.; Yang, F.; Zhang, L.; Zhao, Z.; Xu, C.; Wu, S.; Liu, H.; Yang, H.; Richard, P. Controllable Growth of 1–7 Layers of Graphene by Chemical Vapour Deposition. *Carbon* **2014**, *73*, 252-258.

52. Rodriguez-Lopez, J.; Shen, M.; Nepomnyashchii, A. B.; Bard, A. J. Scanning Electrochemical Microscopy Study of Ion Annihilation Electrogenerated Chemiluminescence of Rubrene and $[Ru(bpy)_3]^{2+}$. *J. Am. Chem. Soc.* **2012**, *134*, 9240-9250.

53. O'Connell, M. A.; Wain, A. J. Combined Electrochemical-Topographical Imaging: a Critical Review. *Analytical Methods* **2015**, *7*, 6983-6999.

CHAPTER 5

ALKALI INTERCALATION ON MULTILAYER GRAPHENE — K ION (CO-)INTERCALATION[†]

5.1 Introduction

The field of portable energy storage is dominated by Li^+ batteries (LIBs), which operate by the reversible insertion and extraction of Li^+ at anode and cathode host materials.[1] Though LIBs meet present portable energy storage needs, the rising cost and material shortage of lithium sources pose challenges to the long-term sustainability of LIB technologies.[2, 3] K-ion batteries (KIBs) are an attractive alternative to LIBs since potassium is ~1000 times more abundant than lithium in the Earth's crust.[4, 5] In addition, the theoretical voltage limits for KIBs and LIBs are similar (-2.925 V *vs.* NHE for K/K^+ and -3.045 V *vs.* NHE for Li/Li^+),[6] so sustained technological developments may be able to bring commercially competitive KIBs to the market. KC_8, like LiC_6, is one of the well know graphite intercalation compounds. Recent experimental studies suggest that carbonaceous materials such as hard carbon,[7] graphite,[8-10] graphene oxide,[10] and nitrogen-doped graphene[11] may be good candidates for a KIB anode. Despite early attractive

[†] Part of this chapter is adapted from the publication: Barton, Z. J.; Hui, J.; Schorr, N. B.; Rodríguez-López, J. Detecting Potassium Ion Gradients at a Model Graphitic Interface. Electrochimica Acta 2017, 241, 98-105.

[†] Collaboration and contribution statement: This work was collaborated with group colleague Zachary J. Barton, and Noah B. Schorr. The Hg d-w probes were fabricated by Zachary J. Barton. *In-situ* SECM experiments were performed together with Zachary J. Barton. Part of SEM and Raman characterizations were carried out by Noah B. Schorr.

[†] This chapter contains currently ongoing projects: K^+ (co-)intercalation (Section 5.2).

results of K ion storage in those carbonaceous materials, there remains a lack of well-established conditions for K ion intercalation for their practical application in batteries. In Chapter 4, we introduced the use of multi-layer graphene (MLG) materials as potential anode materials for LIBs, which have roughly 1000 times faster charge-discharge rates than traditional graphite anodes, stable cycling properties, and plane morphology which enable *in-situ* scanning electrochemical microscopy (SECM) characterizations.[12] Therefore, in this chapter, MLG samples are applied as a model system to establish a stable intercalation condition for K ion intercalation *via* a pre-conditioned Li-based solid-electrolyte interphase (SEI) layer. We first show in section 5.2 that pre-conditioning of MLG inside $LiBF_4$ solution will lead to a stably-packed Li-based SEI layer, which facilitates transportation of K ions into graphene sheets with clear staging-type signatures.

Diversifying the available pool of materials for high performance energy storage requires a deeper understanding of the similarities and differences between LIBs and emerging ion insertion technologies. Building on our previous investigations of interfacial Li^+ fluxes[13] and ionic staging mechanisms in multi-layer graphene,[12] here we turn our attention to a probe-localized method to detect alkali ion flux changes *in-situ*. Scanning probe methods are often employed for surface investigations on energy storage materials, but few methods of *in situ* chemical imaging of ionic reactions at the battery–electrolyte interface exist.[14-17] Recently, we reported the use of Hg-based SECM probes for the detection of alkali ions *via* anodic stripping voltammetry.[18] In this technique, the reduction of the metal ion and subsequent diffusion of the metal into the Hg phase creates a steady-state amalgamation current, which upon reversal of the potential scan direction yields a stripping current peak. Both of these signals can be used for quantitative detection of differences in the local concentrations of various ions as a function of

electrode activation, as well as for accurate positioning of the SECM probe. Furthermore, we recently reported the fabrication and stripping voltammetry of Hg disc-wells, which consist of a level pool of Hg confined to the glass-walled cavity before a recessed Pt microdisc.[19-21] These probes have demonstrated their superior performance as SECM probes for the detection of Li^+ and Na^+, as compared to traditional Hg sphere-caps regarding both detection times and spatial resolution. The K^+/K(Hg) redox pair shares similar electrochemical attributes with Li^+/Li(Hg) and Na^+/Na(Hg), so the same types of probes are able to detect K ion species.[22-24] Due to their chemical and mechanical robustness as well as their unique ability to directly access ion-specific information, Hg disc-wells enable SECM to pursue answers connecting chemical structures to their electrochemical performance in systems involving ionic gradients. In the second part of this chapter (section 5.3), we demonstrate the measurement of ionic gradients on a model material for a KIB anode—highly oriented pyrolytic graphite (HOPG). While insertion of K^+ on this material is not ideal, the detection of ionic gradients over surface features upon activation is accurately tracked, independently from the activity measured at the substrate electrode. The application of SECM techniques for the chemical measurement of ion fluxes at KIB electrodes will enable further understanding of the impact of pre-conditioned Li-based SEI formation and K ion intercalation into emerging materials like MLG.

5.2 K ion (co-)intercalation on MLG

5.2.1 K Ion Intercalation on Pre-conditioned MLG

Similar to previous established methods for Li ion intercalation characteristics,[12] cyclic voltammetry (CV) was used to determine how K ions intercalate into MLG samples. Our first approach to K ion intercalation into MLG was performed by negatively polarizing pristine MLG electrode inside 0.1 M KPF_6 PC-EC solutions until the calculated theoretical plating potential

was reached (0 V *vs.* K^+/K or 0.12 V *vs.* Li^+/Li). As shown in Figure C.1a, no observable K ion intercalation peaks were found at this condition; instead a plating process was observed from the crossing of forward and backward sweep curves.[25] When the solution was replaced with 0.1 M $LiBF_4$ PC-EC solution, the MLG sample maintained good stability to intercalate Li ions after 1.5 days of testing inside KPF_6 media (Figure C.1b). Supporting that, the K ion intercalation process is not preferred in pristine MLG samples.

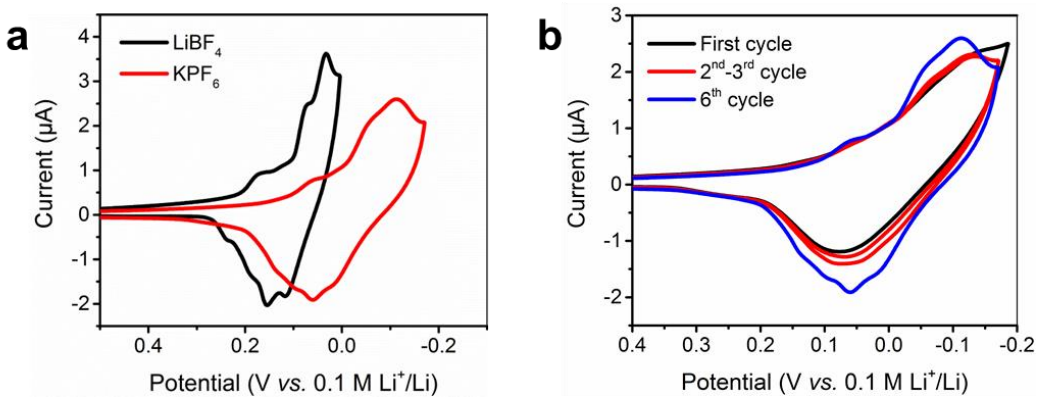

Figure 5.1 K ion intercalation on pre-conditioned MLG sample. a, Comparison of Li ion and K ion intercalation signals on MLG with pre-passivated SEI layer. b, Evolution of staging-type peaks in KPF_6 solution. All solutions are 0.1 M Li or K salt in PC-EC, scan rates are 1 mVs^{-1}.

During the early stage cycling of LIB, a SEI layer is formed on graphite anode.[26] We have proven the electronically insulating yet ionically conducting properties of this SEI layer formed on MLG inside $LiBF_4$ solutions.[12] This layer ensures free transportation of Li ion to the MLG anode during cycling, and intercalation at the interlayer spacing between graphene sheets before reaching the threshold potential of Li plating. Inspired by these promising SEI properties, we hypothesized that a pre-formed SEI layer would facilitate K ion intercalation into MLG. To accomplish this, the MLG sample was pre-conditioned in $LiBF_4$ solution for 10-12 cycles to allow a SEI layer to fully passivate the MLG surface.

Table 5.1 Peak potential and integrated charge analysis of Figure 5.1a.

Peak Potentials (V *vs.* Li^+/Li)					
	$Li_{forward}$	$Li_{backward}$	$K_{forward}$	$K_{backward}$	Transition
1	0.174	0.239	0.063	0.141	Dilute Stage 1 – Stage 4
2	0.119	0.191	0.006	0.100	Stage 4 – Stage 3
3	0.074	0.156	-0.053	0.061	Stage 3 – Stage 2
4	0.034	0.117	-0.112	0.017	Stage 2 – Stage 1
Integrated Charge ($\times 10^{-4}$ C)					
	Li		K		Ratio
$Q_{intercalation}$	2.471		2.023		1.221
$Q_{de\text{-}intercalation}$	2.438		2.050		1.189

The SEI and Li ion intercalation regions exhibited similar behavior as Figure 4.3b, 4.3c and 5.1a black trace. Obvious staging-type K ion intercalation peaks were observed (Figure 5.1a red trace) on the conditioned MLG, which become better resolved upon cycling (Figure 5.1b). Replacing the solution back to $LiBF_4$ recovers the Li ion intercalation signature (Figure C.2). Comparing the Li and K ion signals, four groups of (de-)intercalation peaks can be easily identified (Table 5.1), which show the intercalation stages change upon cycling.[25, 27] In contrast to the trend of standard reduction potential of K^+/K and Li^+/Li redox pairs, K ions intercalate at more negative potential than Li. Since the pre-conditioned SEI layer consist of a major component of decomposed Li salt, larger K ions need more energy overcome the size exclusion when transporting through this Li-based SEI layer. Therefore, more overpotential is required to intercalate K ions. Comparing the integrated charge under all (de-)intercalation peaks, more Li ions intercalated into MLG. This trend agrees well with the stoichiometric changes of graphite intercalation compounds between LiC_6 and KC_8, which yields a theoretical ratio of 1.33 for inserted Li^+/K^+.

5.2.2 Effect of SEI Coverage

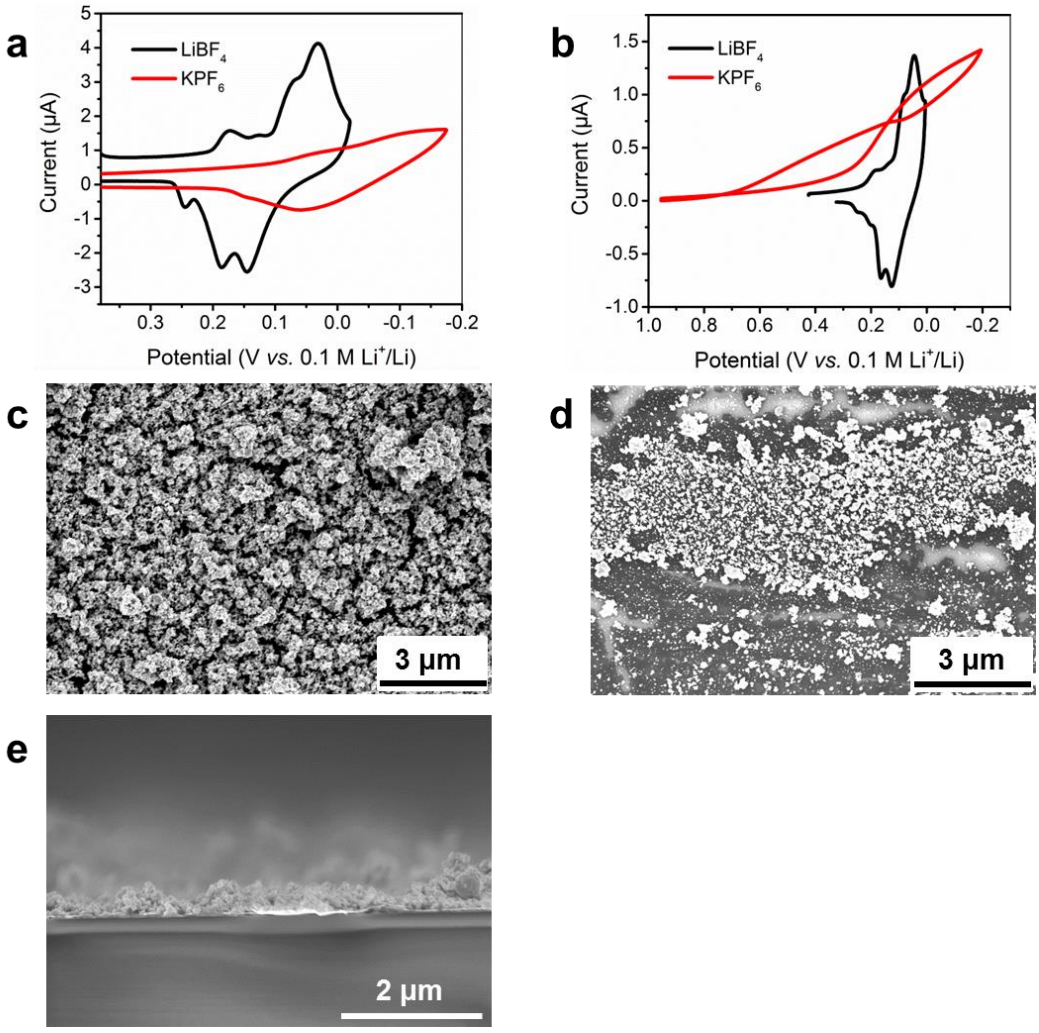

Figure 5.2 Relationship of SEI coverage to K ion intercalation behavior. a and b are CVs of Li and K ion intercalation/plating behavior on a MLG with full (a) and partial (b) SEI coverage. c and d are SEM top-view images of MLG sample tested in panels a and b, respectively. e, SEM side-view image of MLG sample tested in panel a, which has complete SEI coverage. All solutions are 0.1 M $LiBF_4$ or KPF_6 in PC-EC, scan rates are 1 mVs^{-1}.

The formation of the pre-conditioned Li-based SEI layer serves a crucial role for K ion intercalation. Comparing the MLG samples with full SEI coverage to partial coverage (Figure 5.2a, 5.2b), K ion intercalation peaks happen only with fully conditioned MLG samples while the

incomplete SEI coverage leads to K plating. The SEM images of these MLG samples are shown in Figure 5.2c and 5.2d, respectively. The whole surface of MLG capable of intercalating K ions is completely covered by sub-micron sized clusters (Figure 5.2c) with more than 200 nm thickness (Figure 5.2 e). Similar K plating signals on both pristine MLG (Figure C.1a) and MLGs with partial SEI coverage resulting from fewer conditioning cycles (Figure 5.2b) verify the importance of SEI layer when K ion intercalation process is targeted. Therefore, we believe passivating the MLG surface with a SEI layer can selectively suppress the K plating process while promoting K ion intercalation on MLG.

5.2.3 Co-intercalation of Li/K ions into Pre-conditioned MLG

When the MLG sample surface is passivated by a densely-packed SEI layer, both Li^+ and K^+ can transport freely through this interphase to be sandwiched and stabilized by two graphene sheets. In pure Li or K salt solutions, the insertion of plain Li^+ and K^+ dominates the intercalation processes (Figure 5.3a). When both Li^+ and K^+ co-exist in solution, a co-intercalation behavior was seen. Spiking different volumes of Li^+ into K^+ solution (Figure 5.3b) lead to a continuous positive shift of all (de-)intercalation peaks with increased peak currents. After normalizing the peak current of the 4^{th} intercalation peak (largest peak) at different Li^+/K^+ ratios from 0 to 0.025, a linear increase was observed (Figure 5.3c). Furthermore, the potential of the 4^{th} intercalation peak also approaches the pure Li ion intercalation potential with more concentrated Li^+, which maintains a linear positive shift at the logarithmic scale following the Nernst equation. Noticing even in the system of lowest Li^+ concentration of 0.5 mM Li^+ (blue trace in Figure 5.3b and second point in Figure 5.3c), 200 times more Li^+ exist in the solution compare to the calculated amount to occupy all available intercalation sites in MLG. Hence the gradual change of current and potential during Li^+ addition proved the co-intercalation process.

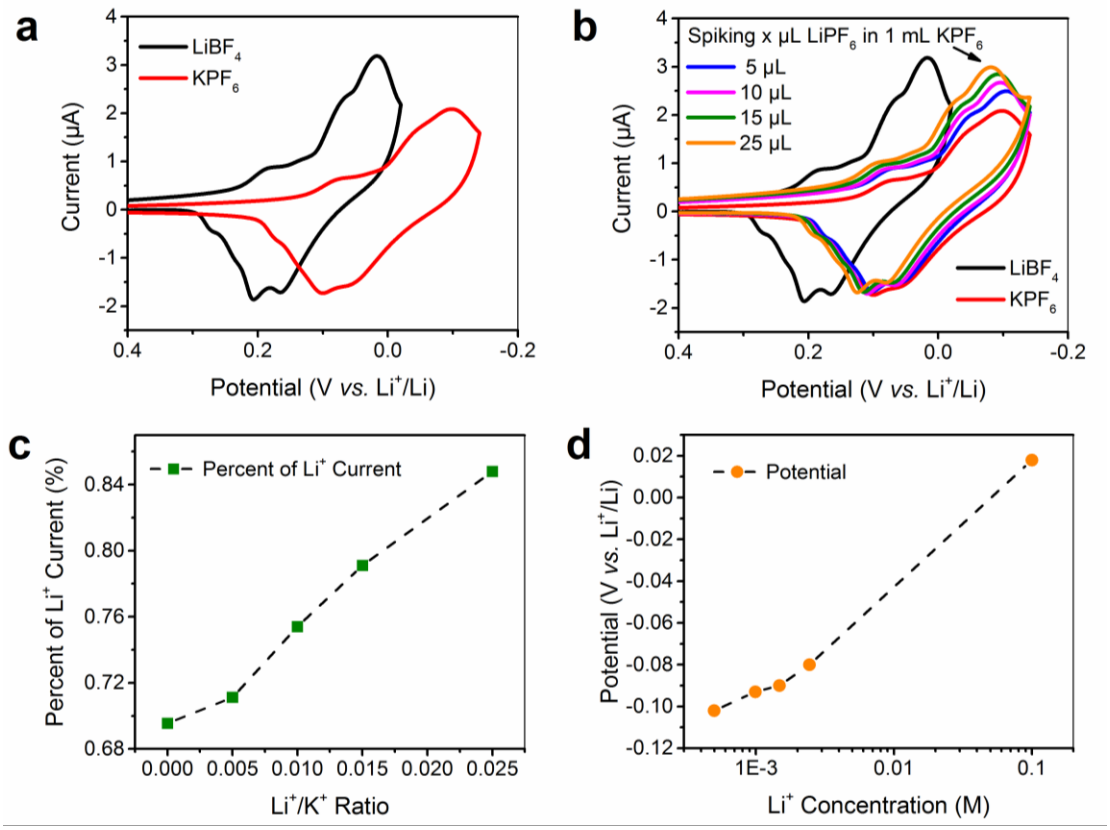

Figure 5.3 Li and K ions co-intercalation process. a, CVs of Li and K ion intercalation peaks on MLG sample used for spiking tests. b, Comparison of intercalation CVs of Li^+, K^+ and different ratio Li^+/K^+ by spiking $LiPF_6$ solution in KPF_6 solutions. c, Relationship of current percentage change and Li^+/K^+ ratio of 4^{th} intercalation peaks in panel b, the percentage changes were calibrated to same peak at Li ion intercalation (black trace). d, Relationship of peak potential and Li^+ concentration of 4^{th} intercalation peaks in panel b. All solutions are 0.1 M $LiBF_4$, KPF_6 or $LiPF_6$ salt in PC-EC, scan rates are 1 mVs^{-1}.

5.2.4 Conclusion

In the section 5.2, we have demonstrated that using a pre-conditioned MLG with complete SEI coverage can reversibly intercalate K ion. The common shape and distributions between K and Li ion intercalation peaks indicate a similar staging type mechanism for K. Using

pristine and SEI partially covered MLG samples as controls, we have proved the importance of a pre-passivated Li-based SEI layer for stable intercalation behavior of K ions. This layer can successfully shuttle the transportation of both Li^+ and K^+, allowing them to intercalate between MLG basal planes. The co-existence of both alkali ions leads to a co-intercalation process. This is to our knowledge the first time well resolved K ion intercalation peaks have been demonstrated with cyclic voltammetry.[7-11] This work will provide a novel strategy for fabrication of new KIB battery anode materials with high cycling efficiency, stability, and energy density.

5.3 Detecting Potassium Ion Gradients at a Model Graphitic Interface

In previous sections, we have demonstrated electrochemical evidences through cyclic voltammetry that of K ion intercalates into MLG samples with a passivated SEI layer. However, there is still a lack of direct evidence to track the actual flux change of K ion during intercalation. One of the solutions is to use a previously developed method in our group using Hg-based SECM probes as localized ionic sensor. To validate the applicability of Hg disk-well probe for K ion detection in our system, we first demonstrate the measurement of ionic gradients on patterned HOPG as model system for K ion intercalation.

5.3.1 *Ex Situ* Optical and Spectroscopic Measurements of Patterned HOPG

An SEM image of patterned HOPG shows a regular array of holes measuring ~43 μm in diameter and separated from their nearest neighbors by 500 μm (Figure 5.4a). The size and center-to-center distance of the holes match with the designed lithography pattern. Raman spectra (Figure 5.4b) show the clear presence of a D band for etched holes but not for pristine HOPG. The D band corresponds to carbon ring "breathing" modes and is indicative of structural disorder, such as exposed graphitic edge planes.[28] In LIBs, uptake of Li^+ is greater at graphitic

edge planes than at the basal plane,[29] so we expected to find similar ionic activity for K^+ in the present system. Following electrochemical cycling and SECM experiments, the D band remained nearly unchanged over un-etched areas but showed a marked increase over etched holes (Figure 5.4b). The increase in D band intensity is consistent with the evolution of structural disorder expected from the repeated K^+ insertion and extraction. The localization of this increase in D band intensity to the etched holes (Figure 5.4c) suggests that exposed edge planes serve as primary sites for potassium ion intercalation.

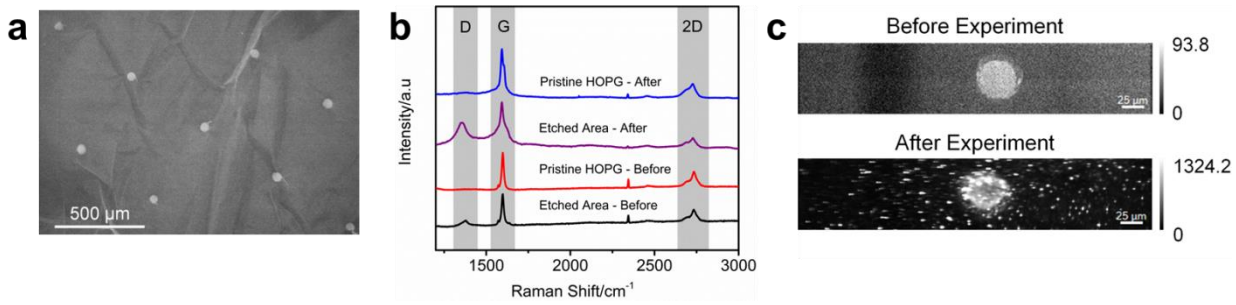

Figure 5.4 SEM and Raman Characterization of Patterned HOPG. a, SEM image shows the pattern etched holes on HOPG. The holes are ~43 µm wide, ~1.4 µm deep, and 500 µm from their nearest neighbors, measured from their centers. b, Raman spectra before and after electrochemical experiments exhibit a D band signal only over the etched holes. c, Raman mapping of the D band intensity before and after electrochemical experimentation shows an increase in D band signal limited to the etched holes.

5.3.2 Substrate Cycling and SEI Formation on HOPG

The HOPG substrate was first cycled at 1 mV s^{-1} in 0.1 M KPF_6 in PC-EC for 6 cycles to form a stable SEI layer. Initial cycles showed broad, irreversible peaks that are likely attributable to solvent and electrolyte decomposition processes, such as those found in LIB systems (Figure 5.5a).[12, 30, 31] The intensity of these peaks diminished with cycling, eventually resulting in a clean

background signal. Following SEI formation, cycling more slowly at 50 μV s^{-1} allowed the identification of K^+ intercalation behavior at E < 0.54 V (*vs.* K/K^+), in addition to various unknown processes from ~1.10 V to 0.54 V (*vs.* K/K^+), and a de-intercalation event at 0.52 V (*vs.* K/K^+) on the return sweep (Figure 5.5b).

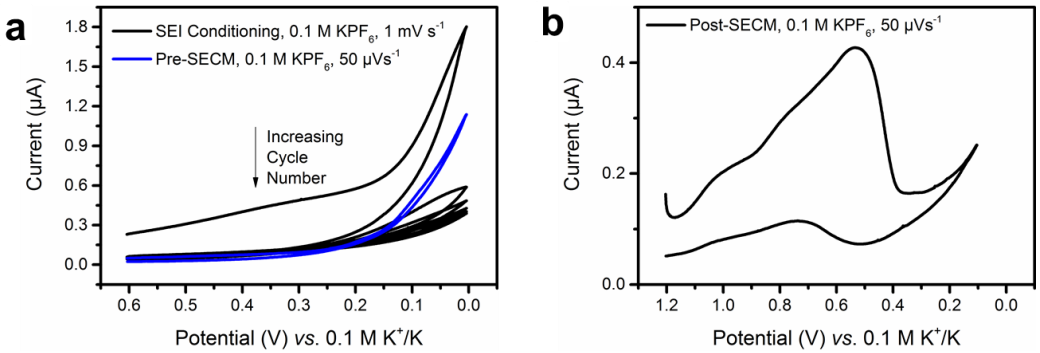

Figure 5.5 Cyclic Voltammetry of K^+ Intercalation and Deintercalation at Patterned HOPG. a, Initially observed broad, irreversible peaks diminished with cycling number, eventually resulting in a clean, stable background signal. b, After forming the SEI, a K-ion de-intercalation process was observed at 0.52 V (*vs.* K/K^+).

5.3.3 Identification of Region of Interest on HOPG

A Hg disc-well UME (a_1 = 12.5 μm, R_G = 2.5) was positioned approximately one probe radius ($L = d/a_1 \sim 1$, d = tip–substrate gap) above the HOPG surface through a probe scan curve (PSC) in the Z direction using TMPD as the redox mediator and with the substrate left at open circuit. After rapidly imaging a large area to identify a region of interest (Figure C.5), an area containing a single etched hole (Figure 5.6a) was slowly imaged at 2.5 μm s^{-1} (Figure 5.6b). This speed was selected to prevent distortions based on forced convective transport.[32] Initial SECM images exhibited negative feedback consistent with the insulating nature of SEIs observed for other alkali ions.[12] However, over time we observed a shift towards partial positive feedback. We

believe this could be a result of some SEI degradation process or the incorporation of TMPD in the SEI.

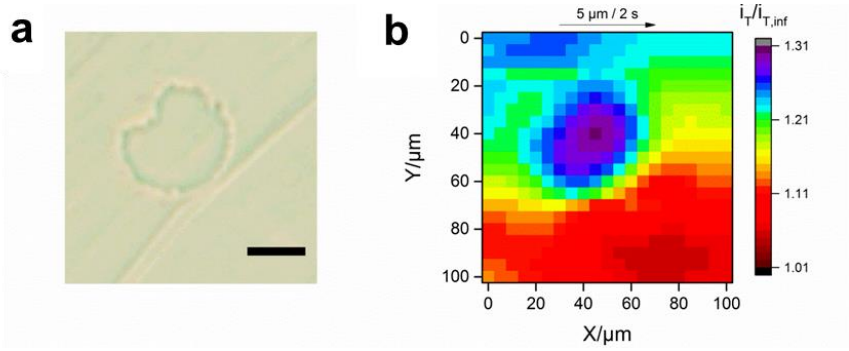

Figure 5.6 Identification of Etched Hole. a, Optical micrograph of an etched hole in HOPG. The scale bar represents 25 µm. b, SECM feedback image of the region shown in panel-a taken with a Hg disc-well in 2 mM TMPD + 0.1 M KPF_6 in PC-EC.

Though positive feedback is observed at all points in the Figure 5.6 b, even greater positive feedback occurs over the etched hole centered at [X, Y] = [45 µm, 45 µm]. If the reactivity of the holes and the basal plane were equal, the SECM feedback current observed over holes would be less than over the basal plane due to the increased tip-substrate gap over holes. The possibility of electron transfer at the HOPG basal plane,[33] the susceptibility of HOPG to adventitious contaminants,[34] and the large number of exposed edge sites on this sample do not allow a straightforward quantification of the contributions from basal and edge planes. However, the observed increase in feedback current over the etched hole is supported by Raman spectra (Figure 5.4b), which suggest far greater planar disorder in the etched holes in comparison to the pristine basal plane, and is consistent with the increased electrochemical activity observed at electronic structure distortion sites in carbonaceous materials, such as graphene.[35-38]

5.3.4 CVs with Substrate Competition on HOPG

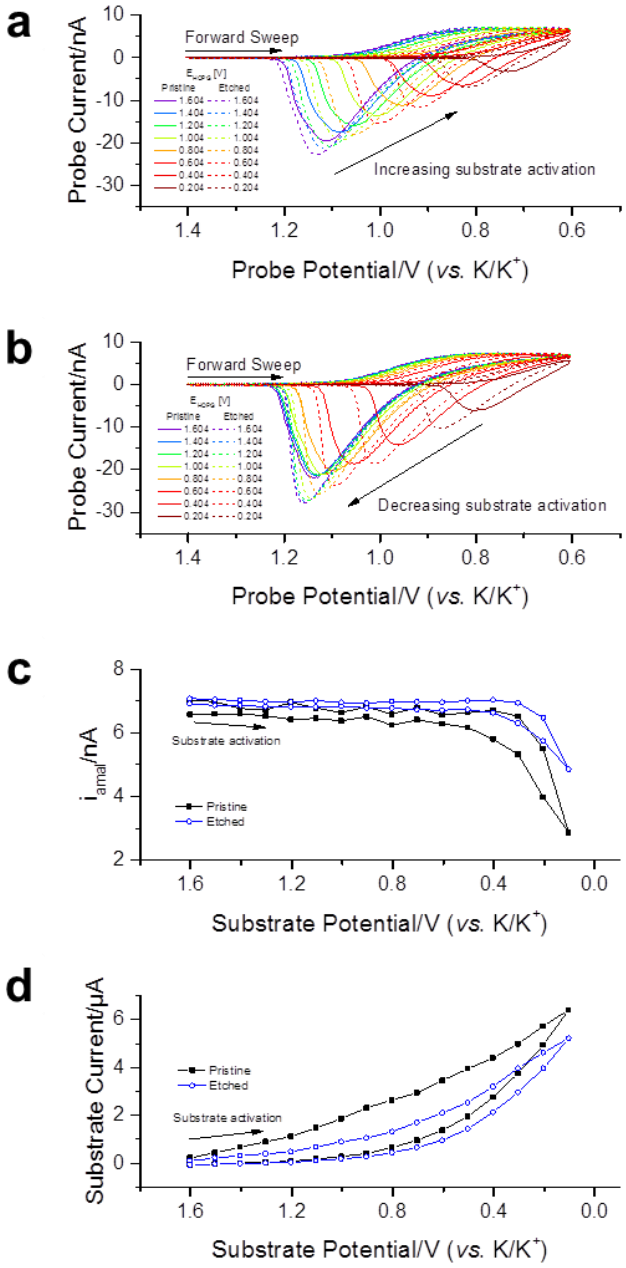

Figure 5.7 Competition for K^+ over Etched Hole. a, Select Hg disc-well CVs taken with increasing substrate activation towards K^+ intercalation. $\nu = 0.2$ V s^{-1}. b, Select Hg disc-well CVs taken with decreasing substrate activation, giving way to K^+ deintercalation. c, Hg disc-well

(*Figure 5.1 Continued*) amalgamation currents extracted from panel a and b. d, Average chronoamperometric signal at the substrate at various activation potentials.

After switching to a 1 mM KPF_6 solution in PC-EC, the Hg disc-well UME was re-approached to the origin in Figure 5.6 to a final distance of 16 μm (Figure C.6). Because ions are regularly stripped from the Hg probe, this method of approaching a surface avoids the risk of damaging the Hg probe by saturation of the amalgam phase. To show that Hg-based electrodes can directly probe changing ionic gradients, the Hg disc-well UME was positioned over unmodified HOPG at [X, Y] = [0 μm, 45 μm] and programmed to record a series of CVs with the substrate following a sequential staircase potential sweep. The amalgamation current (i_{amal}), peak stripping current (i_{strip}), and stripping charge (Q_{strip}) were each extracted from the CV-SECM dataset.[18] As the substrate potential increased (Figure 5.7a), activating K^+ intercalation, all three Hg disc-well signals decreased (Figure 5.7c) while the substrate current increased (Figure 5.7d). Then, as the substrate potential was stepped anodically to allow K^+ deintercalation (Figure 5.7b), the Hg disc-well signals increased in kind as the substrate current decreased, indicating the restoration of the local K^+ concentration. The total decrease in probe signal between inactive and fully active substrate potentials was 3.71 nA (56%) for i_{amal}, 17.6 nA (90%) for i_{strip}, and 3.29 nC (89%) for Q_{strip}. After testing over a pristine region of HOPG, the Hg disc-well UME was positioned directly over an etched hole at [X, Y] = [45 μm, 45 μm] and made to repeat the same test sequence. As before, all three Hg disc-well signals decreased and then recovered in response to substrate activation then deactivation towards K^+ intercalation. The total decrease in probe signal between inactive and fully active substrate potentials was 2.06 nA (30%) for i_{amal}, 17.7 nA (77%) for i_{strip}, and 3.24 nC (77%) for Q_{strip}.

We hypothesize that the probe signal discrepancies, specifically, the larger changes in i_{strip} and Q_{strip} in comparison to i_{amal}, are due to cross-talk between the probe and the substrate in this low K^+ concentration regime.[39] Such low K^+ concentrations were used in order to safely access timescales allowing good ionic resolution and avoid saturating the ionic capacity of the thin HOPG sample but led to larger than ideal shared resistance between the two working electrodes. In the interest of avoiding co-intercalation phenomena,[40-42] no additional supporting electrolyte was present. i_{strip} and Q_{strip} are typically valuable for their ionic specificity and enhanced sensitivity due to pre-concentration of the amalgam phase, but the observed potential shifts compromised their usefulness in this particular system.

Nevertheless, i_{amal} remained a reliable metric of the local K^+ concentration since it reached a quasi-steady-state and does not depend on the accumulation of K^+ within the Hg probe over time. In both sites explored, the relatively stable i_{amal} signal for $E_{sub} \geq 0.5$ V suggests that the cathodic peaks observed in the HOPG voltammetry (Figure 5.5b) are not associated with K^+ uptake. It is reasonable to suspect that these peaks may be associated with changes in the SEI. $i_{amal}(E_{sub})$ is described well by a simple exponential function of the form $i_{amal} = A + B*\exp(C*E_{sub})$, where A, B, and C are freely varying constants, for both the activation ($\chi^2_{red.} = 1.62 \times 10^{-20}$ for pristine HOPG and $\chi^2_{red.} = 2.26 \times 10^{-21}$ for etched holes) and deactivation ($\chi^2_{red.} = 2.13 \times 10^{-20}$ for pristine HOPG and $\chi^2_{red.} = 2.26 \times 10^{-21}$ for etched holes) substrate potential sequences (Figure C.7), which suggests that the Hg disc-well closely followed the electrochemical uptake of K^+ by the substrate. Therefore, despite challenges unique to the system under study, these results demonstrate the ability of Hg disc-well SECM probes to track dynamic ionic fluxes at operating KIB interfaces.

Considering the enhanced positive feedback current in the SECM image (Figure 5.6b) and the pronounced D band in the Raman spectra (Figure 5.4b) over etched holes, we expected to observe a clear increase in K^+ uptake over etched holes in comparison to pristine sites due to the greater concentration of exposed edge planes at etched sites. Contrary to expectations, a greater proportional decrease in i_{amal} was observed over the pristine HOPG than over the etched hole. However, microscopic inspection of the pristine surface does indicate a large density of steps (Figure 5.6a), exposing edge sites at which the ionic flux could rival that of artificially-defective holes. Another possible explanation for the small differences observed between the pristine and hole sites is that the SEI formed on this KIB electrode strongly controls the flux of K^+, thus decreasing contrast between neighboring surface sites. Furthermore, the consistent i_{amal} registered at E_{sub} = 1.604 V, where the substrate is electrochemically inactive, is evidence that the bulk K^+ concentration was not significantly affected. Despite this, the average substrate current decreased with each cycle (Figure 5.7d and Figure C.8). Therefore, we conclude that the substrate's activity towards K^+ uptake and release decreased with use and/or time. Regardless of the cause, this overall decrease in substrate activity was sufficiently large to obscure whatever differences in K^+ uptake and release may have been originally present over the pristine HOPG and etched holes. The decrease in K^+ uptake by the substrate with each cycle was also a contributing factor to the smaller distortions of i_{strip} and Q_{strip} when a test sequence was subsequently repeated at the same locations with a longer normalized timescale—obtained by increasing the overpotential and decreasing the potential scan rate (Figure C.8).

While the measurement of K^+ fluxes at the activated KIB electrode–electrolyte interface was successful, this first exploration did not show significant differences in ionic uptake between two sites with different redox reactivity. Rather than a lack of contrast, the absence of

meaningful differences at the two location types actually demonstrates the sensitivity of Hg disc-wells to local ionic fluxes, which can distinguish between various degrees of substrate uptake of a particular ionic species *in situ*. The probes accurately reported the changing ionic fluxes, but differences in K^+ uptake over pristine and etched regions were overwhelmed by the much larger impact of substrate aging. While HOPG is certainly not an ideal electrode material under the tested conditions, the methodology shown here might be useful to distinguish the different K^+-consuming processes that underlie the complex response observed on KIB electrodes.

5.3.5 Conclusion

We have used a novel electrochemical probe to obtain direct measurements of K^+ uptake by a representative graphitic anode material for KIBs. Our SECM investigations with a Hg disc-well UME revealed increased electronic conductivity as well as reversible K^+ intercalation and deintercalation over exposed HOPG edge planes. When positioned over an electrochemically active feature in HOPG, a Hg disc-well UME responded to activation of the substrate towards K^+ uptake. HOPG CVs confirmed the process under investigation was K^+ intercalation/deintercalation and not plating/stripping. However, the complex electrochemical response observed on the substrate electrode at potentials where the SEI is expected to form was chemically resolved by the probe, which did not identify a significant steady-state flux of K^+ towards the interface until potentials well into the expected intercalation range.

We compared the activity towards K^+ intercalation on two structurally different sites on the HOPG surface. Despite contrast in their Raman signatures, indicating a different degree of disorder, and differences in their redox reactivity as assessed by the use of the feedback mode of SECM, few differences were detected on their K^+ flux activity. While HOPG is likely not a top candidate for KIBs, the new capabilities brought by these probes make them of interest to further

understand the role of heterogeneities on ion insertion mechanisms in energy materials. Hg disc-well UMEs can acquire localized, chemically specific measurements of ionic flux over operating battery electrode materials. This information is inaccessible to existing analytical methods and will help inform the rational design of future alkali ion battery anodes and cathodes. CV-SECM imaging studies of multiple alkali ion intercalation and de-intercalation processes at target energy storage materials are in progress and planned for future publications.

5.4 Materials and Methods

Chemicals and Supplies: All chemicals were purchased as A.C.S. reagent grade or better and used as received without further purification. Nitric acid and water (ChromAr grade) were obtained from Avantor. Platinum wire (25 μm and 0.5 mm diameter) and silver wire (1 mm diameter) were obtained from Goodfellow. Ethylene carbonate (EC, anhydrous, 99%), mercury(II) nitrate monohydrate (≥99.99% trace metals basis), lithium tetrafluoroborate (98%), potassium hexafluorophosphate (99.5%), lithium hexafluorophosphate (≥99.99%, trace metals basis), propylene carbonate (PC, anhydrous, 99.7%), tetrabutylammonium hexafluorophosphate (NBu_4PF_6, 99.0%) and *N*,*N*,*N'*,*N'*-tetramethyl-*p*-phenylenediamine (TMPD, 99%) were obtained from Sigma-Aldrich. Tetramethylammonium nitrate (NMe_4NO_3) was obtained from Southwestern Analytical Chemicals.

25 μm copper foil was purchased from Alfa Aesar. Highly ordered pyrolytic graphic (HOPG, brand grade SPI-2) was purchased from SPI supplies. 3M™ copper conductive tape with a single conductive glue adhesive surface was purchased from Ted Pella, Inc. Microposit S1813 photoresist was purchased from MicroChem. AZ 917 MIF developer was purchased from AZ Electronic Materials. Ultra high purity (UHP) argon was obtained from Airgas.

Multilayer Graphene Fabrication: MLG were grown by chemical vapor deposition (CVD) using methane and 25 μm Cu foil as catalyst. Prior to growth, the Cu foil was treated in acetone (10s), water (10s), glacial acetic acid (10 min), water (10s), acetone (10s), and IPA (10s) to remove any surface oxides. The Cu foil was then put inside a one end sealed 100 mm long, 18 mm ID, 22 mm OD quartz tube. The tube with Cu foil was then mounted in the middle of CVD chamber with sealed end facing gas inlet direction. Multilayer graphene was grown at 960 ℃, 20 sccm CH_4, 60 sccm H_2 and 100 sccm Ar for 20 min. Same graphene transfer procedure (Chapter 4.7) were used to transfer MLG samples.

HOPG Substrate Fabrication and Patterning: Cu tape was used to mechanically exfoliate thin HOPG samples from a larger HOPG block. Following our previously published graphene patterning method,[12] the thin HOPG samples were treated with photolithography to create patterned windows to expose selected areas of the HOPG surface using a mask. The exposed HOPG was then etched by a Plasma Lab Freon/O_2 reactive ion etching (RIE) system with 37 mW RF energy under a pressure of 40 mTorr while flowing 20 sccm O_2 for 1 min. After RIE, the remaining photoresist was removed by rinsing with acetone and isopropanol. The resulting regular array of holes measured ~43 μm wide and ~1.4 μm deep (Figure C.4). Neighboring holes were separated by 500 μm, measured from their centers.

Hg Disc-Well Electrode Fabrication: Hg disc-well probes were fabricated by etching Pt disc ultramicroelectrodes (UMEs), electrodepositing Hg in the cavity, and removing excess Hg with a flexible glass coverslip as previously published.[21] Specifically, Pt UMEs with a Pt radius (a_1) of 12.5 μm and a glass ratio ($R_G = a_2/a_1$, a_2 = total probe radius) smaller than 4 were etched in a solution of 30 v. % sat. $CaCl_2$ + 10 v. % HCl in H_2O for 40 s under ultrasonic agitation while applying a peak-to-peak voltage ($V_{p\text{-}p}$) of 2.70 V at 60 Hz with a variac. This gave an etched

cylindrical cavity with a normalized depth ($H_2 = h_2/a_1$, h_2 = depth of cavity) of 1.1. Hg was deposited potentiostatically at +0.2 V *vs*. Ag/AgCl in 20 mM $Hg(NO_3)_2{\cdot}H_2O$ + 0.2 M NMe_4NO_3 and 0.5 v. % HNO_3 in H_2O until the deposition current reached 0.3 μA, indicating the growth of a Hg sphere-cap protruding from the overfilled cavity. The Hg deposit was then leveled and rinsed with H_2O to remove displaced Hg droplets, resulting in a Hg disc-well with a flat, mirror-like surface having a normalized height ($H_1 = h_1/a_1$, h_1 = Hg sphere-cap height) of 0 (Figure C.3).

***Ex Situ* Optical and Spectroscopic Measurements:** Hg disc-well probe dimensions were verified though optical microscopy (Zeiss AxioLab.A1). In addition to optical microscopy, MLG and HOPG samples were characterized through scanning electron microscopy (SEM, Hitachi S-4800 high resolution SEM), atomic force microscopy (AFM, Asylum Research Cypher), Raman spectroscopy and imaging (Nanophoton Laser Raman Microscope RAMAN-11) (Figure 5.4).

Electrochemical Experiments: All electrochemical measurements were performed with a CHI 760 and CHI 920D SECM under oxygen- and water-free conditions in an MBRAUN UniLab glovebox filled with UHP argon. All solutions were made in a PC and EC solvent mixture with 1:1 ratio (vol./vol.), which is hereafter referred to as PC-EC. The Teflon SECM cell was fitted with a working electrode (4.9 mm^2 MLG, or 19.6 mm^2 patterned HOPG), a Pt wire counter electrode (CE), and a Ag wire quasi-reference electrode (QRE). Substrate CVs and CV-SECM used a Ag/Ag^+ (saturated $AgNO_3$ in PC-EC) reference electrode (RE) instead of the Ag QRE to poise the cell potential. Potentials referenced against a 0.1 M Ag/Ag^+ RE (3.604 V *vs*. 0.1 M K/K^+, and 3.725 V *vs.* 0.1 M Li/Li^+) are reported *vs*. 0.1 M K^+/K or *vs*. 0.1 M Li^+/Li for clarity.

K ion (co-)intercalation on MLG. The MLG samples were first characterized in 0.1 M $LiBF_4$ PC-EC solution at 1 mV s^{-1} to examine their quality of clear staging peaks. After that, a continuous conditioning of MLG in above solution between 3.325 to 0 V *vs*. 0.1 M Li^+/Li at 1 mV s^{-1} for 10 cycles to form stable SEI layer. After through rinsing of 6 times with PC, 0.1 M KPF_6 PC-EC solution were added to testing cell to obtain K ion intercalation peaks between 0.425 to -0.175 V *vs*. 0.1 M Li^+/Li at 1 mV s^{-1}. The following Li-K co-intercalation tests were performed by spiking 5, 10, 15, 25 μL 0.1 M $LiPF_6$ PC-EC solution into previous system and test at similar potential region.

Conditioning and Substrate CV of HOPG. Prior to SECM investigations, the patterned HOPG electrode was cycled in 0.1 M KPF_6 in PC-EC for 6 cycles between 0.604 to 0.004 V *vs*. 0.1 M K^+/K at 1 mV s^{-1} to form a stable SEI layer. In order to better observe K^+ intercalation and deintercalation processes, additional CVs with HOPG were acquired at 50 μV s^{-1} in 1 mM KPF_6 in PC-EC after SECM experiments (Figure 5.5).

CV-SECM Experiments. A Hg disc-well UME performing TMPD oxidation in a solution of 2 mM TMPD and 0.1 M KPF_6 in PC-EC was used to collect an SECM feedback image (Figure 5.6) to find the approximate locations of etched holes. To avoid interference from oxidized TMPD generated at the CE, the cell was rinsed with PC and refilled with 1 mM KPF_6 in PC-EC. The Ag QRE was also swapped for a Ag^+/Ag RE after the removal of TMPD from the cell. The same Hg disc-well probe was then approached to the substrate with a cyclic voltammetry probe scan surface (CV-PSS) in the Z direction (Figure C.6). After reaching the HOPG surface, the probe was positioned directly over an etched hole and used to record a series of CVs with regular sequential incrementing (and then decrementing) of the substrate potential.

5.5 References

1. Etacheri, V.; Marom, R.; Elazari, R.; Salitra, G.; Aurbach, D. Challenges in the development of advanced Li-ion batteries: a review. *Energy & Environmental Science* **2011**, *4*, 3243-3262.

2. Vikstrom, H.; Davidsson, S.; Hook, M. Lithium availability and future production outlooks. *Applied Energy* **2013**, *110*, 252-266.

3. Larcher, D.; Tarascon, J. M. Towards greener and more sustainable batteries for electrical energy storage. *Nat. Chem.* **2015**, *7*, 19-29.

4. Taylor, S. R. Abundance of Chemical Elements in the Continental Crust - a New Table. *Geochim. Cosmochim. Acta* **1964**, *28*, 1273-1285.

5. Xue, L. G.; Li, Y. T.; Gao, H. C.; Zhou, W. D.; Lu, X. J.; Kaveevivitchai, W.; Manthiram, A.; Goodenough, J. B. Low-Cost High-Energy Potassium Cathode. *J. Am. Chem. Soc.* **2017**, *139*, 2164-2167.

6. Bard, A. J.; Faulkner, L. R. *Electrochemical methods: fundamentals and applications, 2nd Edition*. 2001.

7. Vaalma, C.; Giffin, G. A.; Buchholz, D.; Passerini, S. Non-Aqueous K-Ion Battery Based on Layered K0.3MnO2 and Hard Carbon/Carbon Black. *J. Electrochem. Soc.* **2016**, *163*, A1295-A1299.

8. Jian, Z. L.; Xing, Z. Y.; Bommier, C.; Li, Z. F.; Ji, X. L. Hard Carbon Microspheres: Potassium-Ion Anode Versus Sodium-Ion Anode. *Advanced Energy Materials* **2016**, *6*.

9. Jian, Z. L.; Luo, W.; Ji, X. L. Carbon Electrodes for K-Ion Batteries. *J. Am. Chem. Soc.* **2015**, *137*, 11566-11569.

10. Luo, W.; Wan, J. Y.; Ozdemir, B.; Bao, W. Z.; Chen, Y. N.; Dai, J. Q.; Lin, H.; Xu, Y.; Gu, F.; Barone, V.; Hu, L. B. Potassium Ion Batteries with Graphitic Materials. *Nano Lett.* **2015**, *15*, 7671-7677.

11. Share, K.; Cohn, A. P.; Carter, R.; Rogers, B.; Pint, C. L. Role of Nitrogen-Doped Graphene for Improved High-Capacity Potassium Ion Battery Anodes. *ACS Nano* **2016**, *10*, 9738-9744.

12. Hui, J.; Burgess, M.; Zhang, J.; Rodríguez-López, J. Layer number dependence of Li^+ intercalation on few-layer graphene and electrochemical imaging of its solid–electrolyte interphase evolution. *ACS Nano* **2016**, *10*, 4248-4257.

13. Barton, Z. J.; Rodriguez-Lopez, J. Lithium Ion Quantification Using Mercury Amalgams as in Situ Electrochemical Probes in Nonaqueous Media. *Anal. Chem.* **2014**, *86*, 10660-10667.

14. Ventosa, E.; Schuhmann, W. Scanning electrochemical microscopy of Li-ion batteries. *PCCP* **2015**, *17*, 28441-28450.

15. Schwager, P.; Bulter, H.; Plettenberg, I.; Wittstock, G. Review of Local In Situ Probing Techniques for the Interfaces of Lithium-Ion and Lithium-Oxygen Batteries. *Energy Technology* **2016**, *4*, 1472-1485.

16. Barton, Z. J.; Rodriguez-Lopez, J. Emerging scanning probe approaches to the measurement of ionic reactivity at energy storage materials. *Anal Bioanal Chem* **2016**, *408*, 2707-2715.

17. Danis, L.; Gateman, S. M.; Kuss, C.; Schougaard, S. B.; Mauzeroll, J. Nanoscale Measurements of Lithium-Ion-Battery Materials using Scanning Probe Techniques. *Chemelectrochem* **2017**, *4*, 6-19.

18. Barton, Z. J.; Rodriguez-Lopez, J. Cyclic Voltammetry Probe Approach Curves with Alkali Amalgams at Mercury Sphere-Cap Scanning Electrochemical Microscopy Probes. *Anal. Chem.* **2017**, *89*, 2708-2715.

19. Velmurugan, J.; Mirkin, M. V. Fabrication of Nanoelectrodes and Metal Clusters by Electrodeposition. *Chemphyschem* **2010**, *11*, 3011-3017.

20. Danis, L.; Polcari, D.; Kwan, A.; Gateman, S. M.; Mauzeroll, J. Fabrication of Carbon, Gold, Platinum, Silver, and Mercury Ultramicroelectrodes with Controlled Geometry. *Anal. Chem.* **2015**, *87*, 2565-2569.

21. Barton, Z. J.; Rodriguez-Lopez, J. Fabrication and Demonstration of Mercury Disc-Well Probes for Stripping-Based Cyclic Voltammetry Scanning Electrochemical Microscopy. *Anal. Chem.* **2017**, *89*, 2716-2723.

22. Hills, G. J.; Peter, L. M. Electrode-Kinetics in Aprotic Media. *J. Electroanal. Chem.* **1974**, *50*, 175-185.

23. Koper, M. T. M.; Schmickler, W. A theory for amalgam forming electrode reactions. *J. Electroanal. Chem.* **1998**, *450*, 83-94.

24. Burgess, M.; Hernandez-Burgos, K.; Cheng, K. J.; Moore, J. S.; Rodriguez-Lopez, J. Impact of electrolyte composition on the reactivity of a redox active polymer studied through surface interrogation and ion-sensitive scanning electrochemical microscopy. *Analyst* **2016**, *141*, 3842-3850.

25. Komaba, S.; Hasegawa, T.; Dahbi, M.; Kubota, K. Potassium intercalation into graphite to realize high-voltage/high-power potassium-ion batteries and potassium-ion capacitors. *Electrochem. Commun.* **2015**, *60*, 172-175.

26. Verma, P.; Maire, P.; Novak, P. A review of the features and analyses of the solid electrolyte interphase in Li-ion batteries. *Electrochim. Acta* **2010**, *55*, 6332-6341.

27. Eftekhari, A.; Jian, Z. L.; Ji, X. L. Potassium Secondary Batteries. *ACS Appl. Mater. Inter.* **2017**, *9*, 4404-4419.

28. Ferrari, A. C.; Robertson, J. Interpretation of Raman spectra of disordered and amorphous carbon. *Phys. Rev. B* **2000**, *61*, 14095-14107.

29. Yamada, Y.; Miyazaki, K.; Abe, T. Role of Edge Orientation in Kinetics of Electrochemical Intercalation of Lithium-Ion at Graphite. *Langmuir* **2010**, *26*, 14990-14994.

30. Aurbach, D. Review of selected electrode-solution interactions which determine the performance of Li and Li ion batteries. *J. Power Sources* **2000**, *89*, 206-218.

31. Norberg, N. S.; Lux, S. F.; Kostecki, R. Interfacial side-reactions at a LiNi0.5Mn1.5O4 electrode in organic carbonate-based electrolytes. *Electrochem. Commun.* **2013**, *34*, 29-32.

32. Kuss, S.; Trinh, D.; Danis, L.; Mauzeroll, J. High-Speed Scanning Electrochemical Microscopy Method for Substrate Kinetic Determination: Method and Theory. *Anal. Chem.* **2015**, *87*, 8096-8101.

33. Patel, A. N.; Collignon, M. G.; O'Connell, M. A.; Hung, W. O. Y.; McKelvey, K.; Macpherson, J. V.; Unwin, P. R. A New View of Electrochemistry at Highly Oriented Pyrolytic Graphite. *J. Am. Chem. Soc.* **2012**, *134*, 20117-20130.

34. Nioradze, N.; Chen, R.; Kurapati, N.; Khyataeva-Domanov, A.; Mabic, S.; Amemiya, S. Organic Contamination of Highly Oriented Pyrolytic Graphite As Studied by Scanning Electrochemical Microscopy. *Anal. Chem.* **2015**, *87*, 4836-4843.

35. Tan, C.; Rodriguez-Lopez, J.; Parks, J. J.; Ritzert, N. L.; Ralph, D. C.; Abruna, H. D. Reactivity of Monolayer Chemical Vapor Deposited Graphene Imperfections Studied Using Scanning Electrochemical Microscopy. *ACS Nano* **2012**, *6*, 3070-3079.

36. Zhong, J. H.; Zhang, J.; Jin, X.; Liu, J. Y.; Li, Q. Y.; Li, M. H.; Cai, W. W.; Wu, D. Y.; Zhan, D. P.; Ren, B. Quantitative Correlation between Defect Density and Heterogeneous Electron Transfer Rate of Single Layer Graphene. *J. Am. Chem. Soc.* **2014**, *136*, 16609-16617.

37. Unwin, P. R.; Guell, A. G.; Zhang, G. H. Nanoscale Electrochemistry of sp(2) Carbon Materials: From Graphite and Graphene to Carbon Nanotubes. *Acc. Chem. Res.* **2016**, *49*, 2041-2048.

38. Hui, J.; Zhou, X.; Bhargava, R.; Chinderle, A.; Zhang, J.; Rodríguez-López, J. Kinetic modulation of outer-sphere electron transfer reactions on graphene electrode with a sub-surface metal substrate. *Electrochim. Acta* **2016**, *211*, 1016-1023.

39. Trinh, D.; Maisonhaute, E.; Vivier, V. Electrical cross-talk in transient mode of scanning electrochemical microscopy. *Electrochem. Commun.* **2012**, *16*, 49-52.

40. Kim, H.; Yoon, G.; Lim, K. M.; Kang, K. A comparative study of graphite electrodes using the co-intercalation phenomenon for rechargeable Li, Na and K batteries. *Chem. Commun.* **2016**, *52*, 12618-12621.

41. Cohn, A. P.; Muralidharan, N.; Carter, R.; Share, K.; Oakes, L.; Pint, C. L. Durable potassium ion battery electrodes from high-rate cointercalation into graphitic carbons. *Journal of Materials Chemistry A* **2016**, *4*, 14954-14959.

42. Ri, G. C.; Yu, C. J.; Kim, J. S.; Hong, S. N.; Jong, U. G.; Ri, M. H. First-principles study of ternary graphite compounds cointercalated with alkali atoms (Li, Na, and K) and alkylamines towards alkali ion battery applications. *J. Power Sources* **2016**, *324*, 758-765.

CHAPTER 6

REDOX ACTIVE POLYMERIC MATERIALS AS ENERGY STORAGE CARRIERS[1]

6.1 Introduction

Redox flow battery technology offers many advantages for grid energy storage such as load-leveling, long durability, flexible operation, easy scalability, high-efficiency and low cost.[1-3] In this technology, electrochemical energy is stored in highly concentrated solutions of reversible redox active molecules, and separated in compartments for the low and high electrochemical potential species. Non-aqueous redox flow batteries (NRFBs) are a potentially viable alternative to their aqueous counterparts (ARFBs) having a wide range of redox active species and electrolytes available for their design.[1, 4-6] The energy density of NRFBs can be dramatically

---

† Part of this chapter is adapted from the publications: Nagarjuna, G.; Hui, J.; Cheng, K. J.; Lichtenstein, T.; Shen, M.; Moore, J. S.; Rodriguez-Lopez, J. Impact of Redox-Active Polymer Molecular Weight on the Electrochemical Properties and Transport Across Porous Separators in Nonaqueous Solvents. *Journal of the American Chemical Society* **2014**, *136*, 16309-16316. Montoto, E. C.; Nagarjuna, G.; Hui, J.; Burgess, M.; Sekerak, N. M.; Hernandez-Burgos, K.; Wei, T. S.; Kneer, M.; Grolman, J.; Cheng, K. J.; Lewis, J. A.; Moore, J. S.; Rodriguez-Lopez, J. Redox Active Colloids as Discrete Energy Storage Carriers. *Journal of the American Chemical Society* **2016**, *138*, 13230-13237.

† Collaboration and contribution statement: This work was collaborated with Prof. Jeffrey S. Moore Group. Polymeric materials were synthesized and characterized by Dr. Gavvalapalli Nagarjuna, Kevin J. Cheng, and Prof. Jeffrey S. Moore. Part of RACs CV and theoretical fits were obtained by group colleague Elena C. Montoto and Dr. Kenneth Hernández-Burgos.

increased by using redox couples that are highly soluble in organic solvents and that operate at electrode potentials well beyond the window of stability of aqueous electrolytes.[7] Despite these exciting prospects, the lower ionic conductivity observed in non-aqueous electrolytes has prevented the wide-scale development of NRFBs.

Challenges in adapting commonly used ion exchange membranes (IEMs) as separators from aqueous to non-aqueous environments are greatly responsible for the paucity in studies of NRFBs.[4, 8-11] The role of the separator is to physically and electronically isolate the high and low potential redox species compartments. This prevents the mixing of the redox active components (crossover) and simultaneously provides high electrolyte ionic conductivity for minimizing losses due to resistance to current flow.[3, 4] Using IEMs designed for aqueous environments, many of which are proton conductors, decreases the power density of NRFBs by one order of magnitude compared to ARFBs.[4] Moreover, IEMs are expensive and they contribute to ~20% of the battery cost.[12, 13]

Finding improvements in the performance of IEM's is an active research area,[4] but we reasoned that an alternative for NRFBs could be based on electrolyte size-selectivity[14] rather than ionic-selectivity. Size-selectivity using nano-porous membranes has been introduced recently in aqueous vanadium redox flow batteries for separating proton transport from that of larger vanadium cations.[4, 15] A strong emphasis is placed on the complex design of these membranes so they can adjust their sterics and electrostatics to effectively discriminate the redox active species.[12, 16-20] Here, we introduce an alternate approach in which the size of the redox active species is varied and systematically studied through a chemically-flexible synthetic polymer-based approach. This strategy de-emphasizes membrane design and enables an insightful exploration of the properties of potential redox active candidates.

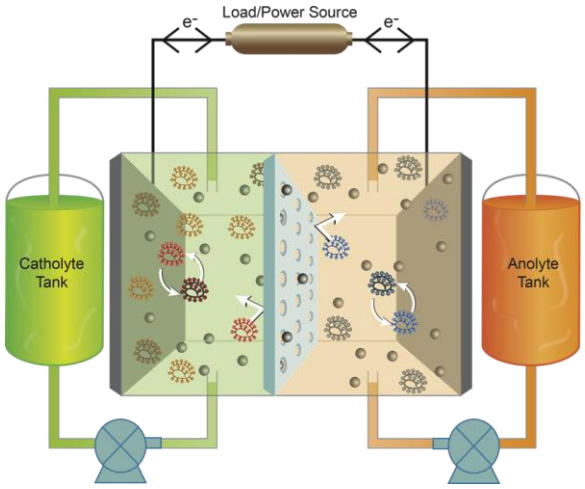

Figure 6.1 Schematic design of NRFB with large polymeric charge carriers and size-selective nano-porous membrane.

Unlike IEMs, porous membranes transport molecules based on size. Thus by careful design of the redox active component for matching an appropriate size, one can take advantage of size-exclusion to selectively and efficiently transport charge-balancing ions across the porous membrane while retaining the active species in its compartment, as shown in Figure 6.1. Commercial off-the-shelf (COTS) porous separators are relatively inexpensive compared to IEMs,[13] hence their utilization in NRFBs could in principle bring down the overall cost of the NRFBs. Although porous separators have been widely used in lithium-ion batteries,[13] their use in NRFBs is not well explored.[4, 15] This could be due to the lack of development in redox active components whose size is easily varied without adversely affecting their electrochemical properties.

Controlling the molecular weight of redox active polymers (RAPs) is an easy way to vary the size of the redox active components. Understanding the size-dependent transport, solubility and electrochemical properties of RAPs may enable their use in conjunction with COTS porous membranes as separators in NRFBs.[3, 4] To the best of our knowledge, there are no known RAPs

with the desired solubility, energy density and (electro)chemical reversibility in NRFBs. Poly(vinyl ferrocene)[21, 22] and poly(vinyl anthracene)[23] are well-studied RAPs for benchmarking the properties of soluble macromolecular designs. In this study, we first focused on the synthesis of viologen based RAPs of different molecular weight (MW), as shown in Scheme 6.1, and study the impact of polymer MW on their electrochemical, solubility, viscosity and transport properties across commercial porous membranes as a means for enabling size-selectivity for NRFBs.

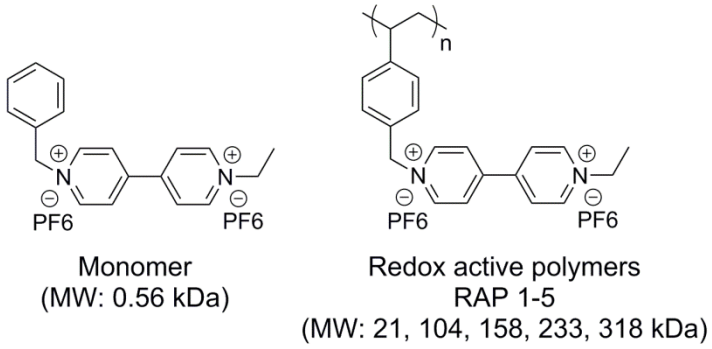

Scheme 6.1 Chemical structures of monomer and redox active polymers (RAP 1-5).

Another polymer-based energy storage architecture we synthesized is redox active colloids (RACs), as shown in Scheme 6.2. RACs act as discrete charge carriers that incorporate redox pendants for facile charge transport within a well-defined 3D geometry. Similar to RAPs, these particles are structurally stable, exhibit high charge density, and retain the redox signatures of the constituent monomer, easily varied via organic synthesis. These large dimension RACs show promising size-exclusion flow batteries by greatly reducing crossover.[24] Since RACs tends to form a densely packed monolayer on the surface of NRFBs electrode. Exploring charge transport property of RACs monolayer would benefit the comprehensive understanding of RAC NRFBs system.

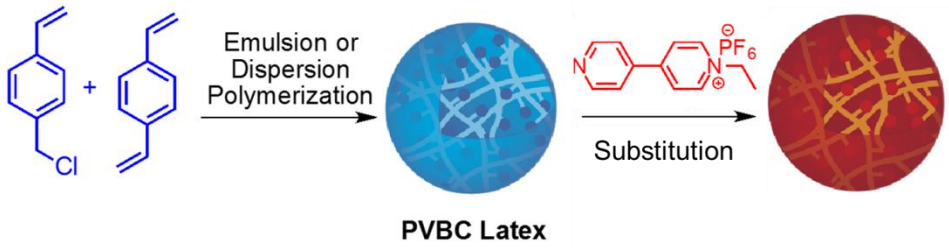

Scheme 6.2 Reaction scheme for the synthesis of polyvinyl benzylchloride and viologen based redox active colloidal particles.

6.2 Characterization of RAPs 1-5

The percent functionalization of PVBC with ethyl viologen was determined using ^{1}H NMR, ATR-IR, UV-Vis absorption spectra and elemental analyses. In PVBC, ν_{CH2Cl} stretch[25] appears at 1280 cm^{-1}. ATR-IR spectra (Figure D.1) of **RAPs 1-5** show a complete disappearance of the peak at 1280 cm^{-1} and also display the peak corresponding to the viologen quaternary amine[25] ($\nu_{>N+<}$) at 1650 cm^{-1}. For a given concentration of repeat units, the molar extinction coefficients of RAPs (Table D.4) were found to be close to that of monomer, indicating the near-quantitative substitution of PVBC with ethyl viologen. ^{1}H NMR, elemental analyses (C, H, N, P, F, and Cl shown in Table D.2), and bulk electrolysis (see below) data further support the near-quantitative functionalization of PVBC with ethyl viologen.

RAPs 1-5 display good solubility in non-aqueous electrolytes such as acetonitrile and propylene carbonate, both commonly used solvents in NRFBs.[1, 4] The 21kDa polymer is soluble up to 2.9 M in acetonitrile, while the highest MW 318kDa polymer is soluble up to 2.1 M (Table D.1). The monomer showed negligible change in viscosity with an increase in concentration from 0.01 to 1.00 M, whereas the viscosity of polymer solutions increased with increasing molecular weight and concentration (Figure D.2 and Table D.3). UV-visible absorption spectra

of monomer and polymers were recorded in acetonitrile at different concentrations and their molar absorption coefficients were determined (Figure D.3 and D.4). The similarity between the absorption spectra of the polymers and monomer (Figure D.4) suggests that there is minimal intrachain and interchain interaction between viologens in polymer solution.[23, 26] This interpretation is also supported by the electrochemical data shown below.

6.3 Electrochemical Characterization of RAPs 1-5

We chose a viologen-based macromolecular design[27-30] since the monomeric units have a small molecular footprint, are highly soluble in polar solvents, show appealing reduction potentials, and undergo facile electron transfer with chemical reversibility.[31, 32] This combination of properties makes them well-suited as low potential redox species in NRFBs as they promise high energy density, high stability during cycling and minimal electrode kinetics losses.

Transient voltammetry of 10 mM solutions of **RAPs 1-5**, shown in Figure 6.2a, 6.2b, was recorded in acetonitrile with 0.1 M $LiBF_4$ as a supporting electrolyte using a 1.15 mm radius Pt electrode. The shape of these voltammograms suggests a mixed adsorptive and diffusive behavior for all tested polymers. In general, two clearly defined reductive processes are observed at c.a. -0.7 V and -1.2 V vs. 0.1 M Ag^+/Ag. For comparison, the monomer exhibits two Nernstian waves at similar potentials and with similar separation between the first (2+/+) and second (+/0) reductions (Figure D.5). In addition to this similarity, the current intensities for different polymers at the same effective concentration of redox pendants are comparable and do not show a strong dependence on MW. These results suggest that viologen motifs do not interact electronically through the polymer backbone, in agreement with results from UV-Vis spectroscopy, and that the redox characteristics of **RAPs 1-5** are essentially the same as that displayed by the monomer.

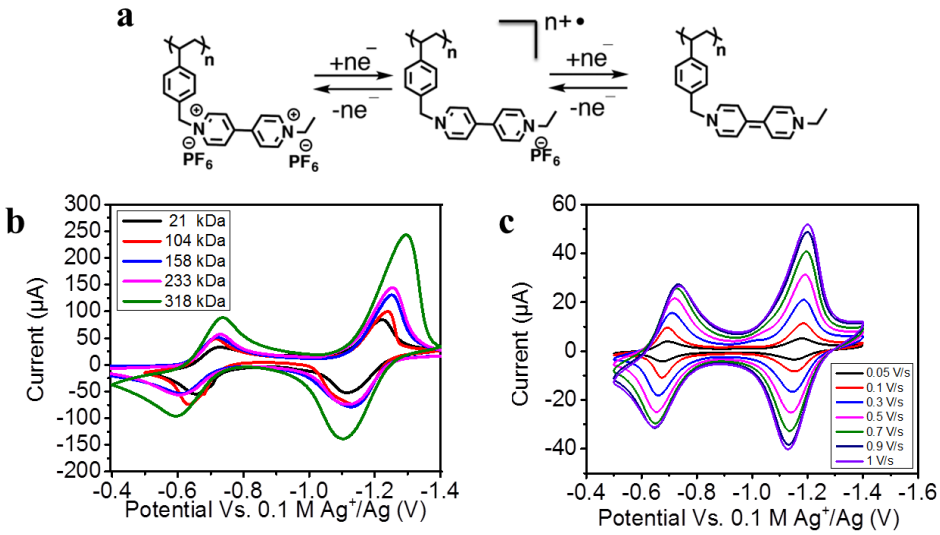

Figure 6.2 a, Two steps reduction reaction of RAP, showing the changes between viologen (2+/+) and viologen (+/0). a, Cyclic voltammograms of **RAPs 1-5** on 0.04 cm^2 Pt disk electrode (v = 100 mV/s). (b) Voltammetry of adsorbed **RAP 1** on 0.04 cm^2 Pt disk electrode in blank supporting electrolyte. In all experiments, RAP concentration was 0.01 M and 0.1 M LiBF4 in acetonitrile was used as supporting electrolyte solution.

In contrast to the monomer, adsorption is likely to be observed in **RAPs 1-5** because of a larger cross-section for interaction between the negatively charged electrode and the positively charged polymer as well as other physisorption interactions. Pt electrodes exposed to solutions containing **RAPs 1-5** were carefully rinsed and transferred to blank electrolyte to confirm irreversible adsorption. The resulting voltammograms displayed the behavior associated with an adsorbed electroactive layer, as shown in Figure 6.2c for **RAP 1**, where both reduction voltammetric peak currents increase proportionally to the scan rate (Figure D.6).[33, 34] The surface density of redox active groups was estimated to be ca. 100-200 μC/cm^2 for **RAP 1**, which is at least one order of magnitude larger than a conservative estimate of a monolayer based on the molecular footprint and loading of the polymer (10 μC/cm^2). Electrode surface roughness and

limited electrostatic interactions with the electrode are possible causes of multilayer formation. Electrochemical data show evidence of charge transport in this polymer layer. A smaller peak splitting and larger intensity observed for the +/0 process in comparison to the 2+/+ is consistent with a larger rate of self-exchange for the viologen +/0 redox couple as has been observed in other polymer films, including those based on viologen.[35, 36] Despite irreversible adsorption, the film formed by **RAPs 1-5** is electroactive and allows solution-based polymer molecules to engage in facile electron transfer and complete bulk reduction as demonstrated by microelectrode and chronocoulometric experiments described below.

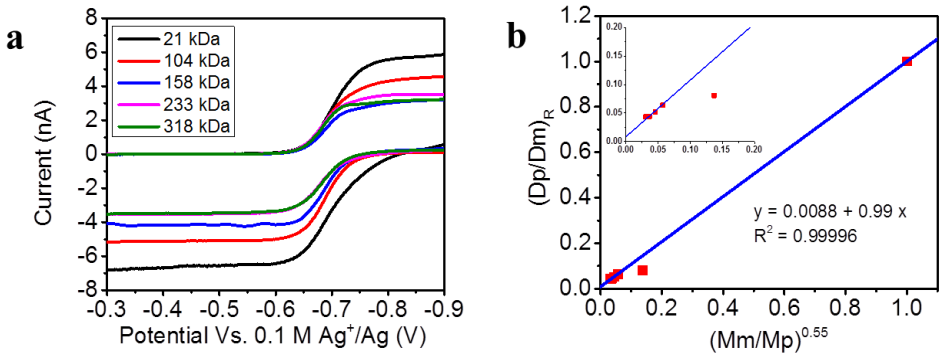

Figure 6.3 a, Steady state voltammograms of **RAPs 1-5** at 12.5 µm Pt UME (v= 10 mV/s) for the original and reduced form. b, Plot of monomer-normalized diffusion coefficient vs molecular weight for **RAPs 1-5**. Insert shows zoom of polymer high molecular weight region. In all experiments, RAP concentration was 0.01 M and 0.1 M LiBF4 in acetonitrile was used as supporting electrolyte solution.

Steady state voltammetry using ultra-microelectrodes (UMEs) were used to selectively study the diffusion behavior of **RAPs 1-5**. At small electrodes, the increase in the mass transfer coefficient of solution species masks the contribution from transient surface processes when voltammetry is conducted at low scan rates. Figure 6.3a shows the UME voltammetry at 10

mV/s for both the reduction of the fully-oxidized (2+) and for the oxidation of the singly-reduced (+) forms of **RAPs 1-5**. These voltammograms show a characteristic sigmoid shape and few indications of kinetic complications as evidenced by their width and correspondence between the position of the cathodic and anodic curves. Despite the possibility of radical-initiated reactions during the transformation of viologen 2+ to the monovalent radical anion +, the position and intensity of the oxidation and reduction waves indicate no profound chemical changes in the sample as the midway potentials, $E_{1/2}$, remains unchanged. Although the limiting current for the oxidation of the + form is consistently slightly higher than that for the reduction of 2+, the similarity between their values suggest a facile and quantitative transformation of either form at the electrode surface. The mass transfer limiting current is estimated as $i_{lim} = 4nFaDc^*$ where n =1, F = 96,485 C/mol, a = 12.5 μm, D is the apparent diffusion coefficient of viologen motifs and c^* is their concentration in the bulk. The diffusion coefficient of viologen groups in **RAPs 1-5** are deduced from i_{lim} for both original and reduced states. The diffusion coefficient values at concentrations below 10 mM are shown in Table 6.1. In general, smaller diffusion coefficients were observed as the molecular weight of the polymer increased. The ratio of the diffusion coefficient of polymer to monomer, D_p/D_m varies linearly with respect to the 0.55 power of the ratio of molecular weight of monomer and polymer, $(M_m/M_p)^{0.55}$, as plotted in Figure 6.3b for the + and Figure D.7 for the 2+ form. This behavior has been empirically observed for non-interacting redox centers in ferrocene redox polymers and explains the decrease in limiting current as a consequence of the impact of molecular weight on the diffusion coefficient following the behavior predicted by the Stokes-Einstein equation.[22] This result allows us to confidently estimate the diffusion coefficients shown in Table 6.1 and strongly suggests the non-

interacting and quantitative transformation of viologen groups in **RAPs 1-5** regardless of their size.

6.4 Charge storage in RAPs

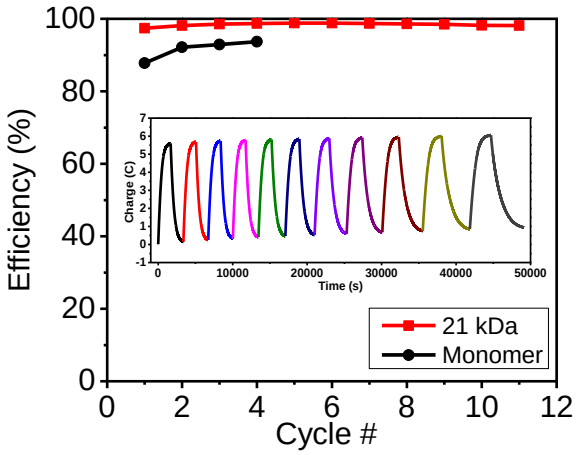

Figure 6.4 Charge storage properties of monomer and **RAP 1** (21 kDa). Inset shows 11 cycles of potential controlled bulk electrolysis of 6 mL 10 mM **RAP 1** in 0.1 M LiBF4 acetonitrile using a Pt mesh working electrode. Pt mesh was held at -0.9 V for BE reduction (2+/+) and at -0.3 V for BE oxidation (+/2+). The charge cycling efficiencies were calculated as the ratio of BE oxidation to BE reduction for each cycle.

RAPs 1-5 display excellent charge storage properties, which make them suitable for NRFBs. Figure 6.4 and its inset show results for the potential-controlled bulk electrolysis over multiple cycles for the 21 kDa polymer for the 2+/+ redox transformation. While there is a small decrease in the initial charge capacity (Table D.5) no further signal decrease attributable to decomposition is observed upon consecutive cycles. Preliminary UME experiments conducted on the reduced form of **RAPs 1-5** obtained by bulk electrolysis did show a decrease in their steady state current over a 2-4 hour period (Figure D.8), however NMR and UV-Vis spectrophotometry did not reveal strong evidence of sample decomposition. We believe that a

slow aggregation process of the reduced polymer molecules is responsible for this observation; however, this does not affect their charge storage capacity. Indeed, **RAP 1** displays a stable > 97% cycling efficiency throughout 11 cycles, which is higher than monomer efficiency (Figure 6.4) under the same experimental conditions. Bulk electrolysis experiments also showed that at least 94% of the nominal viologen loading on **RAPs 1-5** is accessed electrochemically, thus confirming the quantitative UME voltammetry results and strongly suggesting that solution-based RAPs are versatile charge storage media for NRFBs. Table 6.1 summarizes the result of our systematic electrochemical analysis of **RAP 1-5**.

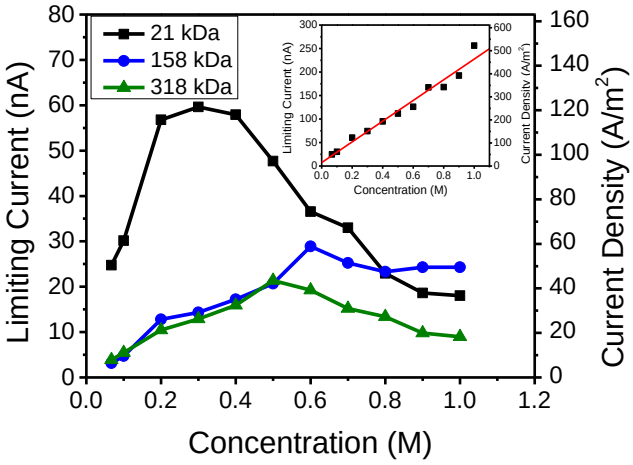

Figure 6.5 Diffusion limited steady-state current change of selected RAPs at high concentration obtained using a 12.5 μm Pt UME in 0.5 M LiBF4 as supporting electrolyte. Inset shows the expected limiting current for **RAP 1** if corrected for viscosity effects as shown in Figure D.2.

For applications in NRFBs, achieving a high concentration of charge storage material is crucial for attaining a practical charge capacity. All five polymers are highly soluble in acetonitrile and propylene carbonate. We tested samples with concentrations up to ~1 M. Using UME voltammetry to minimize solution resistive potential drop, the electrochemical activity of **RAP 1-5** was studied in the high concentration regime as shown in Figure 6.5. The diffusion

limited steady state current increased with the polymer concentration until reaching a certain maximum (0.3 M for 21 kDa, 0.6 M for 158 kDa, and 0.5 M for 318 kDa) and decreased at higher concentration. This behavior has been observed in highly concentrated solutions of organic species.[37, 38] We tested the hypothesis that this decrease was due to an increase in solution viscosity (Figure D.2) which in turn affected the diffusion coefficient. The inset of Figure 6.5 shows the prediction of the limiting current for **RAP 1** at the UME if the experimental limiting currents are corrected for the increase in viscosity using an analogue of Walden's rule (similar plots can be obtained for other RAPs, Figure D.9). The observed linearity in this plot suggests that even at the most concentrated solutions, similar electrode processes to those observed in dilute 10 mM solutions apply, despite the possibility of multiple intermolecular and ion migration effects at high concentrations.[37, 38] Likewise, it is noteworthy that the concentrated solutions remain highly electroactive and able to support a steady state current, both properties are highly desirable for NRFBs and that indicate a lack of observed solution decomposition and electrode fouling. On the other hand, the decrease in current might suggest that increasing the charge capacity and energy density of a solution by concentrating RAPs implies a trade-off in the power density if used in NRFBs.

Another strategy to increase the charge capacity of **RAPs 1-5** is to access the second reductive process. Preliminary experiments on **RAP 1** showed that bulk electrolysis from the 2+ directly to the 0 states results in a recovery of only about 61 % of theoretical charge (Figure D.10). Our laboratories are currently investigating ways to improve this charge utilization. While Figure 6.5 evidences complex interactions between the rheological and electrochemical properties of RAPs in solution, in practical terms, an attainable volumetric energy density of up

to 14 Ah/L as well as their electrochemical and chemical reversibility makes them suitable candidates for NRFBs.

6.5 Size-Based Selectivity of COTS Porous Separators

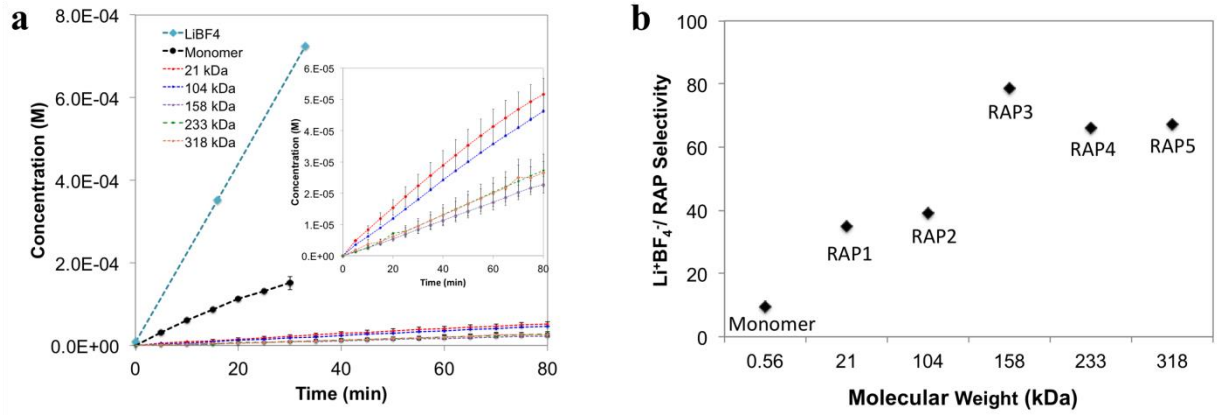

Figure 6.6 a, Time-dependent transport of LiBF4, monomer, and **RAPs 1-5** across Celgard 2325 at 0.01 M. Inset shows the **RAPs 1-5** region of the plot. b, Size-based selectivity of Celgard 2325 for $Li^{+}BF4^{-}$ compared to monomer and **RAPs 1-5**.

In the case of IEMs, the selectivity for ions is mainly due to their charge, whereas in porous separators the selectivity is based on size.[4, 39] To study the size-based selectivity of COTS porous separators for charge balancing ions compared to RAPs, permeability of LiBF4, monomer, and RAPs across porous separators was determined from time dependent transport studies (Figure 6.6a, Figure D.11). Time dependent transport across Celgard 2325 (pore radius = 14 nm) at 0.01 M was carried out using PermeGear Side-Bi-Side cell. The solution in the receiver cell was flowed through a cuvette and the absorbance at absorption maximum was recorded at regular intervals to determine the crossed over monomer and polymer concentrations.[4, 40] Time dependent transport of LiBF4 was determined from its conductance (Figure D.12). The initial linear region of the time dependent transport curves was used to

calculate the permeability of RAPs (see supporting information for details) and is reported in Table 6.1. LiBF4 showed a steep increase in concentration with time, indicating its faster transport across the separator compared to the monomer and RAPs. While permeability of LiBF4 (138.5 x 10^{-12} m^2/s) is only 9 times higher than that of the small molecule monomer, it is ca. 70 times higher than that of high MW RAPs (Figure 6.6b). For vanadium flow batteries, only 15 times higher selectivity was observed for proton permeation compared to Vanadium with porous separators;[15] the porous separators were modified with silica to increase the proton selectivity to 50 times.[18] Gratifyingly, for the high MW RAPs studied here, COTS porous separators show ca. 70 times higher selectivity for charge balancing ions ($Li^+BF_4^-$) compared to RAPs. This observation clearly demonstrates the advantage of using RAPs, instead of small molecules, as charge storage materials for size-selective transport in porous separators. RAPs also showed negligible adsorption on to the COTS porous separators (Table D.7).

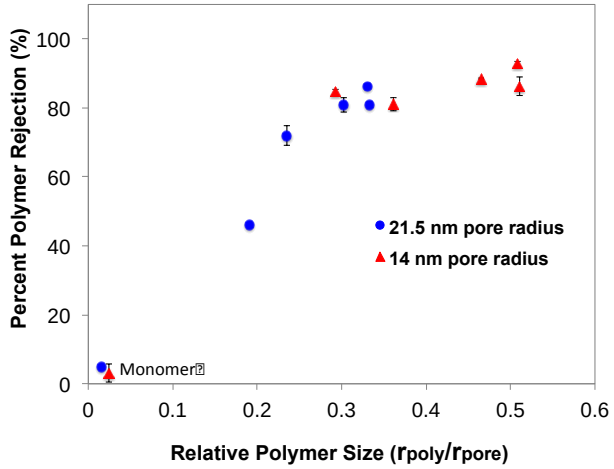

Figure 6.7 Relative polymer size dependent polymer rejection across COTS porous separators for **RAPs 1-5**.

We now turn to evaluate the impact of RAPs molecular weight on their transport properties across porous separators. For macromolecular transport across porous separators, the

steric partition coefficient i.e., the ratio of macromolecule concentration inside the pore and bulk solution, is known to play a key role in both size-exclusion chromatography and ultrafiltration.[41-48] Steric partition coefficient depends on the relative macromolecular size as defined by the size ratio of the macromolecule relative to the pore size. Theoretical models for linear polymers predict a decrease in steric partition coefficient with increase in relative polymer size; only 20% of polymers can access the pore volume for a relative polymer size of 0.33 and polymers are completely size excluded from entering the pore for relative sizes >0.6 (Figure D.13).[41, 43] Other factors such as hindrance to polymer diffusion inside the pores as well as the polymer shape and charge might also influence the polymer transport across porous separators.[48-51]

Relative polymer size (r_{poly}/r_{pore}) dependent RAPs rejection across COTS separators is shown in Figure 6.7 and Figure D.14. Polymer size (solvodynamic radius) was determined using Stokes-Einstein equation (Table D.6), and is shown in Table 6.1. Polymer size increased with increasing molecular weight up to 158 kDa and no significant change was observed with further increase in molecular weight. Relative polymer size of the RAPs increased up to 0.33 and 0.50 for larger (Celgard 2400, 21.5 nm pore radius) and smaller (Celgard 2325, 14 nm pore radius) pore size membranes respectively. As can be seen from Figure 6.7, the percent polymer rejection is seen to increase with increasing r_{poly}/r_{pore}. The percent polymer rejection increased rapidly until $r_{poly}/r_{pore\ of}$ 0.3 and then showed a gradual increase after that. The impact of relative polymer size on percent rejection is more apparent for 21 kDa (**RAP 1**) polymer. For larger pore radius membrane, **RAP 1** showed only 46% rejection while for smaller pore radius membrane ca. 85% rejection is obtained. ca. 80% polymer rejection is observed for all the RAPs as r_{poly}/r_{pore} approaches 0.3, which is in close accordance with the theoretically expected[41] steric exclusion for linear polymers across porous separators. We believe that the loss of conformational freedom

for polymers inside the pores even for the relative polymer sizes smaller than the pore size is the main reason for the observed steric hindrance involved in the size-based separation of RAPs across COTS porous membranes. Among all the studied RAPs, the higher molecular weight polymer **RAP 5** showed the highest percent polymer rejection (93%) across the smaller pore radius membrane. In the case of widely studied vanadium aqueous flow batteries with Nafion 115 as the separator, there is 12% crossover of vanadium and the crossover increases depending on the cell operating conditions.[52, 53] Polymer crossover of as low as 7% (93% rejection) is achieved with the RAPs studied here, which suggests that it is possible to realize high Coulombic efficiency using RAPs in conjunction with porous separators in flow batteries.

6.6 Charge-Discharge Property of Proxy Non-Aqueous Flow Cell

Given the low crossover observed for **RAP 5**, we tested preliminarily its charge/discharge performance in a proxy setup for a non-aqueous flow cell. This consisted of two stirred electrolyte compartments which sandwiched a Celgard 2325 separator. The open circuit voltage of the cell was 1.11 ± 0.05 V (three different cells) which was in good agreement with the 1.27 ± 0.05 V predicted from the initial state of charge of the **RAP 5** solution and a metal oxide auxiliary electrode. Electrolytic conductivity through the Celgard separator allowed the charge/discharge of this cell in LiBF4 electrolyte as shown in Figure 6.8 and 6.9, where stable operation over multiple cycles was observed at C/10 rate. The resulting curves displayed one monotonic and well-defined plateau on the first cycles, corresponding to the conversion of the viologen +/2+ redox pair, and stable operation in subsequent cycles. Furthermore, Figure D.15 and Table D.9 show that the Celgard separator retained its mechanical integrity and that the low crossover observed in the diffusion cell studies was maintained during prolonged periods of operation even for mixed solutions of viologen +/2+. This preliminary evaluation highlights the

potential for using the size-selective strategy enabled by COTS and RAP electrolytes in a practical redox flow cell.

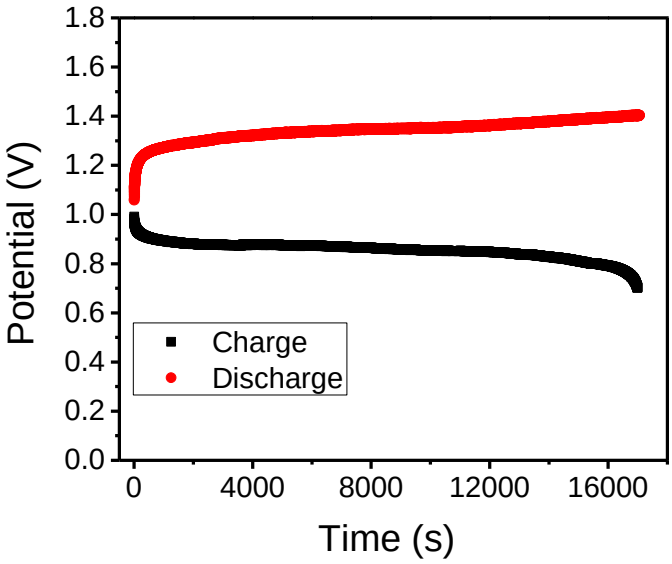

Figure 6.8 First discharge-charge properties of 10 mM RAP 5 in proxy flow cell system with NMC as cathode and Celgard 2325 as separator. Discharge capacity 44.0 %, charge capacity 44.2 %.

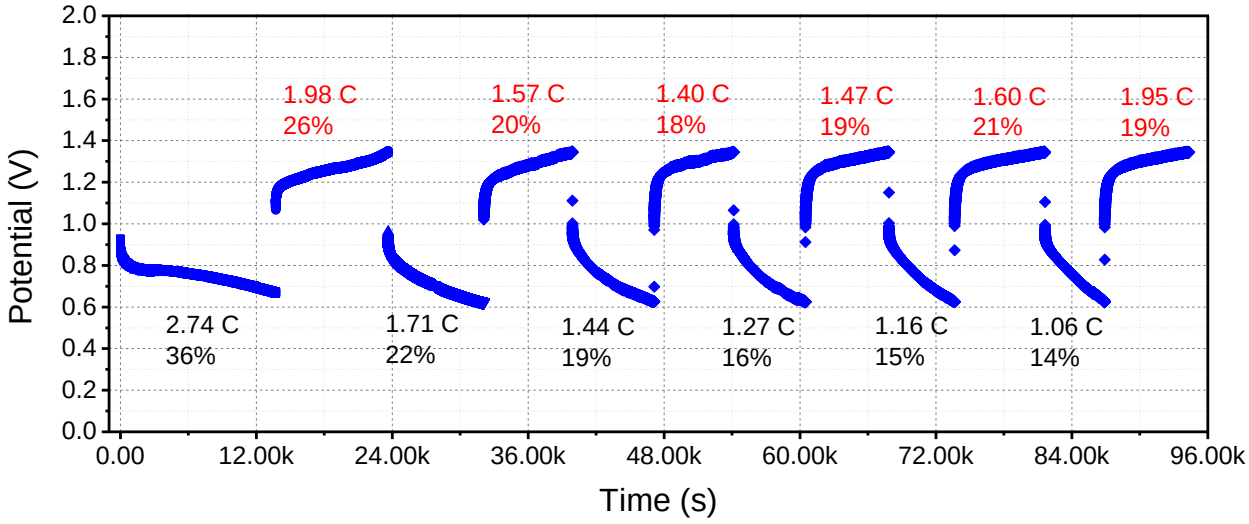

Figure 6.9 Multicycle test of charge-discharge properties 10 mM RAP 5 in proxy flow cell system with NMC as cathode and Celgard 2325 as separator. The absolute charges (C) and

(*Figure 6.9 Continued*) columbic efficiencies (%) of each individual segment are listed above, red for charging steps and black for discharging steps.

Complete rejection of the polymers can be realized with RAPs that have higher r_{poly}/r_{pore} values (>0.6). However, based on the electrochemical studies, it is shown that higher molecular weight polymers have low limiting current as shown in Figure 6.5. Thus, although high molecular weight RAPs offer higher rejection across the porous separators, there will be a trade-off in electrochemical properties such as limiting current. Other macromolecular architectures such as star, branched, and cyclic polymers will be very interesting to vary the relative polymer size and obtain higher polymer rejection without adversely impeding their electrochemical properties.

Table 6.1 Summary of electrochemical characterization and transport properties of **RAPs 1-5**.

Molecular weight (kDa)	Radius of RAPs (nm)	Diffusion coefficient of Original state (10^{-10} m^2/s)	Diffusion coefficient of Reduced state (10^{-10} m^2/s)	Rejection across celgard 2400 membrane	Rejection across celgard 2325 membrane	Permeability (10^{-12} m^2/s)	Percent electro-active units (%)
0.56	0.35	13.9	16.8	4.8±0.5	3.1±2.6	14.82±1.00	100
21	4.1	1.22	1.36	45.9±0.4	84.6±0.9	3.95±0.50	96
104	5.1	0.95	1.07	72.0±2.9	81.1±1.9	3.53±0.03	98
158	7.2	0.67	0.87	80.9±0.7	86.3±2.7	1.76±0.20	94
233	6.5	0.73	0.74	81.0±2.1	88.5±0.3	2.10±0.50	96
318	7.1	0.66	0.73	86.3±0.5	92.8±0.7	2.06±0.30	96

6.7 RAC Monolayer Fabrication

The characterization of synthesized RACs can be found in previous published article, including elemental analysis, UV-Vis absorption, and ATR-IR.[24] A prototype flow cell using RACs for redox active species revealed high reversibility with an average coulombic efficiency

of 94 ± 4 % over 11 cycles at C/20 (43 μA/cm^2).[24] Electrochemical performance of the cell was tracked by energy and voltage efficiencies, which were highly stable and above 90 %.[24]

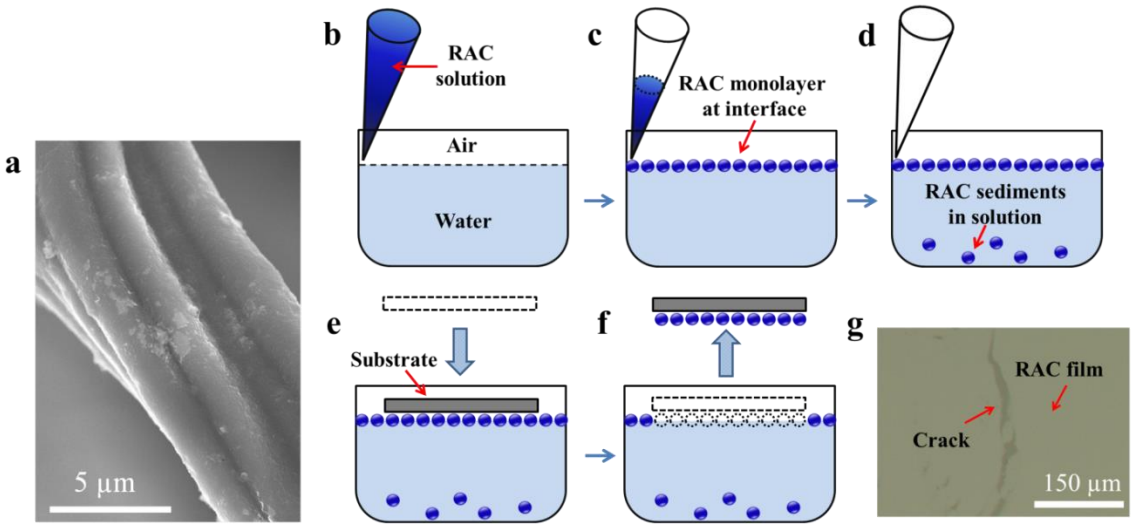

Figure 6.10 Fabrication procedure of RACs monolayer. a, Automatically packed **RAC 2** monolayer film on carbon fiber electrode during NRFBs operation. b–f, Schematic diagram of model RAC monolayer film fabrication, including slow injecting of RACs solution along glass trough wall to allow RACs accumulate at water-air interface (b–d) and picking up stabilized monolayer film *via* Langmuir-Schaefer method (e–f). g, Microscopic image of **RAC 1** monolayer on water surface.

During the flow cell operation, RACs tends to form a densely-packed monolayer film on the current collectors, as shown in Figure 6.10a. Thus understand the charge transport behavior on this RAC monolayer film would help us explore better flow cell operation conditions. In order to do so, we fabricated monolayer RACs on Au coated Si wafer as model substrate for systematic analysis. Three sizes of viologen RACs were produced and studied: **RACs 1-3** of particle diameters 80 ± 11, 135 ± 12, and 827 ± 71 nm, respectively. We used a water-air interface method to fabricate RAC monolayers. As shown in Figure 6.10b–c, slowly injecting 3 mg/mL

RACs MeCN stock solution on top of a water surface leads to accumulating of RACs film at water-air interface. The recess RACs are unable to pack at this interface and sink into water bath (Figure 6.10d). After overnight equilibration, RACs stabilized and form a densely-packed film on water surface, which can be easily picked up with Au substrate *via* Langmuir-Schaefer method (Figure 6.10e–f). Figure 6.10g is the microscope image of a RAC film formed on water surface with a crack in the middle for better contrast, which indicate the homogeneous distribution of RAC monolayer. This method applied only to smaller **RACs 1-2**. **RAC 3** used a similar method using Langmuir Trough to press and obtain the monolayer film.

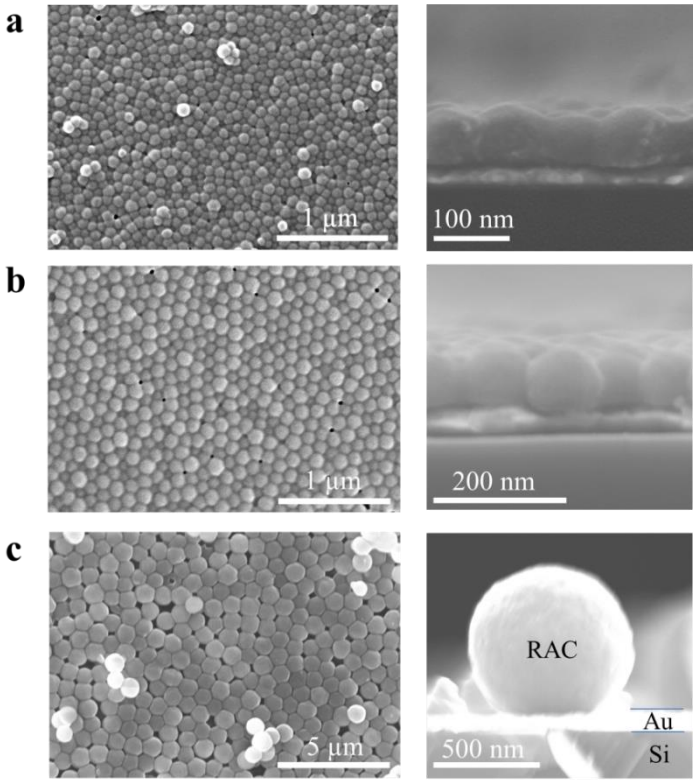

Figure 6.11 Top-view (left) and cross-sectional (right) SEM images of **RAC 1** (a), **RAC 2** (b), and **RAC 3** (c) monolayers on Au substrates.

The quality of RAC films were examined by SEM, as shown in Figure 6.11 for top-view and cross-sectional images of **RAC 1-3** monolayer on Au substrates. All RACs form densely-

packed monolayers with few small islands of 3-5 RAC particles on top (Figure 6.11 left). The cross-sectional images reveal the monolayer structure of **RACs 1-3** on Au substrates, each layer (RAC, Au, Si) can be clearly identified (Figure 6.11 right).

6.8 RAC Monolayer Reactivity

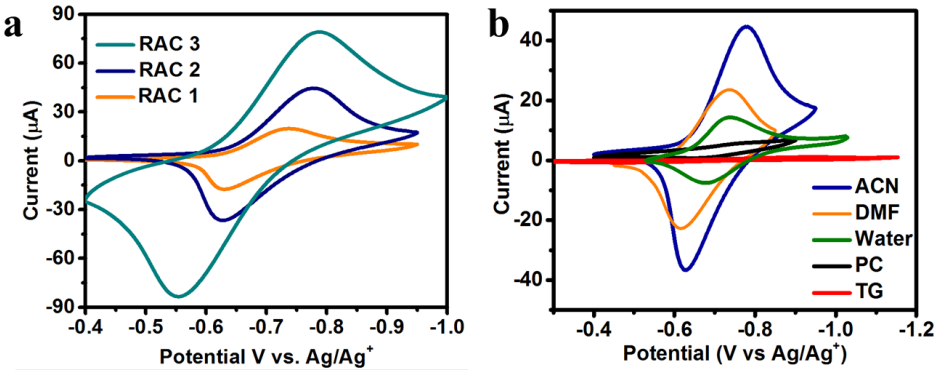

Figure 6.12 Electrochemical properties of RAC 1-3 monolayers. a, Cyclic voltammograms at 20 mV/s for each size RAC in 0.1 M $LiBF_4$ in acetonitrile. b, Solvent dependent cyclic voltammetry for **RAC 2** at 20 mV/s in 0.1 M $LiBF_4$ (organic solvents) and 0.1 M KCl (water). Solvents tested were acetonitrile (ACN), *N,N*-dimethylformamide (DMF), propylene carbonate (PC), tetraglyme (TG).

Well-ordered monolayers of RACs on Au allowed us to probe intra-particle charge transfer within their films using cyclic voltammetry (Figure 6.12a). Monolayer films allowed us to quickly probe the interactions of RACs with various organic solvents and water. CVs indicated marked differences in the charge accessibility as a function of solvent, as evidenced by the different peak heights in Figure 6.12b, despite similar initial RAC coverage and electrolyte concentration. We observed a correlation between peak height and the inverse of solvent viscosity. Viscosity strongly affects diffusion of the supporting electrolyte, suggesting that faster electrolyte transport into the RACs affects their electrochemical performance, although other

effects brought by the wettability towards different solvents might still contribute to the observed differences. Acetonitrile allowed the fastest access to charge into the film, thus comparisons of charge transfer among different RAC sizes are more suitable in this solvent.

The concentration of viologen in RAC monolayers, assuming that their thickness was equal to the particle diameter, was estimated by integrating the charge under the curve of a slow (5 mV/s) voltammogram. This estimation yielded 1.0 and 1.1 M for **RACs 1** and **2** respectively. This value is reasonable given that SEM and cross-sectional SEM analysis (Figure 6.11) indicated a similar packing density for all monolayers, and only small distortions in particle shape upon contact with the electrode. Furthermore, and despite the uncertainties due to swelling in electrolyte, these concentrations are close to the theoretically-estimated 2M based on the density of viologens (1.25 g/cm^3)[54] and volume of the RAC particle.

6.9 Materials and Methods

Materials and Experimental Techniques. Poly(vinylbenzyl ethyl viologen) polymers (**RAPs 1-5, Scheme 1**) of five different molecular weights (M_n = 21, 104, 158, 233, and 318 kDa) were synthesized starting from poly(vinylbenzyl chloride) (PVBC). Typical synthesis of RAPs involved heating a mixture of PVBC and ethyl viologen in dimethyl formamide, followed by anion exchange with ammonium hexafluorophosphate. The resultant polymers were isolated and purified via precipitation. Quantitative functionalization of poly(vinyl benzylchloride) with ethyl viologen was confirmed by ^{1}H NMR, ATR-IR, UV-Vis absorption spectra and elemental analyses (see Supporting information). PVBC of MW = 5.3 kDa, 60 kDa, and 82 kDa were purchased from Polymer Source. The 27 kDa and 41 kDa PVBC polymers were synthesized using Reversible Addition-Fragmentation Chain-Transfer (RAFT) polymerization.[55] The corresponding viologen monomer was also synthesized for comparison (Scheme 1).

RAPs 1-5 were characterized using ^{1}H NMR, ATR-IR, and elemental analysis. The viscosities of the **RAPs 1-5** were measured using parallel plate rheometry at different concentrations from 0.01 to 1.0 M in acetonitrile. UV-Vis absorption spectra were recorded in acetonitrile at different concentrations to determine the molar absorption coefficient of the polymers. For all the studies, polymer concentration is defined as moles of repeat unit per liter. Polymer transport measurements across porous COTS separators were carried out at 0.01 M using PermeGear Side-Bi-Side cell in which the separator was sandwiched between the donor cell (containing polymer solution) and receiver cell (containing acetonitrile).[4] Both solutions were stirred for 24 h to allow the polymer to crossover into the receiver compartment. After 24 h, the concentration of RAP in the receiver cell was determined using UV-Vis absorption spectroscopy, and the percent polymer rejection was calculated (see supporting information for details). The diffusion of LiBF4 under similar conditions was determined from its conductance.

Functionalized RACs (**RACs 1-3**) were prepared from crosslinked colloidal poly(vinylbenzyl chloride) (**xPVBC**) and respective pendants ethyl viologen (**RACs 1-3**). Functionalization involved heating **xPVBC** with the pendant monomer precursor in a mixture of dimethylformamide and tetrahydrofuran followed by purification via centrifugation. Three sizes of viologen RACs were produced and studied: **RACs 1-3** of particle diameters 80 ± 11, 135 ± 12, and 827 ± 71 nm, respectively as confirmed by scanning electron microscopy (SEM) in the dry state from the average of 50 particles. Crosslinked **xPVBC** of varying diameters were synthesized by redox-initiated emulsion polymerization[56] or dispersion polymerization[57] depending on the desired colloid diameter.

Electrochemical methods. All electrochemical experiments were performed on a CHI920D potentiostat and inside of an Ar-filled drybox with stringent control of O2 and

moisture levels. All chemical reagents, except for synthesized RAPs, were purchased from Sigma-Aldrich from the highest available purity and used as received. Unless specified, all voltammetric and bulk electrolysis experiments were carried out using a standard three electrode configuration with either a large-area Pt mesh (bulk electrolysis), 12.5 μm radius Pt ultra-micro electrode (UME), or 1.15 mm radius Pt disk electrode (transient voltammetry) as the working electrode, a non-aqueous Ag/Ag^+ reference electrode (CHI112, 0.1 M AgNO3 in acetonitrile solution) and a graphite rod as counter electrode. Most experiments were carried out in a 3-chamber electrochemical cell with 1.6 μm glass frits. The transient voltammetry of viologen polymers was tested with a 10 mM effective concentration of repeating units for all **RAPs 1-5** in 0.1 M LiBF4 in acetonitrile as supporting electrolyte and using a 1.15 mm Pt disk as working electrode. Multiple scan cycles were performed until an adsorbed film of the RAP was deposited and stable. After rinsing several times with acetonitrile, Pt disk electrodes were immersed into blank 0.1 M LiBF4 in acetonitrile electrolyte to test RAP adsorption at different scan rates.

RAC monolayers for transient voltammetry were prepared by water-air interface methods onto Au substrates fabricated by e-beam evaporation on Si/SiO_2 substrates (see Supporting Information). Prepared monolayer substrates were then used as working electrodes for transient voltammetry. Circular area (3 mm radius) of the substrate was exposed to supporting electrolyte (0.1 M $LiBF_4$) on a home-made substrate holder.

RACs monolayer fabrication. 3 mg/mL solutions of **RACs 1-3** in acetonitrile were prepared and dispersed by sonication for 15 minutes before use as a stock solution. The smooth Au substrates were fabricated via E-beam evaporation with 5 nm Ti adhesion layer and 50 nm Au on Si wafer at a slow evaporation rate of 0.1 - 0.2 Å/s. Water-air interface method was applied to fabricate monolayer films of 80 nm and 135 nm VioRACs, as shown in Figure 6.10 b–f. A glass

trough (22 mm diameter) was cleaned with Nochromix and blow-dried with Ar. 40 μL of stock solution was slowly injected along glass side wall and spread on the surface of deionized water. A microscope slide was used to cover the trough and let film equilibrate overnight. The self-assembled RACs film floated onto the deionized water surface. Langmuir-Schaefer method was applied to transfer monolayer film to Au substrate. Water-air interface method did not successfully translate to the larger RAC 3 since it always forms low density film. Langmuir-Blodgett (LB) Film Trough (NIMA 311D) was used to apply constant pressure to condense RAC 3 film. 1 mL stock solution was slowly spread on the surface of deionized water inside compressing barrier. By slowly approaching the barrier of LB trough and holding constant pressure at 55 mN/m, the RAC 3 monolayer film was formed on water surface. Langmuir-Schaefer methods was applied to transfer monolayer film to Au substrate.

6.10 Conclusion

We have shown that size-based selective transport of supporting electrolyte ($Li^+BF_4^-$) across COTS porous separators is attainable by controlling the size of the charge storage material. Viologen-based redox active polymers **RAP 1-5** of molecular weight between 21-318 kDa were synthesized to vary the size of the charge storage materi-al. The molecular weight dependent RAPs electrochemical properties and transport across porous separators were studied. Although transient voltammetry showed the presence of multilayer RAP adsorption on Pt electrodes from low concentration solutions of **RAPs 1-5** (10 mM), ultra-microelectrode voltammetry revealed facile electron transfer with E1/2 ~ -0.7 V vs. Ag/Ag^+ for the viologen 2+/+ reduction at concentrations as high as 1.0 M in acetonitrile. Controlled potential bulk electrolysis indicates that 94-99% of the nominal charge on different RAPs is accessible and the electrolysis products are stable upon cycling**.** While at high concentration the limiting current of

RAPs in solution is decreased due to a concurrent increase in solution viscosity, **RAPs 1-5** preserve most of the desirable electrochemical properties of the originating viologen-based monomer such as high solubility, similar redox potential, and their electrochemical and chemical reversibility. This makes them suitable candidates for low potential species in NRFBs.

Selectivity for $Li^+BF_4^-$ transport across COTS porous separators increased significantly by changing the charge storage material from small molecule monomer (9 times) to redox active polymers (ca. 70 times). The percent polymer rejection across the COTS separator increased with increase in RAP molecular weight, as well as reduction in pore size. Polymer crossover of as low as 7% (93% rejection) was achieved with the RAPs studied here.

As for advanced 3D RACs architecture, we successfully fabricated model monolayer RAC films on Au substrate. Those monolayers have shown solvent sensitive charge accessibility, which arise from the differential supporting electrolyte diffusion in different solvent viscosities. All RACs yielded a high load of active pendent of more than 1 M concentration with particles.

Our systematic studies show a complex relationship between polymer molecular weight and electrochemical, rheological and transport properties. Nonetheless, they establish the feasibility of the size-selective separator approach aided by redox active polymers to explore new prospects in NRFBs. We preliminarily showed that this combination of elements can lead to an operating cell with adequate performance and substantially decreased redox active component crossover. We are currently exploring other highly soluble redox active components as well as other macromolecular architectures such as star, branched, and cyclic polymers that will be of interest for tuning polymer size, transport and electrochemical properties for enhanced NRFB performance.

6.11 References

1. Brushett, F. R.; Vaughey, J. T.; Jansen, A. N. An All-Organic Non-aqueous Lithium-Ion Redox Flow Battery. *Advanced Energy Materials* **2012**, *2*, 1390-1396.

2. de Leon, C. P.; Frias-Ferrer, A.; Gonzalez-Garcia, J.; Szanto, D. A.; Walsh, F. C. Redox flow cells for energy conversion. *Journal of Power Sources* **2006**, *160*, 716-732.

3. Weber, A. Z.; Mench, M. M.; Meyers, J. P.; Ross, P. N.; Gostick, J. T.; Liu, Q. Redox flow batteries: a review. *Journal of Applied Electrochemistry* **2011**, *41*, 1137-1164.

4. Shin, S.-H.; Yun, S.-H.; Moon, S.-H. A review of current developments in non-aqueous redox flow batteries: characterization of their membranes for design perspective. *Rsc Advances* **2013**, *3*, 9095-9116.

5. Alotto, P.; Guarnieri, M.; Moro, F. Redox flow batteries for the storage of renewable energy: A review. *Renewable & Sustainable Energy Reviews* **2014**, *29*, 325-335.

6. Darling, R. M.; Gallagher, K. G.; Kowalski, J. A.; Ha, S.; Brushett, F. R. *Manuscript Submitted* **2014**.

7. Wang, Y.; He, P.; Zhou, H. Li-Redox Flow Batteries Based on Hybrid Electrolytes: At the Cross Road between Li-ion and Redox Flow Batteries. *Advanced Energy Materials* **2012**, *2*, 770-779.

8. Prifti, H.; Parasuraman, A.; Winardi, S.; Lim, T. M.; Skyllas-Kazacos, M. Membranes for Redox Flow Battery Applications. *Membranes* **2012**, *2*, 275-306.

9. Leung, P.; Li, X.; Ponce de Leon, C.; Berlouis, L.; Low, C. T. J.; Walsh, F. C. Progress in redox flow batteries, remaining challenges and their applications in energy storage. *RSC Advances* **2012**, *2*, 10125-10156.

10. Wang, W.; Luo, Q. T.; Li, B.; Wei, X. L.; Li, L. Y.; Yang, Z. G. Recent Progress in Redox Flow Battery Research and Development. *Adv Funct Mater* **2013**, *23*, 970-986.

11. Skyllas-Kazacos, M.; Chakrabarti, M. H.; Hajimolana, S. A.; Mjalli, F. S.; Saleem, M. Progress in Flow Battery Research and Development. *J Electrochem Soc* **2011**, *158*, R55-R79.

12. Wei, X.; Nie, Z.; Luo, Q.; Li, B.; Sprenkle, V.; Wang, W. Polyvinyl Chloride/Silica Nanoporous Composite Separator for All-Vanadium Redox Flow Battery Applications. *J Electrochem Soc* **2013**, *160*, A1215-A1218.

13. Arora, P.; Zhang, Z. M. Battery separators. *Chemical Reviews* **2004**, *104*, 4419-4462.

14. Belanger, S.; Stevenson, K. J.; Mudakha, S. A.; Hupp, J. T. Perfect electrochemical molecular sieving by thin and ultrathin metallopolymeric films (vol 15, pg 837, 1999). *Langmuir* **1999**, *15*, 900-900.

15. Zhang, H.; Zhang, H.; Li, X.; Mai, Z.; Zhang, J. Nanofiltration (NF) membranes: the next generation separators for all vanadium redox flow batteries (VRBs)? *Energy & Environmental Science* **2011**, *4*, 1676-1679.

16. Li, B.; Luo, Q.; Wei, X.; Nie, Z.; Thomsen, E.; Chen, B.; Sprenkle, V.; Wang, W. Capacity decay mechanism of microporous separator-based all-vanadium redox flow batteries and its recovery. *ChemSusChem* **2014**, *7*, 577-584.

17. Wei, W.; Zhang, H.; Li, X.; Zhang, H.; Li, Y.; Vankelecom, I. Hydrophobic asymetric ultrafiltration PVDF membranes: an alternative separator for VFB with excellent stability. *Phys. Chem. Chem. Phys.* **2013**, *2013*, 1766-1771.

18. Zhang, H.; Zhang, H.; Li, X.; Mai, Z.; Wei, W. Silica modified nanofiltration membranes with improved selectivity for redox flow battery application. *Energy & Environmental Science* **2012**, *5*, 6299-6303.

19. Yang, R.; Xu, Z.; Yang, S.; Michos, I.; Li, L.-F.; Angelopoulos, A. P.; Dong, J. Nonionic zeolite membrane as potential ion separator in redox-flow battery. *Journal of Membrane Science* **2013**, *450*, 12-17.

20. Zhang, H.; Zhang, H.; Zhang, F.; Li, X.; Li, Y.; Vankelecom, I. Advanced charged membranes with highly symmetric spongy structures for vanadium flow battery application. *Energy & Environmental Science* **2013**, *2013*, 776-781.

21. Smith, T. W.; Kuder, J. E.; Wychick, D. VOLTAMMETRIC BEHAVIOR OF POLY(VINYLFERROCENE). *Journal of Polymer Science Part A: Polymer Chemistry* **1976**, *14*, 2433-2448.

22. Flanagan, J. B.; Margel, S.; Bard, A. J.; Anson, F. C. ELECTRON-TRANSFER TO AND FROM MOLECULES CONTAINING MULTIPLE, NONINTERACTING REDOX CENTERS - ELECTROCHEMICAL OXIDATION OF POLY(VINYLFERROCENE). *Journal of the American Chemical Society* **1978**, *100*, 4248-4253.

23. Saji, T.; Pasch, N. F.; Webber, S. E.; Bard, A. J. ELECTROCHEMICAL BEHAVIOR OF POLYMERS IN APROTIC MEDIA .1. POLYVINYLNAPHTHALENE AND POLYVINYLANTHRACENE. *Journal of Physical Chemistry* **1978**, *82*, 1101-1105.

24. Montoto, E. C.; Nagarjuna, G.; Hui, J. S.; Burgess, M.; Sekerak, N. M.; Hernandez-Burgos, K.; Wei, T. S.; Kneer, M.; Grolman, J.; Cheng, K. J.; Lewis, J. A.; Moore, J. S.;

Rodriguez-Lopez, J. Redox Active Colloids as Discrete Energy Storage Carriers. *Journal of the American Chemical Society* **2016**, *138*, 13230-13237.

25. Druta, I.; Avram, E.; Cozan, V. Polymers with pendent functional groups IV. The reaction of chloromethylated polystyrene with N-phenacyl-4,4 '-bipyridinium bromides. *European Polymer Journal* **2000**, *36*, 221-224.

26. Vala, M. T.; Haebig, J.; Rice, S. A. Experimental Study of Luminescence and Excitation Trapping in Vinyl Polymers, Paracyclophanes, and Related Compounds. *Journal of Chemical Physics* **1965**, *43*, 886-897.

27. Heinen, S.; Walder, L. Generation-dependent intramolecular CT complexation in a dendrimer electron sponge consisting of a viologen skeleton. *Angewandte Chemie International Edition* **2000**, *39*, 806-809.

28. Baker, W. S.; Lemon, B. I.; Crooks, R. M. Electrochemical and Spectroscopic Characterization of Viologen-Functionalized Poly(Amidoamine) Dendrimers†. *The Journal of Physical Chemistry B* **2001**, *105*, 8885-8894.

29. Marchioni, F.; Venturi, M.; Ceroni, P.; Balzani, V.; Belohradsky, M.; Elizarov, A. M.; Tseng, H.-R.; Stoddart, J. F. Complete Charge Pooling is Prevented in Viologen-Based Dendrimers by Self-Protection. *Chemistry – A European Journal* **2004**, *10*, 6361-6368.

30. Palmore, G. T. R.; Smith, D. K.; Wrighton, M. S. pH-Dependent Rectification in Redox Polymers: Characterization of Electrode-Confined Siloxane Polymers Containing Naphthoquinone and Benzylviologen Subunits. *The Journal of Physical Chemistry B* **1997**, *101*, 2437-2450.

31. Bird, C. L.; Kuhn, A. T. Electrochemistry of the Viologens. *Chemical Society Reviews* **1981**, *10*, 49-82.

32. Rodríguez-López, J.; Minguzzi, A.; Bard, A. J. Reaction of Various Reductants with Oxide Films on Pt Electrodes As Studied by the Surface Interrogation Mode of Scanning Electrochemical Microscopy (SI-SECM): Possible Validity of a Marcus Relationship. *The Journal of Physical Chemistry C* **2010**, *114*, 18645-18655.

33. Wopschal.Rh; Shain, I. Effects of Adsorption of Electroactive Species in Stationary Electrode Polarography. *Anal Chem* **1967**, *39*, 1514-1527.

34. Laviron, E. General expression of the linear potential sweep voltammogram in the case of diffusionless electrochemical systems. *Journal of Electroanalytical Chemistry and Interfacial Electrochemistry* **1979**, *101*, 19-28.

35. Dalton, E. F.; Murray, R. W. Viologen(2+/1+) and viologen(1+/0) electron-self-exchange reactions in a redox polymer. *Journal of Physical Chemistry* **1991**, *95*, 6383-6389.

36. Buttry, D. A.; Anson, F. C. Effects of Electron Exchange and Single-File Diffusion on Charge Propagation in Nafion Films Containing Redox Couples. *Journal of the American Chemical Society* **1983**, *105*, 685-689.

37. Paulson, S. C.; Okerlund, N. D.; White, H. S. Diffusion currents in concentrated redox solutions. *Anal Chem* **1996**, *68*, 581-584.

38. Ragsdale, S. R.; White, H. S. Analysis of voltammetric currents in concentrated organic redox solutions using the Cullinan-Vignes equation and activity-corrected mutual diffusion coefficients. *Journal of Electroanalytical Chemistry* **1997**, *432*, 199-203.

39. Schwenzer, B.; Zhang, J.; Kim, S.; Li, L.; Liu, J.; Yang, Z. Membrane Development for Vanadium Redox Flow Batteries. *Chemsuschem* **2011**, *4*, 1388-1406.

40. Mai, Z.; Zhang, H.; Li, X.; Bi, C.; Dai, H. Sulfonated poly(tetramethydiphenyl ether ether ketone) membranes for vanadium redox flow battery application. *Journal of Power Sources* **2011**, *196*, 482-487.

41. Casassa, E. F. Equilibrium distribution of flexible polymer chains between a macroscopic solution phase and small voids. *Journal of Polymer Science Part C-Polymer Letters* **1967**, *5*, 773-778.

42. Degoulet, C.; Busnel, J. P.; Tassin, J. F. Study of the steric partition coefficient in size-exclusion chromatography by Monte Carlo simulation. *Polymer* **1994**, *35*, 1957-1962.

43. Renkin, E. M. Filtration, diffusion, and molecular sieving through porous cellulose membranes. *Journal of General Physiology* **1954**, *38*, 225-243.

44. Meireles, M.; Bessieres, A.; Rogissart, I.; Aimar, P.; Sanchez, V. An appropriate molecular size parameter for porous membranes calibration. *Journal of Membrane Science* **1995**, *103*, 105-115.

45. Wang, Y.; Teraoka, I.; Hansen, F. Y.; Peters, G. H.; Hassager, O. A Theoretical Study of the Separation Principle in Size Exclusion Chromatography. *Macromolecules* **2010**, *43*, 1651-1659.

46. Phillip, W. A.; Amendt, M.; O'Neill, B.; Chen, L.; Hillmyer, M. A.; Cussler, E. L. Diffusion and Flow Across Nanoporous Polydicyclopentadiene-Based Membranes. *Acs Applied Materials & Interfaces* **2009**, *1*, 472-480.

47. Silva, V.; Pradanos, P.; Palacio, L.; Hernandez, A. Alternative pore hindrance factors: What one should be used for nanofiltration modelization? *Desalination* **2009**, *245*, 606-613.

48. Haraldsson, B.; Nystrom, J.; Deen, W. M. Properties of the glomerular barrier and mechanisms of proteinuria. *Physiol Rev* **2008**, *88*, 451-487.

49. Deen, W. M. Hindered transport of large molecules in liquid-filled pores. *Aiche Journal* **1987**, *33*, 1409-1425.

50. Casassa, E. F.; Tagami, Y. An Equilibrium Theory for Exclusion Chromatography of Branched and Linear Polymer Chains. *Macromolecules* **1969**, *2*, 14-26.

51. Bohrer, M. P.; Deen, W. M.; Robertson, C. R.; Troy, J. L.; Brenner, B. M. Influence of molecular configuration on the passage of macromolecules across the glomerular capillary wall. *Journal of General Physiology* **1979**, *74*, 583-593.

52. Sun, C.; Chen, J.; Zhang, H.; Han, X.; Luo, Q. Investigations on transfer of water and vanadium ions across Nafion membrane in an operating vanadium redox flow battery. *Journal of Power Sources* **2010**, *195*, 890-897.

53. Jia, C.; Liu, J.; Yan, C. A significantly improved membrane for vanadium redox flow battery. *Journal of Power Sources* **2010**, *195*, 4380-4383.

54. CRC Handbook of Pesticides. Milne, G. W. A., Ed. CRC Press: Boca Raton, 1995.

55. Moraes, J.; Ohno, K.; Gody, G.; Maschmeyer, T.; Perrier, S. The synthesis of well-defined poly(vinylbenzyl chloride)-grafted nanoparticles via RAFT polymerization. *Bielstein Journal of Organic Chemistry* **2013**, *9*, 1226-1234.

56. Chonde, Y.; Liu, L. J.; Krieger, I. M. Preparation and Surface Modification of Poly(vinylbenzyl chloride) Lattices. *J. App. Polym. Sci.* **1980**, *25*, 2407-2416.

57. Margel, S.; Nov, E.; Fisher, I. Polychloromethylstyrene Microspheres - Synthesis and Characterization. *J. Polym. Sci. A Polym. Chem.* **1991**, *29*, 347-355.

APPENDIX A

SUPPLEMENTARY INFORMATION OF CHAPTER 3

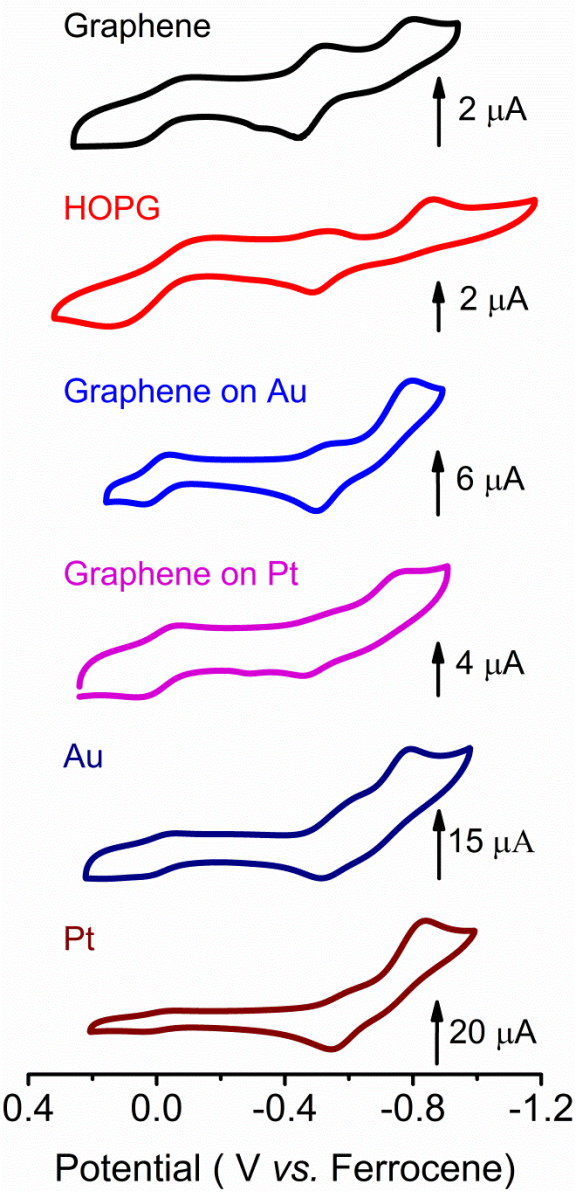

Figure A.1 FeOEP adsorption behavior on various substrates. Small amounts of 1 mM FeOEP solution were spiked into blank solution. Ferrocene was used as an internal standard. In the CV of FeOEP on graphene (top trace, black), the peaks around 0 V correspond to ferrocene, the peak at -0.53 V is the reduction of adsorbed FeOEP on graphene, the peak at -0.80 V relates to the

(*Figure A.1 Continued*) reduction of FeOEP in solution, the peak at -0.70 V is the oxidation of surface-confined FeOEP, and the peak around -0.40 V can be attributed to the oxidation of FeOEP in solution. The other CV traces exhibit peaks at similar potentials for each species. The 1 mL 0.1 M $LiBF_4$ acetonitrile blank solution was spiked with 8, 4, 8, 16, 16, 10 μL of 1 mM FeOEP THF solution for graphene, HOPG, graphene/Au, graphene/Pt, Au, and Pt samples, respectively.

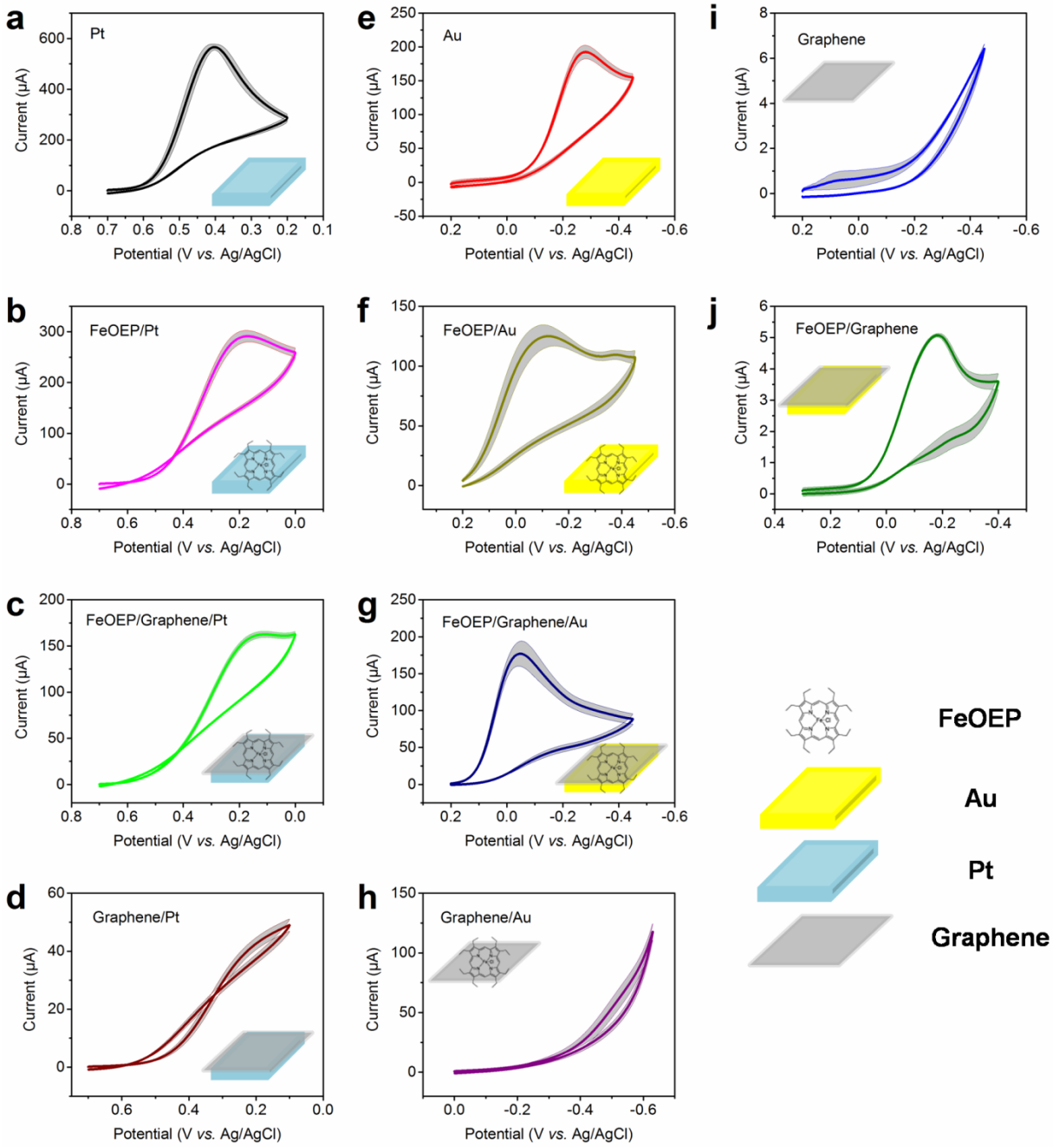

Figure A.2 CVs of ORR at the various electrode combinations used in Figure 3.8d in the main text. All data were collected with a scan rate of 0.1 V s^{-1} in solution consisting of 10 mM H_2SO_4 and 0.1 M Na_2SO_4 in O_2-saturated water. Gray zones indicate the standard deviation of at least 6 CVs.

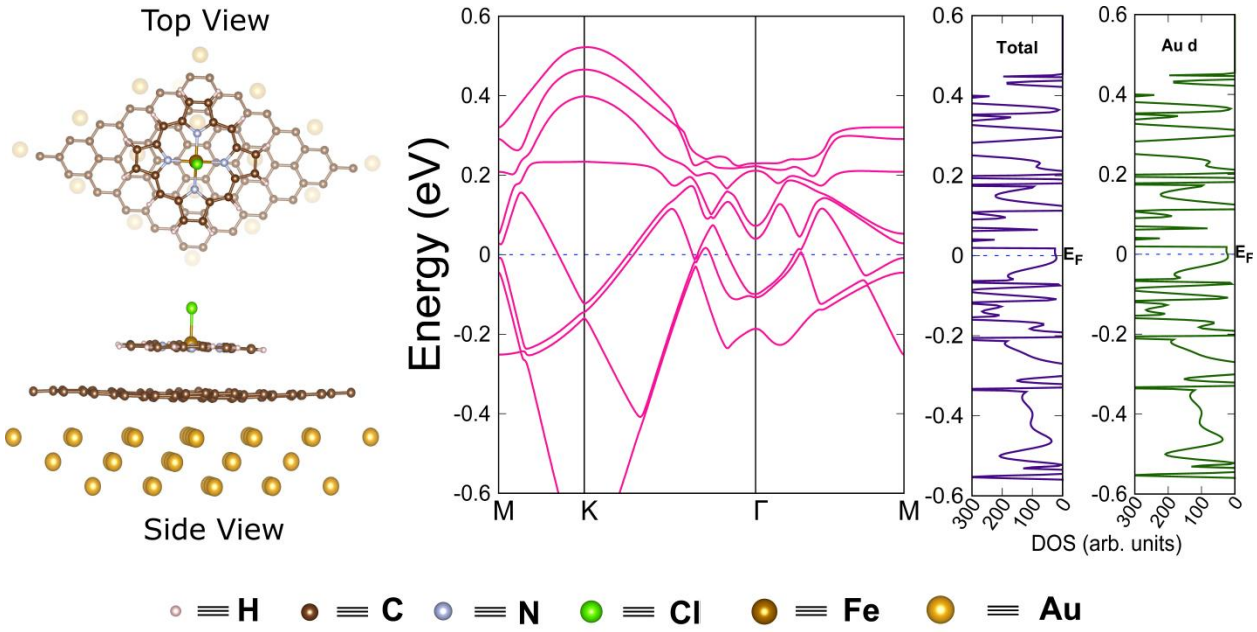

Figure A.3 Electronic structure and electronic properties (band structures and density of states (DOSs), and projected DOSs for Au d-subshell electrons from left to right) of the FeOEP/graphene/Au materials.

APPENDIX B

SUPPLEMENTARY INFORMATION OF CHAPTER 4

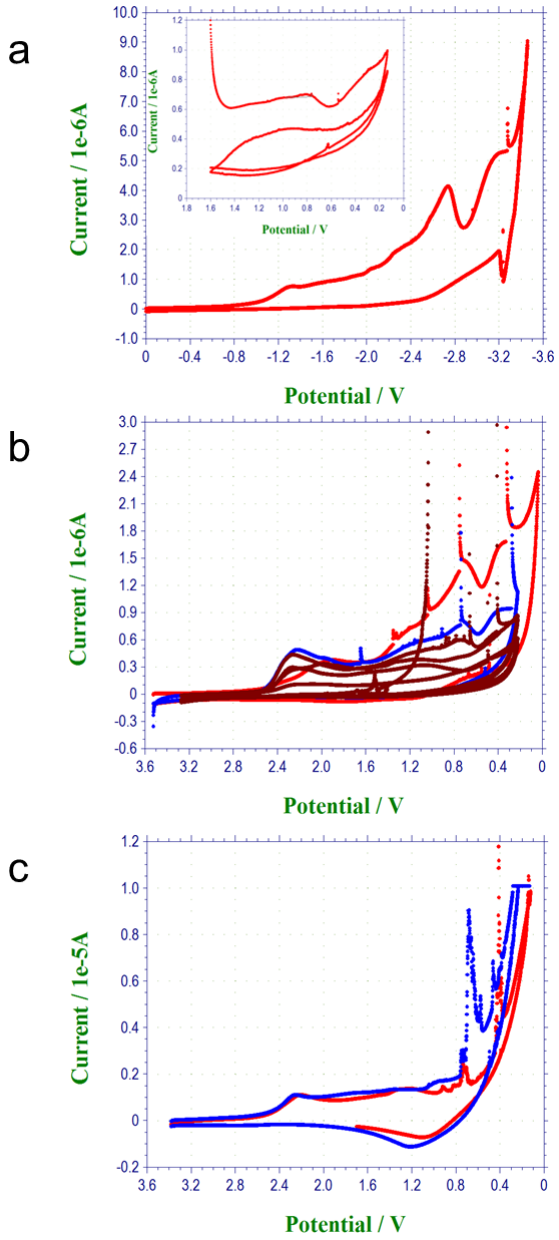

Figure B.1 Cyclic voltammograms of unpatterned carbon samples. a, Bilayer graphene, insert Figure is smaller scale scan after 3 cycles to verify no existence of intercalation peak. b, Four layer graphene. c, HOPG. Test condition: 0.1 M LiBF4 in 50:50 ratio PC/EC, electrode area was 4.9 mm^2.

B.1 Calculation of De-intercalation Charge and Theoretical Charge for FLG

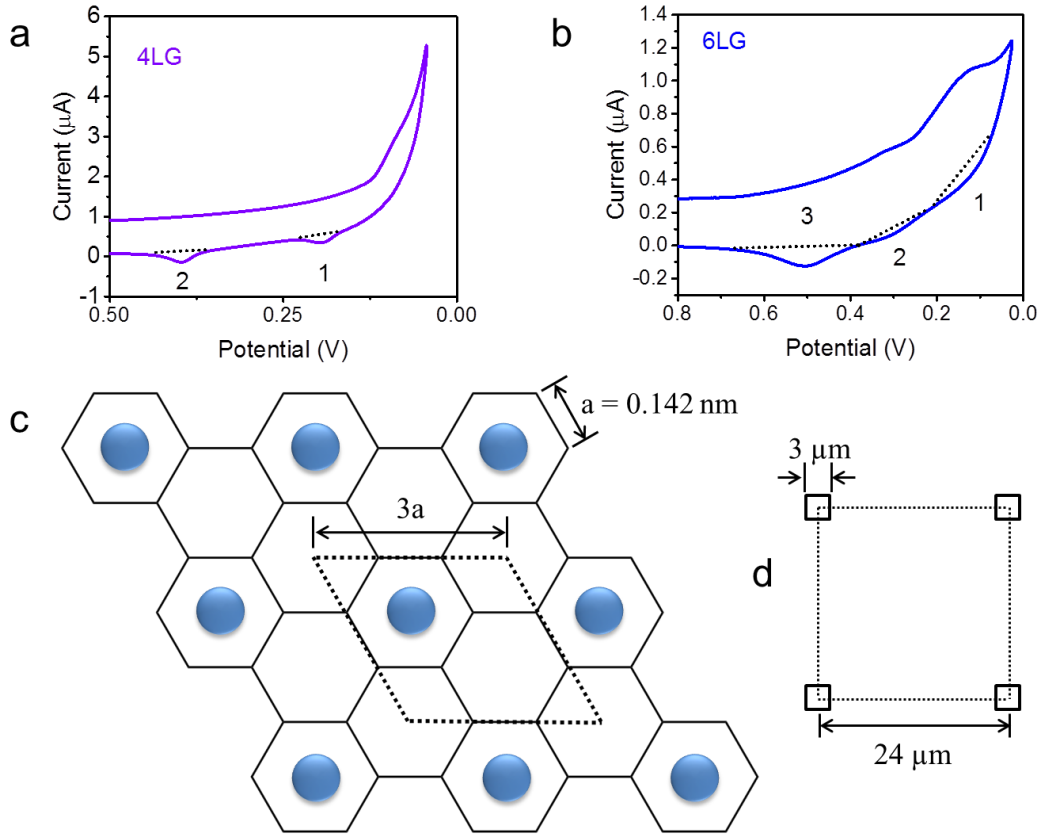

Figure B.2 Integration baselines of de-intercalation charge for 4LG (a) and 6LG (b). c, crystal structure of LiC_6 – stage 1. Example unit cell for intercalated Li is highlighted with dash lines. Cell constant are labelled in Figure. d, Photolithography mask design for etched window for Li ion intercalation.

As discussed in the main text, there are two de-intercalation peaks for 4LG and three for 6LG. The integrating baseline for each peak are indicated in Figure B.2a and B.2b. The integrated charges for each peak are listed as follows:

4LG Peak 1: 3.28 μC Peak 2: 8.93 μC Total charge: 12.2 μC

6LG Peak 1: 3.36 μC Peak 2: 1.94 μC Peak 3: 10.4 μC Total charge: 15.7 μC

According to Figure B2.c, one unit cell contains one Li ion, with a size of 0.1574 nm^2.

Exposed electrode area for FLG samples are 0.048 cm^2.

Consider about the etched openings (Figure B2.d), 1/64 of graphene area has been removed by photolithography and reactive ion etching procedure. The effective area for FLG sample is 0.04725 cm^2.

Total number of Li for one layer of stage-1 LiC_6: 0.04725 cm^2/0.1574 nm^2 = 3.002×10^{13} atoms.

Total charge of Li for one layer of stage-1 LiC_6: 3.002×10^{13} atoms/(6.02×10^{23} atoms/mol) * 96485 C/mol = 4.81 μC.

For 4LG, there are at most three layers Li insertion with graphene sheets, then the theoretical intercalation charge is: 4.81 × 3 = 14.43 μC. Similarly, the theoretical charge for 6LG is : 4.81 × 5 = 24.05 μC.

Compare with experimental data calculated from de-intercalation charge, Li ion filled up to 85 % available sites in 4LG and 65 % available sites in 6LG.

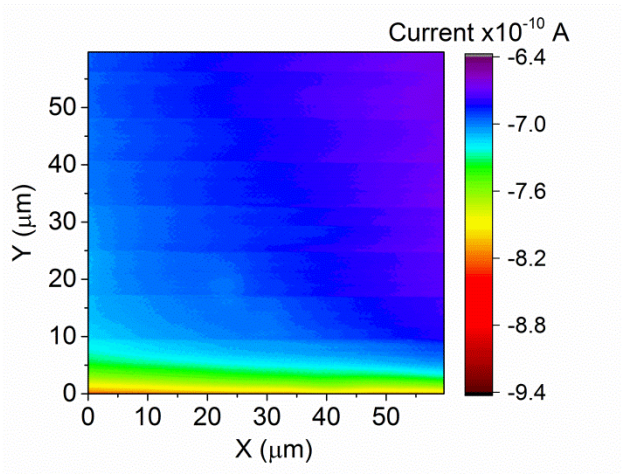

Figure B.3 SECM feedback images of N,N,N',N'-tetramethyl p-phenylenediamine (TMPD) after SEI fully formation. Substrate potential: 2.6 V. This image was taken after Figure 4.4 d, e and f in main text. The image has no obvious contrast between graphene and etched ionic channel area, which means the SEI remains stable under higher potential. Tip-substrate distance: 133 nm.

APPENDIX C

SUPPLEMENTARY INFORMATION OF CHAPTER 5

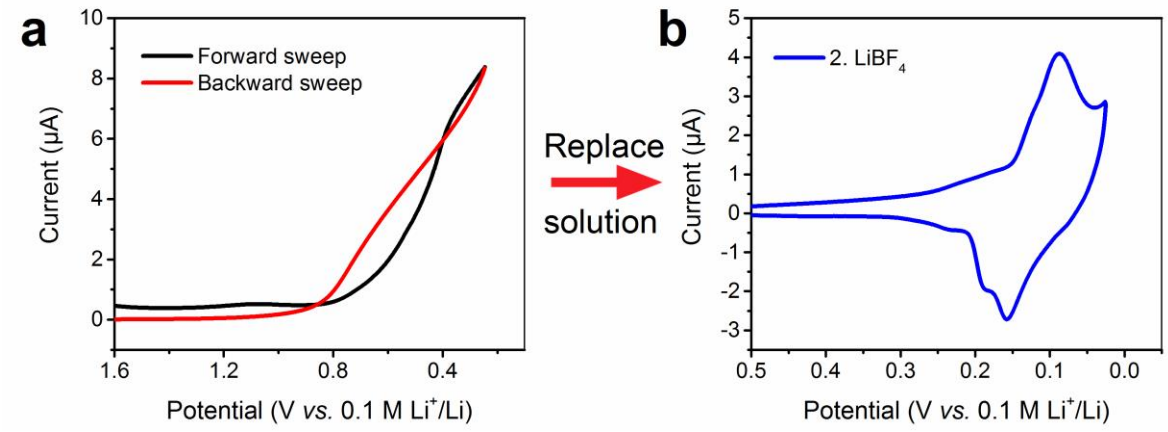

Figure C.1 Cyclic voltammograms of K plating and Li ion intercalation. a, Pristine MLG sample was first exposed to 0.1 M KPF_6 PC-EC solution, no intercalation signals were observed. b, Replace solution to 0.1 M $LiBF_4$ PC-EC solution, Li ion intercalation peaks were observed. All CVs are taken at scan rates of 1 mVs^{-1}.

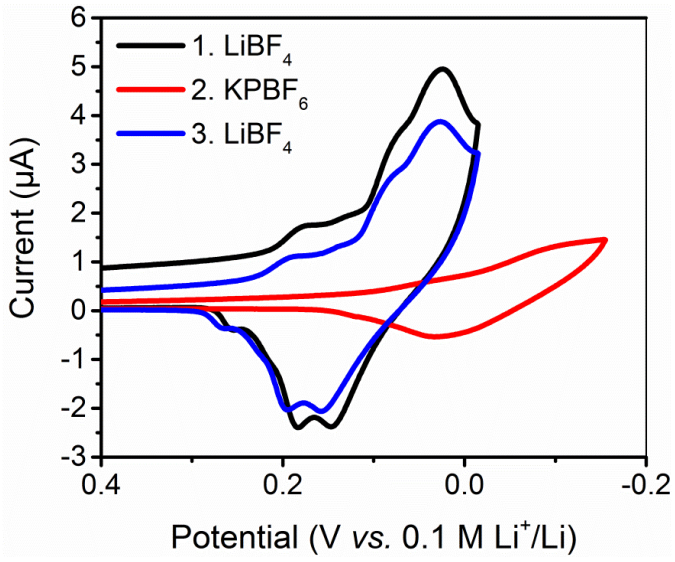

Figure C.2 Cyclic voltammograms of Li and K ion intercalation on MLG with pre-conditioned SEI. Black trace shows the Li ion intercalation after conditioning. Red trace is the sample

(*Figure C.2 Continued*) response in KPF_6 solution after thorough rinsing. Blue trace is tested in $LiBF_4$ solution again after K ion intercalation (red trace). All solutions are 0.1 M Li or K salt in PC-EC, scan rates are 1 mVs^{-1}.

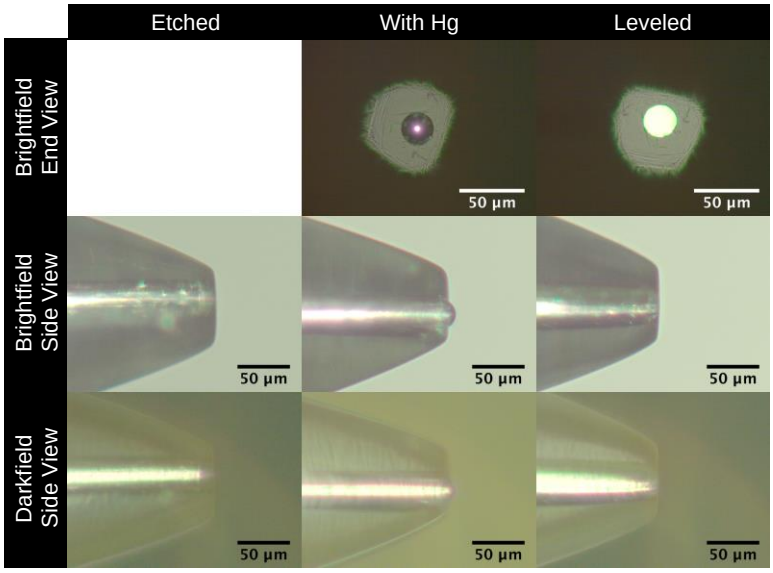

Figure C.3 Hg Disc-Well Probe Fabrication Process. Electrochemical etching with sonication produces an evenly etched surface. Electrodeposition of Hg is terminated after over-filling the etched cavity. After leveling, the Hg disc-well is evenly filled and has a flat, mirror-like surface. The Hg disc-well shown here has a_1 = 12.5 µm, R_G = 2.5, H_1 = 0, and H_2 = 1.1.

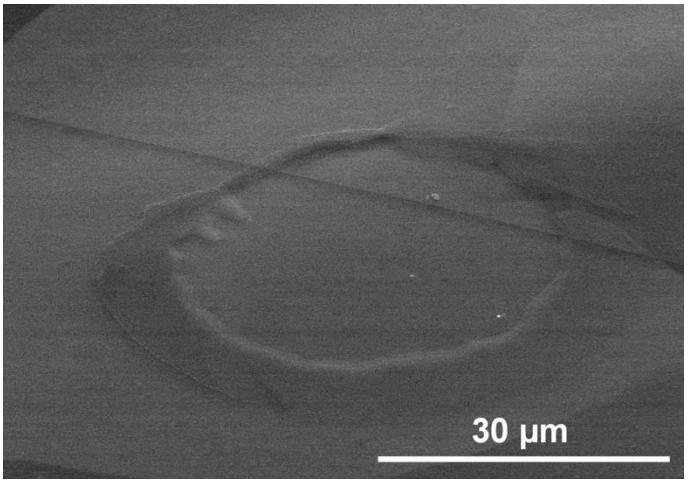

Figure C.4 SEM Image of Etched Hole. The etched holes are ~1.4 µm deep. The tilt angle is 50°.

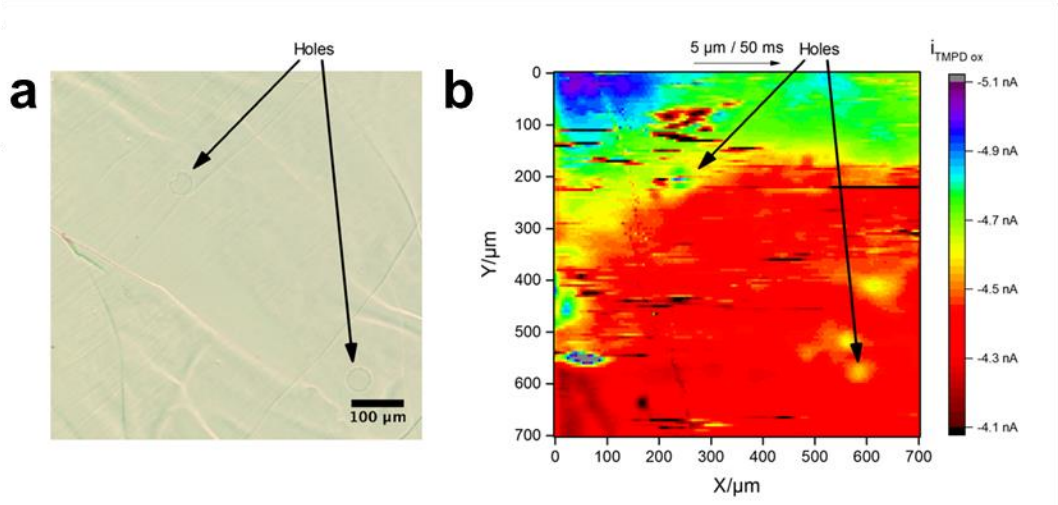

Figure C.5 Overview of Region of Interest. a, Photomicrograph of the region of interest. b, SECM image with positive feedback from TMPD regeneration at the substrate. The SECM probe is the same Hg disc-well UME used in the main text. The hole at [X, Y] = [240 µm, 200 µm] is featured in Figure 5.6a, 5.6b.

C.1 Stripping-Based Approach to HOPG

After switching to a 1 mM KPF_6 solution in PC-EC, the Hg disc-well UME was re-approached to the origin in Figure 5.6 by recording stripping CVs between Z motor increments (Figure C.6) with the HOPG left unbiased at its open circuit potential. Because ions are regularly stripped from the Hg probe, this method of approaching a surface avoids the risk of damaging the Hg probe by saturation of the amalgam phase. The amalgamation current (i_{amal}), peak stripping current (i_{strip}), and stripping charge (Q_{strip}) were each extracted from the CV-PAS dataset to give three CV-PACs.[1] Of these, Q_{strip} exhibited the least noise, which is consistent with the general insensitivity of integrated values to temporal fluctuations in a source signal. The negative feedback stripping charge CV-PAC was fit with an analytical model derived from COMSOL finite-element simulations[2] to obtain the final approach distance of $L = 1.28 \pm 0.02$ ($\chi_{red}^2 = 4.0401 \times 10^{-5}$). Though smaller gaps are possible, wrinkles in the HOPG surface (Figure 5.4a) warranted caution to avoid mechanical damage to either the probe or the substrate. The final approach distance is consistent with the normalized timescale ($T_{amal} = D_{ox}*\Delta E/(v*a_1^2)$ of 1.9 ± 0.2, for which the average Nernstian diffusion layer thickness (δ_N) is 7.7 ± 0.1 μm.[3] This timescale ensures that the depletion volume expanding from the SECM probe during amalgamation propagates far enough into solution to overlap with ionic gradients emanating from the substrate. The overlap between the probe and substrate diffusion fields is the source of informational probe signal perturbations. Negative feedback was observed for all three signals due to the increasingly hindered diffusion field with decreasing tip-substrate gap. The observation of positive feedback from TMPD redox signals and negative feedback from K(Hg) amalgamation and stripping signals demonstrates one of the key benefits of Hg disc-well SECM probes, namely, that amalgamation and stripping signals allow negative feedback SECM probe

positioning over any substrate regardless of the substrate's electrical conductivity.[1] Furthermore, since stripping signals afford potential-based ionic specificity, Hg-based CV-SECM signals may provide accurate measurements even in concentrated solutions that are traditionally challenging for methods lacking this specificity, such as those based on resistance, conductance, or impedance.[4]

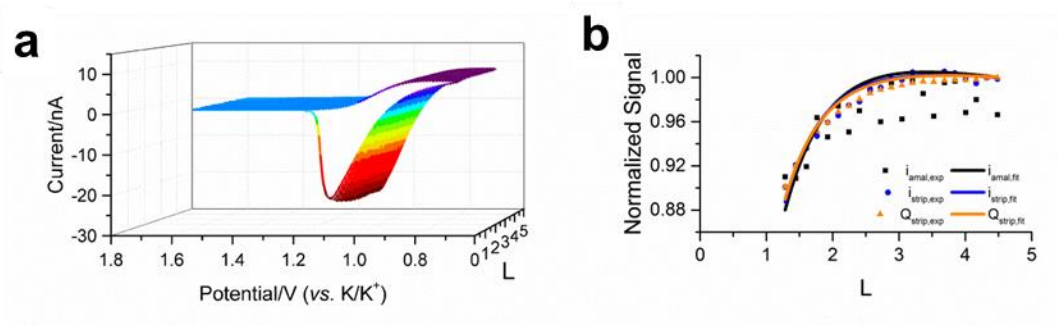

Figure C.6 CV-SECM Stripping-Based Approach. a, CV-PAS based on $K^+ + e^- \rightleftarrows K(Hg)$ ending with $L = 1.28 \pm 0.02$ at [X, Y] = [0 μm, 0 μm] in Figure 5.6b. b, Extracted CV-PACs and fits based on COMSOL simulations. Key simulation conditions include: a_1 = 12.5 μm, R_G = 2.5, H_1 = 0, H_2 = 1.1, C_{ox}* = 1 mol m^{-3}, $D_{K+,PC\text{-}EC} = 2 \times 10^{-10}$ m^2 s^{-1}, and $D_{K(Hg),Hg} = 7.9 \times 10^{-10}$ m^2 s^{-1}, ΔE = 0.295 V, ν = 0.2 V s^{-1}, α = 0.5, and $k^o = 1 \times 10^{-2}$ m s^{-1}.

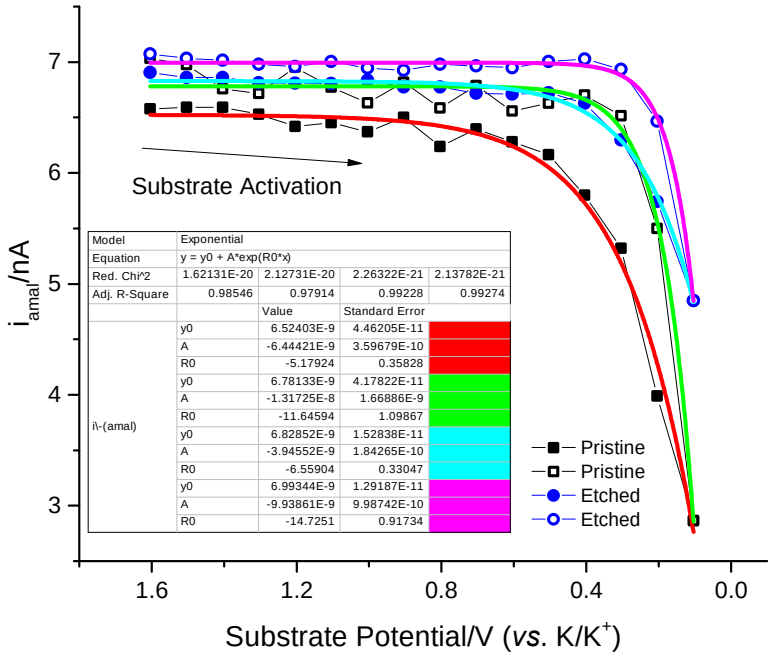

Figure C.7 Exponential Fits of Hg Disc-Well Amalgamation Currents. These are fits of the data presented in Figure 5.7c in the main text.

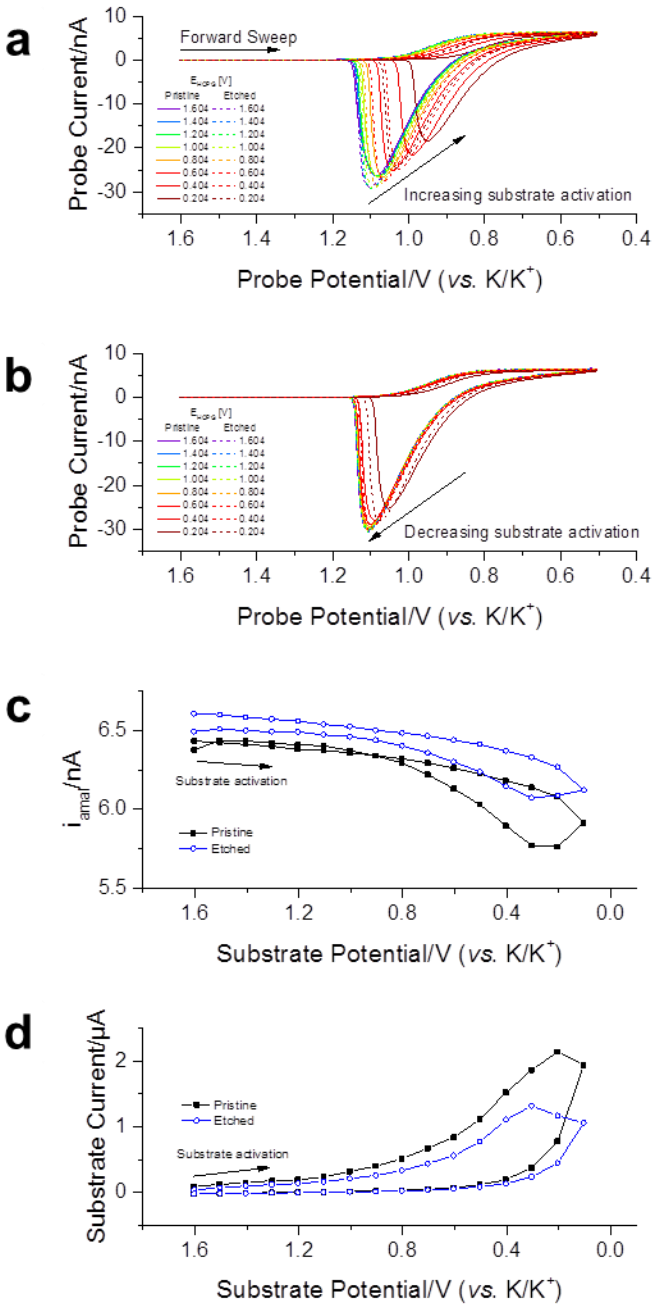

Figure C.8 K^+ Competition at a Longer Timescale. a, Select Hg disc-well CVs taken with increasing substrate activation towards K^+ intercalation. $\nu = 0.1$ V s^{-1}, $T_{amal} = 5.6 \pm 0.6$. b, Select Hg disc-well CVs taken with decreasing substrate activation, giving way to K^+ deintercalation. c, Hg disc-well amalgamation currents extracted from a and b. d, Average chronoamperometric

(*Figure C.8 Continued*) signal at the substrate at various activation potentials. The probe, solution, substrate, probe positions, and substrate potentials are identical to those used in Figure C.6. Though the probe voltammetry benefits from the lengthened timescale, non-specific decreases in K^+ uptake by HOPG mask information regarding spatial differences in ionic uptake. In other words, the probe is correctly tracking the local changes in K^+ concentration, but the overall passivation of HOPG dominates the signals and masks the smaller differences of interest.

C.2 References

1. Barton, Z. J.; Rodriguez-Lopez, J. Cyclic Voltammetry Probe Approach Curves with Alkali Amalgams at Mercury Sphere-Cap Scanning Electrochemical Microscopy Probes. *Anal Chem* **2017**, *89*, 2708-2715.

2. Barton, Z. J.; Rodriguez-Lopez, J. Fabrication and Demonstration of Mercury Disc-Well Probes for Stripping-Based Cyclic Voltammetry Scanning Electrochemical Microscopy. *Anal Chem* **2017**, *89*, 2716-2723.

3. Molina, A.; Gonzalez, J.; Henstridge, M. C.; Compton, R. G. Analytical expressions for transient diffusion layer thicknesses at non uniformly accessible electrodes. *Electrochim Acta* **2011**, *56*, 4589-4594.

4. Barton, Z. J.; Rodriguez-Lopez, J. Emerging scanning probe approaches to the measurement of ionic reactivity at energy storage materials. *Anal Bioanal Chem* **2016**, *408*, 2707-2715.

APPENDIX D

SUPPLEMENTARY INFORMATION OF CHAPTER 6

D.1 General Information

All air or moisture-sensitive manipulations were performed under nitrogen atmosphere using standard schlenk techniques. All glassware was oven-dried prior to use. Unless otherwise stated, all starting materials and reagents were purchased from Sigma-Aldrich or Matrix Scientific and used without further purification. Poly(vinylbenzyl chloride) (over 90% are 4 substituted) of different molecular weights (5.3, 60, and 82 kDa) were purchased from Polymer Source. Poly(vinylbenzyl chloride) of molecular weights 27 and 41 kDa were synthesized using Reversible Addition-Fragmentation Chain-Transfer (RAFT) Polymerization. Dimethyl formamide (DMF) was obtained from a Solvent Delivery System (SDS) equipped with activated neutral alumna columns under argon. ^{1}H and ^{13}C NMR spectra were recorded on Varian Unity 500, and VXR 500 spectrometers. Chemical shifts are reported in δ (ppm) relative to the residual solvent peak ($(CD_3)_2SO$: 2.50, $(CD_3)_2CO$: 2.05 for ^{1}H; $(CD_3)_2CO$: 29.84 for ^{13}C). Coupling constants (J) are expressed in hertz (Hz). Splitting patterns are designated as s(singlet), d(doublet), t(triplet), dd(doublet of doublets), m(multiplet), and q(quartet). Low and high resolution EI mass spectra were recorded on a Micromass 70-VSE spectrometer. Infrared spectra (percent transmittance) were acquired on a Nicolet Nexus 670 FT-IR spectrometer with an ATR-IR attachment. UV-Vis absorption spectra were recorded on Perkin Elmer and Shimadzu instruments. Dynamic light scattering was recorded on NICOMP zetasizer. Elemental analyses were performed on the following instruments: CHN analysis - Exeter Analytical CE 440 and Perkin Elmer 2440, Series II; ICP analysis - ICP-MS and ICP-OES; Halide analysis - Titration &

ISE. Analytical gel permeation chromatography (GPC) analyses were performed on a system composed of a Waters 515 HPLC pump, a Thermoseparations Trace series AS100 autosampler, a series of three Waters HR Styragel columns (7.8’ 300 mm, HR3, HR4, and HR5), and a Viscotek TDA Model 300 triple detector array, in HPLC grade THF (flow rate = 1.0 mL/min) at 30 ℃. The GPC was calibrated using a series of monodisperse polystyrene standards. Viscosity was measured on a TA Instrument AR-G2 rheometer. Flow cell UV-Vis experiments were performed using Masterflex L/S Digital Economy Drive Model 7524-40 pump and a Masterflex EW-77390-0 PTFE-Tubing Pump Head with spectroscopy grade acetonitrile (flow rate = 1.0 mL/min)Conductance of LiBF4 was measured on YSI Model 35 Conductance Meter with BASi MW-4130 platinum wire auxiliary electrodes.

D.2 Synthesis of Monomer and Polymers

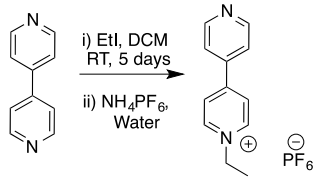

1

Ethyl viologen hexafluoro phosphate (**1**): **1** was synthesized following the reported procedure.[1] ^{1}H NMR ($(CD_3)_2SO$): δ 9.24 (d, *J* = 10 Hz, 2H), 8.87 (dd, *J* = 5 Hz, 2H), 8.63 (d, *J* = 10 Hz, 2H), 8.02 (dd, *J* = 5 Hz, 2H), 4.65 (q, *J* = 5 Hz, 2H), 1.58 (t, *J* = 7.5 Hz, 3H). HRMS (EI+) calculated for C12H13F6N2P $(M)^+$ 330.07, C12H13N2 $(M\text{-}PF_6)^+$ 185.11; Found $(M\text{-}PF_6)^+$ 185.11.

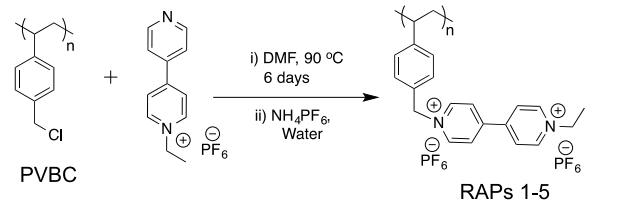

PVBC

RAPs 1-5

PVBC Mn (kDa)	PDI
5.3	1.9
27	1.9
41	1.6
60	1.9
82	1.6

$DP_{PVBC} = Mn_{PVBC}/152.62$ Da

RAP Mn (kDa)
21
104
158
233
318

$Mn_{RAP} = DP_{PVBC} \times 592.35$ Da

Redox active polymers (**RAPs 1-5**): Dry DMF (15 mL) was added to a flask containing **PVBC** (500 mg, 3.27 mmol) and **1** (5.4 g, 16.38 mmol) under nitrogen. Reaction mixture was stirred at 90 ^{o}C for 6 days.[2] Concentrated solution of ammonium hexafluoro phosphate (5 g) solution was prepared in water and added to the above reaction mixture. The resultant solution was stirred at room temperature for 12 h and precipitated in methanol. Collected polymer was redissolved in acetonitrile and reprecipitated in diethyl ether. Polymers were dried under high

vacuum for 24 h. ^{1}H NMR were recorded in $(CD_3)_2CO$. See sections 3.0, 4.0, and 8.0 for complete characterization of polymers (^{1}H NMR, ATR-IR, and elemental analyses).

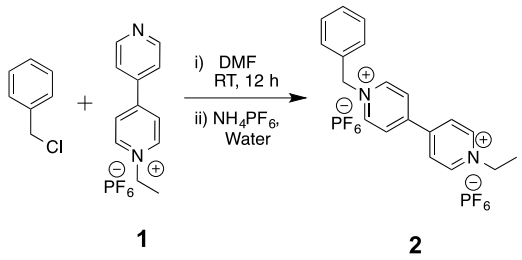

1 **2**

Benzyl-ethyl viologen dihexafluorophosphate (**2**): Dry DMF (8 mL) was added to a flask containing benzyl chloride (1.10 g, 8.76 mmol) and **1** (2.0 g, 6.06 mmol) under nitrogen. The reaction mixture was stirred at room temperature for 12 h. The solution changed from transparent red to cloudy red. Concentrated solution of ammonium hexafluoro phosphate (1.98 g) was prepared in water and added to the above reaction mixture. The resultant solution was stirred at room temperature for 4 h. The precipitated product was filtered and dried under high vacuum for 24 h to yield the product as a pale yellow powder (2.89 g 84.3%). ^{1}H NMR ($(CD_3)_2CO$): δ = 9.53 (d, J = 5 Hz, 2H), 9.45 (d, J = 5 Hz, 2H), 8.84 (m, 4H), 7.69 (m, 2H), 7.52 (m, 3H), 6.19 (s, 2H), 5.01 (q, J = 5 Hz, 2H), 1.8 (t, J = 7.5 Hz, 3H). HRMS (ES+) calculated for $C_{19}H_{20}F_{12}N_2P_2$ $(M)^+$ 566.09, $C_{19}H_{20}F_6N_2P$ $(M\text{-}PF_6)^+$ 421.13; Found $(M\text{-}PF_6)^+$ 421.1265.

D.3 Redox Active Polymer Characterization

D.3.1 Solubility Limit of RAPs

Table D.1 Solubility limits of RAPs in acetonitrile.

Polymer MW (kDa)	Solubility Limit (M)
21	2.9
104	2.9
158	2.4
233	2.6
318	2.1

D.3.2 ATR-IR Spectra

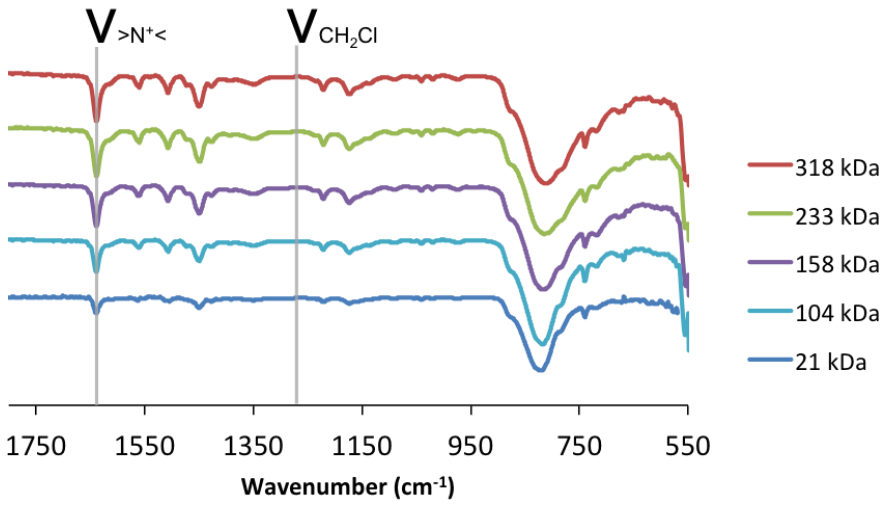

Figure D.1 ATR-IR spectra of **RAPs 1-5**.

D.3.3 Elemental Analyses

Table D.2 Elemental (C, H, N, P, F, Cl) analysis of RAPs.

	Element	C	H	N	F	P	Cl
21 kDa	Theoretical (%)	42.58	3.74	4.73	38.49	10.46	0.00
	Experimental (%)	44.34	3.62	4.58	43.19	9.94	0.15
	Difference	1.76	-0.12	-0.15	4.70	-0.52	0.15
104 kDa	Theoretical (%)	42.58	3.74	4.73	38.49	10.46	0.00
	Experimental (%)	42.23	3.37	4.61	32.09	10.77	0.26
	Difference	-0.35	-0.37	-0.12	-6.40	0.31	0.26
158 kDa	Theoretical (%)	42.58	3.74	4.73	38.49	10.46	0.00
	Experimental (%)	42.50	3.57	4.68	29.49	10.49	0.30
	Difference	-0.08	-0.17	-0.05	-9.00	0.03	0.30
233 kDa	Theoretical (%)	42.58	3.74	4.73	38.49	10.46	0.00
	Experimental (%)	43.00	3.60	4.59	29.26	10.50	0.27
	Difference	0.42	-0.14	-0.14	-9.23	0.04	0.27
318 kDa	Theoretical (%)	42.58	3.74	4.73	38.49	10.46	0.00
	Experimental (%)	42.45	3.52	4.56	28.21	10.50	0.31
	Difference	-0.13	-0.22	-0.17	-10.28	0.04	0.31

D.4 Redox Active Polymer Physical Properties

D.4.1 Viscosity

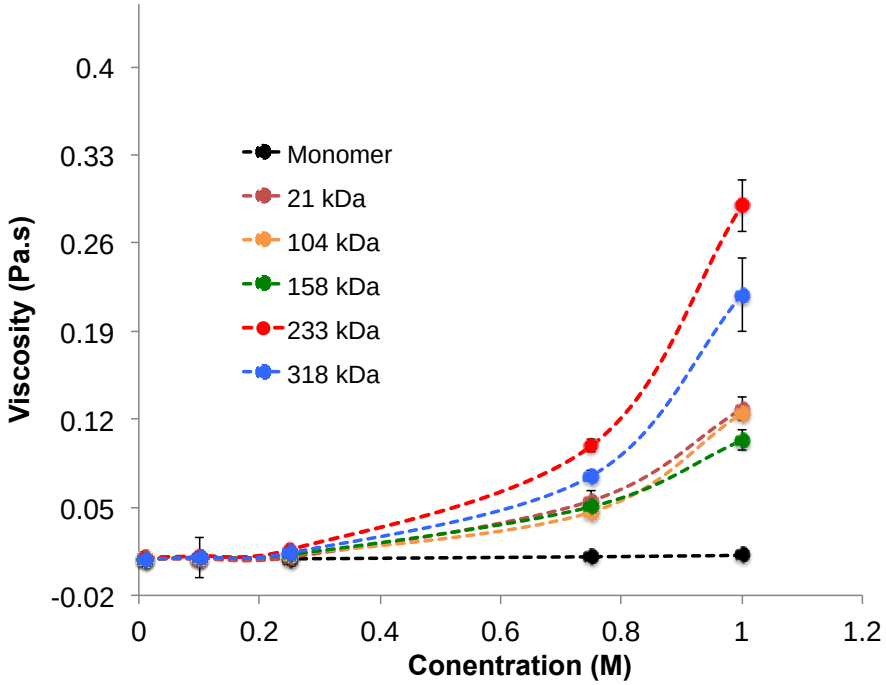

Figure D.2 Viscosity of polymers at different concentrations.

Table D.3 Viscosity of polymers at different concentration.

Polymer (kDa)	Viscosity (mPa*s)				
	0.01 M	0.1 M	0.25 M	0.75 M	1.0 M
0.56 (Monomer)	9.31 ± 0.05	9.3 ± 0.1	9.12 ± 0.03	11 ± 2	11.8 ± 0.1
21	8.9 ± 0.1	9.25 ± 0.08	10.2 ± 0.1	55 ± 8	128 ± 9
104	9.55 ± 0.04	10.10 ± 0.02	12.26 ± 0.03	50 ± 5	120 ± 20
158	9.18 ± 0.04	10.3 ± 0.3	12.39 ± 0.04	50 ± 4	103 ± 8
233	11 ± 1	11 ± 2	16.3 ± 0.1	100 ± 5	290 ± 20
318	9.1 ± 0.1	10.35 ± 0.02	13.7 ± 0.4	75 ± 4	220 ± 30

D.4.2 Molar Extinction Coefficient

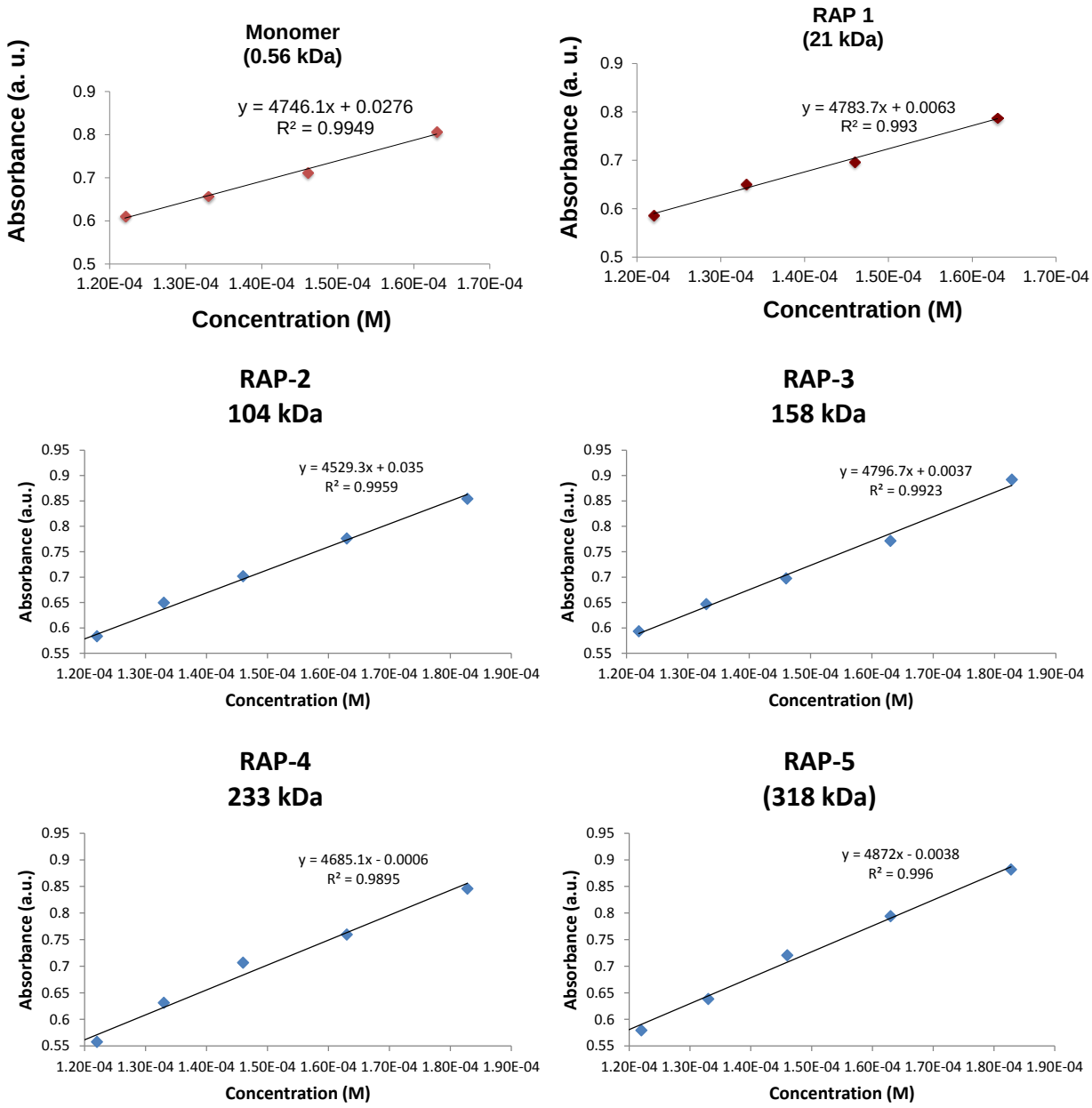

Figure D.3 Absorbance *vs.* concentration plots to determine molar extinction coefficient of monomer and **RAPs 1-5**.

Table D.4 Molar extinction coefficients of monomer and RAPs in acetonitrile.

Molecular weight (kDa)	Molar extinction coefficient (ε M^{-1} cm^{-1})
0.56	23730
21	23918
104	22646
158	23983
233	23425
318	24360

D.4.3 UV-Vis Absorption Spectra

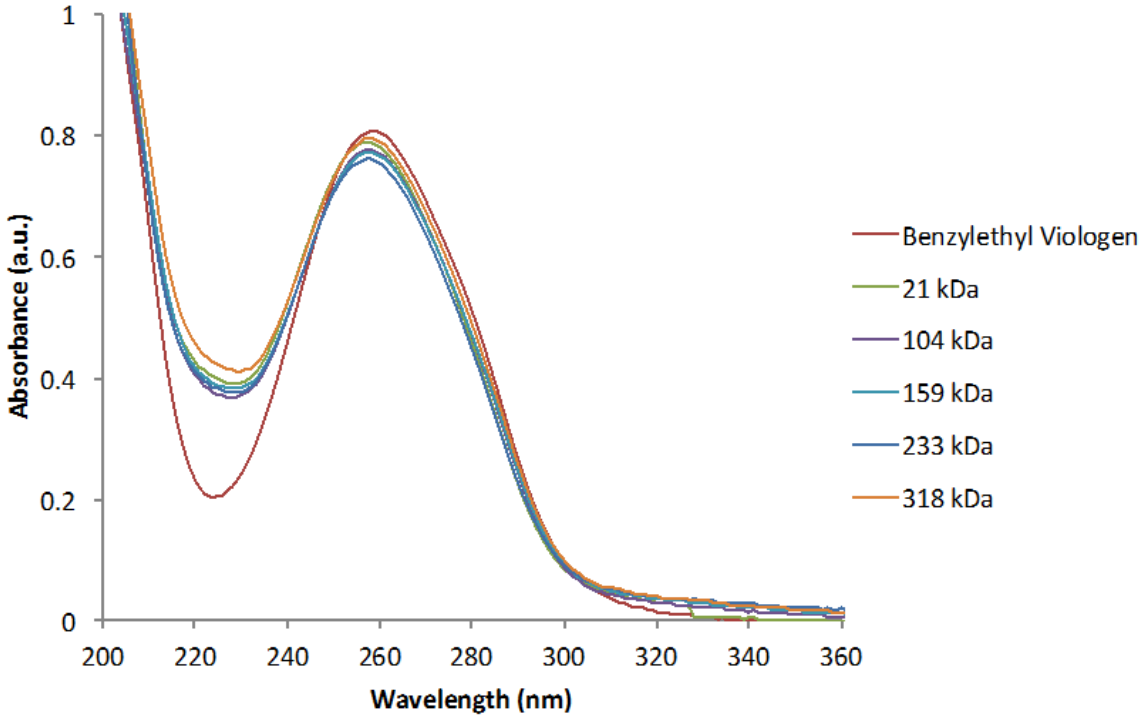

Figure D.4 Absorbance spectra of monomer and **RAPs 1-5** at 1.63×10^{-4} M in acetonitrile.

D.5 Electrochemical Characterization of RAPs 1-5

D.5.1 Electrochemical Property of Viologen Monomer

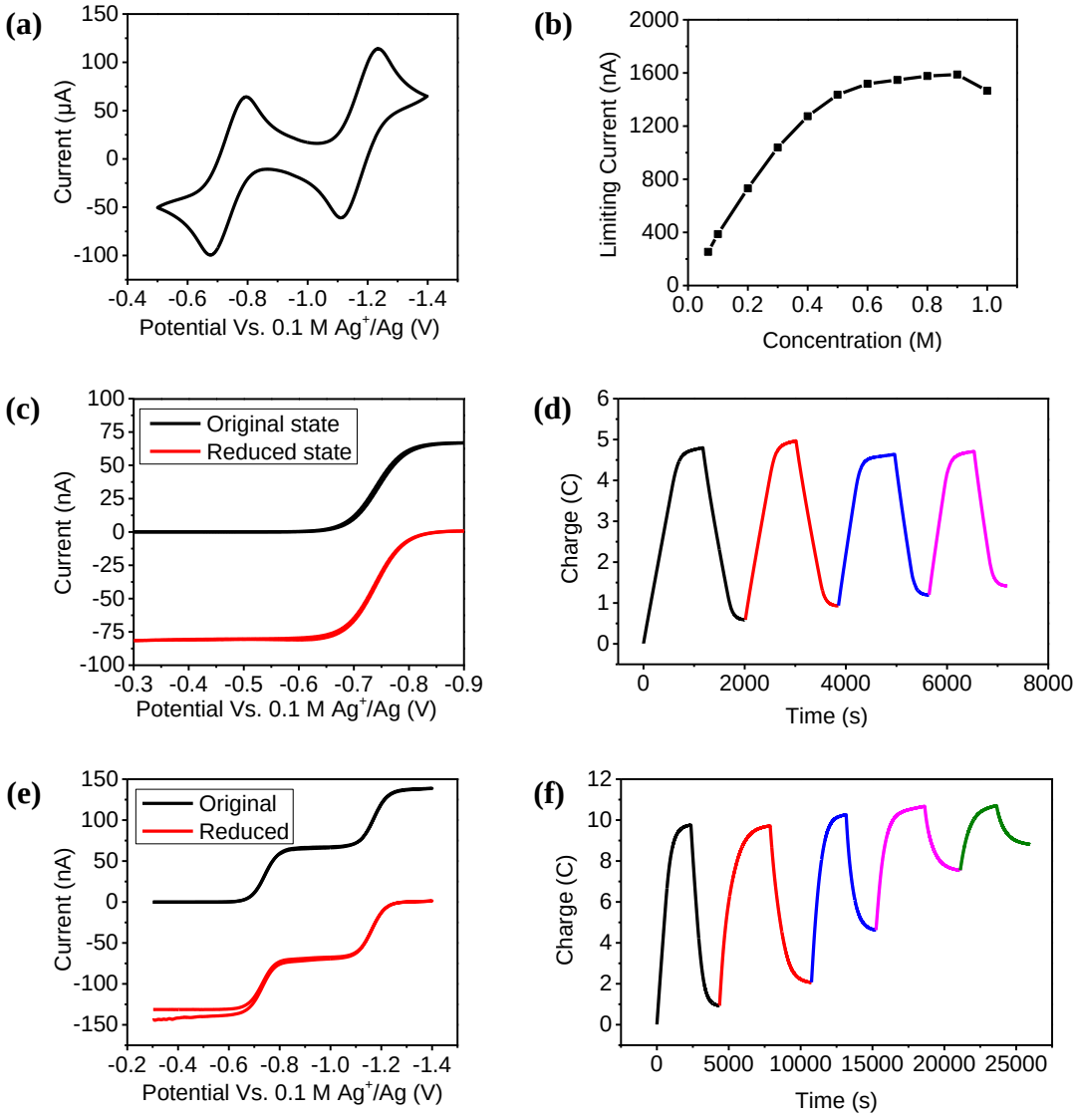

Figure D.5 Electrochemical properties of viologen monomer. Solution: 6 mL 10 mM monomer in 0.1 M $LiBF_4$ acetonitrile supporting electrolyte. (a) Complete cyclic voltammograms at 0.04 cm^2 Pt disk electrode (ν= 100 mV/s). (b) Diffusion limited steady-state current change of monomer at high concentration regime. (c) Steady state voltammograms of monomer at 12.5 μm Pt tip (ν= 10 mV/s). Upper part 2+/+ and lower part +/2+. (d) Four cycles potential controlled

(*Figure D.5 Continued*) bulk electrolysis of first reduction state. (e) Steady state voltammograms of monomer at 12.5 μm Pt tip (ν= 10 mV/s). Upper part: 2+/0 and lower part 0/2+. (f) Five bulk electrolysis cycle of second reduction state.

D.5.2 Adsorption Properties of RAPs 1-5

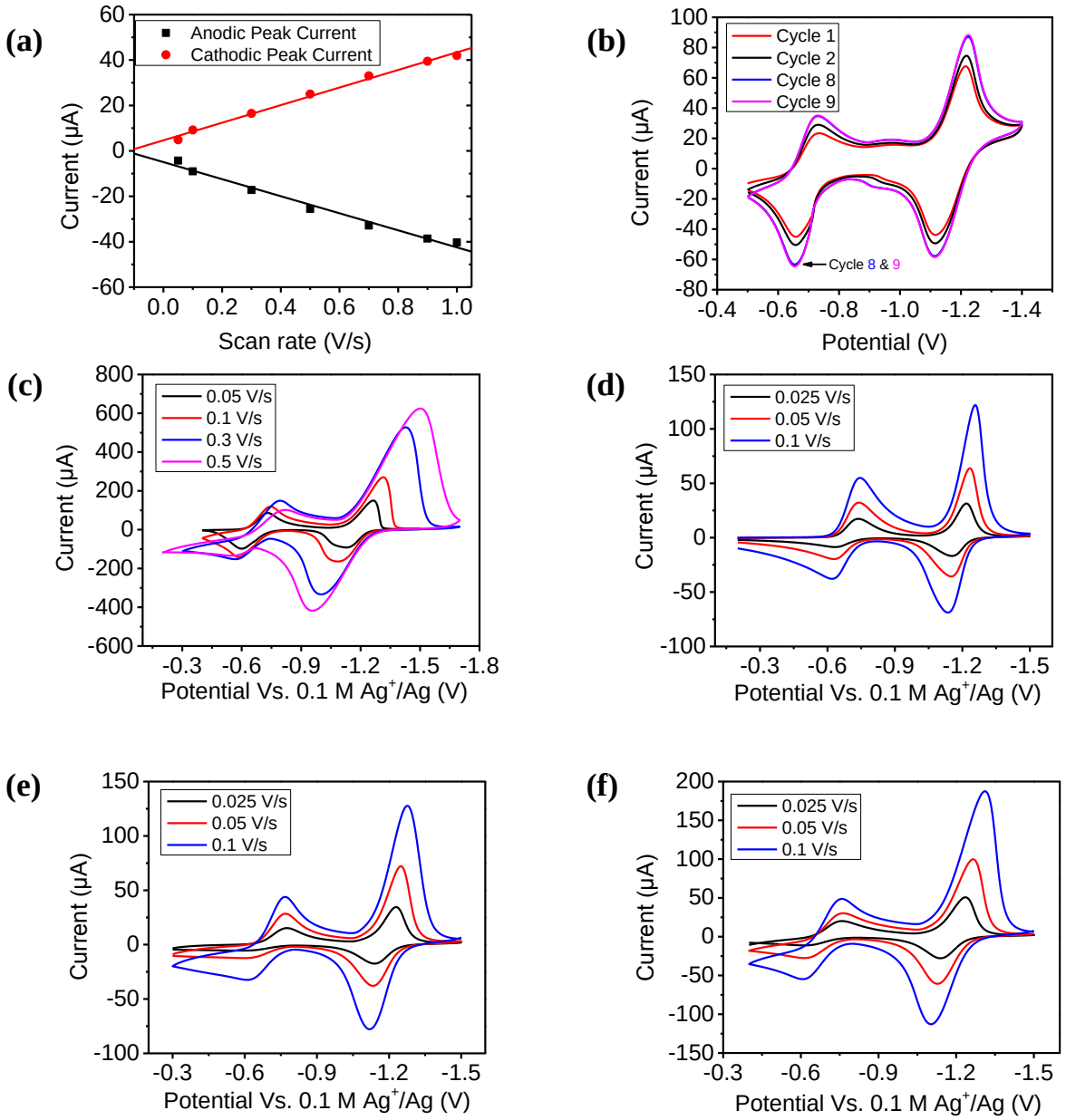

Figure D.6 Adsorption Properties of RAPs 1-5. (a) Peak current – scan rate relationship of 21 kDa RAP. Second reduction peak current of 21 kDa (Figure 6.2b) were extracted, plotted with

(*Figure D.6 Continued*) scan rate, and fitted with linear relationship. Black: anodic peak current, red: cathodic peak current. (b) Adsorption peak evolution of 21 kDa RAP with cycling number. The first several cycles CVs of 10 mM 21 kDa in 0.1 M LiBF4 acetonitrile supporting electrolyte. Peak current increase quickly at first 2 cycle, and saturate after 9 cycles (cycle 8 & 9 overlap). (c-f) CVs of adsorbed RAPs on 0.04 cm^2 Pt disk electrode at different scan rate. (c) 104 kDa, (d)158 kDa, (e) 233 kDa, (f) 318 kDa.

D.5.3 Diffusion Coefficient – Molecular weight Relationship

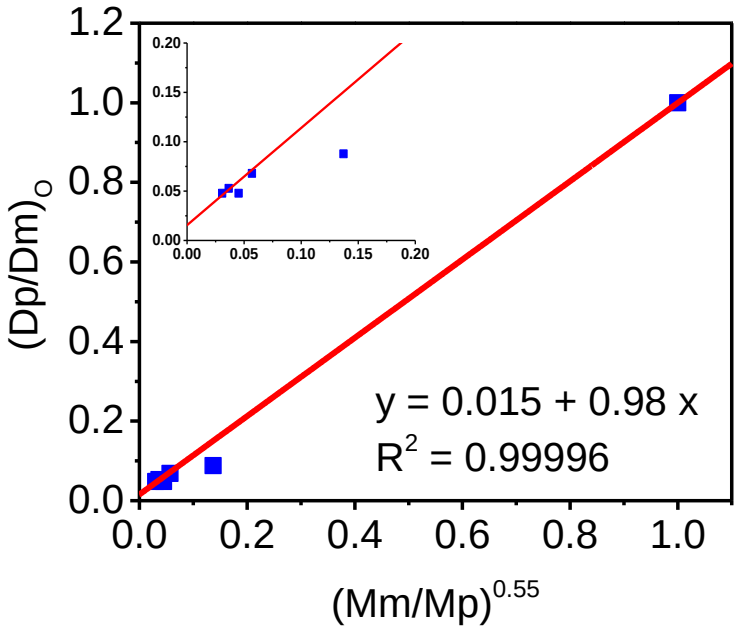

Figure D.7 Original viologen polymer diffusion coefficient *vs.* molecular weight relationship. This Figure show a good linear relationship between ratio of the diffusion coefficient of polymer to monomer: (Dp/Dm) to 0.55 power of the ratio of molecular weight of monomer and polymer $(Mm/Mp)^{0.55}$. Fitting result is shown in above equation. Polymer region is shown in the inset Figure.

D.6 Charge Storage in RAPs

D.6.1 Time Dependent Change of Viologen Polymer Radicals

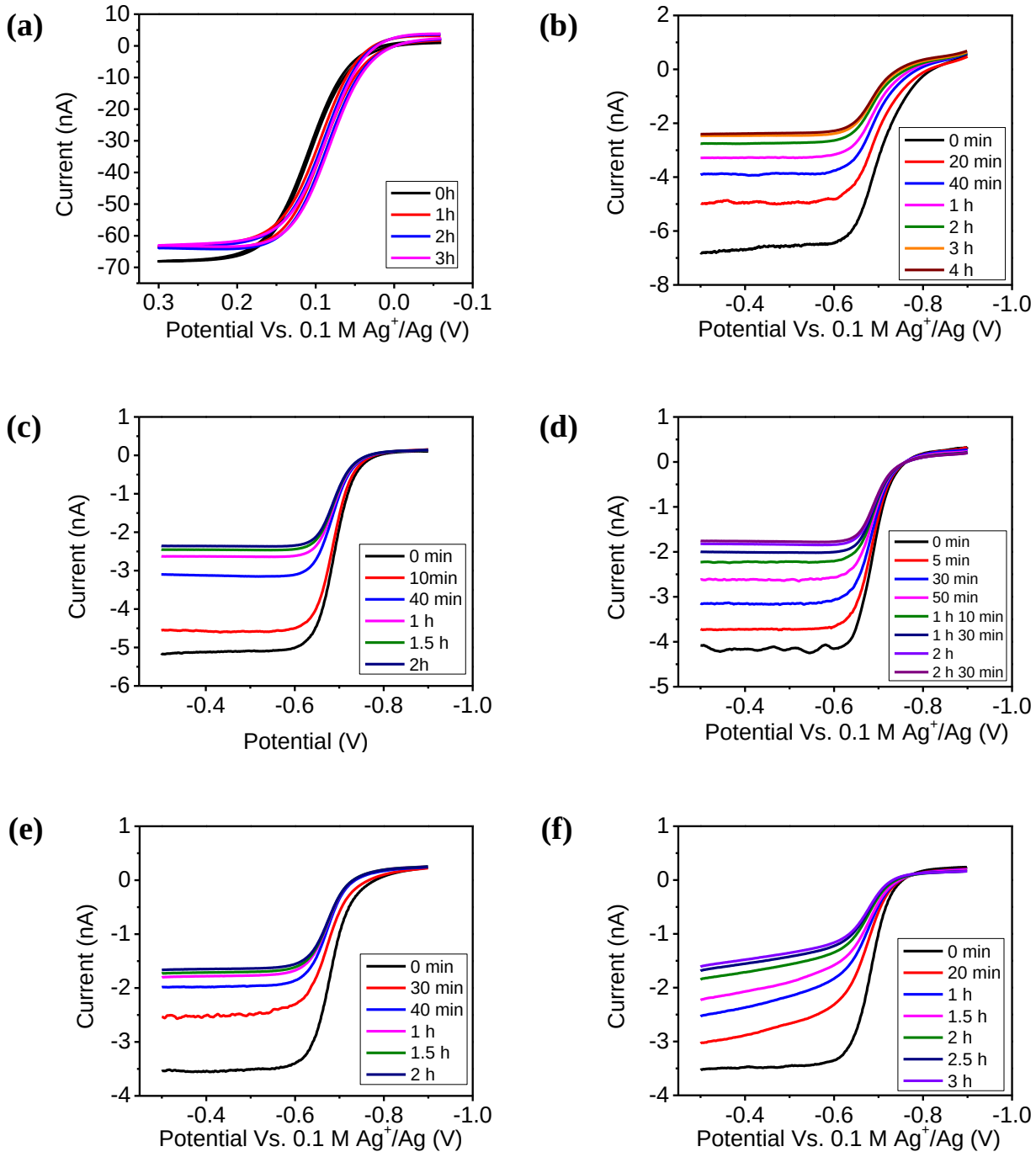

Figure D.8 Time dependent change of viologen monomer/polymer radicals. Steady state voltammograms were obtained approximately every 10 min after the first reduced state BE until

(*Figure D.8 Continued*) it is stabilized and saturated. Several curves are selected to show as examples. (a) monomer, (b) 21kDa, (c) 104 kDa, (d) 158 kDa, (e) 233 kDa, (f) 318 kDa.

D.6.2 Viscosity Corrected Limiting Current for RAPs 1-5

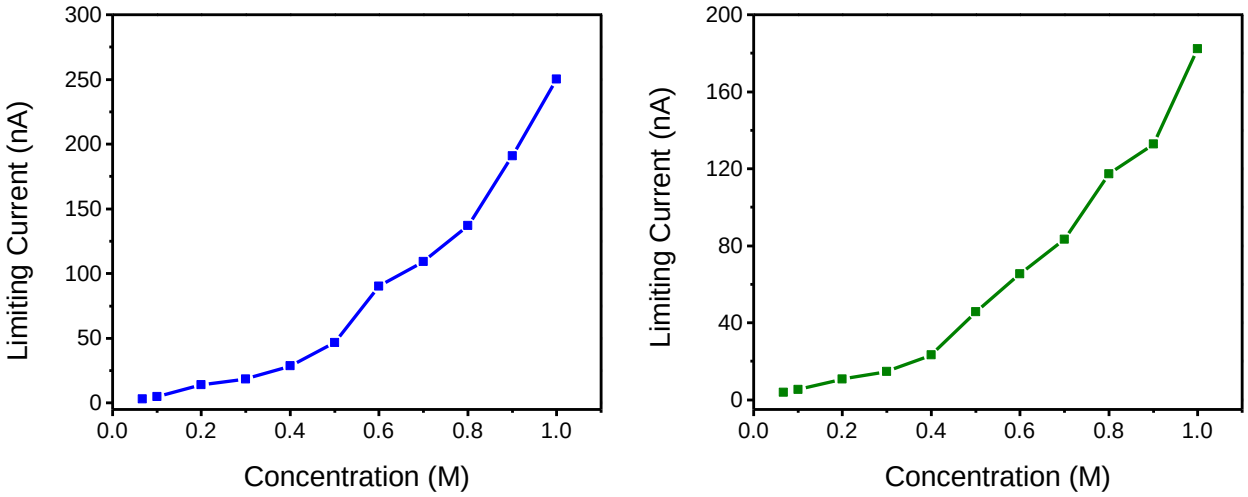

Figure D.9 Expected limiting current for RAPs 3 (left) and 5 (right) if data in Figure 6.5 in the main text were corrected for solution viscosity (Figure S1).

D.6.3 Bulk Electrolysis

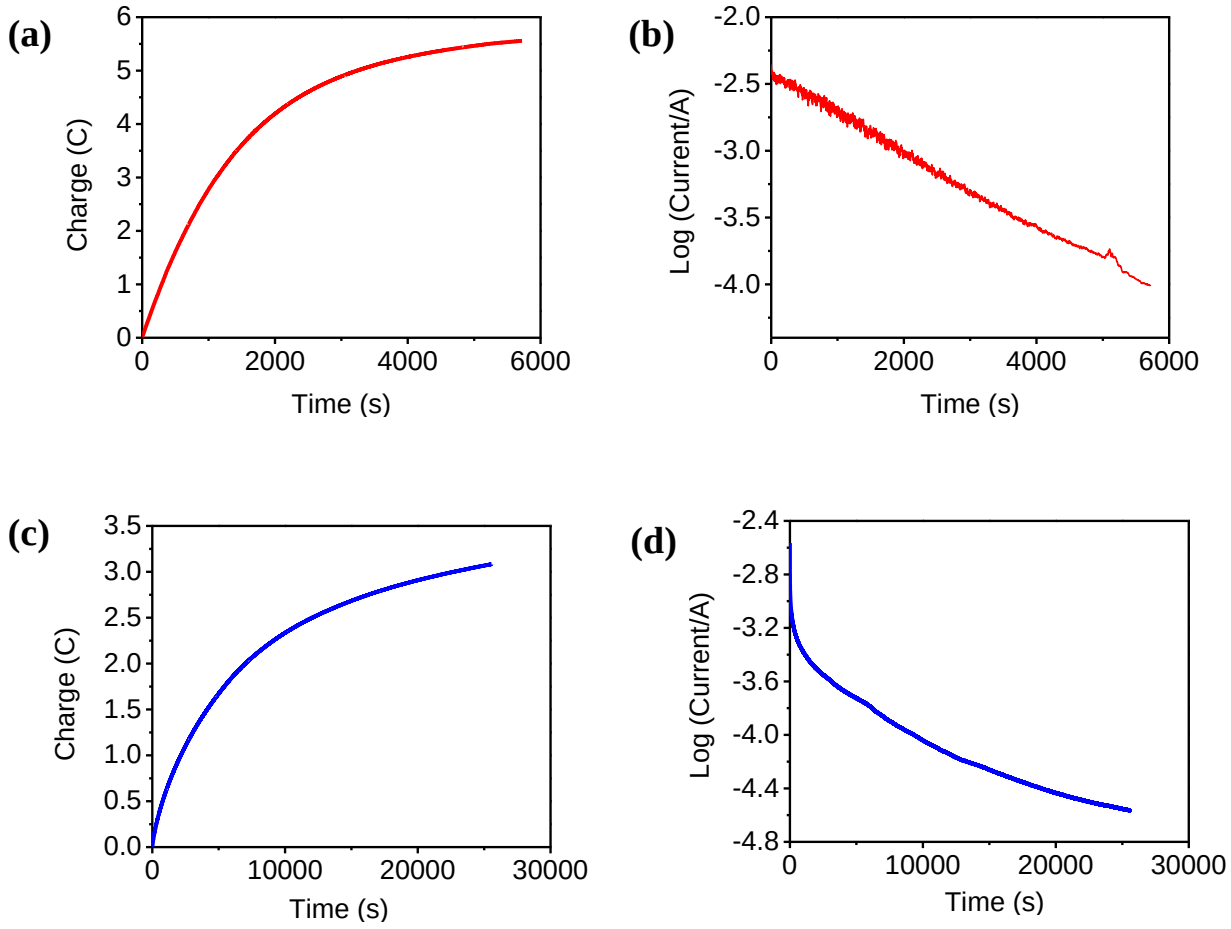

Figure D.10 Bulk electrolysis result of RAP 1 (21 kDa). (a) Charge – time relationship of BE first reduction state, which obtained 96% of nominal charge. (b) Log(current) – time relationship of BE first reduction state. (c) Charge – time relationship of BE directly to second reduction state. (b) Log(current) – time relationship of BE directly to second reduction state, which obtained 61% of nominal charge. a&b: 6 mL 10 mM RAP 1 in 0.1 M LiBF4 acetonitrile supporting electrolyte. c&d: 15.51 mg RAP 1 in 3 mL 0.1 M LiBF4 acetonitrile supporting electrolyte.

Table D.5 Bulk Electrolysis Cycling Properties of 21 kDa **RAP**. The detailed cycling data of Figure 6.4 is listed in this Table, including the total amount of charge transferred at each bulk electrolysis half cycle (reduction/oxidation), percent of charge transferred compare with calculated theoretical charge (5.79 C), and cycling efficiency at each individual cycle.

Cycle Number	Total Charge Transferred at BE Reduction (C)	Percent of Charge Transferred at BE Reduction (%)	Total Charge Transferred at BE Oxidation (C)	Percent of Charge Transferred at BE Oxidation (%)	Cycling Efficiency (%)
1	5.60	97	5.46	94	97
2	5.55	96	5.44	94	98
3	5.50	95	5.41	94	99
4	5.45	94	5.38	93	99
5	5.42	94	5.35	92	99
6	5.38	93	5.32	92	99
7	5.35	92	5.29	91	99
8	5.32	92	5.25	91	99
9	5.28	91	5.20	90	98
10	5.25	91	5.16	89	98
11	5.21	90	5.11	88	98

D.7 Hindered RAP Transport Across COTS Separators

D.7.1 Time Dependent Polymer Transport across Celgard 2325 Separator.

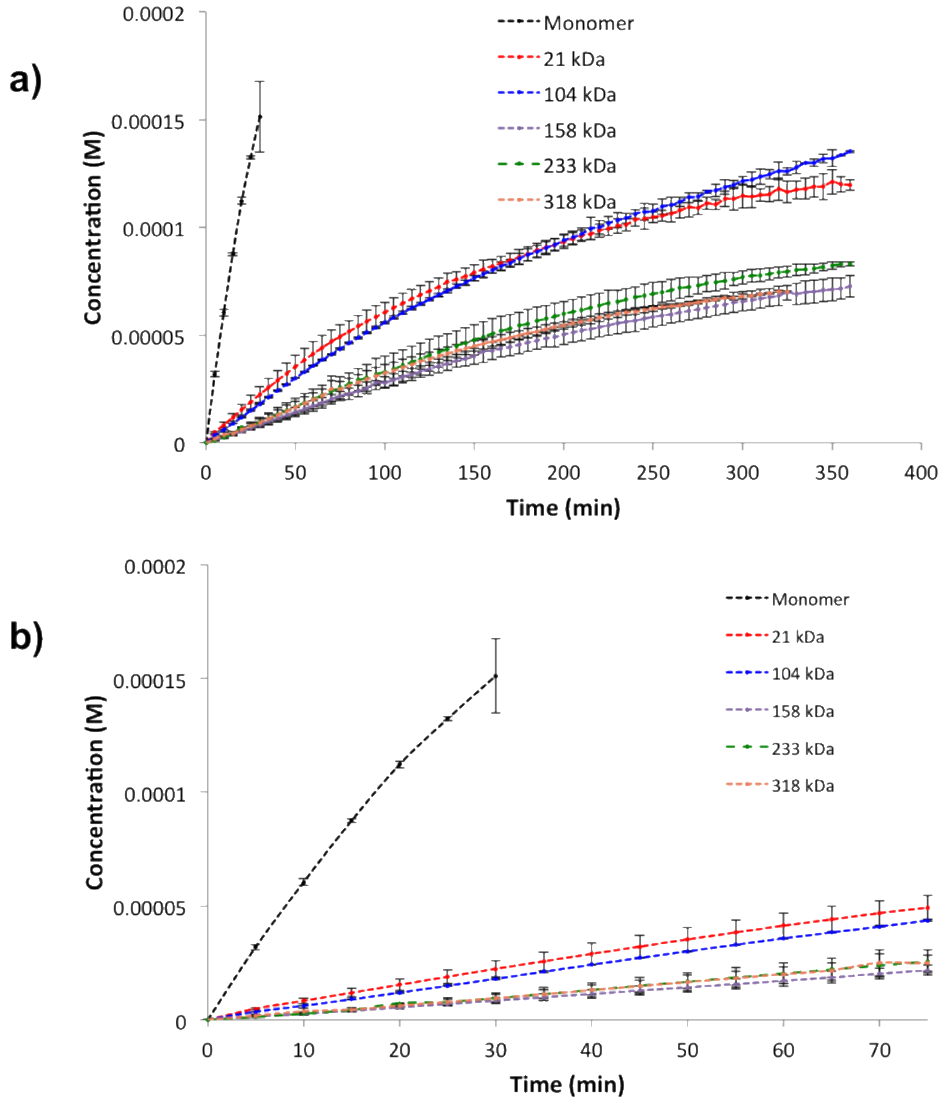

Figure D.11 a) time dependent polymer transport across Celgard 2325 at 0.01M in acetonitrile; b) linear region of the time dependent polymer transport.

D.7.2 Time Dependent $LiBF_4$ Diffusion across Celgard 2325 Separator

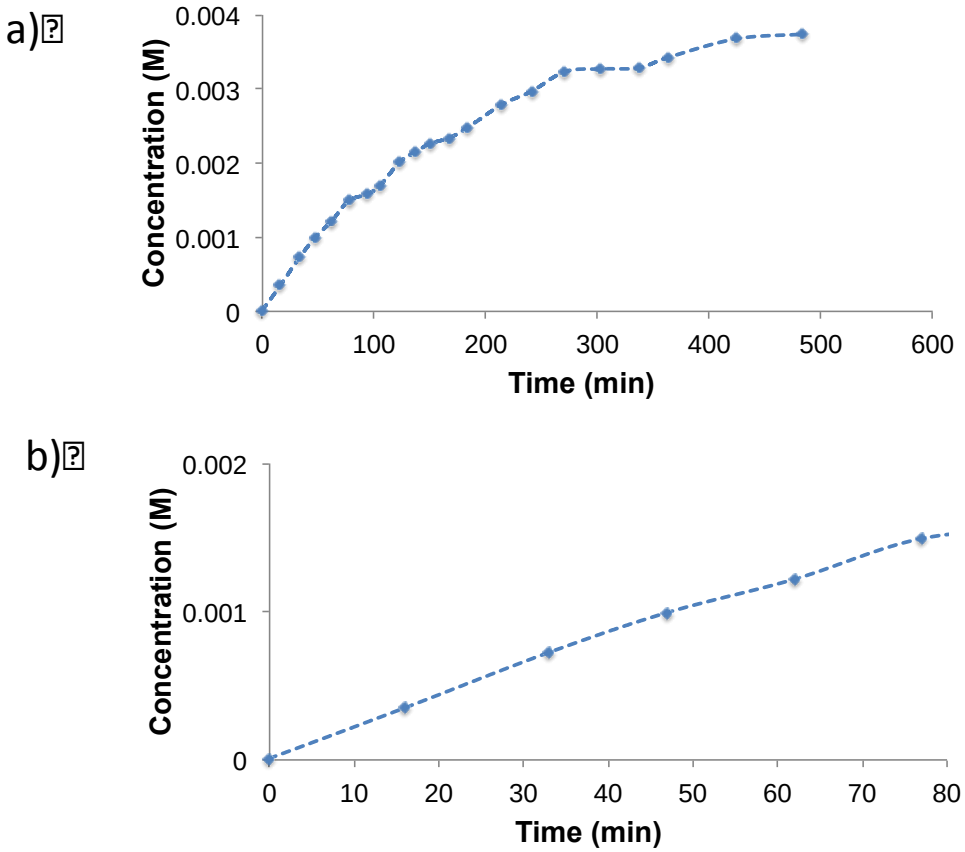

Figure D.12 a) time dependent $Li^+BF_4^-$ transport across Celgard 2325 at 0.01M in acetonitrile; b) linear region of the time dependent $Li^+BF_4^-$ transport.

D.7.3 Theoretically Predicted Steric Partition Coefficient for Linear Polymers as a Function of Relative Polymer Size[3]

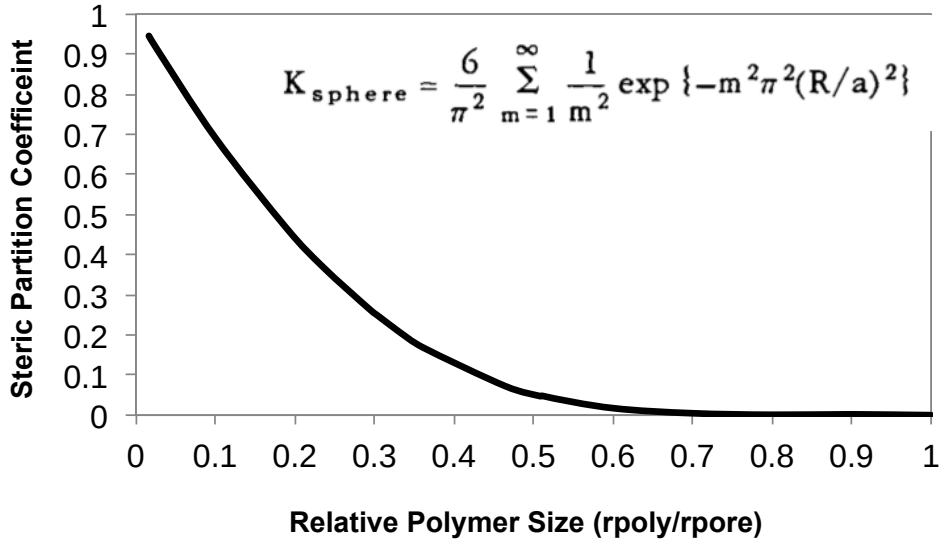

Figure D.13 Theoretically Predicted Steric Partition Coefficient (K_{sphere}) for Linear Polymers as a Function of Relative Polymer Size (R= r_{poly}= polymer Solvodynamic radius; a= r_{pore}= separator pore radius).

D.7.4 RAP Molecular Weight Dependent Rejection Across COTS Separators

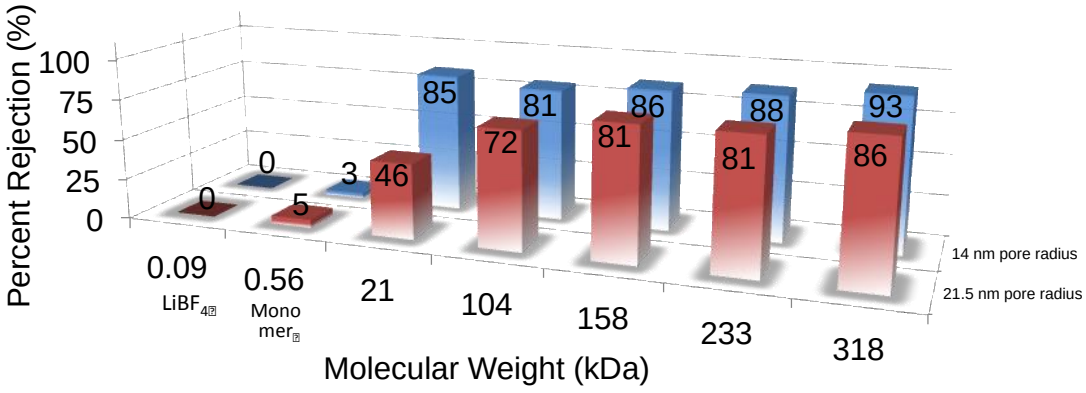

Figure D.14 Percent rejection of monomer and **RAPs 1-5** across COTS porous separators.

D.7.5 Equations to Calculate Polymer Rejection and Permeability[4]

$$\text{Percent Rejection across membrane (\%)} = [1- (2C_f /C_i)] \times 100$$

C_f = concentration in the receiver compartment after 24 hours; C_i = initial concentration in the donor compartment

$$\text{Permeability} = V_B \times L \times (dC_B /dt) / (A \times (C_A – C_B (t)))$$

P = Permeability; $dC_B(t)/dt$ = Slope from the linear region of concentration vs. time plot; C_A = initial concentration in donor compartment; V_B = solution volume in the receiver compartment; A = Area of orifice; L = Thickness of Celgard 2325 separator; C_B (t) = time dependent polymer concentration in the receiver compartment

D.7.6 RAPs Solvodynamic Radius

Table D.6 Data used in the calculation of the solvodynamic radius for RAPs 1-5.

Molecular weight (kDa)	Diffusion Coefficient (D) at 10^{-2}M (10^{-10} m^2/s)	Viscosity (V) at 10^{-2}M (Pa.s)	Relative size (D_mV_m/D_pV_p)	Solvodynamic radius (Relative size * 0.35) nm
0.56	13.9	0.009311	1	0.35
21	1.22	0.009060	12	4.1
104	0.95	0.009426	14	5.1
158	0.67	0.009451	20	7.2
233	0.73	0.009532	19	6.5
318	0.66	0.009636	20	7.1

m= monomer, p=polymer; radius of the monomer (0.35 nm) was obtained from Spartan

D.7.7 RAPs Adsorption onto Membrane

Two types of experiments were carried out to test the adsorption of RAPs on to the membrane. In the first experiment, the membrane used for the transport measurements was rinsed with acetonitrile and soaked in acetonitrile for 6 hours to dissolve any polymer adsorbed on to the membrane into the solution. The absorption spectrum of the resultant solution was recorded to determine the amount of polymer adsorbed on to the membrane. Negligible amount of polymer adsorption (~0.05%) is observed even for the highest molecular weight RAP and the adsorption is even low (<0.02%) for the monomer and the lowest molecular weight RAP. In the second experiment, the membrane was soaked in 0.01M, the concentration at which the transport measurements was carried out, polymer solution for 24h. Percent polymer adsorption was determined by recording the UV-Vis absorption spectrum of the solution before and after soaking the membrane. Negligible amount of polymer adsorption is observed, which corroborates well with the results from the first experiment.

Table D.7 Weight percent of polymer adsorbed onto the membrane.

	Initial amount of polymer in the bulk solution (mg)	**Amount of polymer adsorbed (mg)**	**Weight percent of polymer adsorbed**	**Amount of polymer adsorbed per unit area (mg/ cm^2)**
0.56 (Monomer)	19.2	0.0015	0.0080	0.0079
21	20.1	0.0027	0.013	0.0138
318	20.1	0.0084	0.042	0.0428

D.8 Charge/Discharge Behavior in a Proxy Non-Aqueous Redox Flow Cell

Electrochemical cell: We used a home-built two-chamber Teflon cell where the Celgard separator was sandwiched between the two electrolyte receptacles and making a tight seal using o-rings. The solution containers were stirred using similar settings to those used in the bulk electrolysis experiments, Figure 6.4 in the main manuscript. The electrolyte used in these experiments was 0.25 M $LiBF_4$ in acetonitrile. The first chamber contained 10 mM RAP and used an immersed Pt mesh electrode as the working electrode. The auxiliary electrode compartment used a commercial $LiNi_{0.33}Mn_{0.33}Co_{0.33}O_2$ electrode (NMC) from Sigma-Aldrich. This electrode is supported on an Al current collector. Both the RAP solution and the NMC electrode were charged in separate experiments previous to use in the electrochemical cell: the RAP solution was electrolyzed following the procedure of Figure 6.4 and the NMC electrode was charged to a capacity at least two times that of the nominal RAP charge but within stable limits for the metal oxide. Experiments were performed in galvanostatic mode. We experimentally determined that a C rate of 1/10 was adequate for this system. For the ~7.7 C of species used in the RAP compartment, this corresponded to 0.2 mA of current passed. The cell was not charge/discharged to completion, in order to avoid unwanted reactions, however, a charge capacity of 44% was observed under these conditions.

Results: All experiments were conducted in Ar-filled drybox with low traces of water and oxygen. The open circuit voltage of the cell approximated very well the predicted value calculated based on the state of charge of each individual electrode/compartment as shown in Table D.8.

Figure D.15 shows that the cell showed stable charge and discharge with a single plateau during the first cycle. Because the voltage limits were constrained to a narrow range in order to

prevent the second viologen reduction process or decomposition of the cathode, we observed approximately a ~45% Coulombic efficiency for this system. Upon multiple cycles, a stable profile was obtained, as shown in Figure D.16, however a decrease in the absolute charge passed on the system was observed. Electrolyte samples from each compartment were obtained after the end of each run, typically after operating for more than 18 h. These samples were analyzed through UV-Vis (Table D.4) to compare the crossover of RAP. Visually, Figure D.17 shows that the RAP compartment displayed a vivid color due to the presence of viologen species, but the auxiliary electrode compartment showed a much lower viologen concentration. Table D.9 shows the ratio of viologen concentration in the RAP compartment to that of the auxiliary electrode compartment for selected RAP 5 and RAP 1 experiments. These numbers are in good agreement with the trends observed in the diffusion cell experiments shown in the main text, Figure 6.7. Figure D.17 also shows that the Celgard separator showed excellent mechanical stability in the used setup and after hours of continuous stirred operation. As a simple confirmation of the data shown in Table D.7, few RAP residues where observed to remain on the membrane.

Table D.8 Summary of open circuit potentials (OCP) changes in charged NMC cathode ($LiNi_{0.33}Mn_{0.33}Co_{0.33}O_2$), anolyte (RAP 5), and combined flow cell system in 0.25 M $LiBF_4$. Average OCP in flow cell was 1.11 ±0.05 V. Predicted OCP based on summation of cathode and anode OCPs is 1.27 ±0.05 V.

OCP of charged metal oxide	OCP of electrolyzed RAP 5 solution	Predicted Open circuit voltage / V	Observed open circuit voltage in flow cell / V
0.54	-0.78	1.32	1.17
0.43	-0.81	1.24	1.07
0.41	-0.83	1.24	1.09

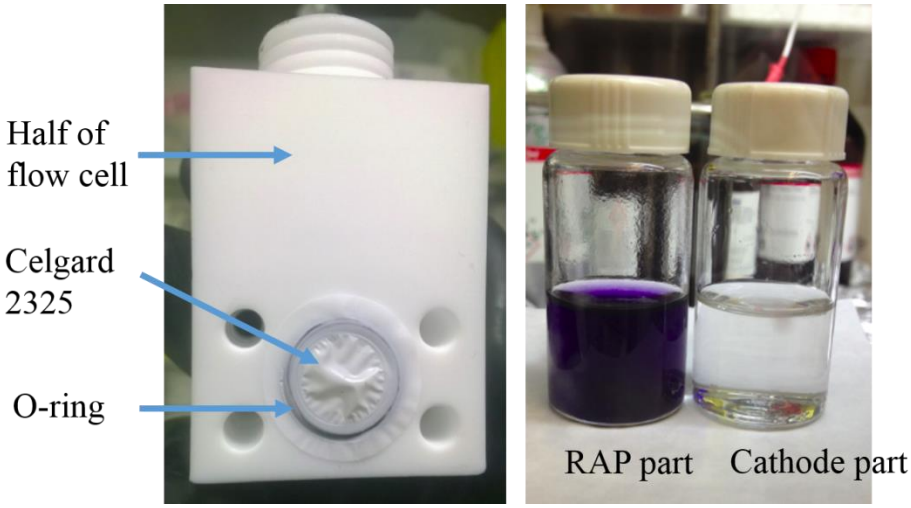

Figure D.15 Electrolytes and membrane after prolonged redox flow cell operation. Right: RAP compartment solution (on the left) and NMC compartment solution (on the right) evidence that crossover was limited between these two compartments. Left: Celgard separator shows mechanical stability during setup and prolonged use, as well as little evidence of RAP adsorption.

Table D.9 RAP cross-over ratios after operation of flow cell during at least 18 h. Representative results for RAP 1 and RAP 5.

Sample	RAPs concentration ratio of anode side over cathode side	RAPs Crossover (%)
RAP 1	5.7	15
RAP 5 – test 1	30.4	3
RAP 5 – test 1	42.9	2

D.9 References

1. Heinen, S.; Walder, L. Generation-dependent intramolecular CT complexation in a dendrimer electron sponge consisting of a viologen skeleton. *Angewandte Chemie International Edition* **2000**, *39*, 806-809.

2. Okawara, M.; Hirose, T.; Kamiya, N. Preparation of Polymers Containing Viologen Structure and Their Redox Behavior. *J. Polym. Sci., Part A: Polym. Chem.* **1979**, *17*, 927-930.

3. Casassa, E. F. Equilibrium Distribution of Flexible Polymer Chains Between a Macroscopic Solution Phase and Small Voids. *Journal of Polymer Science Part C-Polymer Letters* **1967**, *5*, 773-778.

4. Mai, Z.; Zhang, H.; Li, X.; Bi, C.; Dai, H. Sulfonated poly(tetramethydiphenyl ether ether ketone) membranes for vanadium redox flow battery application. *Journal of Power Sources* **2011**, *196*, 482-487.